Trinity College Dublin
Coláiste na Tríonóide, Baile Átha Cliath
The University of Dublin

ANALYSING THE EFFECTS OF 3D PRINTING DEFECTS AND SURFACE ROUGHNESS ON THE PROPERTIES OF ACOUSTIC MATERIALS

Agnieszka Helena Ciochon

Supervisor: Dr. John Kennedy

Department of Mechanical, Manufacturing & Biomedical Engineering
Trinity College Dublin, *the University of Dublin*
Ireland

2024

A dissertation submitted to the University of Dublin in partial fulfilment of the requirements for the degree of Doctor of Philosophy

Declaration

I declare that this thesis has not been submitted as an exercise for a degree at this or any other university and it is entirely my own work.

I agree to deposit this thesis in the University's open access institutional repository or allow the library to do so on my behalf, subject to Irish Copyright Legislation and Trinity College Library conditions of use and acknowledgement.

Agnieszka Helena Ciochon,
December 2023

Abstract

The principal aim of the research reported in this thesis was to investigate the influence of additive manufacturing on the acoustic performance of 3D printed periodic materials. First, a benchmark material design was manufactured using three different 3D printing technologies. The quality of produced samples was inspected using several non-destructive testing techniques. Realistic computational geometries of samples produced via extrusion-based additive manufacturing were created based on surface profiles obtained with confocal microscopy. This data was then used to update an existing numerical model, which initially assumed a smooth surface finish of the benchmark unit cell. The rough computational geometries were proposed as an enhanced unit cell design and produced using photopolymerisation-based additive manufacturing technology in the next step. Finally, a new 3D printed acoustic-material solution was also designed based on the benchmark unit cell. This acoustic material solution was produced via extrusion-based additive manufacturing and inserted into the interior of a commercial building acoustics silencer for performance enhancements.

The presently-reported research confirmed that additive manufacturing has an acoustic impact (increase of magnitude of absorption, operating frequency shift) on the performance of designed material due to the distortion of idealised, smooth computational geometry caused by layer-by-layer fabrication and additional 3D printing defects. Surface roughness resulting from the staircase effect is partially responsible for the mismatch between numerical predictions and experimental results. It can be used for acoustic gains by enhancing the smooth, benchmark design with additional artificial roughness applied to its surfaces. This thesis has also shown that acoustic materials can be designed for target frequencies of interest to enhance the broadband behaviour of foam liners and improve the acoustic performance of the off-shelf components.

Żegnaj Irlandio, czas w drogę mi już
W porcie gotowa stoi moja łódź.
Na wielki ocean przyjdzie mi zaraz wyjść
I pożegnać sie z dziewczyną na Lough Sheelin.

- szanta "Jasnowłosa"
(na podstawie tradycyjnej irlandzkiej piosenki "Lough Sheelin Side")

To my Family,
for their everlasting support and faith in me.

Acknowledgements

I want to express my deepest gratitude to my supervisor, Dr John Kennedy, for the patient guidance, encouragement and advice he has provided during my PhD degree.

I am also thankful to my funding agency, the Irish Research Council, for sponsoring my research through the Government of Ireland Postgraduate Scholarship Programme. My work was funded through the IRC Postgraduate Award GOIPG/2019/2927 "Advanced acoustic metamaterials for noise reduction, optimised for additive manufacturing technologies".

I wish to acknowledge the COST Action DENORMS (CA 15125) and, in particular, Dr Tomasz G. Zielinski, Department of Intelligent Technologies, Institute of Fundamental Technological Research of the Polish Academy of Sciences, who proposed the design of the unit DENORMS cell.

I would like to acknowledge the AMBER Additive Research Lab for facilitating the manufacturing of metal test specimens and the AR Lab staff for providing training and guidance on the manufacturing process.

I would like to thank Prof. Avraham Hirschberg for his valuable insights and help with developing analytical models.

I want to extend my sincere thanks to Dr Raphaël Leiba for his insights and guidance.

I also had the pleasure of collaborating with Dr Lara Flanagan and Dr Muhammad.

Special thanks to Michael Reilly and all the Technical Staff at the Department for all their help during my PhD.

I cannot begin to express my thanks to Lionelek for his relentless support, patience and helpful advice, and for always encouraging me to write, write, write.

The completion of my dissertation would not have been possible without the support of my great friends, Elena and Tuhina, thanks to whom I know where (not) to eat alone in Dublin.

I very much appreciate Aga Szot and all the artists and volunteers involved in The Icon Factory, thanks to whom Dublin became a home away from home during these years.

I would also like to extend my deepest gratitude to my family: my parents, Elżbieta and Krzysztof, my brother Piotr, and my sister-in-law Anna, who were always there for me in good and bad times, and never wavered in their support.

List of publications

The following is a list of key publications associated with this work:

Journal publications

- A. Ciochon, J. Kennedy, R. Leiba, L. Flanagan, and M. Culleton, “The impact of surface roughness on an additively manufactured acoustic material: An experimental and numerical investigation”, Journal of Sound and Vibration, vol. 546, p. 117434, Mar. 2023, doi: 10.1016/j.jsv.2022.117434.

- A. Ciochon, J. Kennedy, “Efficient modelling of surface roughness effects in additively manufactured materials” *(Manuscript submitted to Applied Acoustics, September 27 2023)*

Conference proceedings

- A. H. Ciochon, J. Kennedy, R. Leiba, and L. Flanagan, “The Impact of Additive Manufacturing on the Acoustic Performance of Novel Porous Materials”, in 28th AIAA/CEAS Aeroacoustics 2022 Conference, Southampton, UK, Jun. 2022. doi: 10.2514/6.2022-2903

- A. Ciochon, J. Kennedy, and M. Culleton, “Evaluation of surface roughness effects on additively manufactured acoustic materials”, in 30th ISMA - International Conference on Noise and Vibration Engineering, Leuven, Belgium, Sept. 2022.

- A. Ciochon, J. Kennedy, “Practical guidance on the additive manufacturing of acoustic materials”, in 52nd International Congress and Exposition on Noise Control Engineering (INTER-NOISE 2023), Chiba, Greater Tokyo, Japan, Aug. 2023

- A. Ciochon, J. Kennedy, “3D printed acoustic materials for the performance enhancement of a building acoustics silencer”, in 52nd International Congress and Exposition on Noise Control Engineering (INTER-NOISE 2023), Chiba, Greater Tokyo, Japan, Aug. 2023

List of conference presentations

The following is a list of conference presentations associated with this work:

- A. H. Ciochon, J. Kennedy, R. Leiba, and L. Flanagan, "The Impact of Additive Manufacturing on the Acoustic Performance of Novel Porous Materials", in 28th AIAA/CEAS Aeroacoustics 2022 Conference, Southampton, UK, Jun. 2022. doi: 10.2514/6.2022-2903
- A. Ciochon, J. Kennedy, and M. Culleton, "Evaluation of surface roughness effects on additively manufactured acoustic materials", in 30th ISMA - International Conference on Noise and Vibration Engineering, Leuven, Belgium, Sept. 2022.
- A. Ciochon, J. Kennedy, "Practical guidance on the additive manufacturing of acoustic materials", in 52nd International Congress and Exposition on Noise Control Engineering (INTER-NOISE 2023), Chiba, Greater Tokyo, Japan, Aug. 2023
- A. Ciochon, J. Kennedy, "3D printed acoustic materials for the performance enhancement of a building acoustics silencer", in 52nd International Congress and Exposition on Noise Control Engineering (INTER-NOISE 2023), Chiba, Greater Tokyo, Japan, Aug. 2023

Contents

List of Figures

List of Tables

List of Abbreviations

ABS	Acrylonitrile Butadiene Styrene
CAD	Computer-Aided Design
CT	Computed Tomography
DENORMS	Designs for Noise Reducing Materials and Structures
DIW	Direct Ink Writing
DLP	Digital Light Processing
DMD	Digital Micromirror Device
EU	European Union
FDM	Fused Deposition Modeling
FEM	Finite Element Method
FFF	Fused Filament Fabrication
FS	Fluid Shell
HVAC	Heating, Ventilation, and Air Conditioning
IPA	Isopropyl Alcohol
LCD	Liquid Crystal Display
LH	Layer Height
MSLA	Masked Stereolithography
NDT	Non-Destructive Testing
PDMS	Polydimethylsiloxane
PLA	Polylactic Acid

PBF	Powder Bed Fusion
SLA	Stereolithography
SLM	Selective Laser Melting
SLS	Selective Laser Sintering
STAM	Science and Technology in Advanced Manufacturing
STL	Standard Tessellation Language
TPP	Two-Photon Polymerization
VAV	Variable Air Volume
WHO	World Health Organisation

Nomenclature

Acronyms

α	Sound absorption coefficient
β_T	Isothermal compresibility [Pa^{-1}]
δ_t	Thermal boundary layer thickness [m]
δ_v	Viscous boundary layer thickness [m]
γ	Adiabatic index
κ	Bulk modulus [$\mathrm{N\,m^{-2}}$]
λ	Wavelength [m]
μ	Dynamic viscosity [Pa s]
μ_b	Bulk viscosity [Pa s]
ν	Kinematic viscosity [$\mathrm{m^2\,s^{-1}}$]
ω	Angular frequency [$\mathrm{rad\,s^{-1}}$]
Φ	Porosity
ρ	Mass density [$\mathrm{kg\,m^{-3}}$]
ρ_0	Density of air [$\mathrm{kg\,m^{-3}}$]
$\tilde{R}$	Gas constant [$\mathrm{J\,mol^{-1}\,K^{-1}}$]
$\tilde{T}$	Temperature [K]
A_c	Cross-sectional area of the neck of a Helmholtz resonator [$\mathrm{m^2}$]

b	Distance between hole centres of a microperforated panel [m]
c	Speed of sound [$\mathrm{m\,s^{-1}}$]
C_d	Maximum cure depth in photopolymerization-based additive manufacturing [m]
c_0	Speed of sound in air [$\mathrm{m\,s^{-1}}$]
C_p	Heat capacity [°C]
D	Depth of a the airspace of a microperforated panel [m]
d	Perforation diameter [m]
D_p	Penetration depth in photopolymerization-based additive manufacturing [m]
d_v	Displacement thickness [m]
E_c	Critical energy required to initiate polymerization [J]
E_{max}	Maximum exposure energy at the surface [J]
f	Frequency [Hz]
f_r	Resonance frequency of a Helmholtz resonator [Hz]
H	Distance between perforations [m]
H_{12}	Complex transfer function
I^+	Energy flux along the duct in a positive direction [$\mathrm{J\,m^{-2}\,s^{-1}}$]
I^-	Energy flux along the duct in a negative direction [$\mathrm{J\,m^{-2}\,s^{-1}}$]
k	Wave number [$\mathrm{m^{-1}}$]
L	Perforation depth [m]
l_{eff}	Effective neck length of a Helmholtz resonator [m]
L_p	Perimeter of the duct cross-section [m]
L_{SP}	Measurement length of a surface profile [m]
M	Number of perforations in a multiple side branch model

N	Number of rows in a multiple side branch model
n	Number of perforations in a single lumped side branch model
p	Wave amplitude [Pa]
p^+	Wave amplitude of the acoustic wave propagating in a positive direction [Pa]
p^-	Wave amplitude of the acoustic wave propagating in a negative direction [Pa]
p_i^+	Wave amplitude of the acoustic wave leaving the muffler [Pa]
p_t^+	Wave amplitude of the acoustic wave entering the muffler [Pa]
Pr	Prandtl number
R	Sound reflection coefficient
Ra	Average roughness [µm]
S	Surface area of the duct cross-section [m^2]
S_H	Open area of a single tube in a simplified porosity model [m^2]
S_h	Surface area of the side branch (lumped row of M perforations) in a multiple side branch model [m^2]
S_{in}	Cross-sectional area of the duct at the muffler inlet [m^2]
S_{out}	Cross-sectional area of the duct at the muffler outlet [m^2]
S_p	Cross-sectional area of one perforation of a microperforated panel [m^2]
S_T	Surface area of a single tube in a simplified porosity model [m^2]
S_t	Surface area of a lumped perforation [m^2]
St	Stoke's number
T	Sound transmission coefficient
t	Time [s]
T_0	Temperature of air [K]

TL	Sound transmission loss [dB]
u	Acoustic particle velocity [$\mathrm{m\,s^{-1}}$]
V	Enclosed cavity volume of a Helmholtz resonator [$\mathrm{m^3}$]
V_{pore}	Accesible pore volume in the simplified porosity model [$\mathrm{m^3}$]
V_{total}	Total volume in the simplified porosity model [$\mathrm{m^3}$]
W_i	Acoustic energy flux entering the muffler [$\mathrm{J\,m^{-2}\,s^{-1}}$]
W_t	Acoustic energy flux leaving the muffler [$\mathrm{J\,m^{-2}\,s^{-1}}$]
$y(x)$	Distance of the measurement point on the surface profile from the measurement centerline [m]
Z	Acoustic impedance [$\mathrm{kg\,m^{-2}\,s^{-1}}$]
z	Acoustic impedance
Z_0	Specific acoustic impedance [$\mathrm{kg\,m^{-2}\,s^{-1}}$]

Chapter 1

Introduction

1.1 Context and research motivation

Public awareness of noise and its associated health risks has improved over the last few years. According to the Directive 2002/49/EC of the European Parliament and of the Council relating to the assessment and management of environmental noise, all member states of the European Union (EU) are obliged to compose strategic noise maps, develop noise action plans and inform the public about the present situation [1]. From 2007 onwards, noise maps shall be prepared for all significant agglomerations, roads, railways and airports within the territory of a given country.

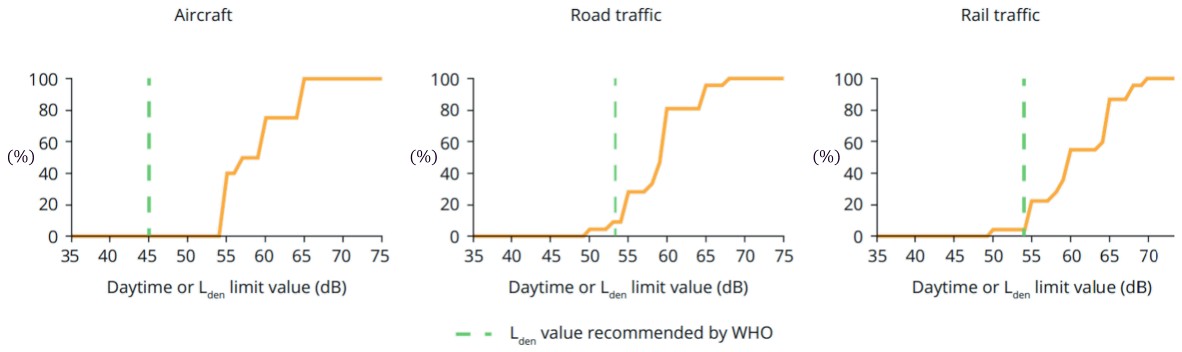

Figure 1.1: Percentage of European countries with a limit value of aircraft, road and rail traffic noise lower than or equal to x-axis value (reproduced from [2])

Each member state establishes for itself the maximum level of environmental noise to which its citizens may be exposed. The national limits primarily target industrial and transportation sources, such as road, rail and air traffic. In most cases, however, they do not reflect the values recommended by the World Health Organisation (WHO) published in their report 'Environmental Noise Guidelines for the European Region' in 2020, as illustrated in Figure 1.1 [2]. For example, in the case of aircraft noise, none of the EU members meets the WHO requirements. Regarding road and rail traffic, only about 5 % of member states comply with the WHO recommendations.

For this reason, noise pollution remains a critical issue to tackle in the near future. Standard acoustic solutions to reduce excessive noise include: decreasing its level at the source or the receiver's position. This is traditionally achieved by applying acoustic treatments in the form of conventional acoustic materials capable of absorbing sound waves. However, these materials have several disadvantages, such as being effective only in the higher-frequency range and the fact that these are often bulky. As the wavelength is inversely proportional to frequency, absorbers designed for low-frequency sounds require much space to be effective.

Porous materials absorb sound waves well when their thickness is at least a quarter of a wavelength or when placed at a distance of about a quarter of a wavelength from the wall. For instance, the quarter wavelength of a 63 Hz wave in the free air is around 1.4 m. On the other hand, the speed of sound in air-saturated porous materials is lower than in air, which means that at a given frequency, the corresponding wavelength is also shorter. Moreover, at low frequencies, the speed of sound in porous media is usually much less than 343 m/s, so, for example, a quarter wavelength at 63 Hz in a porous medium is much shorter than 1.4 m.

The development of alternative acoustic solutions has mostly been industry-driven. Indeed, the EU is the world's second-largest consumer market, and it is in manufacturers' interest to comply with the binding standards and regulations. Above all, the aviation industry could benefit from introducing novel acoustic materials. Considering the rapid growth of air traffic and its negative environmental impact, authorities have introduced penalties for airlines operating non-compliant machines [3]. Such sanctions and potential future taxes are supposed to encourage companies to invest in new technologies.

Several factors must be considered for the commercial success of alternative acoustic treatments addressing aviation noise, including that the material weight must be reduced to a minimum so that the fuel efficiency and aeroplane performance are not significantly affected. Currently, commonly used solutions include acoustic liners with a resonant honeycomb structure, which are incorporated into the inner walls of the nacelle of a jet engine. Although classical liners can achieve quite a good absorption around a specific 'noisy' frequency, it makes research sense to explore the potential benefits of novel materials. This is because modern aircraft engines can lead to a reduction in the emitted noise but, at the same time, widen its frequency band, which would require the development of new noise-absorbing nacelle liners.

Acoustic comfort is another driving force behind the development of novel noise-reduction technologies, as it undoubtedly plays a significant role in consumer behaviour regarding purchase decisions. This is, for example, crucial in the automotive industry. Indeed, the passenger cabin of an automobile behaves like a resonance chamber. Automobile manufacturers employ sound absorption elements to reduce the noise level of their vehicles. However, these materials require additional space and weight, which can result in reduced: fuel efficiency, mileage, tires and trackpads lifetime and vehicle acceleration [4]. Ergo, as was asserted above, investigating novel materials makes sense.

The aeronautic and automotive industries are just two examples of potential sectors that would be interested in the development of novel acoustic materials. These should overcome two major limitations of conventional materials: size, weight and ability to operate in the entire frequency spectrum, or at least at frequencies lower than those typical for conventional acoustic materials.

Improved material properties would also be useful for architectural acoustics. Efficient, accessible, durable, low-cost, low-tech materials would find many applications across private homes, industrial sites and offices. These acoustic solutions would be beneficial in minimising the negative effects of noise exposure in terms of human health, acoustical comfort, communication and speech privacy, which affect our personal and professional lives.

For instance, the heating, ventilation, and air conditioning (HVAC) systems commonly present in workplaces and private homes are significant sources and transmitters of noise, leading to disturbances and annoyance. A combination of different processes causes the HVAC noise. The primary sources contributing to the overall noise levels differ over the frequency range.

The fan and pump noise dominates the lower-frequency range (125 Hz - 500 Hz octave bands). The medium-frequency (250 - 1000 Hz octave bands) noise is airflow or turbulence-generated and is caused predominantly by variable-air-volume (VAV) units. Finally, dampers, diffusers and grilles are the primary noise sources in the higher-frequency range (1000 Hz - 4000 Hz octave bands) [5, 6].

Acoustic treatments are often applied to noise sources to decrease noise levels, improve speech communication, and meet environmental noise criteria. Among them, acoustic silencers are commonly used in industrial settings to reduce noise from machines and fluid-flow systems. Unlike acoustic enclosures, their primary objective is to reduce the transmission of acoustic energy without obstructing the airflow [7]. The silencer's open area, the silencer's length, and the air's velocity determine the silencer's acoustic and aerodynamic performance [6].

Among different acoustic silencers, absorptive silencers are especially popular in building acoustics. They are designed as waveguides lined with layers of fibrous or porous materials. However, as mentioned previously, these conventional absorptive materials, if not bulky, are less effective in the lower-frequency range. For that reason, acoustic silencers perform better at higher frequencies.

The need for improvements in the field of acoustic materials has recently evoked a lot of interest in metamaterials. Metamaterials are defined as a new class of composite materials whose properties exceed the boundaries of conventional materials and are not traditionally encountered in nature [8]. The chemical composition of the material used for their production influences their behaviour to a relatively minor extent [9]. Their unusual properties result primarily from the design of individual unit cells that make up the lattice structure. The main advantage of metamaterials over conventional solutions lies in their tunability.

The benchmark material analysed in the thesis is presented in Section 1.2, and the experimental methods used to evaluate its acoustic performance, in terms of normal incidence absorption and transmission loss, are outlined in Section 1.3. The information on 3D printers used for additive manufacturing is given in Section 1.4.

In the context of this study, while the benchmark geometry may not necessarily be classified as a metamaterial from a technical standpoint, its purpose is to explore the impact of 3D printing on acoustic characteristics. This investigation aims to pave the way for future material and metamaterial concepts suitable for additive manufacturing. More background information related to this thesis is provided in Chapter 2 and Chapter 3. In particular, acoustic materials and metamaterials are discussed in Chapter 2.

Scientific interest in the area of metamaterials requires accompanying advancements in production engineering. Notably, additive manufacturing, commonly referred to as 3D printing, in which objects are formed layer-by-layer, has been focused on. Essential information on 3D printing is summarised in Chapter 3.

What distinguishes additive manufacturing from traditional production methods is its ability to fabricate individually customised and highly complex functional parts [10]. However, several obstacles slow down its further growth. The most crucial ones include the following: the insufficient quality of finished parts (in terms of both geometric inaccuracies and the presence of defects), the lack of certification standards and protocols, the need for the development of real-time process monitoring techniques and the limited knowledge of the raw materials [11]. More details regarding 3D printing defects is provided in Section 3.2.

A better understanding of the additive manufacturing process must first be established for it to become a reliable tool for metamaterial production. Currently, 3D printing has an immense influence on the acoustic performance of fabricated parts (this will be discussed later in Section 3.3).

Once all the issues occurring during prototyping are eliminated, and the final design has been refined, the whole process must be transferred into an industrial setting. Commercializing metamaterials and adjusting the additive manufacturing process for mass production emerge as the next challenge and a growth opportunity for the research community. This, however, lies outside of this work's scope. In fact, large-scale manufacturability can be a real concern here since, as for now, 3D printing is more suitable for prototyping, and it should rather be replaced by faster and cheaper technologies suitable for mass production of large-area materials.

1.2 Benchmark geometry

Although the first acoustic metamaterials were proposed over 20 years ago, to this day, they remain mainly a matter of scientific curiosity. They have yet to progress towards being commercialized at an industrial scale. The working principles behind some metamaterial designs need to consider real-world operating conditions and realistic performance for industrial applications. The major issues hindering the practical development of acoustic metamaterials include their small-scale features, mechanical properties and large-scale manufacturability [12].

Industrially relevant design tools are required to unlock the potential of metamaterials, and developing these tools requires benchmark problems. Therefore, the first part of this thesis takes the form of a case study of a periodic porous acoustic material that was produced using three different additive manufacturing technologies: Fused Deposition Modelling (FDM), Masked Stereolithography (MSLA) and Selective Laser Melting (SLM). In the second part, we consider using a geometry similar to the DENORMS geometry to improve a resistive muffler designed for air conditioning systems by adding a reactive component.

1.2.1 DENORMS cell

The benchmark material examined in this study was proposed as a part of the European COST action DENORMS (Designs for Noise Reducing Materials and Structures). The design comprises periodically arranged unit cells. The resulting material array forms an open pore network, acting as a chain of resonators with multiple degrees of freedom.

From the point of view of effective elastic properties, i.e. the fourth-order elasticity tensor, this cell has a cubic anisotropy characterized by three elastic material constants depending on the isotropic properties of the material of the skeleton, but when considering the viscous flow through the pore network, i.e. the second order permeability tensor, the cell can be treated as an isotropic permeable material. It consists of an internal spherical cavity connected to neighbouring cells by cylindrical openings on each face. Incorporating spheres into the tube resonator results in a frequency shift, causing the peak frequency to move towards lower frequencies, which will be discussed later in Appendix E.

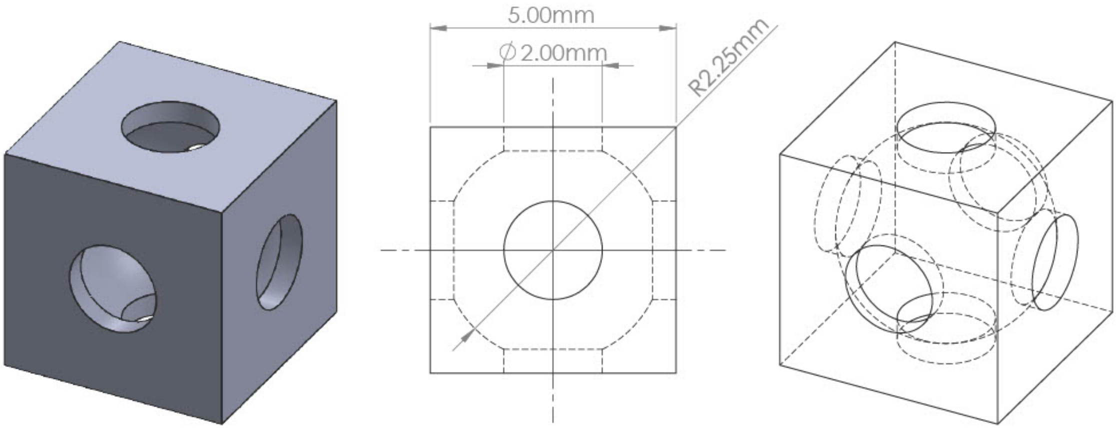

Figure 1.2: DENORMS cell geometry

The geometrical simplicity makes this design easy to manufacture and perform numerical modelling. The present work is a continuation of the DENORMS project [13–16]. In particular, the numerical modelling of sound absorption upon normal incidence used in the present study is based on the work of Flanagan [15].

The considered geometrical design depends on a couple of tunable dimensional parameters that can be easily altered to adjust the acoustic behaviour of the material. The analytical models presented in Appendix E can be used to find dimensions for the optimum absorption, as per Appendix E.1.1. However, in the first part of this study, the DENORMS cell is a cube with an edge length of 5 mm containing a spherical cavity of a 2.25 mm radius and connected by six cylinders with a diameter of 2 mm, as illustrated in Figure 1.2. Different geometrical parameters will be used in Chapter 7, which will be discussed thoroughly in Section 7.2.1.

It should be noted, however, that due to the additive manufacturing process, the actually obtained sample of the DENORMS geometry differs to a certain extent from the Computer-Aided Design (CAD). The occurring 3D printing inaccuracies are not uniform among different additive manufacturing technologies and impact the acoustic performance of the 3D printed lattices, which will be discussed in more detail in Section 3.3.

1.3 Acoustic measurements

1.3.1 Basic acoustic concepts

Before introducing the acoustic experimental techniques used in this work, a summary of the basic acoustics used for these measurements will be provided. The focus of the present work is on wave propagation in ducts at low frequencies, such that in first approximation, the acoustic field can be described by plane waves [17, 18].

We assume small perturbations of a stagnant uniform fluid of density ρ_0 and speed of sound c_0. In a duct of uniform cross-section harmonic acoustic perturbations $p'(x,t)$ at a given frequency f are given by:

$$p'(x,t) = \mathrm{Re}[\mathrm{p}(\omega,\mathrm{x})\mathrm{e}^{(\mathrm{i}\omega\mathrm{t})}] = \mathrm{Re}[\mathrm{p}^{+}\mathrm{e}^{\mathrm{i}(\omega\mathrm{t}-\mathrm{kx})} + \mathrm{p}^{-}\mathrm{e}^{\mathrm{i}(\omega\mathrm{t}+\mathrm{kx})}] \tag{1.1}$$

where $\omega = 2\pi f$ is the angular frequency, f is the frequency of the wave with the complex amplitude p, p^{+} is the amplitude of the pressure wave propagating along the duct in the positive x-direction, p^{-} is the amplitude of the wave propagating in the opposite direction, and k is the wave number.

In the applications considered, the viscous dissipation is limited to a thin boundary layer (Stokes layer) on the wall. As the duct considered is much wider than the Stokes layer, the wave number is given by:

$$k = \frac{\omega}{c_0}\left(1 + \frac{1}{4}(1-i)\frac{L_p}{S}\delta_v\left(1 + \frac{(\gamma-1)}{\sqrt{Pr}}\right)\right) \tag{1.2}$$

where L_p is the perimeter of the duct cross-section, S is the surface area of the duct cross-section, $\delta_v = \sqrt{\frac{2\nu}{\omega}}$ is the Stokes-layer thickness, ν is the kinematic viscosity, γ is the adiabatic index (i.e. heat capacity ratio) and Pr the Prandtl number for air [17, 18]. In Appendix A, the values used for the properties of air in this thesis are specified.

The order of magnitude of the Stokes layer thickness is $\delta_v \sim 10^{-4}$ m for 0.2 kHz $\leq$ f $\leq$ 3 kHz (the experimental conditions considered). When considering non-uniform duct cross-sections (actual DENORMS pore geometry), a numerical model will be used to predict the acoustic properties.

The energy flux along the duct I^{+} at $x = 0$ associated with the p^{+} wave is in first order approximation:

$$I^{+} = \frac{|p^{+}|^2}{\rho_0 c_0} \tag{1.3}$$

The energy flux I^- in the opposite direction is:

$$I^- = \frac{|p^-|^2}{\rho_0 c_0} \tag{1.4}$$

Considering wave reflection of an incoming p^+ wave at the plane $x = 0$, in a duct of uniform cross-section, we define the reflection coefficient R as:

$$R = \frac{p^-}{p^+} \tag{1.5}$$

It is assumed that the positive x-direction is towards the plane (wall) at $x = 0$. The absorption coefficient α of the wall is defined as the fraction of non-reflected energy flux:

$$\alpha = 1 - \frac{I^-}{I^+} = 1 - \left|\frac{p^-}{p^+}\right|^2 = 1 - |R|^2 \tag{1.6}$$

In practice, the wave amplitudes are determined by using the two-microphone transfer function method [19]. The schematic of the two-microphone impedance tube is illustrated in Figure 1.3.

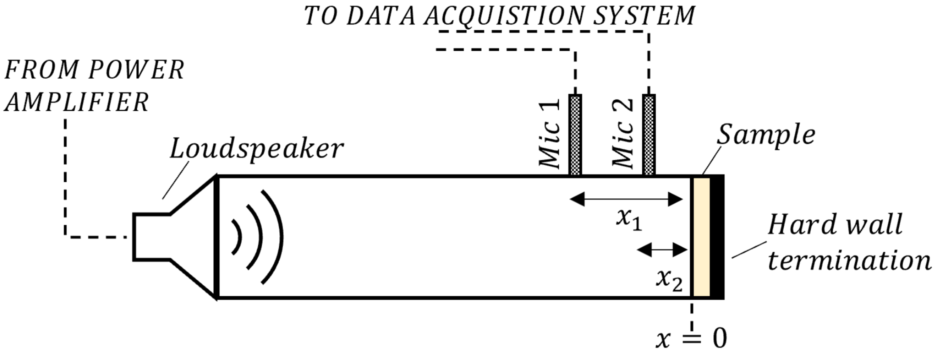

Figure 1.3: Two-microphone impedance tube schematic

For a set of two calibrated microphones placed at positions x_1 and x_2, the amplitudes of the pressures p_1 and p_2 can be related to the wave amplitudes p^+ and p^- at $x = 0$ by using the d'Alembert wave equation 1.1 for harmonic waves (neglecting friction losses):

$$p_1(\omega) = p(\omega, x_1) = p^+ e^{-ikx_1} + p^- e^{ikx_1} \tag{1.7}$$

and:

$$p_2(\omega) = p(\omega, x_2) = p^+ e^{-ikx_2} + p^- e^{+ikx_2} \tag{1.8}$$

This is a set of two equations from which p^+, p^- and R can be determined for a sample of absorbing material whose front face is at $x = 0$, and the back face is set on a hard wall, see Figure 1.3. Often the complex transfer function $H_{12} = \frac{p_2}{p_1}$ is determined experimentally. In terms of this transfer function, the reflection coefficient is given by:

$$R = \frac{p^-}{p^+} = \frac{e^{-ik(x_2-x_1)} - H_{12}}{H_{12} - e^{ik(x_2-x_1)}} e^{-2ikx_1} \tag{1.9}$$

This is the so-called two-microphone method [19].

When considering a muffler placed along a tube, we define the pressure transmission coefficient T as the ratio:

$$T = \frac{p_t^+}{p_i^+} \tag{1.10}$$

where p_i^+ is the amplitude of the acoustic wave entering the muffler (incident) and p_t^+ is that of the pressure wave leaving the muffler (transmitted).

The amplitudes p_i^+ and p_t^+ are, in practice, determined by applying the two-microphone method on each side of the muffler. The corresponding power transmission loss TL is defined as:

$$TL = -10 \log_{10} \frac{W_t}{W_i} \tag{1.11}$$

where W_i is the flux of acoustic energy entering the muffler (incident power) and W_t is the energy flux leaving the muffler (transmitted power).

In terms of the ratio T of the acoustic pressure amplitudes, this is:

$$TL = -10 \log_{10} \left(\frac{S_{out}}{S_{in}} |T|^2 \right) \tag{1.12}$$

where S_{in} is the cross-sectional area of the duct at the muffler inlet and S_{out} is that of the duct at the muffler outlet.

1.3.2 Normal incidence absorption

In this thesis, measurements of sound absorption coefficient under the normal incidence setup were performed using the two-microphone method according to ISO 10534-2 [19]. In this test, the sample is placed at one end of an impedance tube opposite to the loudspeaker at the other end. The loudspeaker generates an incoming pressure wave, and microphones measure sound pressures at two locations near the sample. The impedance is calculated based on the complex acoustic transfer function H_{12} of the two microphone signals, allowing then to compute R and α.

A custom test rig was used for the acoustic measurements, as shown in Figure 1.4 and previously reported in [13, 20, 21]. The impedance tube has a circular cross-section with an internal diameter of 40 mm and operates within the frequency range of 300 Hz to 5000 Hz. Analysed samples were precisely fitted into a sample holder and backed by a hard, reflective termination. A BMS 4591 loudspeaker connected through an amplifier to a National Instruments DAQ was mounted at the other end of the tube. The test signal used during measurements was chosen as a band-limited (250 - 5500 Hz) white noise at 90 dB.

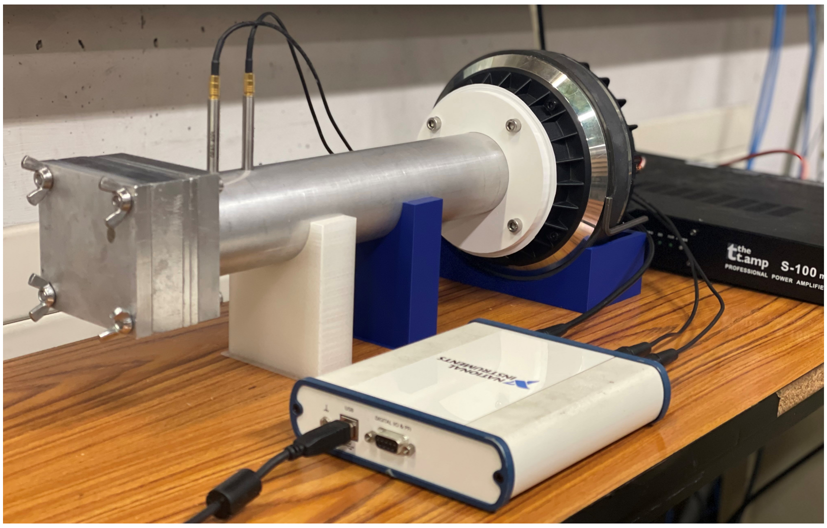

Figure 1.4: Experimental set-up (normal incidence absorption)

Two GRAS 40PL array microphones, which have a uniform frequency response within ±1 dB in the range of 50 Hz - 5 kHz and a dynamic range topping at around 150 dB, connected to the National Instruments DAQ, were used to record the test signal using a MATLAB interface. The microphones were first calibrated using the switching method described in the ISO standard [19]. In this work, the resulting spectral resolution was approximately 5 Hz, with the usage of the sample rate of 40 kHz and measurement duration of 240 s. A Hanning window with a 50 % overlap was used to compute the cross-power spectral density.

Each of the individual measurements of every sample investigated in this thesis was repeated three times, with the complete disassembly and reassembly of the sample holder, to account for repeatability in the testing procedure.

1.3.3 Transmision loss

In this thesis, the transmission loss was measured using an impedance tube in a normal incidence setup according to ASTM E2611 [22]. In this test, a sample (in this case, an acoustic silencer) is placed between two tube sections. The loudspeaker located at one end of the tube generates an incoming pressure wave. Two sets of calibrated microphone pairs, placed at two locations on each side of the sample, measure the sound pressure amplitudes p_i^+ and p_t^-, allowing then to compute the transmission loss.

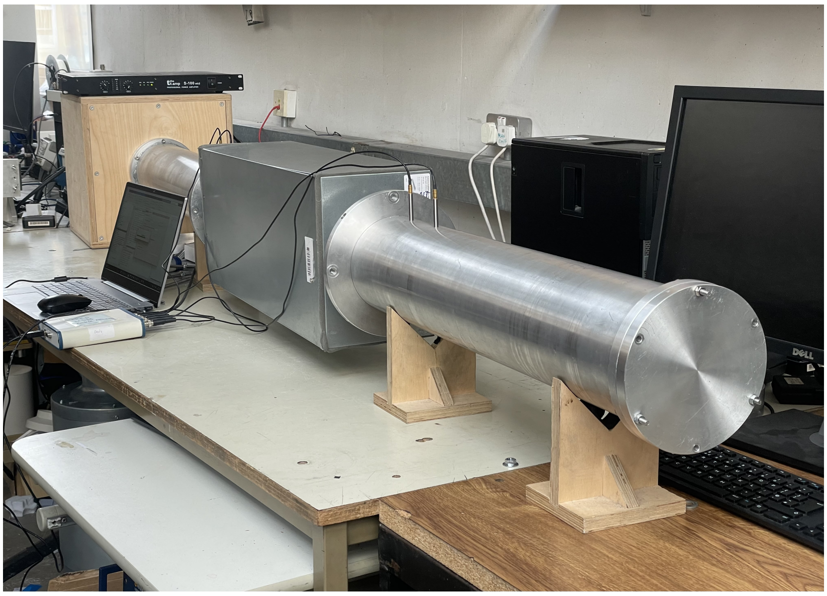

Figure 1.5: Experimental set-up (transmission loss) used in Chapter 7

The custom rig, shown in Figure 1.5, with a 12.7 cm internal diameter, was used for these tests. On the left-hand side of Figure 1.5, inside the wooden enclosure, there was the BMS 4591 speaker, which was driven by the output signal of a National Instruments DAQ amplified by a power amplifier. The test signal used during measurements was chosen as a band-limited (20 - 1500 Hz) white noise at 90 dB.

Four GRAS 40PL array microphones were chosen to instrument the rig as they have a frequency response (± 1 dB) in the region of 50 Hz - 5 kHz and an upper limit of the dynamic range of 135 dB re 20 μPa allowing for testing up to high-pressure amplitudes. The microphones were first calibrated using the switching method described in the ASTM standard [22]. The microphones were connected to the National Instruments DAQ, and the signals were recorded using a MATLAB interface. Similar to absorption measurements, the resulting spectral resolution was approximately 5 Hz, with the usage of the sample rate of 40 kHz and measurement duration of 240 s. A Hanning window with a 50 % overlap was used to compute the cross-power spectral density.

1.4 Additive manufacturing

In this thesis, the analysed samples were produced using different additive manufacturing technologies and different 3D printers, some of which are displayed in Figure 1.6.

The samples suitable for sound absorption tests were manufactured using all three machines: FDM-based Original Prusa MINI+ (Figure 1.6a), MSLA-based ELEGOO Mars 3 Pro (Figure 1.6b) and SLM-based Systems Prox DMP 200 (Figure 1.6c). The samples suitable for transmission loss tests were only produced using the FDM technology.

(a) Original Prusa MINI+ (b) ELEGOO Mars 3 Pro (c) Systems Prox DMP 200 [23]

Figure 1.6: 3D printers used to produce samples in this thesis

The technical specifications of 3D printers, as per manufacturers' data sheets, are summarised in Table 1.1. MSLA excels in achieving the smallest (finest) z-axis resolution values among considered technologies.

Machine	Original Prusa MINI+	ELEGOO Mars 3 Pro	Systems Prox DMP 200
Technology	FDM	MSLA	SLM
Materials	Polymers	Photopolymers	Metals
Layer height	0.05-0.25 mm	0.01-0.2 mm	0.03-0.05 mm
Build volume	180x180x180 mm	143x90x175 mm	140×140×125 mm
z-axis resolution	0.05 mm	0.00125 mm	0.05 mm

Table 1.1: Technical parameters of 3D printers used in this thesis

1.5 Research problem statement

The effects of the additive manufacturing process, particularly surface roughness, on the acoustic performance of 3D printed materials must be better understood.

Previous research did not include surface roughness arising from layer-by-layer fabrication during computational modelling. The presence of the staircase effect was commonly used to explain the lack of congruence between numerical or analytical predictions and experimental results. In these cases, a direct link from the surface roughness effect to the deviation between numerical and experimental results was not established, leaving the possibility of other contributing factors open.

From the acoustic point of view, 3D printing inaccuracies and other casual errors influence the designed material's behaviour [13, 24–26]. Generally speaking, the presence of most of these defects is usually considered a benefit as it improves the overall acoustic performance of the fabricated material. However, these are unplanned and, as such, usually uncontrollable, although the results of this and other recent works [14] show that their presence and the overall effect can be reproduced using the same 3D printer, material and process parameters. This was evidenced in this work for the effect of surface roughness. Other recent results confirm that such reproducibility can be achieved for the microporosity of the 3D printed skeleton [27, 28] and undesigned microfibers. For this reason, understanding the link between additive manufacturing and acoustic performance and then actively implementing this information into the optimisation of the target material design is of great value.

1.6 Research goal

The main goal of this research project was to gain a better understanding of the additive manufacturing process and use this information to help achieve acoustic improvements in the performance of 3D printed materials. This project was undertaken to design a novel cellular acoustic material suitable for additive manufacturing that has been enhanced through an iterative loop of numerical modelling and experimental validation and demonstrate a practical application of 3D printed materials.

In order to achieve this, several intermediate objectives were identified:

- To assess the acoustic influence of additive manufacturing on the performance of the benchmark material and compare it among different 3D printing technologies.

- To update existing numerical models to capture the actual manufactured material's performance and improve their suitability as a material design tool.
- To propose a novel material based on the benchmark unit cell's geometry but altered in such a way as to improve its acoustic performance, additively manufacture it and perform an acoustic evaluation to assess its effectiveness.
- To demonstrate a practical application of additively manufactured acoustic materials by designing, manufacturing and implementing a 3D printed lattice to enhance the performance of a commercial off-the-shelf building-acoustics silencer.

1.7 Thesis outline

This thesis consists of eight chapters and five appendices.

Chapter 1 serves as a general introduction to the reader and outlines the motivations for the project and the main research objectives.

Chapter 2 contains an extensive literature review on acoustic materials, and Chapter 3 discusses the additive manufacturing process, including its influence on the acoustic properties of 3D printed materials.

Chapter 4 is an acoustic assessment of three distinctive additive manufacturing technologies applied in this research: FDM, MSLA and SLM to produce the same benchmark geometrical design.

Chapter 5 outlines the research findings on the impact of surface roughness on the acoustic performance of additively manufactured parts. It explores the idea of accounting for 3D printing defects during numerical modelling.

Chapter 6 presents research findings on utilising the acoustic potential of 3D printing defects, such as surface roughness, during the design phase of novel materials. In such a way, lessons learnt from Chapter 5 were actively implemented to propose a new geometry based on a benchmark unit cell but altered for acoustic improvements.

Chapter 7 demonstrates a practical application of additively manufactured acoustic materials. It discusses the relevance of surface roughness consideration during the design of practical acoustical systems. Moreover, this chapter also exhibits the potential of novel solutions for the performance enhancement of off-the-shelf components, in this case, a commercial building acoustics silencer.

Chapter 8 serves as the summary of the thesis and presents the key conclusions drawn from the literature review and research results. It also contains suggestions for future work.

Appendix A outlines in detail the air parameters used in all models in this thesis.

Appendix B provides information on the meshing and mesh independence study of numerical models discussed in this thesis.

Appendix C discusses the impact of the bulk viscosity value of air set in models on the numerical sound absorption coefficient results.

Appendix D and Appendix E report work, which is related to the research treated in the main text. However, it was judged that their content is not central to the attainment of the research objectives laid out in Section 1.6. Given the peripheral nature of this information, it was relegated to the appendices. Specifically, Appendix D discusses the quality improvement of FDM parts. Appendix E introduces simplified analytical models used to describe occurring acoustic phenomena theoretically and compares analytical predictions with the numerical and experimental results presented in the previous chapters.

Chapter 2

Literature review on acoustic materials

2.1 Sound absorbing materials

The excessive noise emitted by various sources, including means of transport, machinery and equipment, can be reduced with the help of sound absorbers. Moreover, these materials are also utilised to decrease sound transmission through ducts and silencers. The functional principle of sound absorbers is to convert acoustic energy into heat [29].

Among different sound absorbers, the nonresonant and resonant are the two major groups. Nonresonant absorbers, also known as porous absorbers, are typically made of materials with a porous structure, such as mineral or glass wool [30–34]. Resonant absorbers employ resonant acoustic or vibratory mechanisms in their construction, utilizing elements like air columns or volumes, membranes, and plates [31, 33].

The sound absorption properties of most materials exhibit a significant frequency dependence, with porous materials being more effective at higher frequencies. However, by combining porous materials with resonant systems, it is possible to achieve a more uniform sound absorption across a wide range of frequencies.

2.2 Porous absorbers

The conversion of the acoustic energy into heat within porous absorbers occurs due to the viscous behaviour of air flowing through canals, pores and air pockets created by the skeleton of the material (accessible pore volume) [32]. Unsteady heat transfer between the air in the accessible pores and the walls also contributes to the damping of acoustic energy [34]. The viscous dissipation is most effective when the pore size is comparable to the Stokes layer thickness [35].

Porous materials, in which viscous dissipation effects predominate, can sometimes be modelled using an extremely simplified geometrical representation shown in Figure 2.1. The absorber is considered a skeleton with narrow air passages, represented by parallel and thin tubes extending into the material. The propagation of acoustic waves sideways can be neglected due to the assumption that the pressure is uniform in the directions transversal to the incoming plane wave and the porous material is homogeneous [33].

In this simplified model, the material thickness is assumed to be so large that there is no reflection of the acoustic waves propagating in the narrow pores (tubes). Reflection occurs only at the external surface of the porous material (inlet of the pores). In this model, the open area of a single tube has a surface area S_H, and each tube requires a surface area S_T. Assuming

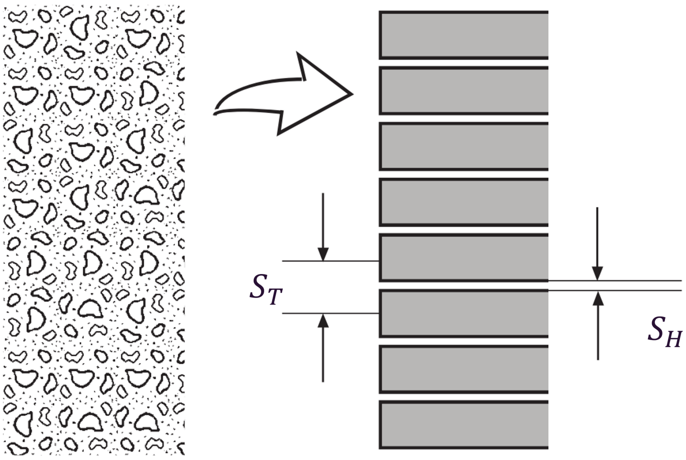

Figure 2.1: Simplified model of a porous sound absorber [18, 33]

the dimension of the region associated with one perforation is small compared to the acoustic wavelength, one can neglect the mass change in that region. Hence, in linear approximation (as considered here), the volume flux must be equal on both sides of the considered boundary. Therefore, the ratio of particle velocities, respectively, outside and inside the tube, is given by the ratio S_T/S_H. Furthermore, one assumes that the pressure field is continuous. Hence, the pressure of the external acoustic field at a distance of a few pore diameters from the surface of the porous material is the same as the pressure at the inlet of the pores. These two conditions (continuity of flux and pressure) imply an impedance transformation having the ratio S_T/S_H as the wave enters the porous material. The impedance ratio is then inserted into the expression for the reflection coefficient R, and the absorption coefficient α is given as per Equation (2.1) [33].

$$\alpha = \frac{4S_T S_H}{(S_T + S_H)^2} \tag{2.1}$$

The surface ratio S_H/S_T is a measure of the porosity of a material ϕ and given by Equation (2.2) [30, 32]

$$\phi = \frac{V_{pore}}{V_{total}} \simeq \frac{S_H}{S_T} \tag{2.2}$$

where V_{pore} is the accessible pore volume and V_{total} is the total volume. Indeed, resistive sound-absorbing porous materials should have high porosity and pore structures allowing flow through the material as only open pores are useful.

This simple approach is only valid in the higher frequency range. The absorption coefficient will approach the value given by Equation (1.6) asymptotically as the thickness of the porous layer increases, provided that S_H and S_T are correctly chosen. In particular, S_H should be similar to the so-called viscous characteristic length of the porous material modelled in this simple way. Note that for the actual slitted material, this length equals the slit width, whereas, for example, for the benchmark geometry shown in Figure 1.2, the viscous length will be similar to the cylindrical channel radius. When S_H is selected, S_T should be chosen with respect to it and the porosity in order to satisfy Equation (2.2).

The conversion of the acoustic energy carried by the wave into heat, which occurs in the air inside the material's pores, is caused by the losses induced by the viscosity of air. The generated heat is then transmitted to the material's skeleton. The viscous losses will be substantial, especially if the canals are very narrow. Porous materials are dispersive media, which means that the wave speed strongly depends on the frequency. For a porous material with a rigid frame saturated with air, the speed of airborne waves is always lower than the speed of sound in the free air, and it regularly decreases with frequency. In some high-frequency range, it may be roughly approximated by some value, but the specific value should depend on the type of porous material (acoustic foam or fibrous material), its porosity, etc. Note also that at low frequencies, the waves slow down dramatically.

Porosity is a critical parameter for sound absorption. The flow resistance, defined as a ratio between the pressure required for the flow and the flow speed [Ns/m^3], also determines the absorptive properties of the material. The absorption coefficient α increases with the increase in frequency. Other essential parameters for sound absorption include: sample thickness, extension, placement and form of the material [31, 33].

A high-quality acoustic porous material is usually designed to have very high porosity, approaching unity. Furthermore, when a high absorption is needed, the porous material will be placed on a hard wall as pyramids of a height of about a quarter of the lowest wavelength one wants to absorb. The waves approaching the top of the pyramids or wedges will hardly reflect because the surface ratio S_H/S_T is almost unity. As they propagate further, the wave is gradually dissipated in the porous bulk of the pyramids. This construction is used in anechoic rooms.

A thin layer of porous material placed on a wall does not absorb sound efficiently because the acoustic velocity normal to the wall vanishes as one approaches a hard wall. Hence, the viscous dissipation due to air displacement is impeded by the hard wall. The sound absorption in the lower-frequency range can be improved by implementing an airspace between the porous layer and a rigid wall, as shown in Figure 2.2. Subsequently, the absorber is relocated from its previous position near zero particle velocity to a new location where air can be forced through the pores [36]. The alternative is to place a perforated plate backed by some porous material instead of the porous layer. This forms a resonant sound absorber with peaks of absorption at critical frequencies. A discussion of resonant absorbers is provided in the following section.

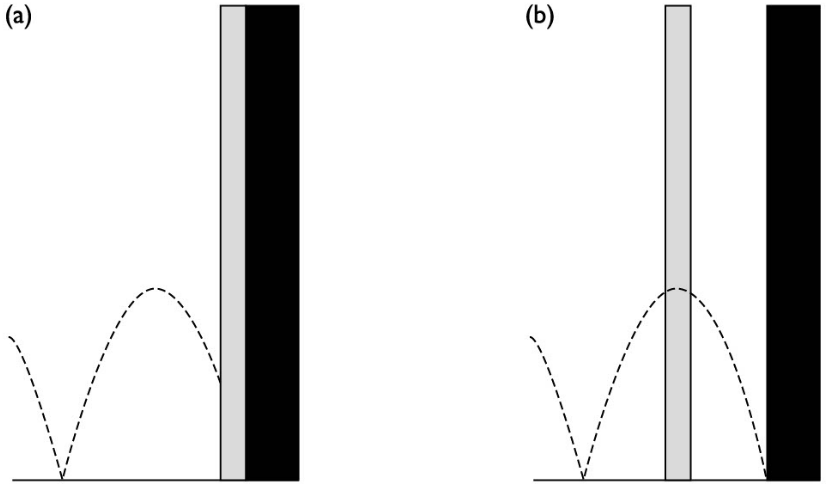

Figure 2.2: Porous layer in front of a rigid wall (dotted line: particle velocity when the layer is absent): (a) layer immediately on the wall, (b) layer mounted with air backing [31, 36]

As an alternative to pyramids, foam panels with gradually decreasing pore size and porosity have been designed. For incidence on the large porosity side, such panels display large sound absorption coefficients at medium to high frequencies [34]. Although some porous materials, such as packs of loosely packed thin fibres [34], are relatively affordable and good sound absorbers for medium and high frequencies, they are subject to a few limitations and problems. Among some of the issues, porous absorbers are prone to mechanical damage. Moreover, they collect dust (particularly in close proximity to air exhausts and intakes) and are likely to release fibres hazardous to human health [33].

2.3 Resonant absorbers

When a sound field forces a flexible plate to vibrate, part of its energy is subsequently emitted back into the environment. This part is removed from the incident sound energy, which, as a result, provides the effect of absorption [37]. In resonant absorbers, acoustic waves set the acoustical and mechanical components in motion, leading to losses and, consequently, sound absorption. Resonant absorbers can be classified into two main categories, i.e. the ones based on vibrating elastic elements (such as plates, membranes, etc.) and those based on air volumes and cavities (such as Helmholtz resonators, etc.) [31, 33]. Resonant absorbers are used to target low-frequency sound.

2.3.1 Tube resonators

Acoustic resonance occurs when the frequency of a sound wave matches the natural frequencies of vibration in an acoustic system, leading to the amplification of the signal. The resonance of a tube of air depends on its length, shape and whether it has closed or open ends. Any cylindrical tube resonates at multiple frequencies, and the lowest frequency is called the fundamental frequency or the first harmonic.

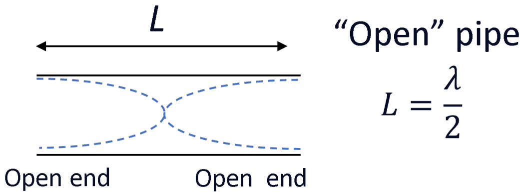

(a) Half wavelength resonator

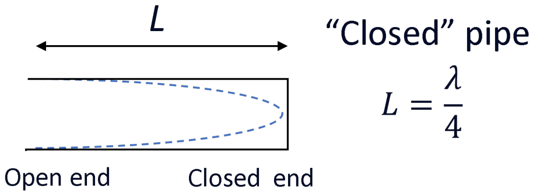

(b) Quarter wavelength resonator

Figure 2.3: Tube resonators (the dotted lines indicate the amplitude of the fluctuations in particle velocity)

A tube open at both ends is a half wavelength resonator, shown in Figure 2.3a. It enters a resonant state when its length equals an integer multiple of half the wave's wavelength. A tube closed at one end is a quarter wavelength resonator, illustrated in Figure 2.3b. It enters a resonant state when its length equals an odd multiple of a quarter of the wave's wavelength. Maximum absorption is observed at these resonant frequencies [38, 39]. An extensive review of the literature on classical quarter wavelength absorbers is provided by van den Eerder [38] and Hannink [39]. These panels have, by definition, a thickness of a quarter wavelength.

However, ultra-thin sound-absorbing panels can be designed based on spiral or labyrinth co-planar tubes [40]. By using different resonator lengths in a panel, one can achieve broadband sound absorption [15, 41].

2.3.2 Helmholtz resonators

A Helmholtz resonator is a single resonator which consists of a neck (opening) and a cavity (volume). It behaves as an ideal acoustical mass-spring system. The schematic of a Helmholtz resonator and an equivalent mass-spring system is shown in Figure 2.4.

The resonant frequency of a Helmholtz resonator is given by Equation (2.3)

$$f_r = \frac{c}{2\pi}\sqrt{\frac{A_c}{V l_{eff}}} \tag{2.3}$$

where c is the speed of sound in air, A_c is the cross-sectional area of the neck, l_{eff} is the effective neck length (related to the actual neck length l), and V is the cavity volume.

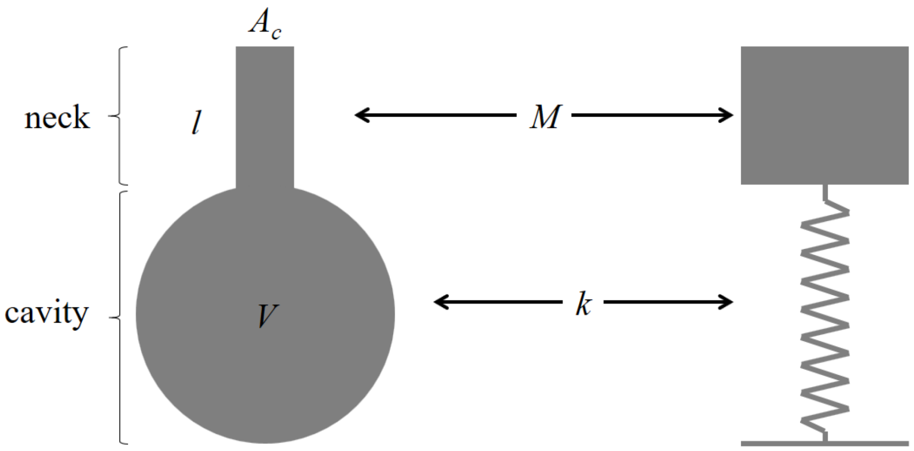

Figure 2.4: Helmholtz resonator [42]

Here, it is assumed that all the inertia is concentrated in the neck, while the compressibility is only relevant in the volume. In this approximation, the pressure in the volume is uniform, and the flow in the neck is incompressible. In the mass-spring system, this corresponds to a massless spring (of the air cavity volume) and a rigid mass (of the air in the neck). The effective length of the neck includes end corrections, taking into account the inertia and friction losses in the acoustic flow in the vicinity of the neck openings. The end-corrections are of the order of magnitude of the neck diameter and depend next on the details of the geometry [43, 44], on the interaction between neighbouring resonators and the acoustic level [45]. As for resonant tubes, one can obtain thin, sound-absorbing panels by using coplanar Helmholtz resonators [40].

The wide frequency bandwidth can be achieved by utilising a large enclosed volume. However, the shape of this volume is not significant as long as the airspace dimensions are small compared to the wavelength [33]. A broad absorption range can also be achieved by combining several resonators tuned for different resonance frequencies [15, 21, 46].

A notable advantage of Helmholtz resonators is that their resonance does not rely on the standing wave formation within the structure. As a result, resonance occurs at frequencies with wavelengths much longer than the physical dimensions of the Helmholtz resonator itself. This characteristic has made Helmholtz resonators highly relevant and widely used in the design of acoustic metamaterials, which by definition are sub-wavelength in size [47].

2.3.3 Perforated panels

Perforated plates backed by a rigid wall (forming a narrow air gap) are another example of resonant absorbers. Resonator panels can be thought of as several individual adjacent Helmholtz resonators. The internal side walls of the neighbouring air volumes can be erased due to symmetry, and the resonant frequency of the panel can be calculated in the same manner as for the single resonator [31, 48].

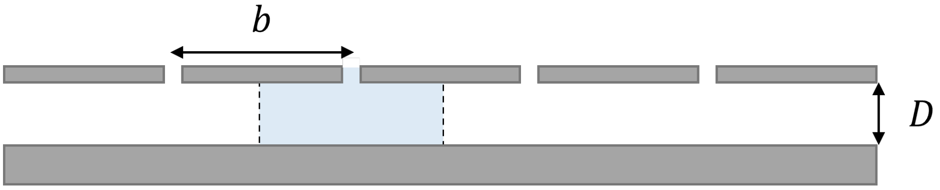

Figure 2.5: Perforated panel

The enclosed air volume is then given as per Equation (2.4)

$$V = S_p D \tag{2.4}$$

where D is the depth of the airspace, $S_p = b^2$, and b is the distance between hole centres (assuming a square hole pattern).

Neglecting friction, the resonance frequency of a slit resonator panel is given as per Equation (2.5)

$$f_r = \frac{c}{2\pi}\sqrt{\frac{S_p}{V l_{eff}}} \tag{2.5}$$

where S_p is the cross-sectional area of one perforation, $V = b^2 D$ is the enclosed-slit volume associated to the perforation and l_{eff} is the effective neck length [31].

In some applications, the perforation diameter is of the order of the Stokes layer. This implies a large frictional loss in the perforation. This type of perforated plate is referred to as a microperforated plate [43, 44, 49].

2.4 Acoustic metamaterials

The propagation of acoustic waves in a non-viscous homogeneous fluid, which can be described as per Equation (2.6), depends solely on the acoustic pressure p and the speed of sound c, which is defined as per Equation (2.7). The characteristic impedance of a medium, which describes the opposition of a medium to wave propagation, is given by Equation (2.8).

$$\nabla^2 p - \frac{1}{c^2}\frac{\partial^2 p}{\partial t^2} = 0 \tag{2.6}$$

$$c = \sqrt{\frac{\kappa}{\rho}} \tag{2.7}$$

$$Z_0 = \sqrt{\kappa\rho} \tag{2.8}$$

where κ is the bulk modulus and ρ is the mass density.

Rigid-frame porous media and some acoustic metamaterials can also be modelled using these equations. As a result of model homogenisation carried out for such media, they can often be replaced by a homogeneous acoustic fluid characterized by effective bulk modulus and mass density. These effective properties are usually complex-valued functions and have little in common with the properties of the saturating fluid. However, they are crucial parameters for acoustic materials determining the propagation characteristics of acoustic waves in the medium.

Conventional materials, like polymers or composites, have positive values of both κ and ρ, which depend on the composition and microstructure of the medium. However, by introducing local resonant units into the material, the equivalent acoustic parameters can become negative within a specific frequency range that is not observed in natural materials. This phenomenon enables the achievement of negative equivalent mass density, equivalent bulk modulus, and remarkable acoustic properties such as a negative refractive index [50].

These characteristics open up exciting possibilities for manipulating sound waves and designing unconventional acoustic materials with unique properties and functionalities. Desired acoustical behaviour is achieved by adequately designing metamaterial structures using conventional acoustical elements fabricated from traditional materials [51]. The subwavelength system consists of designed unit cells aligned to create hidden degrees of freedom. Commonly used dynamic microstructural elements include Helmholtz resonators, resonant scatterers, and elastic membranes [52]. Unit cells might be arranged periodically, but this condition is not necessary.

Low-frequency sound attenuation, superior sound absorption, and acoustic cloaking are a few of the effects achieved with acoustic metamaterials. The concepts commonly used in the design process include subwavelength resonant structures (sonic crystals), membrane-type metamaterials, non-resonant metastructures (space coiling metamaterials), labyrinthine structures, negative, double negative or near-zero metamaterials [53]. Such complex applications are not considered in the present thesis.

Chapter 3

Literature review on additive manufacturing

3.1 Additive manufacturing technologies

Note that 3D printing is (only) a form of additive manufacturing, which in general refers to the creation of objects by 'adding' material. However, in this work, we use the terms 'additive manufacturing' and '3D printing' interchangeably, which has been quite commonly used lately.

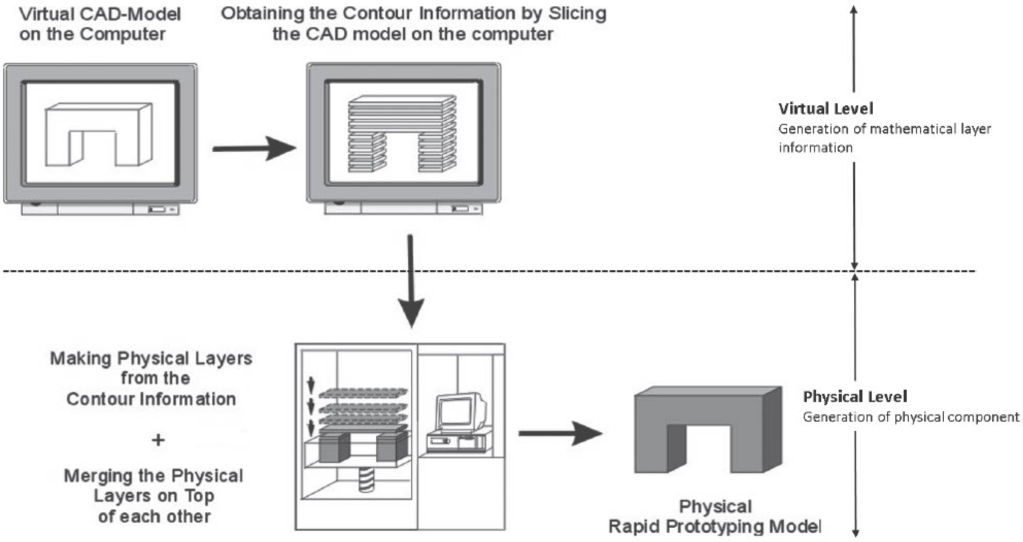

Figure 3.1: Additive manufacturing process chain [54]

The industrial potential of additive manufacturing has evoked great interest in the development of different 3D printing technologies. The main advantages of additive manufacturing include design flexibility and customization ease. Objects are formed directly from the CAD data in a layer-by-layer manner. This approach enables the creation of complex geometries that would not be manufacturable using conventional technologies, including traditional subtractive methods such as milling, carving, or machining.

Irrespective of the chosen 3D printing technology, any additive manufacturing workflow consists of two operations, one carried out on a virtual level and the other on a physical level, as illustrated in Figure 3.1. First, a 3D object is created in CAD software. The geometry is then exported to the slicing software as a Standard Tessellation Language (STL) file.

Although the STL format was initially developed for Stereolithography (SLA) by 3D Systems, it is commonly used for various 3D printing technologies. STL converts any 3D geometry into a set of unstructured triangulated surfaces, which do not represent any of the model features, such as colour or texture. The main advantage of the STL format is its simplicity as the original geometry is transformed into its most basic form. On the other hand, this transition comes at the cost of reduced resolution, especially in the complicated, curved regions of the considered geometry. Errors arising from these approximations can be ignored as long as they are smaller than the inaccuracies occurring due to manufacturing process [55].

In the next step, the slicing software splits an STL file horizontally into separate thin layers of a predefined thickness specific to the chosen additive manufacturing technology. Each of them represents a 2D contour. These outlines stacked one on top of the other form a final object that accurately depicts the original geometry. As a result of this conversion, a set of specific pathway instructions is created and then transmitted to the printer. This information, known as the G-Code, contains not only the contour (x-y) and thickness (dz) data but also the layer number (z-coordinate) of each layer.

This approach is valid for most additive manufacturing technologies. However, in projection-based resin printing (such as Masked Stereolithography), slicer software generates a series of images corresponding to each layer to be cured instead of creating a G-code.

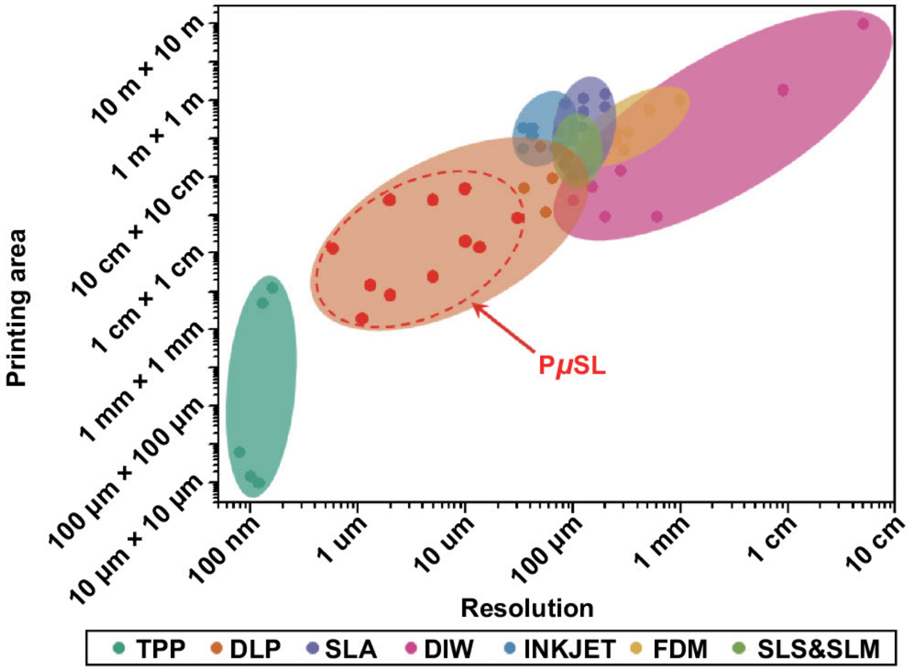

Figure 3.2: Printing area and resolution relation for different additive manufacturing technologies, including Two-Photon Polymerization (TPP), Digital Light Processing (DLP), Stereolithography (SLA), Direct Ink Writing (DIW), Inkjet, Fused Deposition Modelling (FDM), Selective Laser Sintering and Melting (SLS & SLM) [56]

Several additive manufacturing technologies are available on the market, varying in complexity and exploitation costs. The difference between them in terms of the achievable resolution and printing area is displayed in Figure 3.2. Although print quality improves for more complex 3D printing technologies, none of these processes guarantees total reliability and reproducibility of fabricated parts. In this thesis, three different additive manufacturing technologies will be examined and compared: Fused Deposition Modelling (FDM), Masked Stereolithography (MSLA), and Selective Laser Melting (SLM).

3.1.1 Extrusion-based additive manufacturing

Material extrusion is a rapidly growing branch of additive manufacturing processes. The first technology of this kind, Fused Deposition Modelling (FDM), was developed by Stratasys in the late 1980s for rapid prototyping. Although this technology was patented until 2009, and nowadays, other enterprises are allowed to manufacture machines operating on the same principle, the original name has been trademarked. Therefore, other extrusion-based techniques are known under different names, such as Fused Filament Fabrication (FFF).

Initially, due to limited technological capabilities, parts produced with rapid prototyping served primarily for visual aids purposes. Manufactured objects were used more as presentation models rather than being considered fully functional prototypes. Over the years, however, significant technological advancements in extrusion-based additive manufacturing have occurred. Nowadays, produced parts find other, more complex uses and must meet the demands regarding dimensional accuracy and mechanical properties. Additive manufacturing machines are used across many application fields, in private homes, manufacturing plants, educational institutions and government settings. Owing to its versatility, extrusion-based additive manufacturing has grown from a relatively small technical field to a thriving market, with shares growing each year [57].

Process overview in extrusion-based additive manufacturing

In FDM, a filament feedstock is provided into the system through a pinch roller feed mechanism, as shown in Figure 3.3a. Commonly used printing materials include thermoplastic polymers, such as Polylactic Acid (PLA) or Acrylonitrile Butadiene Styrene (ABS). Inside a liquefier, the filament is heated up to its melting point. The material in the semi-molten state is fed through a printing nozzle and distributed onto the build plate. Owing to their semi-liquid consistency, newly formed layers easily blend in with the previously deposited ones. The melted material that has already been distributed is referred to as a bead or a road. A stepper motor connected to the system controls the movements of the print head along the gantries, limiting the built environment. The 3-axis system enables movements in x, y and z directions. The build plate, on which separate layers are distributed, moves along the z direction. In such a way, 3D objects can be created in a layer-by-layer manner. The path followed by the extrusion head is referred to as a toolpath.

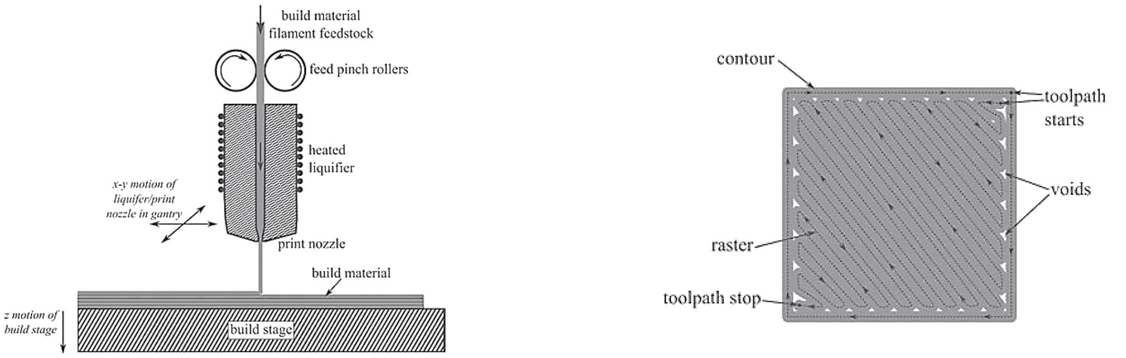

(a) Process overview

(b) Generic cross-section of a printed part

Figure 3.3: Extrusion-based additive manufacturing [58]

The toolpath plays a significant role in the quality of parts produced via extrusion-based additive manufacturing technologies. A cross-section of an exemplary part is illustrated in Figure 3.3b. The manufacturing of each layer begins with the creation of the outline of the shape, the contour. The interior is then filled with a raster of roads distributed at a certain angle. Roads can be either adjacent to each other or separated by air gaps, depending on a predefined infill pattern. The contour and road thickness are factors that contribute significantly to the dimensional accuracy and surface roughness of printed parts.

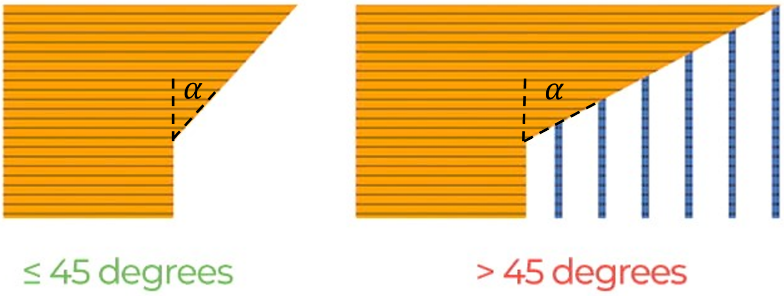

Figure 3.4: The overhang angle α in extrusion-based additive manufacturing (adapted from [59])

More complicated designs require manufacturing additional supports attached to the printed object, as illustrated in Figure 3.4. When an overhang angle of the walls is smaller than 45° from the horizontal, upper roads overhang the contour below them, and the structure is likely to collapse. Supports may be manufactured using an additional nozzle supplying a different feedstock or similarly printed along the desired object. Support structures may need to be removed chemically or mechanically, depending on the material used.

Parts fabricated via extrusion-based additive manufacturing technologies suffer from a lack of uniformity. The characteristics of the manufacturing process result in the anisotropic behaviour of printed objects. For instance, part orientation significantly influences the component's accuracy, strength, and build time.

Printing parameters in extrusion-based additive manufacturing

A better understanding of processing technology is needed to ensure the continuous improvement and growth of additive manufacturing technologies, especially extrusion-based ones, such as FDM. However, currently, too many factors contribute to the processing output, and their mutual relations are not yet well understood. This results in the need for more manufacturing repeatability and consistency of the printed parts. Therefore, extrusion-based additive manufacturing is often not considered a viable and reliable manufacturing technology. Furthermore, correlations between process parameters and the final properties of the build parts need to be studied to develop advanced control strategies for 3D printing systems and enable their commercial implementation [57]. Other vital aspects that should also be considered include efficiency factors, such as the build time and material usage [60].

The accuracy of additive manufacturing technologies is highly dependent on the predefined build parameters. The quality of printed parts, in terms of their dimensional accuracy, resolution and surface roughness, stems from the combination of the chosen process and design parameters [58]. Therefore, the acceptable variation from the benchmark should be within the desired tolerance range.

The first group of factors affecting print quality encompasses product design parameters related to the toolpath, as illustrated in Figure 3.5. Among them is the road or bead width, the thickness of the path deposited by the printing nozzle. The achievable resolution is highly dependent on this dimension. The reduction of the road width results in improved surface quality, but this is at an increased build time.

The layer height is the thickness of the deposited layer measured in the vertical direction. In terms of the resistance to the axial load, parts produced with smaller layer thickness tend to be stronger [61]. The combination of the maximum layer height, the lowest level of infill and the number of shells should be chosen to maximise the printing process's efficiency in terms of build time and energy consumption [60]. Standard layer heights utilised in extrusion-based additive manufacturing vary from 0.10 mm to 0.25 mm.

Another parameter affecting the dimensional accuracy is the air gap, which can be defined as the space between adjacent roads of the deposited material. By default, the air gap is set to zero, which results in the precise alignment of distributed beads; see Figure 3.5c for $g = 0$. In case of a positive air gap, conterminous roads do not connect as free spaces are left between them (see Figure 3.5c for $g > 0$), leading to a faster build time.

When a negative gap is chosen in the design software, neighbouring beads overlap (see Figure 3.5c for $g < 0$), resulting in a longer structure build-up. Parts manufactured with a negative air gap are characterised by higher tensile strengths [61, 62] and stiffness [55]. However, this can come with the loss of surface quality and dimensional accuracy and should only be used when the mechanical properties of the produced parts are the main priority. The value of the negative air gap should not fall below 0.003 inches (0.0762 mm) as it has been demonstrated that FDM machines are not capable of achieving such high resolutions, and printing processes are expected to fail [55].

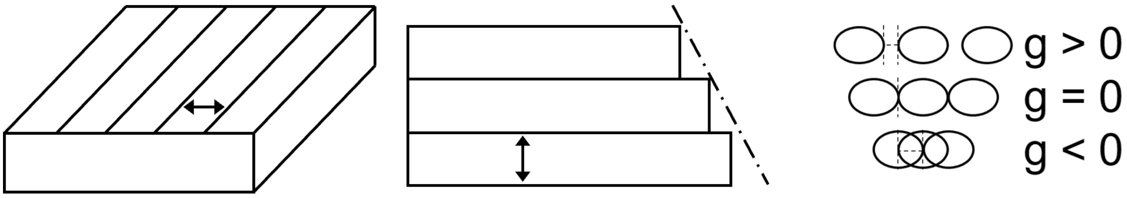

(a) Road width (b) Layer height (c) Air gap

(d) Build orientation (e) Raster angle

Figure 3.5: Product design parameters (adapted from [61])

Build orientation indicates the position in which the part is manufactured. Manufactured parts have anisotropic characteristics and tend to be stronger in the direction of the road axis than in the direction of road-to-road bonds. Therefore, components should be built so that tensile loads will be transferred axially along the fibres. The influence of the 3D printing process on structural strength is outside the scope of this work, which focuses on acoustic materials. The achievable accuracy is also dependent on the build orientation.

The raster angle is the angle of the raster tool path deposited in regard to the x-axis of the build plate. The infill raster pattern resulting from it relates to the direction in which roads are distributed inside the structure's interior. These parameters significantly impact the mechanical properties of produced parts, especially in the more complex regions of the geometry. Distributed roads show discontinuities at corners arising from the rasterization process. These areas are subject to stress concentrations and should be approached with caution during the design process. The selected raster angle has a significant impact on the internal structure of the finished part. It has been demonstrated that increasing the raster angle improves tensile strength [61].

Among all build parameters, road width, slice thickness and air gap influence the dimensional accuracy and surface roughness to a great extent. On the other hand, build orientation and raster angle are crucial for optimising build times and mechanical properties of manufactured parts.

The second group of build parameters includes process parameters. Critical are variables concerning build temperatures, such as liquefier and environment temperatures, and the cooling rate. Warping and other thermal deformations occur due to shrinkage during the cooling phase when the semi-molten material solidifies. Internal stresses within the manufactured part arise due to the uneven heat distribution and are the main reason for distortion and the consequent reduced dimensional accuracy [63]. In extreme cases, they not only affect the printing accuracy but also reduce the durability of components and cause cracking. It has been suggested that the issue of emerging thermal gradients can be eliminated by shortening toolpaths so the time between the deposition of neighbouring roads is reduced to the minimum, which could improve the dimensional accuracy [64].

These adverse effects are also related to the filament feed rate, which controls the pace at which the printing material is deposited onto the build plate. Variations in the road thickness arise from changes in the material deposition, which cause reduced dimensional accuracy. In addition, the studies on the feed rate found that a sudden drop in the filament feed rate can result in structural weakness of produced components because of the lower extrusion temperature [65]. This effect is significant for part certification in the aerospace industry, where understanding and control over the whole manufacturing process is required.

Aside from design and process parameters, the properties of the feedstock filament themselves play an essential role in determining the final quality of finished parts in terms of dimensional accuracy and print resolution. This consideration is of great importance for an accurate representation of the geometrical model, especially regarding the finer details. Possible issues could not only affect the visual aspects of the product but also cause problems during part alignment of more complex systems.

Post-processing in extrusion-based additive manufacturing

Parts produced using extrusion-based additive manufacturing usually do not require any additional post-treatments. However, the surface quality of printed components may need to be improved by applying additional post-processing. Two primary approaches include mechanical and chemical finishing techniques. Mechanical post-processing includes manual sanding, abrasive milling and hot cutter machining. Chemical post-processing is usually applied to ABS parts and includes vapour smoothing and acetone dipping [66].

3.1.2 Photopolymerisation-based additive manufacturing

The limitations of extrusion-based additive manufacturing, which include slow printing speed and reduced printing precision, contributed to the development of alternative rapid prototyping processes. Photopolymerisation-based 3D printing is another broad group of 3D printing technologies that are becoming increasingly popular as they overcome previously mentioned issues at relatively affordable operating costs. Several photopolymerisation technologies exist, among which the most popular are: Stereolithography (SLA), Masked Stereolithography (MSLA) and Digital Light processing (DLP). Among these, MSLA is the fastest and usually also faster than FDM.

The main idea behind these technologies is the selective curing of a photopolymer resin by a light source. Parts produced in such a way are characterised by the smoothest surfaces, which do not usually require additional finishing post-processing, and by good z-axis strength since the neighbouring layers are bonded chemically [67].

Photopolymerisation-based additive manufacturing technologies are characterised by relatively unconstrained material requirements, mostly requiring photopolymerizable resins only to flow sufficiently for recoating and enable the usage of materials for target applications with desired material properties [68]. Different photosensitive resins may be used as build materials, enabling these manufacturing processes to find use across various technical fields. For instance, aside from conventional materials science and engineering applications, photopolymerisation-based additive manufacturing implementations include the pharmaceutical industry [69], dental industry [70], tissue engineering [71], electronics industry [72], jewellery and fashionwear [73]. In the case of traditional applications, such as aerospace, automotive and other industries, for which the product performance is highly dependent on the changes in mass, low-density materials with high strength-to-weight ratios may be used to optimise the performance efficiency and lower the production cost [68].

Zhou *et al.* (2015) state that SLA can achieve the best dimensional accuracy and surface quality of manufactured parts among all the additive manufacturing technologies [74]. The high resolution is accomplished owing to laser-based vector-by-vector scanning, in which photopolymer resin is solidified in a point-by-point manner. The major disadvantage of this method lies in the extended build time. Therefore, new technologies operating on an improved but similar principle have been developed, among which DLP and MSLA are the most widespread. They operate on the principle of projection-based layer-by-layer exposure. A projector or a Liquid Crystal Display (LCD) screen masking the light source is used to illuminate and cure the whole layer simultaneously in a planar-by-planar manner during a single exposure. In such a way, projection-based technologies can achieve faster build speed without sacrificing the printing resolution [74], although voxel raster may lower the surface quality.

Compared with SLA, projection-based additive manufacturing technologies are more efficient, faster and operate at a broader range of wavelengths. Moreover, unlike SLA machines, DLP printers offer more flexibility regarding the amount of resin needed for manufacturing as they are adaptable to customized tanks and small volumes of photopolymers [69].

Since desired voxels (volume elements forming a 2D grid of a specified voxel depth) are simultaneously cured in a 2D plane, which allows the creation of an individual layer during a single exposure, the printing time does not depend on the in-plane dimensions of the geometry and instead is dominated by the vertical dimension. For this reason, projection-based photopolymerisation is more suitable for large-scale production than other additive manufacturing technologies, which require serial deposition in all three dimensions of the geometry and therefore need more time to complete [68].

Process overview in photopolymerisation-based additive manufacturing

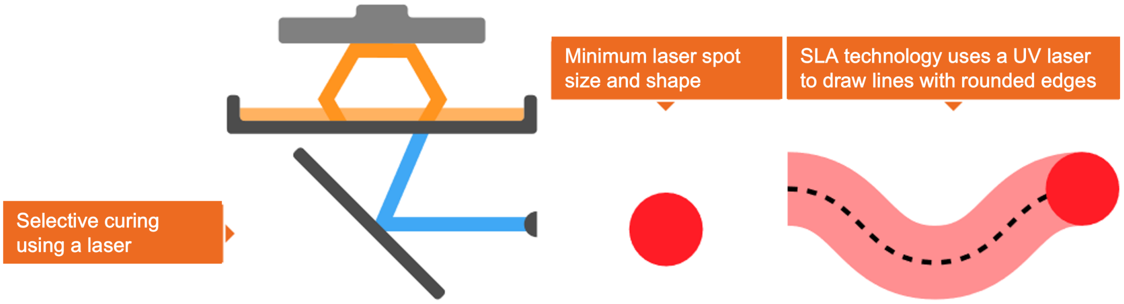

Figure 3.6: Stereolithography (SLA) process [75]

The original SLA technology, presented by 3D Systems in 1986, operates on the principle of localized photopolymerisation and solidification of the photosensitive liquid resin by exposure to a rastering UV laser. The geometrical pattern is illuminated on the surface of the resin in a row-by-row manner using a laser beam controlled by a set of two mirrors, one for the x-axis and the other one for the y-axis, known as galvanometers. The photopolymerisation occurs on the surface, resulting in the solidification of the base layer to a predefined depth and its adhesion to the support platform. Between each layer, the platform is repositioned, and the built layer becomes recoated with liquid resin. The process is repeated in a layer-by-layer manner until the complete, solid object is created [76]. The process overview is illustrated in Figure 3.6

After the manufacturing process is completed, the excess resin, which may later be reused, must be washed off of the structure. Potential support structures should be physically removed before the next step. Depending on the type of resin used, parts produced with SLA usually require additional post-treatment in the form of UV curing in order to improve their mechanical properties, in particular, the material's stiffness and strength. The surface roughness of SLA objects is generally minor and resembles the finish of moulded components. The final surface finish may be improved through additional treatments, such as primers, paints or metallic coatings [67].

Two other photopolymerisation technologies related to the laser SLA are MSLA and DLP. In MSLA, the laser is replaced by an LCD photomask, which serves as a projector, flashing the entire geometrical shape onto the resin during a single exposure. It can cure a complete layer at once, which usually results in much shorter 3D printing times. The process overview is shown in Figure 3.7.

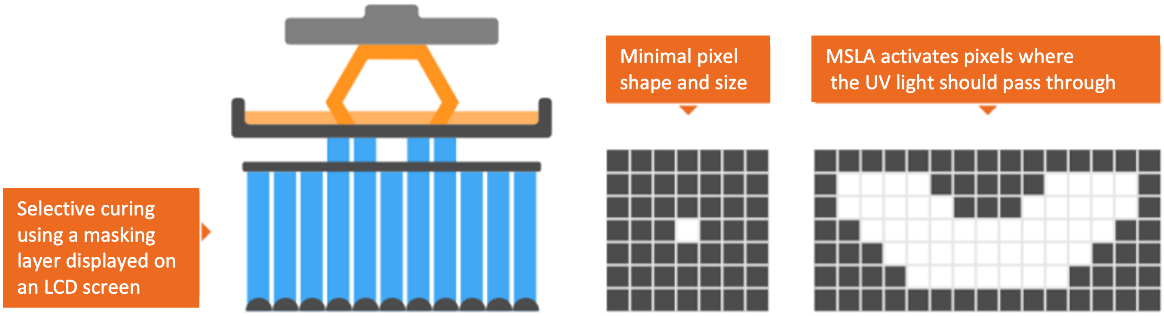

Figure 3.7: Masked Stereolithography (MSLA) process [75]

DLP works based on the same principle. However, instead of an LCD, a Digital Micromirror Device (DMD) is used as the light projection device. DMD is an array of millions of microscopic mirrors that can be rotated independently and correspond to image pixels. The process overview is illustrated in Figure 3.8.

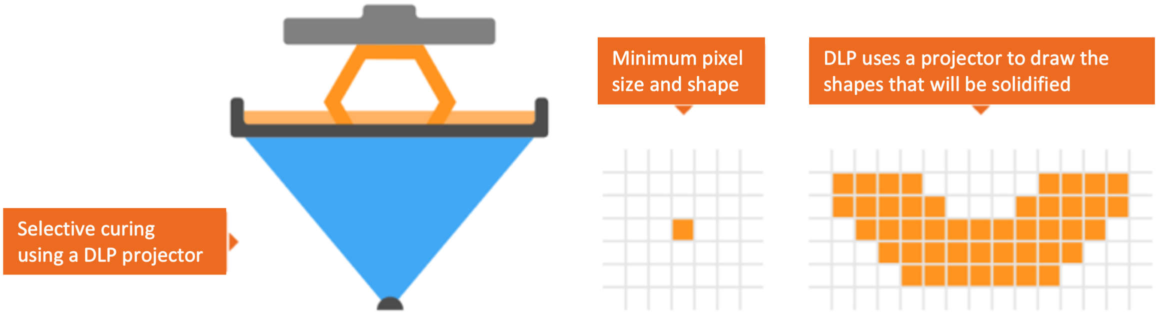

Figure 3.8: Digital Light Processing (DLP) process [75]

Printing parameters in photopolymerisation-based additive manufacturing

The quality of parts produced with photopolymerisation-based additive manufacturing depends on several predefined printing parameters, properties of the chosen photosensitive resin and the applied post-treatment. The first category, i.e. process parameters, include: layer height, UV exposure time to UV radiation and light source intensity, printing temperature, platform lifting speed, and, in the case of DLP and MSLA, voxel size. These parameters and their impact on the 3D printing process are discussed below.

The layer height relates to the cure depth and determines the z-axis resolution. The printing time and surface quality highly depend on its chosen value: typically, smaller curing depths allow for better surface quality but increase the printing time. Depending on the chosen resin, the cure depth is determined by the exposure conditions (wavelength, power, and exposure time/speed), the properties of the photoinitiator, and the presence of additional dyes, pigments and added UV absorbers [67]. A higher resolution of the z-axis is obtained by reducing the individual layer height. That results in an increased number of layers cured on top of each other. The chosen cure depth should be a balanced compromise between the build time and printing resolution. Standard layer heights utilised in photopolymerisation-based additive manufacturing include 0.03 mm and 0.05 mm.

Zhang *et al.* (2019) investigated the correlation between the layer height and the printing accuracy for SLA and DLP technologies [77]. For SLA, a decrease in layer height consistently increased printing accuracy, with the best results achieved at a layer thickness of 0.025 mm. For DLP, an error threshold value of layer thickness of 0.05 mm existed, below which the reduction of layer height led to a decrease in accuracy. 0.05 mm was also determined to be the best compromise between surface accuracy and printing error. Moreover, at the same layer thickness of 0.1 mm, DLP printers achieved a better printing speed and better printing accuracy than SLA machines. Wu *et al.* (2019) demonstrated that layer height is among the most crucial parameters affecting the UV-induced bending phenomenon, which leads to the distortion of manufactured parts and can be diminished with proper printing parameters [78].

Other important process parameters are the UV exposure time and intensity of the light source that directly influence the curing of individual layers. The first four to eight layers should have an extended exposure time, with a value equal to three to four times the standard printing exposure time, to secure firm adhesion of the first layer to the build platform [79]. The relationship between the amount of UV radiation and the cured depth is given by an adapted Beer-Lambert equation, known as the cure-depth equation:

$$C_d = D_p \ln\left(\frac{E_{max}}{E_c}\right) \tag{3.1}$$

where C_d is the maximum cure depth, D_p is the penetration depth, E_{max} is the maximum exposure energy at the surface and E_c is the critical, minimum energy required to initiate polymerization [80].

When the energy emitted from the UV source reaches E_c, gelation occurs in the photopolymer. This process cannot be reversed, as a permanent molecular network is formed. During gelation, the viscosity of the resin sharply increases, and the system will no longer flow. As a result, two phases, a gel and a solution, coexist. With the further energy increase above E_c, the crosslinking phase is initiated, during which covalent bonds are created between the developed polymer chains and the molecular mobility decreases. That leads to the solidification of the photopolymer [81].

Steyrer *et al.* (2018) investigated the influence of the printing temperature on the properties of printed components using DLP [82]. It was shown that the same exposure time at higher temperatures results in a higher curing depth due to the increased mobility in the system. Moreover, longer exposure time at lower temperatures leads to an increased over-polymerisation that causes the surface to be smoother but at the cost of reduced dimensional accuracy. Therefore, printing at elevated temperatures reduces the manufacturing time, positively influences the overall process efficiency, and results in higher conversion and better mechanical properties of manufactured parts. Moreover, it also enables the usage of high-viscosity resins, as the liquid viscosity decreases with increasing temperature.

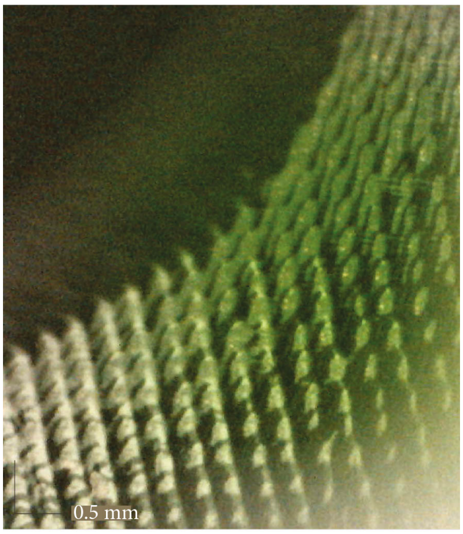

Figure 3.9: Microscopic image of an MSLA part showing the voxel effect on the surface finish [13]

The minimum voxel size achieved during the DLP process determines the printing resolution. In the vertical direction, it depends solely on the layer thickness and the accuracy of the position control system, provided that enough energy is supplied. In the horizontal direction, it depends on several parameters: micromirror size, the degree of crosslinking, the amount of energy provided, the exposure time, the reflection and refraction in the light occurring due to passing through different media and the PDMS clouding resulting from the surface roughness and the prolongated UV exposure [79]. The voxel size is also an inherent parameter of the

MSLA process. In this case, it depends on the LCD matrix used. An exemplary voxel effect occurring on the surface finish is illustrated in Figure 3.9.

The lift speed is another parameter that can be adjusted in the slicing software. It is the pace at which the build plate is moved away from the resin tank between each layer. The set value should be a compromise between the printing time and the secure adhesion of cured layers attached to the moving platform. Finally, the part orientation has a similar effect on the parts produced through photopolymerisation as on parts produced through extrusion-based additive manufacturing, described in detail in the previous subsection. However, as mentioned by Monzón *et al.* (2017), this influence of the build orientation on the mechanical properties primarily applies to parts that do not require further post-curing [83].

Post processing in photopolymerisation-based additive manufacturing

Photopolymerisation technologies usually require additional post-processing, as the manufactured parts are covered with excess and uncured resin that needs to be mechanically removed through a combination of ultrasonic isopropyl alcohol (IPA) baths and compressed air cleaning. In addition to the clean-up of the remaining resin, newly manufactured parts are usually left on the build platform in a fragile ‘green’ state and require post-curing. Although the printing process of the geometry has been completed, the photopolymerisation still needs to be fully finished, and the mechanical properties of the component still need to be obtained. During a UV post-curing, additional chemical bonds form within the part that improve the material’s strength, stiffness, and temperature resistance [84].

3.1.3 Powder bed fusion-based additive manufacturing

Powder Bed Fusion (PBF) is the group of most advanced additive manufacturing processes that utilise a heat source, typically a laser, to sinter or fuse metal or nylon powder particles in a layer-by-layer manner. Parts produced in such a way achieve high accuracy, superior surface finish and resolution and are characterised by excellent mechanical properties. Several PBF technologies exist, among which the most popular are Selective Laser Melting (SLM) and Selective Laser Sintering (SLS).

Unlike previously mentioned additive manufacturing technologies, PBF processes are highly hazardous and must be undertaken under strictly controlled laboratory conditions. Only highly skilled personnel perform the 3D printing, as potential risks include mechanical, electrical, thermal, radiation, and material/substance hazards [85]. Powder management, which includes storage, loading in the machine, removal from the machine and waste disposal, must be carried out safely and in a controlled manner.

Extrusion- and photo polymerisation-based additive manufacturing machines are desktop 3D printers that are low-cost and easy to use by beginners in the field. PBF machines, on the other hand, are costly and can only be used by trained operators. As a result, metal prints are usually commissioned to be performed by internal or external units. For that reason, in this subsection, the principles behind PBF-based additive manufacturing will be covered in less detail than the previously discussed 3D printing technologies.

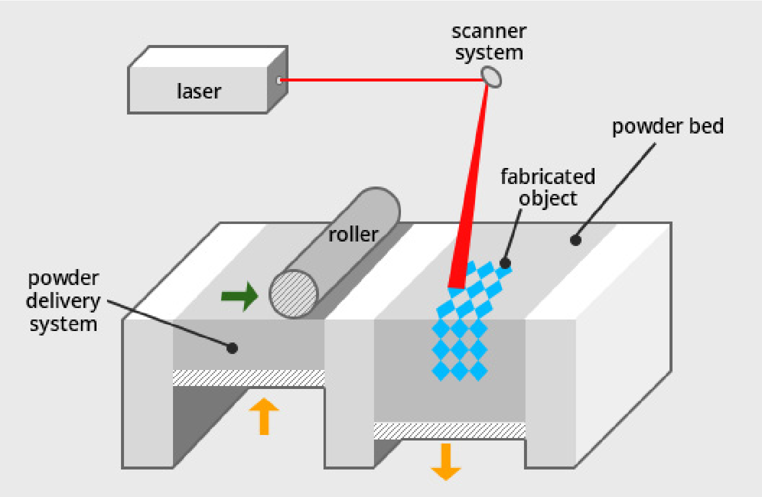

Figure 3.10: Selective Laser Melting (SLM) process [86]

Process overview in PBF-based additive manufacturing

In laser-based PBF additive manufacturing, a laser beam is used to scan specified locations of the powder bed at controlled speeds. Then, each 2D slice of the part geometry is fused to the previously created layers underneath by either complete melting (SLM) or partial melting (SLS). After laser radiation in one layer is finished, the powder bed is lowered by the amount of the fixed layer height and a recoating mechanism deposits and levels the new layer of metal powder. The process repeats in a layer-by-layer manner until the complete object is created [87]. The overview of the SLM process is shown in Figure 3.10. The same scheme applies to SLS.

The process takes place inside the built chamber containing a tightly controlled inert gas atmosphere (argon, nitrogen) to prevent oxidation. Moreover, the gas flow helps to remove the condensate created during powder melting. The quality and properties of SLM parts are heavily influenced by the gas flow uniformity across the build area [88].

In PBF additive manufacturing, the ability to achieve a homogenous thickness of metal (or polymer) powder in each layer plays a significant role in the quality control of fabricated parts. For that reason, several techniques targeting powder delivery and its uniform levelling on the powder bed in each layer before laser scanning have been developed. A popular one uses a recoater to supply enough powder to create each layer by dropping a controlled volume into the chamber. Next, a counterrotating roller uniformly distributes the metal powder over the build platform. The powder delivery system's primary goal is to maximise powder flow, minimise the creation of a particle cloud and minimise the shear forces over the previous layer [87].

Printing parameters in PBF-based additive manufacturing

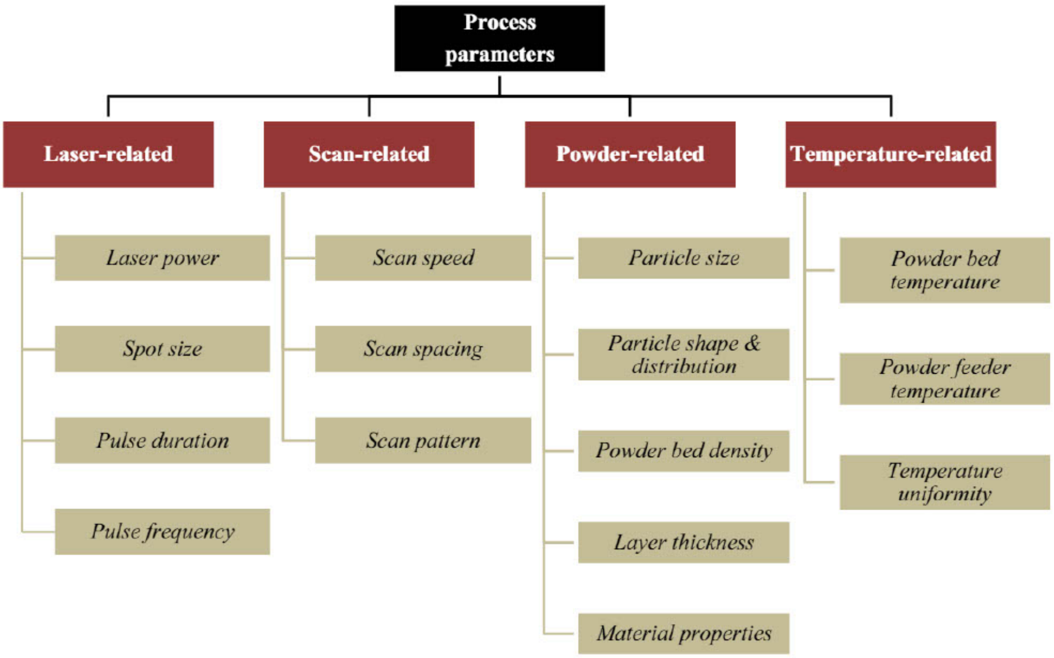

Figure 3.11: Selective Laser Melting (SLM) process parameters [89]

The PBF printing techniques are controlled by a set of processing parameters, which are: laser-, scan-, powder- and temperature-related. An outline of the principal process parameters involved in SLM is illustrated in Figure 3.11. Among them, the major ones include laser scanning speed, scan spacing, laser power and layer thickness. The standard layer height in PBF-based additive manufacturing varies from 0.02 to 0.05 mm.

The feedstock powders' properties are another vital factor affecting the quality of parts produced via PBF-based additive manufacturing. The particle morphology, size, and distribution influence powder flowability, laser energy absorption and the thermal conductivity of the powder bed. A higher powder bed density should be obtained during additive manufacturing to minimise internal stresses, part distortion, porosity and surface roughness in the built components [87].

Powders with spherical particle morphology are preferred, as they improve the powder's flowability and achieve higher packing density in the powder bed. They improve the final quality of the SLM or SLS parts in terms of geometric and mechanical properties [90]. For that reason, gas-atomized powders with a spherical shape are commonly used as feedstock for additive manufacturing processes.

Post-processing in PBF-based additive manufacturing

One of the major issues resulting from using metal (or polymer, etc.) powders in PBF additive manufacturing is the rough surface finish of produced parts, which makes them insufficient for most applications. However, the surface quality of manufactured components can be improved using additional post-processing. Several finishing treatments exist, among which the most conventionally used include grinding and sandblasting. These post-processing techniques are skilled operator-dependent and labour-intensive. Another issue is that they are difficult to apply uniformly on parts with complex geometries [91].

3.2 3D printing defects

Although 3D printing has created new opportunities for acoustic material development, existing process issues must first be addressed and tackled to establish additive manufacturing as a reliable production method. The quality of the product must be improved, which will be of great importance, especially for future aerospace, automotive and building acoustics applications.

Additively manufactured parts are subject to flaws, primarily regarding surface finish and dimensional accuracy, irrespective of the chosen technology. Another issue is the microporosity of the build material, which is present in extrusion-based and PBF-based technologies. All these issues with regard to different additive manufacturing processes will be discussed in more detail in the following section.

3.2.1 Surface roughness

A rough surface finish is closely related to the nature of the layer-by-layer fabrication technique. This method of applying flat layers on top of each other inevitably leads to the creation of rough outer surfaces in addition to other problems, such as voids and porosity in the component. Components produced in such a manner are generally of inferior quality to components constructed via conventional manufacturing, such as machining on a lathe or using cutting machines and other numerically controlled machine tools [92]. The improvement and control over surface roughness remain one of the top priorities in additive manufacturing, as in many cases, the surface finish of produced parts is not satisfactory enough for general engineering applications.

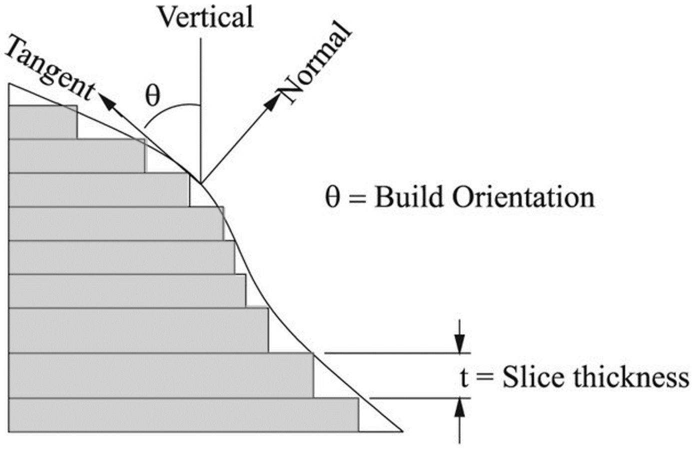

Figure 3.12: Staircase effect in additive manufacturing (reproduced from [93])

In terms of surface finish and dimensional accuracy, produced designs differ to a certain extent from the CAD models from which they were created. This effect is caused by the tessellation of the original geometry, during which surfaces are approximated by a triangular mesh irrespective of their curvature. In comparison, traditional manufacturing techniques utilise a mathematically precise representation of geometries [94]. Tessellated data not only discretise the surface but may also lead to faults within the file format, which will require additional modifications in repair software [93].

Another manufacturing error leading to the creation of overly rough surfaces is known as the staircase effect, illustrated in Figure 3.12. It emerges from the deposition of sliced layers on top of each other and remains an issue in nearly all of the current functional additive manufacturing technologies [95]. The staircase effect can, however, be diminished by a proper adjustment of printing parameters. The layer height contributes significantly to the final roughness, and by decreasing it, the surface finish will improve. Although this problem cannot be completely eliminated, its effects depend on the surface build angle and can, therefore, be minimized by choosing the optimal value of this variable [96–98].

Although roughness formation is similar across various 3D printing processes, some dissimilarities have been reported. Parts manufactured via extrusion-based additive manufacturing technologies are usually rougher than the ones produced with liquid resin-type processes, like SLA [99]. However, the surface roughness achieved through extrusion-based additive manufacturing is more predictable and can be more easily considered during the design phase. This is essential as surface roughness distribution needs to be modelled before the fabrication process to optimize the manufacturing procedure and improve the quality of produced parts [92].

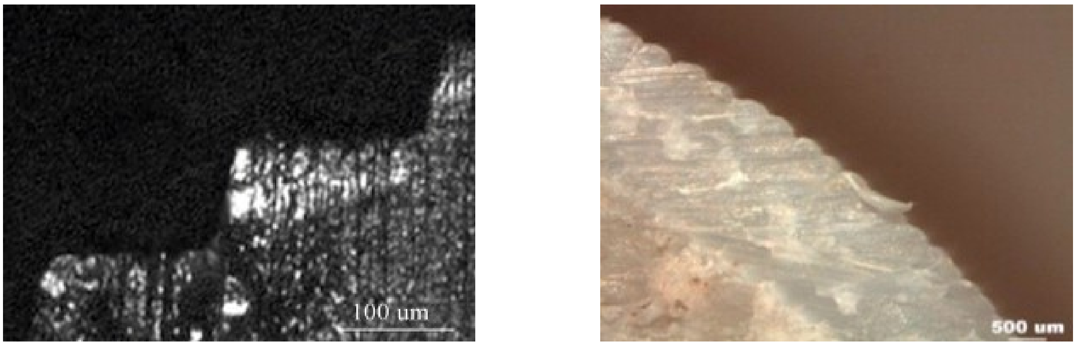

(a) SLA-processed part

(b) FDM-processed part

Figure 3.13: Surface profiles of additively manufactured parts parts [100]

Pandey *et al.* (2003) studied the difference between the surface profile of parts produced via SLA and extrusion-based additive manufacturing [101]. The surface profile resembles a rectangular staircase for most layer-based 3D printing technologies, as illustrated in Figure 3.13a. However, the shape of the ABS filament approximates a parabolic curve, which was observed during micrometre measurements of an FDM part surface, as shown in Figure 3.13b. Ahn *et al.* (2009) observed the same phenomenon by comparing microscopic images of surface profiles of SLA-processed and FDM-processed parts [100].

It has been suggested that the shape difference occurs due to diverse working principles of additive manufacturing processes. In the case of FDM, the fabrication process combines layer-based manufacturing with different thermal energy and surface chemistry processes. Parts are created by heating a thermoplastic filament to a liquid state, depositing it on the build plate as it solidifies, and stacking layers next to and on top of each other. Barari *et al.* (2017) noted that processes utilising the phase change of the build material from liquid to solid do not allow the creation of sharp edges due to surface tensions [95]. On the contrary, subtractive and cutting procedures lead to the formation of sharp edges.

In the case of PBF additive manufacturing, the surface roughness shape is dominated by the features of the melt pool rather than by the layer height parameter. There are two types of roughness of metal parts: primary one occurring due to the solidification of the melt pool and secondary one induced by partly melted powder particles [102]. Roughness is affected by the so-called balling effect, during which the melt pool ejects spherical particles that settle on created surfaces. This phenomenon constricts the creation of sharp geometries and leads to irregular material deposition onto the former layer, which can lead to porosity and delamination between layers [103].

Quantifying surface roughness

Several attempts have been made to model the surface roughness created within additive manufacturing mathematically. Dolence and Makela (1994) were the first to interpret the staircase effect in terms of cusp height tolerance and use it to determine the optimal layer height [104]. Other research groups followed the same concept and developed it further [105, 106]. However, this approach assumes a rectangular representation of distributed layers and is not suitable for extrusion-based additive manufacturing. Ahn *et al.* (2009) proposed a model suitable for the FDM process, in which distributed layers have an elliptical shape [100].

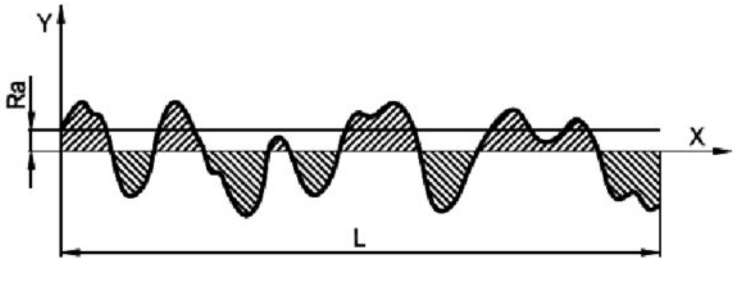

Figure 3.14: Determination of the average roughness (Ra) [107]

The average roughness Ra is one of the standard parameters used for surface description and can be defined as the mean deviation of the distance between the measurement centreline and the surface profile [58], see Figure 3.14; therefore:

$$Ra = \frac{1}{L} \int_0^L |y(x)| \, dx \tag{3.2}$$

where L is the measurement length and $y(x)$ is the distance of the measurement point on the surface profile from the measurement centreline.

Many researchers use Ra to characterise the surface roughness of additively-manufactured materials and metamaterials. However, it has been argued that this parameter might be too inexact to properly reflect the character of the measured surface and should be just used as a point of reference [108]. The main issue with Ra is that entirely different topologies may have the same average roughness value.

In this work, the average roughness is not considered a suitable surface parameter. Therefore, it should not be used to draw a link between the acoustic performance of the fabricated material and the roughness effect. This issue indicates a need to establish a more suitable parameter for the surface roughness of additively manufactured metamaterials.

Influence of surface roughness on acoustics

In the case of acoustic materials, surface roughness influences the magnitude and operating frequency of the sound absorption or transmission loss peak, as well as their values at off-peak frequencies. It is usually used to explain the mismatch between the experimental results and numerical or analytical predictions [13, 24–26, 109]. For that reason many authors have analysed the influence of surface roughness on the performance of various acoustic materials.

Cortis and Berryman (2010) performed a numerical investigation on the influence of fractal-like wall surfaces in porous media on oscillatory fluid flow [110]. The authors demonstrated that in the intermediate-frequency region, the boundary layer closely follows the contour of the fluid-solid interface. In higher frequencies, on the other hand, the boundary layer is almost identical to the bounding surface. Moreover, in the fluid region, the phase of the velocity field is equal to $-\pi/2$, which suggests an interia-dominated flow regime. In this frequency region, the thickness of the boundary layer is much lower than the smallest elements of the pore-fluid surface.

Ning and Zhao (2017) proposed a sound propagation model of a roughened porous material, which derived from a model of a smooth porous material [25]. It was established that increased acoustic impedance and sound absorption occur as a consequence of a rise in viscous and thermal dissipation of the roughened porous material, which is caused by the presence of relative roughness. This effect is related to the increase in the flow resistivity ratio, which is also triggered by the rise in relative roughness. The results of sound absorption were verified by experimental measurements of the roughened porous material.

It is understood that pore wall roughness within porous acoustic material leads to a non-uniform pore network. The non-uniformity increases the tortuosity, reducing the frequency of the quarter wave absorption resonance in a hard-backed layer as a consequence of lowering the sound speed within the material. Tortuosity is a measure of pore or streamline curvature [111] and describes the porous internal structure of the material. The effects of this increased tortuosity on the acoustic performance are documented in [112–115].

Song *et al.* (2018) established that the periodic roughness on the inner surface of circular pipe influences the boundary layer by increasing the viscous dissipation and results in enhanced pressure reduction [116].

A recent study by Hoppen *et al.* (2021) concluded that the presence of surface roughness improved the sound absorption of slit resonators in terms of achieving broader bandwidth without diminishing the peak value [24]. However, in this study, the transmission loss was reduced with the rise of the surface roughness, which was explained by increased damping effects. The experimental sound absorption results matched the analytical model for the smooth resonator, while the rough resonator showed a mismatch. The actual measured sound absorption curve had a broader bandwidth, and the peak was located in a higher frequency region than the analytical curve, which was attributed to the limitations of the analytical model.

Using surface roughness to improve the performance of acoustic materials

Recently, investigators have examined the effects of introducing surface roughness to the classical sound absorbers at the design stage to improve their performance.

Xu *et al.* (2019) performed an analytical and numerical investigation of microperforated panels with traditional, smooth and altered, roughened perforations [117]. It was determined that by introducing roughness, the peak absorption coefficient increased its magnitude and shifted towards lower frequencies. A sound energy dissipation density graph was generated from the numerical results to understand better the losses occurring in the roughened channel. It was determined that a periodic change in the sound energy dissipation occurred because of periodic variations in the channel diameter.

Moreover, the reduction in channel diameter improved friction and energy dissipation in the system, however, up to a certain point. This was explained by the fact that absorptive properties depend on the sound wave's entry energy and the considered channel's dissipation capability. Therefore, it is essential to consider both factors as their combination defines the real dissipated sound energy and the sound absorption properties. Thus, although the reduction of the channel diameter leads to a rise in the dissipation ability, this occurs at the cost of a decrease in the entry sound energy.

Duan *et al.* (2020) proposed a metamaterial based on a Helmholtz resonator with a periodic axial roughness applied to its embedded neck and compared its behaviour to a material based on a traditional neck embedded Helmholtz resonator [118]. The analysed samples were manufactured using SLA. By comparing the results of the traditional and altered Helmholtz resonators, it was established that the inclusion of surface roughness improved low-frequency sound absorption. Both numerical and experimental curves of the modified design shifted towards lower frequencies and achieved higher sound absorption compared to the traditional one. Authors suggest that the roughness creates additional, tuneable degrees of freedom in the system. Therefore, the observed improved sound absorption arose from regulating the material's acoustic impedance to meet the impedance-matching condition.

Furthermore, surface roughness enhanced the resonator's neck's relative acoustic mass and relative acoustic resistance. As the authors suggest considering the analysed material as a spring-oscillator system, an increased acoustic mass and a greater acoustic resistance lead to lower resonance frequency and enhanced energy dissipation, respectively. Finally, particle vibration velocity graphs were generated from the numerical results, allowing the comparison between the smooth and rough necks at their resonant frequencies. In the case of the smooth neck, most energy dissipation occurred close to the inner wall, and lower losses occurred in the centre.

On the other hand, high-velocity levels accumulated at every narrow fraction of the rough neck's periodic pattern, resulting in concentrated friction between the fluid and the inner surface, which led to enhanced energy dissipation. The results of this study indicate that surface roughness causes the periodic concentration effect of vibration velocity, which induces improvements in the acoustic mass and acoustic resistance of the neck. As a result, acoustic impedance regulation can be achieved.

3.2.2 Limited geometrical accuracy

Another defect present in all additive manufacturing technologies is the reduced dimensional accuracy of manufactured parts. In 3D printing, the XYZ resolution of the three spatial dimensions determines the geometrical accuracy. The XY plane defines the minimum feature size, while the resolution of the z-axis defines the layer thickness [119]. Therefore, the achievable resolution will vary significantly among different 3D printing processes. On the other hand, other parameters and phenomena specific to different additive manufacturing technologies affect dimensional accuracy, which will be discussed in this subsection.

In extrusion-based additive manufacturing, the combination of process and design parameters influences the dimensional accuracy of produced components to a great extent, as mentioned in Section 3.1.1. Among them, especially crucial is the printing speed. An increase in printing speed has a detrimental effect on the precision of the FDM process [120]. Moreover, the nozzle diameter also impacts the geometrical accuracy due to the radial expansion of the liquified polymer exiting the nozzle [121]. Another issue affecting the dimensional accuracy of parts produced via extrusion-based additive manufacturing technologies is the shrinkage of polymer materials, which leads to warping and thermal deformations [122].

3D printers based on photopolymerisation and PBF techniques produce much more accurate parts due to higher resolution. However, in the case of resin-based technologies, the major drawback of working with photopolymers is the material shrinkage during curing [123]. Other process parameters are also of significance in photopolymerisation-based additive manufacturing, as discussed previously in Section 3.1.2. Mostafa *et al.* (2017) demonstrated in their study that exposure time is the most influential process parameter that affects the dimensional accuracy of DLP parts [79]. Furthermore, based on the parameter significance calculation results, they concluded that it has more effect on the print quality than the layer thickness.

On the other hand, in the latest SLA devices, the layer thickness is usually the most important, if not the only, parameter that must be consciously set by the user, while the remaining parameters can and usually are selected automatically and optimally by the software depending on the type of photopolymer resin used. This means that in practice, it is the layer thickness that is responsible for the print quality and accuracy.

The geometrical accuracy of components produced via PBF-based additive manufacturing technologies is impacted primarily by shrinkage and warping, which affects mainly flat surfaces. In SLS, over-sintering may result in metal powder melting around the determined points and lead to a loss of dimensional accuracy [119].

3.2.3 Microporosity

The third major 3D printing defect is microporosity, which is present in extrusion and PBF-based additive manufacturing technologies. It is usually referred to as the porosity of the build material. Although the 3D printing process can be optimised to produce nearly fully dense parts with minimal porosity, this issue cannot be fully eliminated [124].

In extrusion-based additive manufacturing, variations of the internal structures of the 3D printed parts are caused primarily by the chosen process parameters. The main parameters affecting the porosity of FDM parts are bead width, air gap [125] and raster angle [126]. Furthermore, polymers used during manufacturing have their own internal composition, which may also be subject to microporosity [127].

In PBF-based additive manufacturing, microporosity may occur in various forms and distributions in the 3D printed part because of different underlying causalities leading to its formation [124]. There are two leading causes responsible for microporosity. First, a lack of fusion occurs when insufficient energy is applied during the process, which causes a small melt pool and incomplete melting. The resulting porosity depends mainly on the laser power and scan velocity [128]. Secondly, the so-called keyhole porosity may develop, which depends mostly on laser power, scan speed, laser beam profile and its interactions with the powder bed. When the laser power is too high or the scan velocity is too low, the emerging deep melt pool with a vapour cavity becomes unstable, creating and leaving rounded pores in the solidified material [124]. Keyhole porosity is, therefore, predominantly a melt-pool level effect.

From the acoustic point of view, microporosity can be, in fact, very beneficial for 3D printed sound-absorbing materials as it provides additional losses.

3.3 Influence of additive manufacturing on acoustics

Deviations between numerical results and experimental data with regard to additively manufactured acoustic materials are often attributed partly to manufacturing defects.

These discrepancies typically include the presence of excessive broadband absorption in experimental results compared to predictions from numerical models, which, in general, tend to underestimate overall acoustic material performance, although they may sometimes overestimate at ('narrow-banded') peaks. More serious deviations result primarily from the mismatch of the model to the actual sizes of acoustically important dimensions (such as the diameter of necks, channels or perforations, the width of slits, etc.).

Several studies have investigated the influence of additive manufacturing on the acoustic properties of fabricated parts.

Sakagami *et al.* (2020) fabricated microperforated panels using FDM [26]. Compared to theoretical results, experimental curves of sound absorption coefficient shifted towards higher frequencies and, in two out of three cases, were underestimated in terms of the peak magnitude. This was explained by the limitations of the theoretical model assuming homogeneous surfaces, which in practice was not achieved due to deviations in the geometrical parameters of manufactured microperforated panels. These deviations were caused by the reduced dimensional accuracy during the manufacturing process.

Sailesh *et al.* (2021) manufactured microperforated panels with varying perforation cross-sections using FDM and achieved a good match between the numerical and experimental sound absorption coefficient values in terms of peak magnitude and frequency position [129]. Nonetheless, the experimental results were more absorbent in lower and higher frequency regions, which was thought to be caused by failure to fulfil the perfect rigidity and smooth surface assumptions. The rise in absorbtivity was attributed to viscothermal losses and solid-fluid friction caused by rough and non-rigid surfaces. Properly optimising print parameters allowed PLA parts to behave consistently owing to good surface finish, dimensional accuracy and impeccable layer deposition.

In an investigation into differences between micro-lattices manufactured via FDM with their idealised, theoretical representation, Boulvert *et al.* (2020) found that neglecting 3D printing imperfections reduced the accuracy of the model [130]. One of the considered defects was the assumption of the perfectly circular filament section, which in reality, had an elliptical shape. Another issue was the filament section shrinkage occurring during extrusion. Finally, the filament surface was not perfectly smooth and had some rugosity.

Kumar *et al.* (2020) produced ventilated acoustic metamaterial window panels using FDM [131]. The numerical and experimental results of sound transmission loss matched in frequency. However, measured values were higher than simulated. This was explained by the surface roughness that was not considered in simulations and could have provided extra resistance to the incoming sound wave at the wall-air interface.

In a study by Carbajo *et al.* (2021), the mismatch between numerical and experimental results of the sound absorption coefficient of macro-perforated porous media fabricated using FDM was explained by reduced manufacturing accuracy and a finite circular cross-section of the sample, in contrast to its square-type assumption in the model [132]. Almeida *et al.* (2021) produced a metamaterial with symmetrical-coiled-up spaces using FDM [133]. The observed differences between numerical and experimental results of the sound absorption coefficient were attributed to the surface roughness of the internal walls of the symmetrical coiled-up spaces.

Kennedy *et al.* (2019) compared experimental and numerical values of the sound absorption coefficient of a periodic porous structure fabricated using FDM, SLA, DLP and SLM [13]. The observed deviations were explained by distorted geometric accuracy and surface roughness. The most considerable discrepancies were observed for the FDM sample, while SLM and SLA samples were in close agreement with the numerical models.

In order to determine the reproducibility of additive manufacturing, Zielinski *et al.* (2020) compared the performance of periodic porous material fabricated using various technologies in several European laboratories and research institutes in a round-robin test [14]. The discrepancy in sound absorption coefficient between samples fabricated by different institutions could be caused by varying manufacturing quality and the presence of 3D printing defects (surface roughness, microporosity of print material, material stringing in voids), the quality of the fit adjustment of the sample to the diameter of the impedance tube, the cylindrical cut of the sample, which was defined on a cubical unit cell.

Chapter 4

Additive manufacturing assessment

4.1 Introduction

This chapter examines the influence of the additive manufacturing process on the acoustic performance of the 3D printed material. For this reason, three distinctive additive manufacturing processes were chosen for comparison: extrusion-based FDM, photopolymerisation-based MSLA and PBF-based SLM. 3D printed parts are always subject to surface roughness and other defects, irrespective of the applied production method, as discussed previously in Section 3.2, although in the case of some 3D printing technologies (e.g. SLA) and raw materials (resins), the surfaces of manufactured parts can be relatively smooth. However, the extent of these issues varies among additive manufacturing processes, leading to the difference in sound absorptive properties of the same geometrical design manufactured using different 3D printing techniques. Here, a very important issue is the accuracy and quality of the geometry mapping by different technologies.

To investigate the relative impact of surface roughness and other 3D printing defects on the acoustic performance of additively manufactured materials, a benchmark porous material, called 'DENORMS', described in detail in Section 1.2.1, was fabricated using three different 3D printing machines: FDM-based Prusa Mini, MSLA-based Elegoo Mars and SLM-based Systems Prox DMP 200, using standard layer heights utilized in these technologies (which will be discussed later). Two types of samples were produced, suitable for investigating surface topology and acoustic properties. A combination of numerical and experimental approaches was used in the data analysis.

4.2 Additive manufacturing

To evaluate the strengths and weakness of each of the considered additive manufacturing technologies, two sets of samples were fabricated using the default print settings recommended by the 3D printers' manufacturers: (1) cylindrical samples (see Figure 4.1a), which are suitable for sound absorption measurements, (2) cross-sectional samples (see Figure 4.1b) which are suited for surface quality inspection.

This chapter is based on a conference paper: A. Ciochon, J. Kennedy, and M. Culleton. Evaluation of surface roughness effects on additively manufactured acoustic materials. In *Proceedings of ISMA2022 International Conference on Noise and Vibration Engineering, USD2022 International Conference on Uncertainty in Structural Dynamics*, Leuven, Belgium, 2022

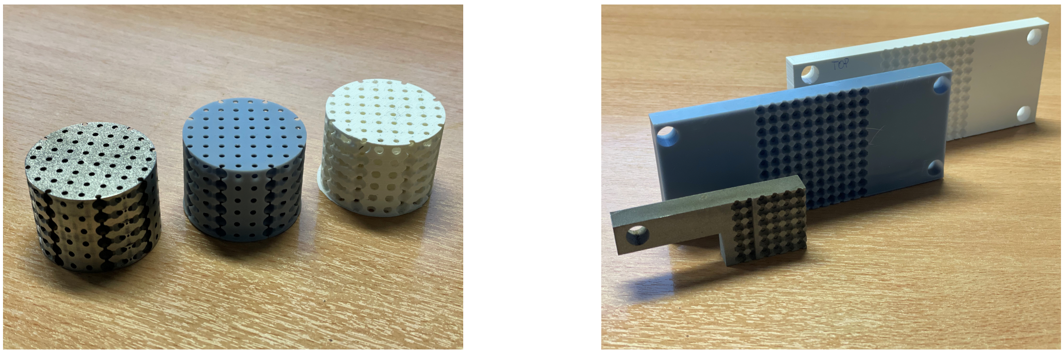

(a) Suitable for sound absorption testing (b) Suitable for confocal microscope testing

Figure 4.1: Additively manufactured samples left to right:
SLM (metallic), MSLA (grey), FDM (white)

Standard layer heights for each of the three processes were used during the fabrication of parts; these are: 0.10, 0.15, 0.20 and 0.25 mm (FDM), 0.03 and 0.05 mm (MSLA) and 0.03 mm (SLM). The main printing parameters for these processes are summarised in Table 4.1. The FDM samples presented in this chapter were manufactured using standard printing settings before implementing parameter modifications discussed in Appendix D.

Parameter	Value
FDM	
Layer height	0.10, 0.15, 0.20, 0.25 mm
Nozzle temperature	195°C
Bed temperature	60°C
Fill density	15 %
Infill printing speed	80 mm/s
MSLA	
Layer height	0.03, 0.05 mm
Exposure time	2.5 s
Bottom exposure time	30 s
Lifting speed	80 mm/min
Retract speed	210 mm/min
SLM	
Layer height	0.03 mm

Table 4.1: 3D printing parameters for different additive manufacturing technologies

For each of the chosen layer heights, three cylindrical samples were manufactured to account for the repeatability of the additive manufacturing process. Each of these samples corresponded to a six-cell deep array. Figure 4.1 depicts only a subset of samples and layer heights used within this study.

4.3 Non-destructive testing

Several non-destructive testing (NDT) techniques were implemented in this study as inspection methods for the quality control of fabricated parts. They provided an in-depth insight into the surface quality and were a valuable tool for assessing external and internal component properties.

4.3.1 Digital microscopy

A qualitative assessment was carried out using digital microscopy. The Dino-Lite Premier AM7013MT digital microscope was used to capture close-up pictures of the surface of both samples. The machine has a 5-megapixel sensor and can magnify up to 200 times magnification with a resolution of up to 2592x1944.

FDM

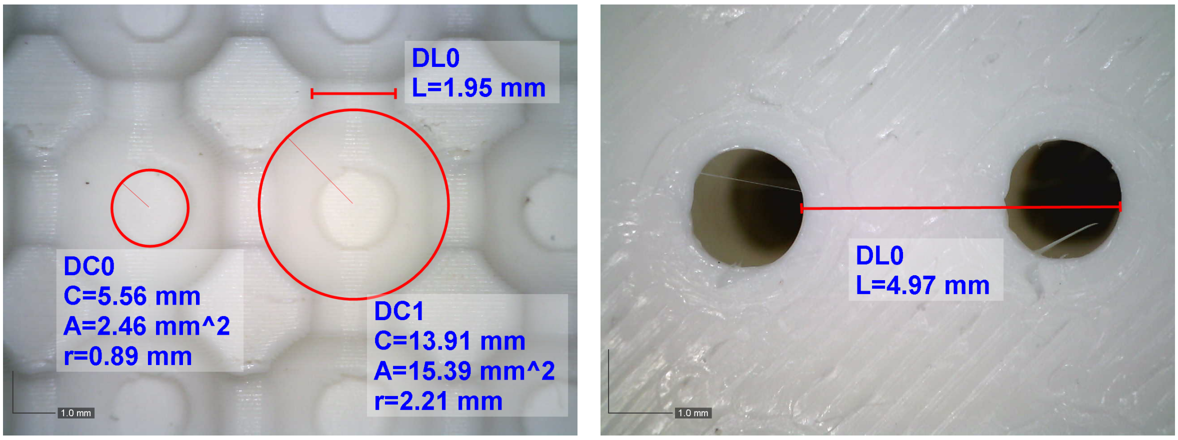

(a) Cross-sectional sample

(b) Top of a cylindrical sample

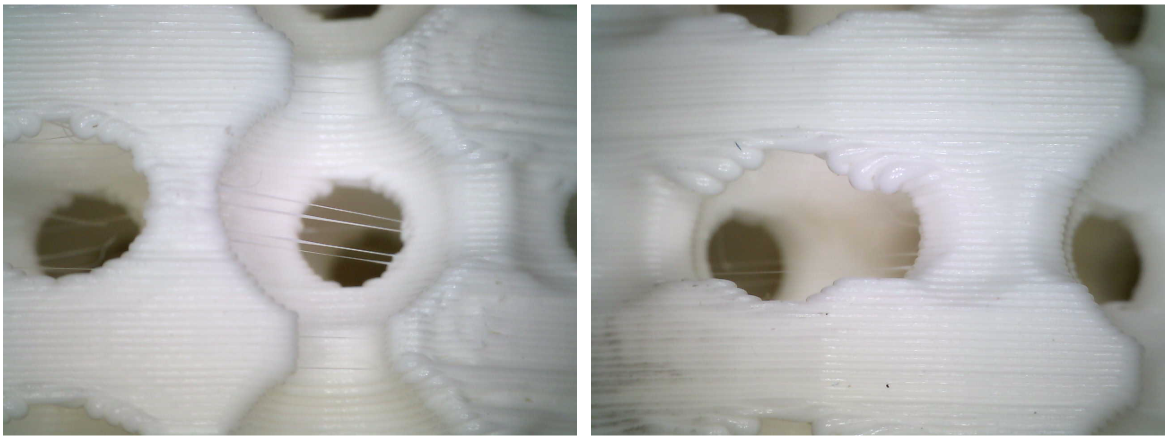

(c) Surface finish of cavities (note filament fibres)

(d) Filament blobs

Figure 4.2: Digital microscopy: FDM

Microscopic images of cylindrical and cross-sectional FDM samples manufactured with an exemplary layer height of 0.10 mm are illustrated in more detail in Figure 4.2. Figure 4.2a, which depicts an exemplary cross-sectional sample at close range, indicates that the FDM printer had issues correctly capturing geometry. The sphere's radius was measured to be 2.21 mm, whereas it was set to be 2.25 mm in the CAD software. The printer succeeded better at creating cylinders, in the case of which the diameter was achieved at 1.95 mm, whereas it was set to be 2 mm. No technology is able to map the CAD model geometry precisely, and FDM is perhaps the one which produced the largest discrepancies. The expert knowledge of the type and size of these errors should allow for necessary corrections after or even before the 3D printing process.

Figure 4.2b shows the top of the cylindrical sample and reveals the unevenness of the surface. Adjacent roads are visible as some dust gets trapped in between. However, the distance between neighbouring cells falls slightly below 5 mm. Figure 4.2c illustrates the presence of filament fibres trapped in air cavities, which is another issue in FDM, reported previously in [14]. Such fibres will improve sound absorption of the 3D printed materials, and recent studies show that they are reproducible on the same 3D printers by using the same 'incorrect' choice of process parameters and raw materials. In Figure 4.2d, a significant difference between curvatures created vertically can be observed. The lower arch is created accurately. However, the upper, unsupported one is made of uneven filament blobs, which highly exceed the set layer height and cause shape deformation.

MSLA

Microscopic images of cylindrical and cross-sectional MSLA samples manufactured with an exemplary layer height of 0.05 mm are illustrated in more detail in Figure 4.3. The cross-sectional sample's close-up image, shown in Figure 4.3a, reveals that uneven geometrical distortion occurs during post-processing of the photosensitive resin. The inner sphere of the DENORMS design underwent shrinkage to a similar extent as the FDM sample - with a radius of 2.22 mm instead of 2.25 mm set in CAD. On the other hand, the cylindrical shape experienced slight expansion - with a diameter of 2.06 mm instead of a set 2 mm.

Figure 4.3b illustrates the top of the cylindrical sample. The surface finish is relatively smooth, having only a few shallow scuff marks. Furthermore, holes have a smooth surface finish and an even spherical shape. The distance between adjacent unit cells is measured as 5 mm.

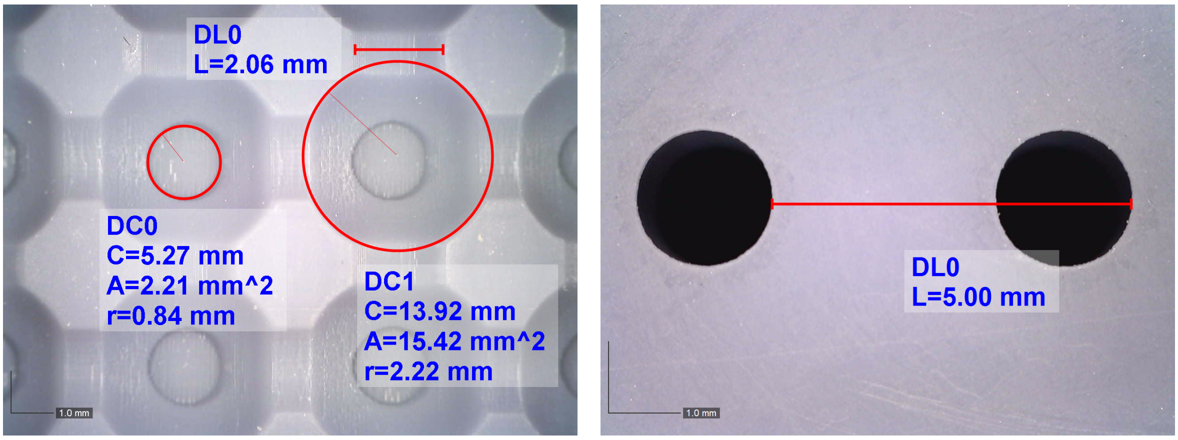

(a) Cross-sectional sample (b) Top of a cylindrical sample

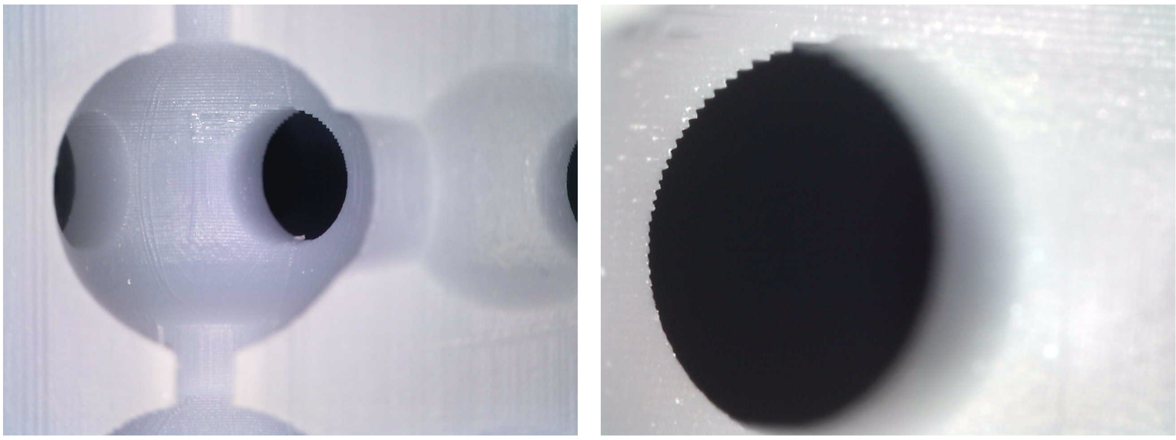

(c) Surface finish of cavities (d) Spherical curvature finish

Figure 4.3: Digital microscopy: MSLA

The inner surface of the unit cell is shown in Figure 4.3c. Although the surface finish is much better than in FDM, the individual layers can still be observed.

Figure 4.3d depicts the spherical curvature of the DENORMS cell. A difference in the quality of the curve printed in the vertical orientation can be observed. The upper part of the sphere is rugged and rough, whereas the lower part has an almost even surface finish.

SLM

Microscopic pictures of cylindrical and cross-sectional SLM samples manufactured with a layer height of 0.03 mm are illustrated in Figure 4.4. Figure 4.4a shows a close-up of the cross-sectional sample and displays the geometrical accuracy of the printer in capturing the set CAD drawing. The diameter of a cylinder was measured at 1.95 mm, whereas it was set to be 2 mm in the CAD model. In the case of the sphere, the radius was achieved at 2.21 mm, whereas it was set to be 2.25 mm.

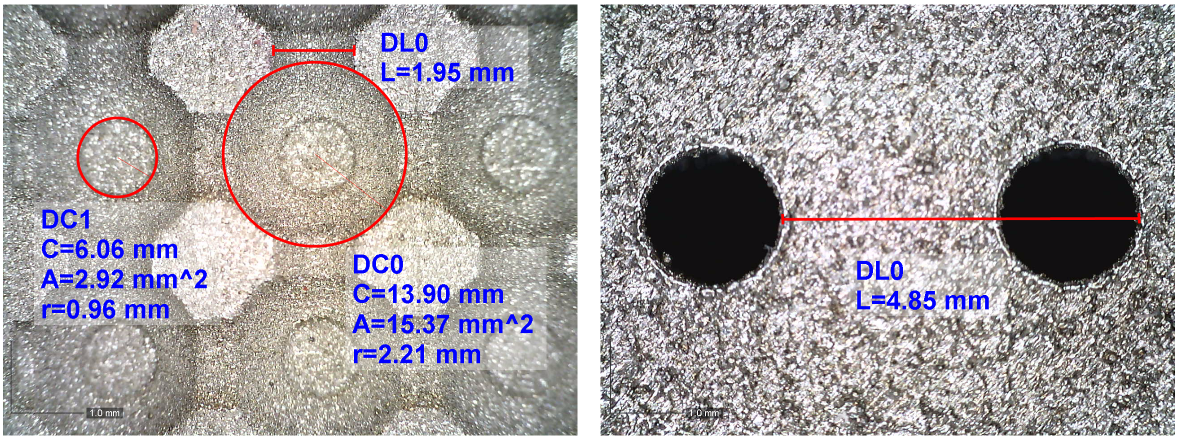

(a) Cross-sectional sample (b) Top of a cylindrical sample

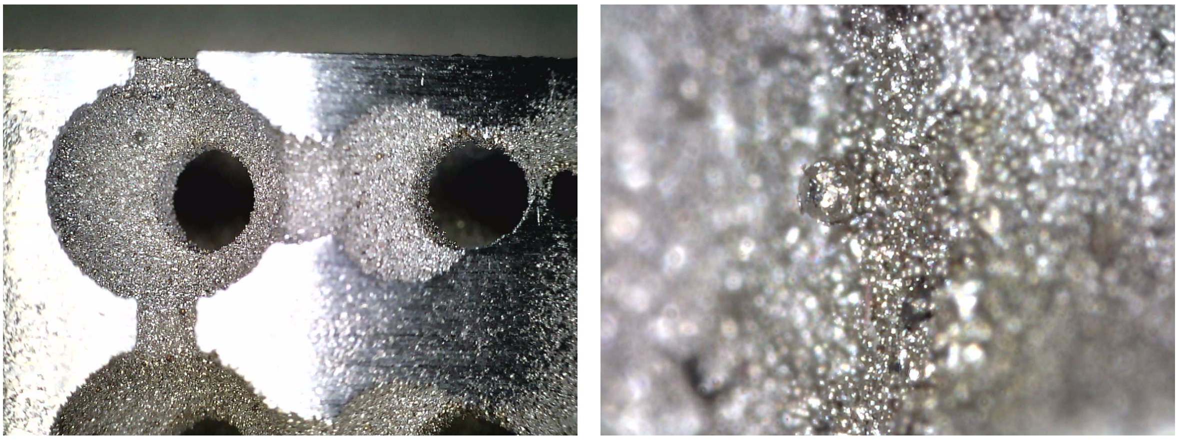

(c) Surface finish of cavities (see satellite particle) (d) Satellite particle

Figure 4.4: Digital microscopy: SLM

Figure 4.4b displays the top of the cylindrical sample. As can be seen, the distance between adjacent cells falls below the set 5 mm, which can be caused by the distortion of cylinder heights. The roughness of the inner cavities is shown in Figure 4.4c. It is due to powder grains and related to the grain size. It should also be noted that the cylindrical samples underwent sanding on the outside face to fit better into the sample holder of the impedance tube.

A satellite particle can be spotted on the surface of the cavity in the upper left corner. Figure 4.4d shows it in more detail. Satellite particles result from the balling effect, during which the melt pool ejects spherical particles that settle on surfaces. These particles create local, relatively large-scale features which are randomly distributed around the inner surfaces of the cells. However, they are quite rare.

4.3.2 Confocal microscopy

The surface quality of manufactured cross-sectional samples was investigated using an automated, 3-axis measurement system developed in-house in Trinity College Dublin, as illustrated in Figure 4.5.

The inspected part is attached on top of a motorized XY stage, which moves across the pathway of a Keyence CL-PT010 chromatic confocal sensor (spot diameter of ø 3.5 µm, linearity of ±0.22 µm and resolution of 0.25 µm). The acquired 2D line scans can be used for surface roughness calculations and dimensional accuracy evaluation.

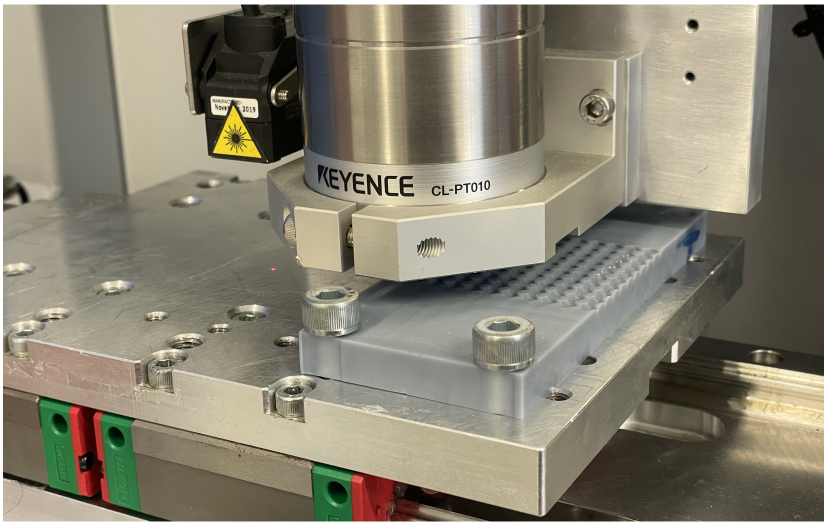

Figure 4.5: Confocal microscope

FDM

Surface profiles obtained using the confocal microscope for FDM samples with different layer heights are shown in Figure 4.6. Each profile was acquired by combining two separate measurements with the measurement centreline set at different heights to cover the whole unit cell.

Since the considered cross-sectional samples were manufactured in a vertical direction, it can be seen that the geometric fidelity depends on whether the printer was creating a bottom or a top part of the DENORMS cell inner cavity.

A noticeable difference between the sphere's left-side (top) and right-side (bottom) arches is observed. The upper surfaces of the sphere are unsupported overhangs, and all print processes will have difficulty creating this geometry with the accuracy also influenced by the layer height. Lower values of the layer height will improve the geometry accuracy.

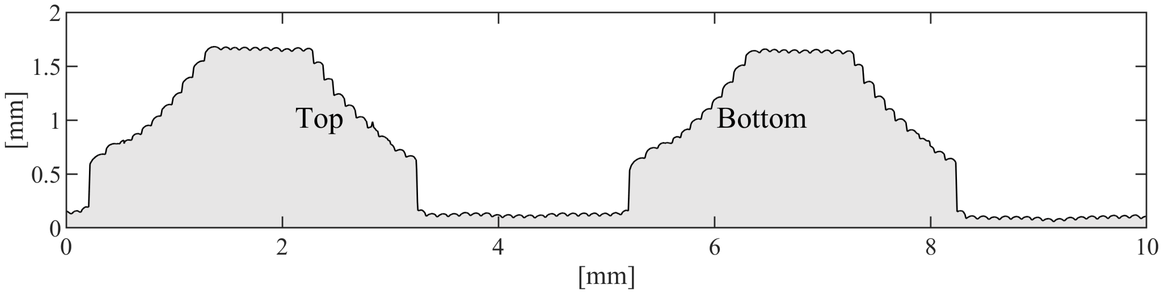

(a) 0.10 mm LH

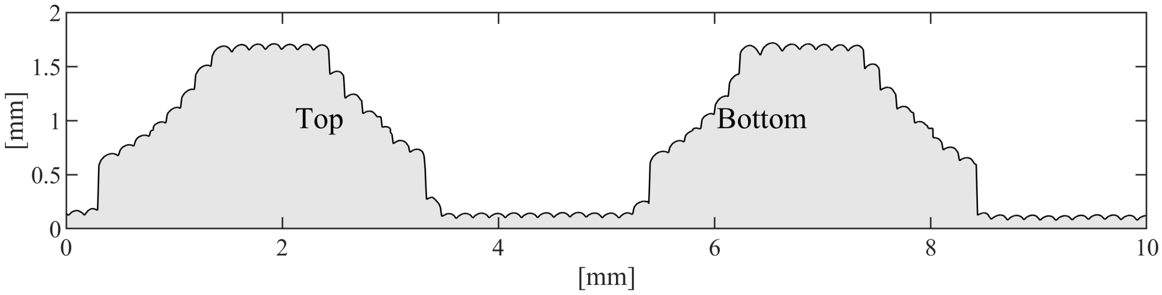

(b) 0.15 mm LH

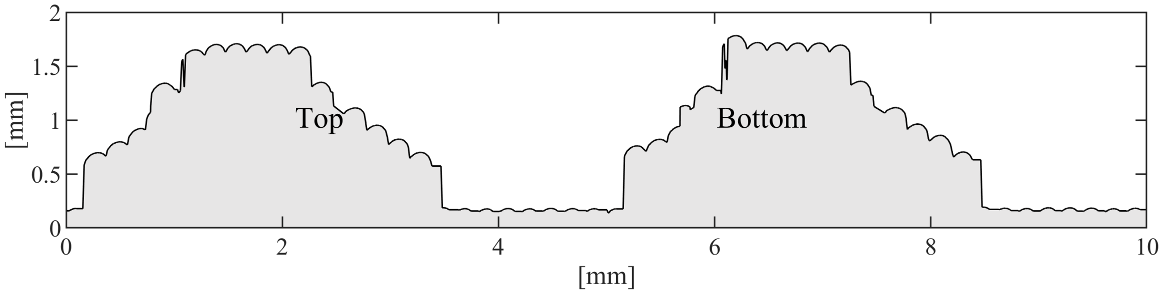

(c) 0.20 mm LH

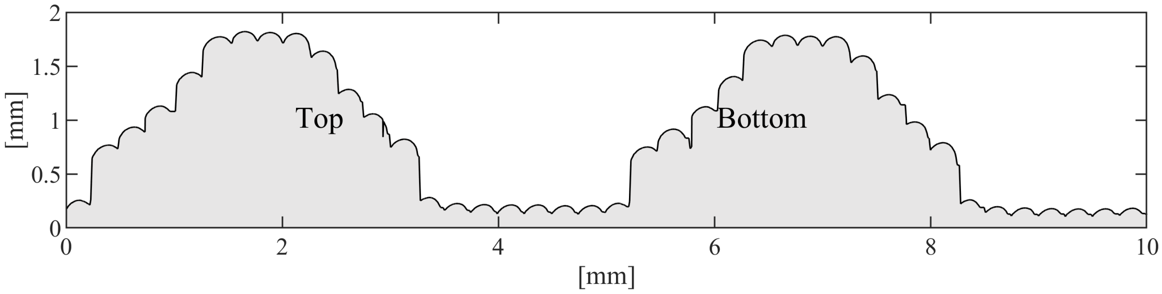

(d) 0.25 mm LH

Figure 4.6: Confocal microscopy: FDM

MSLA

Surface profiles obtained for MSLA samples produced using two layer heights are illustrated in Figure 4.7. Compared to the FDM profiles, MSLA profiles are almost smooth. However, a noticeable geometrical distortion can be observed regarding both the shape and the dimensional accuracy. Furthermore, the difference between the sphere's left-side (top) and right-side (bottom) arches is even more substantial than for the FDM samples. Moreover, the created geometry has undergone shrinkage, a primary issue of this print process. As a result, the dimensions are smaller than those specified in the input CAD file. This shrinkage is affected by the part's geometry and may be greater in the confocal microscope samples due to the sizeable contiguous volume.

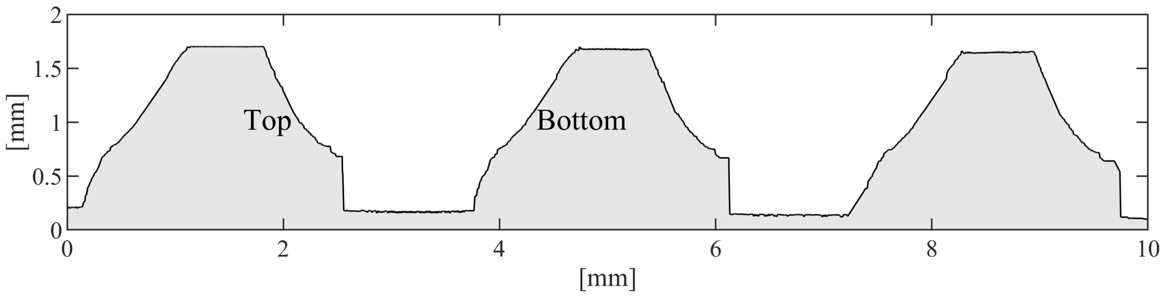

(a) 0.03 mm LH

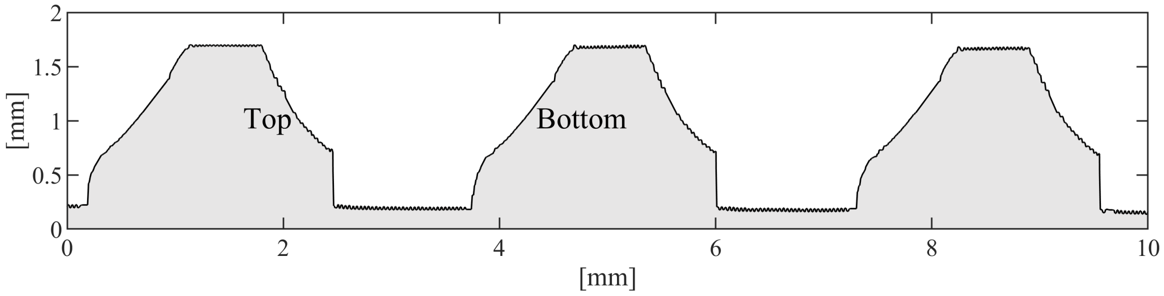

(b) 0.05 mm LH

Figure 4.7: Confocal microscopy: MSLA

SLM

The surface profile obtained for the SLM sample is shown in Figure 4.8. SLM profile is rougher than the MSLA one. However, better dimensional accuracy was achieved. The main cause of surface roughness in SLM is the powder grains, and the roughness should be related to their size. The grains are sintered, so they form a rough texture on surfaces. In the SLA technology, the structure is solidified from liquid (photopolymer resin), so one may expect smoother surfaces even in the MSLA technology. The upper and lower arcs of spherical pores are almost identical in the case of SLM samples (see Figure 4.8). This is because 3D printing takes place in a powder bed, i.e. overhanging structures are supported by powder.

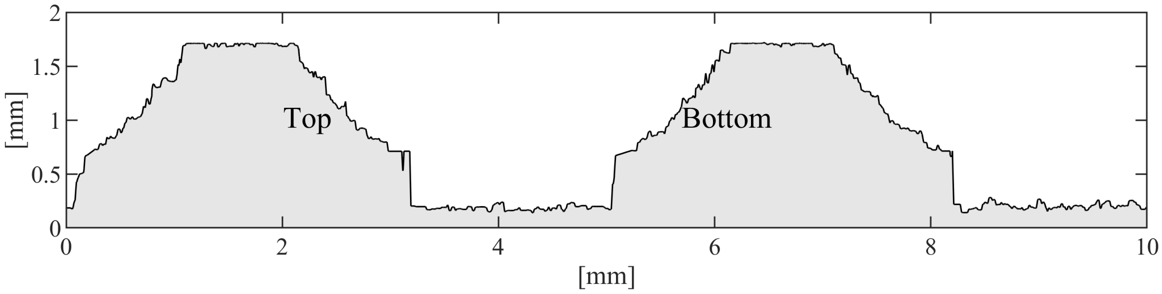

Figure 4.8: Confocal microscopy: SLM - 0.03 mm LH

4.3.3 CT scanning

The internal structure of additively manufactured samples was examined using the Nikon XT H 225 ST industrial computed tomography (CT) system available at Trinity College Dublin. The scan had an 8 µm pixel resolution.

The cylindrical sample manufactured via FDM was the only one fully scanned. For practical reasons (length of the process, the inability of the CT scan to penetrate fully inside the metal cylinder produced via SLM), in addition, smaller cubical lattices were produced. They are composed of one whole, central DENORMS cell and trimmed adjacent cells, as illustrated in Figure 4.9.

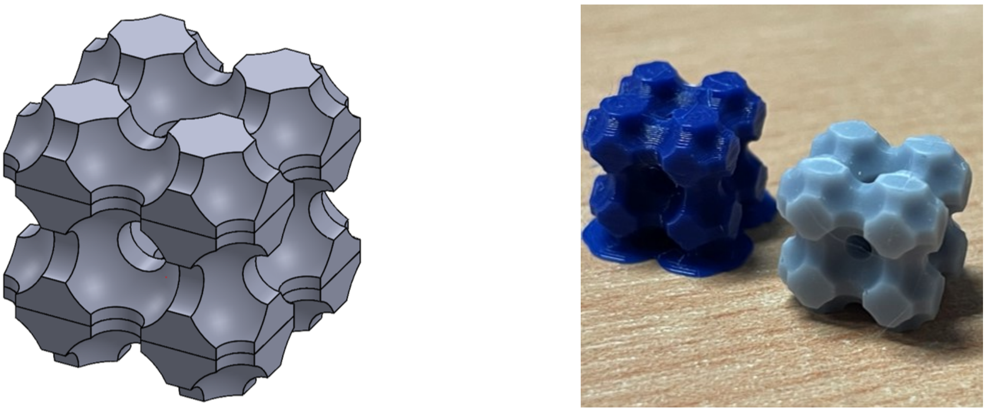

(a) CAD model

(b) FDM (blue) and MSLA (grey) samples

Figure 4.9: Cubical DENORMS lattice

In the case of SLM, an electrical discharge machining (EDM) cutting was used to extract a central segment of the cylindrical sample so the CT scan could easily penetrate the metal structure. Corresponding lattices were manufactured using FDM and MSLA; see Figure 4.9b. These arrays were fabricated using the following layer heights: 0.1 mm (FDM), 0.05 mm (MSLA) and 0.03 mm (SLM).

FDM

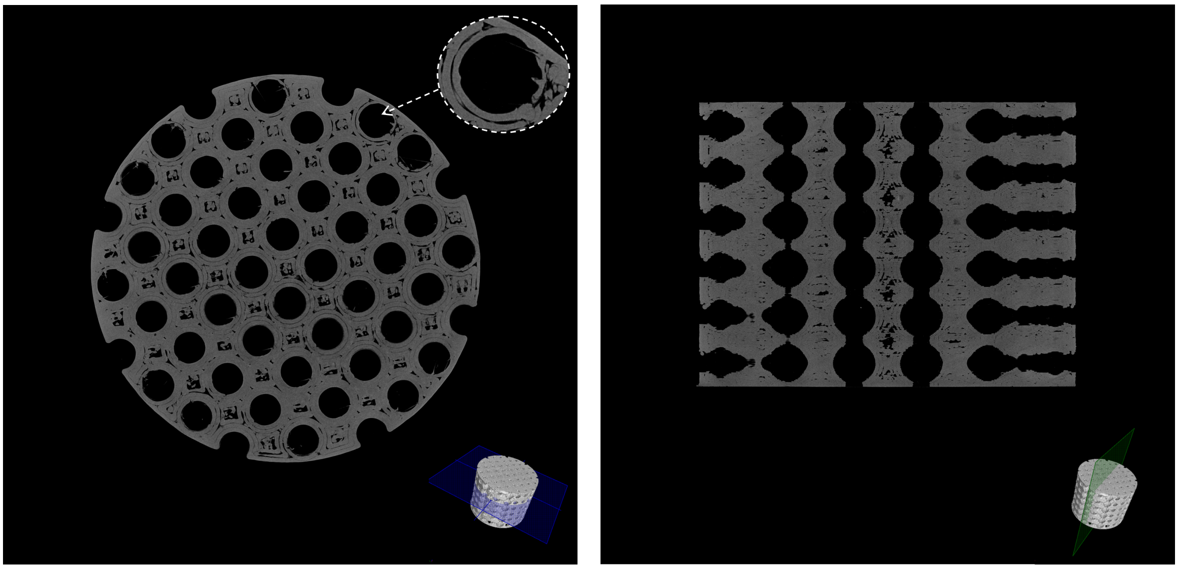

(a) Top slice

(b) Front

Figure 4.10: CT scanning: FDM (entire cylinder)

The exemplary top and front slices of the cylindrical sample based on the DENORMS periodic cell produced via FDM are displayed in Figure 4.10; their respective locations within the sample are shown in the lower right corner of each scan. It is worth noting that discontinuities at the edges of spheres unintentionally connect the DENORMS pore network with the small voids (micropores) within the 3D printed skeleton, which is depicted at the close-up in Figure 4.10a. The microporosity of FDM specimens is influenced by the chosen process parameters, such as raster orientation [126]. The top slice shown in Figure 4.10a shows the internal infill pattern set in the slicing software to 15%. This is the minimum design value, and in practice, the filling is much higher than 15%.

The exemplary top and front slices of the DENORMS lattice produced via FDM are shown in Figure 4.11. Figure 4.11a shows a horizontal slice of the sample. This orientation of the cross sections corresponds to an image within a single print layer. It can be seen that

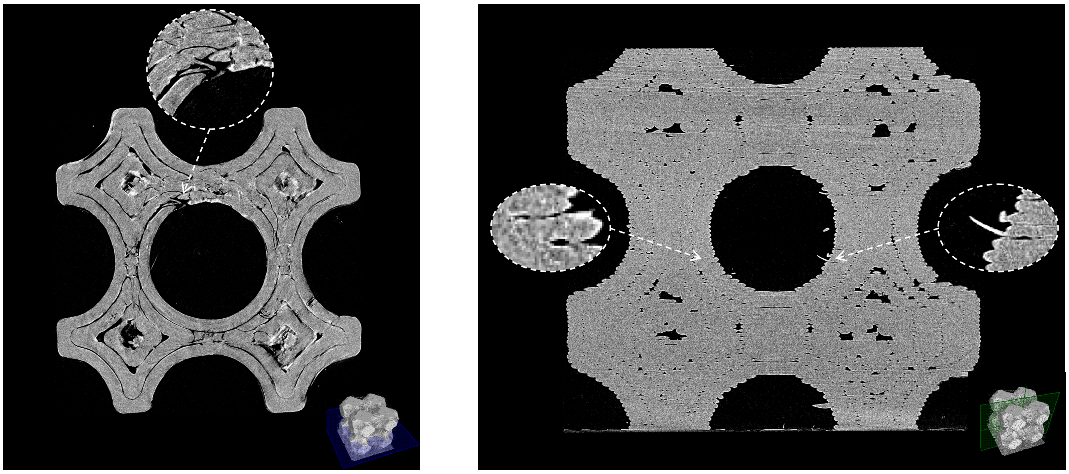

(a) Top slice (b) Front slice

Figure 4.11: CT scanning: FDM

FDM parts are characterized by delamination between adjacent filament roads. Furthermore, discontinuities at the surface's edge connect the DENORMS pore network with small air cavities (crevices) branching deeper inside the skeleton. Figure 4.11b illustrates a vertical slice of the lattice. This orientation of the cross sections corresponds to an image across many layers of the print. The skeleton of the FDM sample is relatively porous, and delaminated beads connect the DENORMS pore network with small voids. Moreover, filament fibres are trapped within the main spherical pore.

MSLA

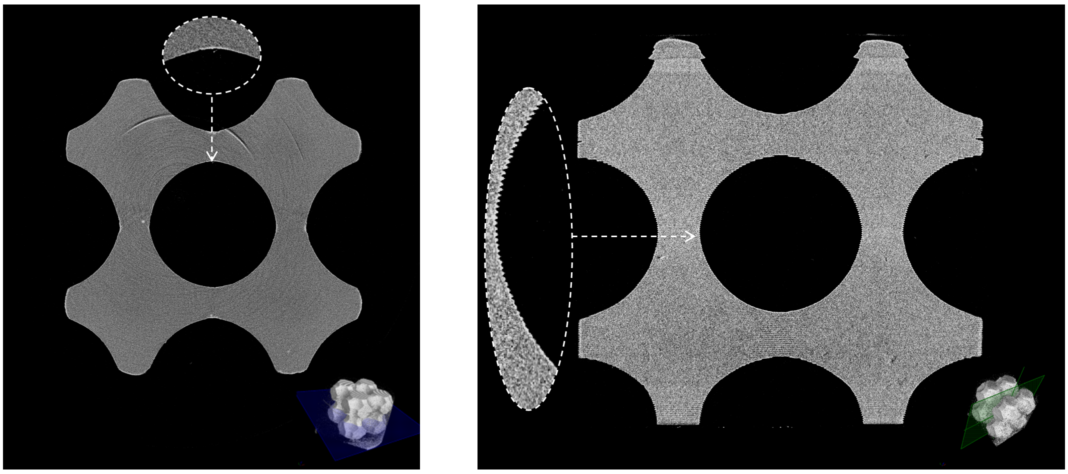

(a) Top slice (b) Front slice

Figure 4.12: CT scanning: MSLA

The exemplary top and front slices of the DENORMS cubical lattice produced via MSLA are shown in Figure 4.12. The horizontal slice shown in Figure 4.12a displays the interior of an MSLA part that is almost perfectly solid. Moreover, all the edges are smooth and mapped coherently. It should be pointed out that the noticeable circular pattern, or so-called ring artefacts, is a result of the rotation of the part and the back projection during CT scanning. The vertical slice illustrated in Figure 4.12b shows the difference between the fidelity of the spherical pore in MSLA. The print technology successfully produced a smooth surface finish on the lower part of the sphere. However, that changes to a slightly rough surface in the upper part of the sphere, which is depicted in the close-up in Figure 4.12b. Although some discontinuities are occasionally present in the solid part, they do not seem connected to the main pore network, which means that the 3D printed skeleton, and in particular its surfaces, are impermeable.

SLM

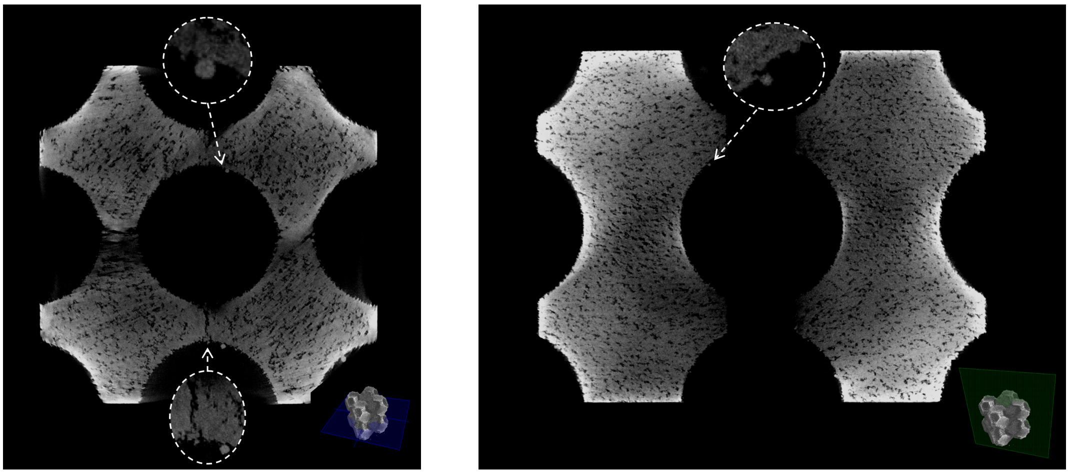

(a) Top slice

(b) Front slice

Figure 4.13: CT scanning: SLM

The exemplary top and front slices of the DENORMS cubical lattice produced via SLM are depicted in Figure 4.13. The SLM part's horizontal slice illustrated in Figure 4.13a is subject to flaws similar to the FDM sample. Similarly, there are discontinuities present that connect the bulk to small inner voids (micropores) inside the 3D printed structure. This is a very important issue because significant microporosity in the skeleton can lead to a material with double porosity.

Another issue is the rough finish of the edges and all surfaces as a result of sintering the structure from grains of metal powder. Moreover, spherical satellite particles can be spotted in certain regions. The vertical slice illustrated in Figure 4.13b shows additional satellite particles on the surfaces.

Microporosity analysis

Finally, the CT scanner was used for the microporosity analysis of the SLM sample with the aim of acquiring a general overview of the extent of this defect. Therefore, only an exemplary cuboid volume was chosen for the examination. Its location within the sample is illustrated in Figure 4.14

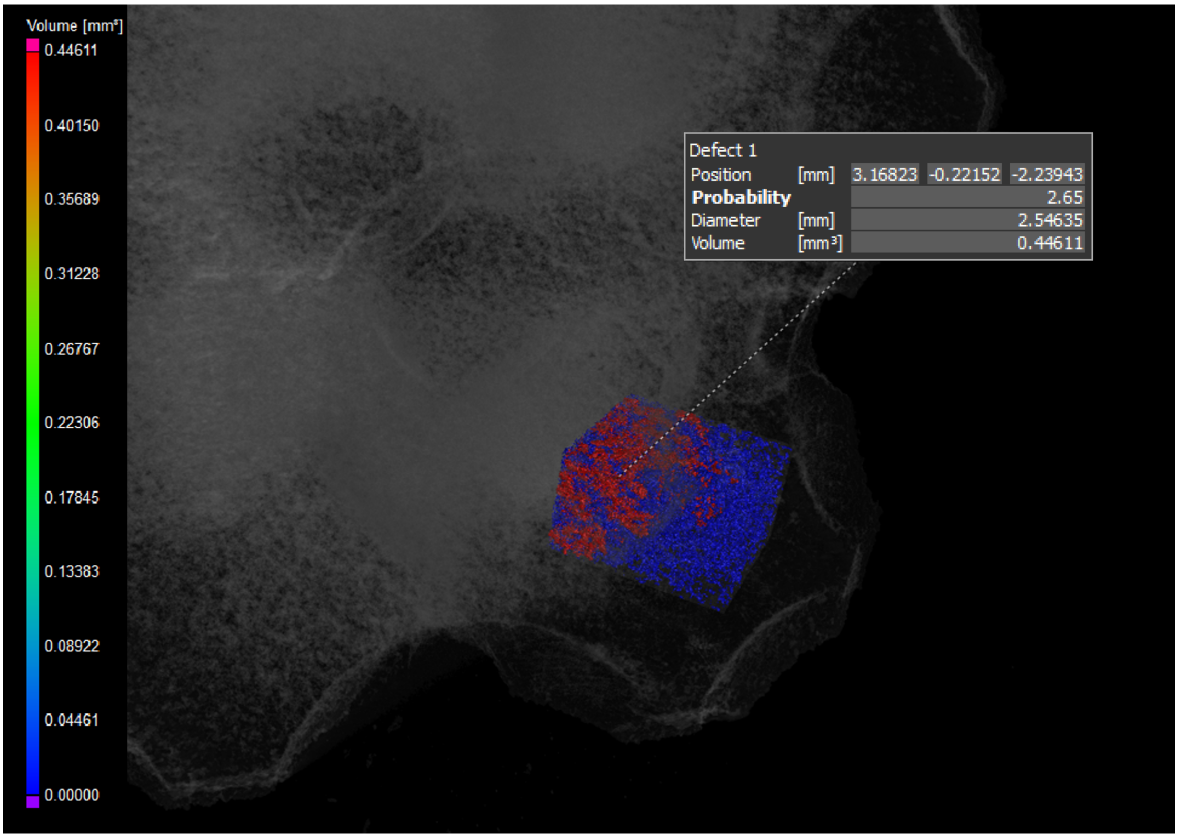

Defect 1
Position [mm] 3.16823 -0.22152 -2.23943
Probability 2.65
Diameter [mm] 2.54635
Volume [mm³] 0.44611

Figure 4.14: CT scanning: microporosity analysis (location within the sample)

The results of the microporosity analysis within the examined cuboid are illustrated in more detail in Figure 4.15. The colourmap legend on the left side of the scan indicates the volume of the micropores. Most of the micropores within the cuboid are shown in blue, meaning they have a small volume and, therefore, are not interconnected with each other.

However, the micropore shown in red has a substantial volume resulting from the interlinking of neighbouring micropores, which likely occurs due to surface discontinuities.

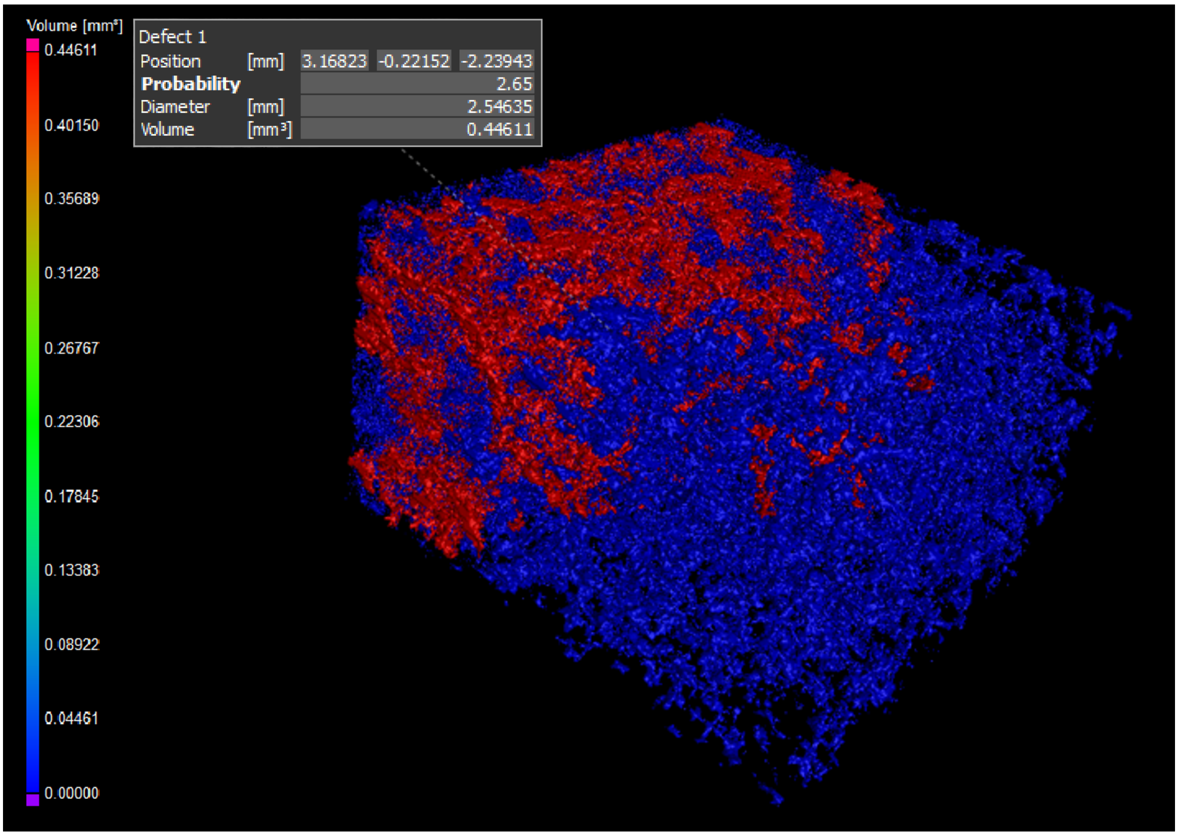

Figure 4.15: CT scanning: microporosity analysis

The microporosity within the analysed cuboid is 13.74%. This value is rather low compared to, for example, microporosities of about 44% found in structures 3D printed from gypsum powder, see [27]. The value of the microporosity should not affect the acoustic behaviour of the produced samples as long as the additive manufacturing process would produce sealed surfaces. However, the slices of the sample discussed previously in Section 4.3.3 revealed that this is rather not the case for FDM and SLM samples.

In general, based on microscopic observations (some of which are presented in this section), it is concluded or expected that: (a) The voids in the skeletons of FDM samples are larger than the voids (micropores) in the skeletons of SLM samples. (b) Most of these voids and micropores are closed or only form local micropore networks that are isolated and unconnected to the main pore network based on the DENORMS design. (c) However, some micropore networks are connected with the main pore network: through cracks (crevices) in the surface of FDM samples or open micropores in parts of the surface of SLM samples. This may lead to limited heterogeneous double porosity, which is difficult to model due to this heterogeneity since only some unspecified parts of the skeleton are significantly microporous, while others are impermeable (i.e. may only have closed microporosity).

It should also be noted that the possible local double porosity may differ significantly between FDM samples and SLM samples. This is because the internal voids in the skeleton of FDM samples are larger, so the permeability contrast to the main pore network is smaller. Such double porosity should influence the overall viscous permeability and tortuosity of the samples and lead to a change (increase) in the viscous dissipation effects. However, in the case of the SLM samples, the skeleton contains genuine micropores that are much smaller than the main spherical pore and cylindrical channels of the DENORMS design. This should result in a high permeability contrast between both networks, meaning that viscous flow (and therefore dissipation) in the micropores is negligible, but a new phenomenon of pressure diffusion occurs, which introduces a new, powerful mechanism for dissipating acoustic wave energy. Unfortunately (from the point of view of the acoustic material performance) or fortunately (from the point of view of acoustic modelling), due to the limited presence of double porosity, the above effects do not seem significant and are neglected in the modelling.

4.4 Acoustic evaluation

A combination of numerical and experimental techniques was applied in this study to perform the acoustic analysis. The assessment was done by comparing the numerical results of a smooth idealised geometry of a periodic DENORMS unit cell with the experimental results of the samples manufactured based on this geometry using three different additive manufacturing technologies.

The DENORMS cell, described in detail in Section 1.2.1 and shown in Figure 4.16a, is the solid skeleton of the structure arranged into a three-dimensional array and additively manufactured. The internal structure of the individual unit cell is illustrated in Figure 4.16b. The array of air-saturated spheres linked by cylindrical channels resulting from assembling the unit cells into a lattice forms a periodic pore network considered in the numerical model.

In this investigation, the numerical model is based on the smooth, idealised geometry of the pore network inside a single unit cell. The geometry of such an individual DENORMS cell used for the computational modelling is depicted in Figure 4.16c.

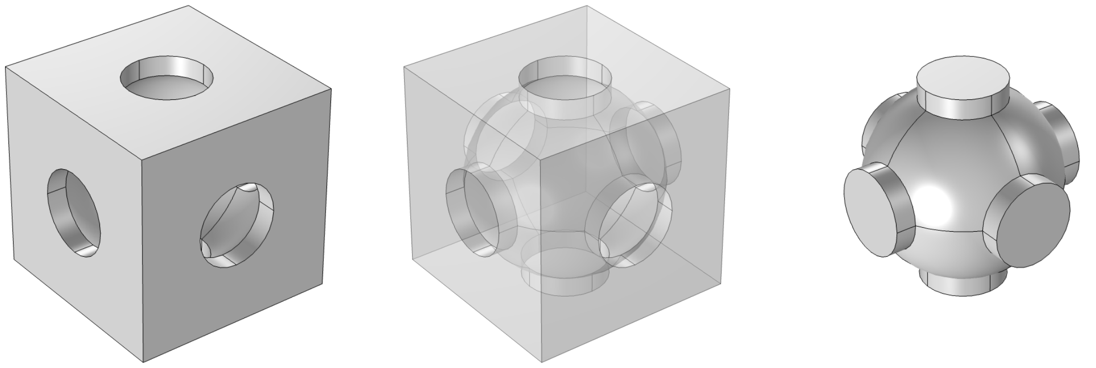

(a) Unit cell (b) Inner structure (c) Pore network (single cell)

Figure 4.16: DENORMS benchmark design

4.4.1 Viscothermal acoustics

The numerical simulations were carried out using a commercial finite element analysis software package, COMSOL Multiphysics. The Thermoviscous Acoustics interface available within COMSOL 6.1 is a suitable modelling tool for acoustic systems with small geometric dimensions, such as metamaterials and porous materials. In those cases, viscous and thermal losses occurring within the boundary layer must be considered to capture the physics accurately.

The Thermoviscous Acoustics interface within COMSOL uses direct, fully coupled modelling, which is not based on a homogenization approach. It uses the linearised version of the Navier Stokes equations with linear acoustics (by default) and an ideal gas assumption. The modelling strategy implemented in this study has been previously described in [13, 21]. The time-harmonic variation is assumed, using the $e^{+\jmath\omega t}$ convention, and the corresponding equations of the continuity, momentum and energy conservation for viscothermal acoustic fluid are, respectively:

$$\jmath\omega\frac{\rho}{\rho_0} + (\nabla\cdot\mathbf{u}) = \jmath\omega\left(\frac{p}{p_0} - \frac{\tilde{T}}{T_0}\right) + \nabla\cdot\mathbf{u} = 0 \tag{4.1}$$

$$\jmath\omega\rho_0\mathbf{u} = \nabla\cdot\left[-p\mathbf{I} + \mu(\nabla\mathbf{u} + \nabla\mathbf{u}^{\tilde{T}}) - (\frac{2\mu}{3} - \mu_b)(\nabla\cdot\mathbf{u})\mathbf{I}\right] + \mathbf{F} \tag{4.2}$$

$$\jmath\omega(\rho_0 C_p\tilde{T} - T_0\alpha_0 p) = -\nabla\cdot\left(-k\nabla\tilde{T}\right) + Q \tag{4.3}$$

where the dependent variables are the complex amplitudes of pressure p, velocity $\mathbf{u}$, temperature $\tilde{T}$ and fluid density ρ. $\mathbf{F}$ and Q represent a volume force and a heat source, respectively.

I is the second-order identity tensor represented in orthogonal systems by the 3 x 3 identity matrix, and μ and μ_b are the dynamic and bulk viscosity of the fluid, respectively, while ρ_0 and T_0 are the equilibrium density and temperature. Finally, C_p is the heat capacity at constant pressure, and k is the coefficient of thermal conduction of the fluid (which in this work is air).

Following Stokes's assumption, the bulk viscosity for a Newtonian fluid μ_b is omitted and set to zero because of its negligible contribution to the total dissipation. It is also possible to set this value to $\mu_b = 0.6 \times \mu$, which will be discussed in the Appendix C.

In the ideal gas case, the following relationships can be derived from the state equation $p = \rho\tilde{R}T$, where $\tilde{R}$ is the universal gas constant and β_T the isothermal compressibility.

$$\beta_T = \frac{1}{p_0} \qquad \alpha_0 = \frac{1}{T_0} \tag{4.4}$$

$$\rho = \rho_0 \left(\frac{p}{p_0} - \frac{\tilde{T}}{T_0} \right) = \rho_0 \left(\beta_T p - \alpha_0 \tilde{T} \right) \tag{4.5}$$

Viscous and thermal boundary layers are created during sound propagation in a fluid surrounded by walls. Their thicknesses, δ_v and δ_t, respectively, are given by the following formulas:

$$\delta_v = \sqrt{\frac{2\mu}{\omega\rho_0}} \tag{4.6}$$

where μ is the dynamic viscosity, ω is the angular frequency and ρ_0 is the density of air.

$$\delta_t = \sqrt{\frac{2k}{\omega\rho_0 C_p}} \tag{4.7}$$

where C_p is the heat capacity at constant pressure and k is the coefficient of thermal conduction.

4.4.2 Model configuration

The model of six layers of the unit cell was created with a smooth surface finish, as shown in Figure 4.17. Geometric symmetries were exploited to reduce the computational cost associated with thermoviscous modelling. Therefore, only quarters of the cells were modelled with the appropriate symmetric boundary conditions applied to the symmetry planes. Symmetry conditions were also applied to the semicircular boundaries of fragments of cylindrical channels because they are also symmetrical planes of a material that is infinitely periodic in these directions.

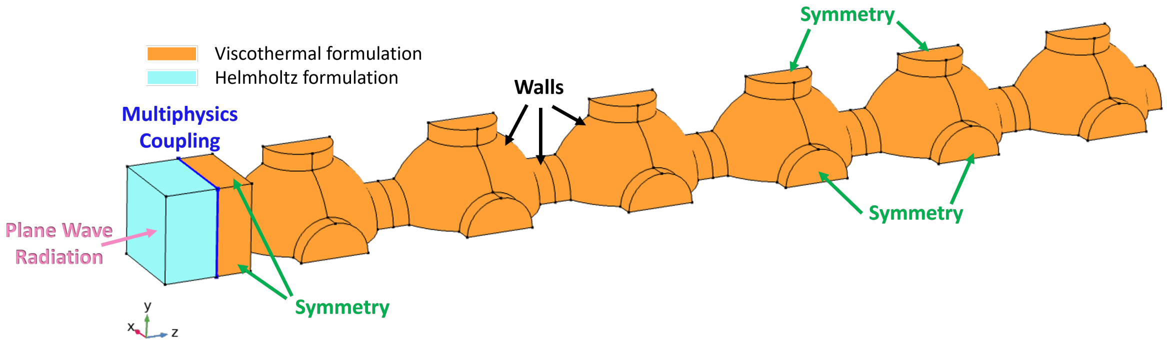

Figure 4.17: Model set up of the 6 layer deep DENORMS cell

A multiphysics coupling between thermoviscous and pressure acoustics was used in the models and applied on the rectangular interface between the orange domain and the light-blue one (the latter is modelled using the Helmholtz equation for an inviscid acoustic fluid), as shown in Figure 4.17. An inlet manifold (the light-blue cuboidal domain) with a thickness of 1.5 mm was created as a waveguide. A plane wave loaded with a unity pressure excitation, p_i, was imposed at the inlet to the waveguide. The transition to a full viscothermal formulation occurred within the waveguide. That allowed capturing losses at the entry to the cell.

Most of the boundaries were solid walls. Moreover, a hard wall termination was set at the end of the periodic structure. On these walls, at the solid-fluid interface, we have no-slip and isothermal boundary conditions. While this thesis treats these surfaces as rigid walls, it would be possible to account for the 3D printing microporosity effects by applying the impedance boundary condition to these surfaces instead of treating them as hard walls. It should be noted that determining the accurate impedance values poses a significant challenge. In FDM and SLM, it is difficult to quantify where and how the voids (micropores) are connected to the main pore network. In these samples, microporosity is present; however, it is usually closed from the main pore network.

The governing equations were discretised using second-order Lagrangian elements with quadratic shape function interpolation for the velocity field and temperature nodal variables. Linear interpolation was used for the pressure variable. The viscous boundary layer thickness was used as a meshing parameter closed to the solid walls (see Figure 4.17) in the simulations considered in this study. The meshes comprised tetrahedral elements for the bulk and sweep elements for the boundary layer.

4.5 Results and discussion

Figure 4.18 presents experimental results plotted against the numerical curve of the theoretical, smooth model. The numerical model underestimates the sound absorption in comparison to the experimental curves obtained for 3D printed samples manufactured using various print processes. In general, for FDM and SLM, the sound absorption coefficient rises with the increase in the layer height. Furthermore, the position of the peak moves towards lower frequencies. What is interesting in this data is that MSLA prints do not follow this trend. The magnitude of the MSLA experimental curve is closest to the numerical values. Moreover, the position of the peak moves towards higher frequencies. In the case of all experimental curves, broadband absorption can be observed in lower and higher frequencies that is not present in the numerical curve.

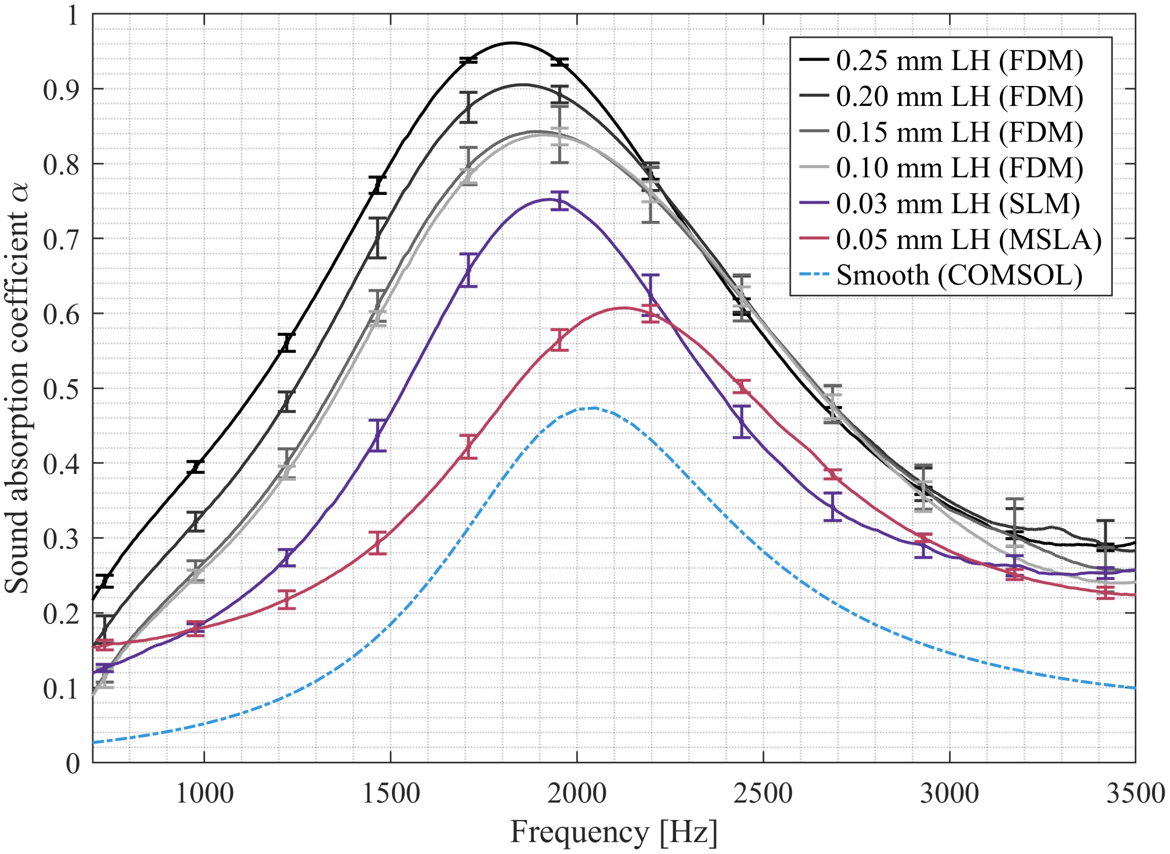

Figure 4.18: Experimental and numerical results of the sound absorption coefficient

These results are likely to be related to the individual characteristics of the processes used in each additive manufacturing technology. In the case of FDM and SLM, CT scans revealed discontinuities at the edges connecting the main pore network to small cavities and micropores within the solid walls. The excess sound absorption could be related to the rise in microporosity, which is also linked to the increase of layer height that can lead to greater delamination.

Distinctive features are present for each of these print processes. For FDM, thin material strings introduce fibrous material into the resonator cavity volumes. These fibres are likely to produce a more broadband acoustic behaviour. In the case of SLM, although this technology achieves the highest precision, a rough surface finish is an inevitable effect of utilising metal powder. In addition, the satellite particles are distributed randomly on printed surfaces. These additional, relatively large-scale features on exterior parts will disrupt the visco-thermal boundary layer development and potentially lead to enhanced acoustic losses in the material.

Interestingly, MSLA behaved differently than other additive manufacturing technologies. The lowest experimental absorption can be attributed to the smoothest surface finish and lack of porosity due to discontinuities at the edges. On the other hand, CT scanning and confocal microscopy revealed a considerable dependency of the position along the z-axis on the geometrical fidelity of the produced spheres. There are noticeable differences between the bottoms and tops of spheres. This issue results in lower dimensional accuracy, which could explain the peak shift towards higher frequencies, unlike the FDM and SLM samples and the smooth numerical model.

It is important to remember that each experimental curve was plotted as an average of 9 separate measurements, and the error bars represent the standard deviation of the data set. Intrinsic losses in the impedance tube produce a systematic error in addition to the error bars (see hard wall measurement in an empty impedance tube in Figure E.3). This impact of the impedance tube itself was not calibrated out of the data.

It should also be noted that various methods were employed to find a perfect fit in the importance tube for different types of experimental samples. For FDM, multiple printing attempts were made to determine the optimal diameter for the cylindrical sample. In contrast, MSLA samples underwent sanding, while SLM samples were subjected to machining processes to attain the desired fit.

From the numerical point of view, corrections of pore network dimensions to their actual values, especially for key dimensions, are crucial. In this case, it is the actual diameter of the cylindrical channel (pore diameter is less important but should also be corrected as it affects the porosity). The channel diameter strongly influences the viscous permeability and the characteristic viscous length - two key parameters of (dynamic) flow through a porous medium and the resulting viscous dissipation of acoustic wave energy.

The discrepancy between experimental and numerical results could be decreased by incorporating 3D printed tolerances, as measured using digital microscopy, to update the numerical model. Section 4.3.1 showed that cylindrical channels have larger diameters in materials 3D printed using MSLA technology than in the case of FDM or SLM technologies. However, these differences were not taken into account during the numerical modelling. It was decided that the additive manufacturing assessment would be carried out by comparing the experimental results from physical samples, constructed based on CAD models with specified dimensions, to the numerical results derived from COMSOL models replicating the exact geometries of these CAD models. Therefore, all curves shown in Figure 4.18 were obtained for the same geometrical dimensions of the unit cell (as per Figure 1.2).

4.6 Conclusions

This study set out to assess three distinctive additive manufacturing technologies: extrusion-based FDM, photopolymerisation-based MSLA and PBF-based SLM, and investigate the influence of 3D printing on the acoustic performance of a benchmark design.

This study has shown that the additive manufacturing process influences the experimental results compared to numerical predictions. In the experimental results, the sound absorption coefficient increases and a shift of the peak frequency and broadband absorption in lower and higher frequencies can be observed.

The experimental results of FDM and SLM samples showed similar trends. MSLA samples behaved differently. By investigating the physical features of different samples through a combination of NDT techniques, it was also shown that this is due to the individual characteristics of each additive manufacturing process.

The issues present in FDM samples were discontinuities at surfaces and edges, microporosity, roughness due to the layer height, and filament fibres. The problems of SLM samples included discontinuities at surfaces and edges, microporosity, and roughness due to the usage of metal powder and locally due to satellite particles. MSLA samples were not subject to discontinuities at edges and microporosity. They also had the smoothest surface finish. However, MSLA samples were affected by lower dimensional accuracy (varying build quality along the z-axis) and the influence of post-processing (material shrinkage and expansion).

Much higher quality of geometry mapping is often reported in the case of acoustic material samples manufactured using SLA technology. The lower quality observed in this study may be related to the specific 3D printer and/or resin used for 3D printing the samples and/or MSLA technology.

Generally, the deviation between numerical and experimental results occurs due to rough surface finish, geometric accuracy, and microporosity. The optimal design of acoustic materials for additive manufacturing must consider these features. It is also clear that even a relatively simple concept, such as the DENORMS cell, will never have an equal performance when produced across these different print processes.

Some of the 3D printing defects enhance the acoustic performance of the manufactured material. Despite this improvement in the magnitude of the acoustic absorption, none of the produced designs operated at the target frequency, with deviations of as much as 200 Hz observed. This discrepancy is mainly due to the fact that the geometry used for numerical calculations assumed uncorrected diameters of cylindrical channels and spherical pores that were in the CAD model used for 3D printing. The most important dimension here is the channel diameter. In any case, if these values were corrected (which is not easy as different corrections are needed for different 3D printing technologies and materials), the target peak absorption frequency could better match the predictions, at least for samples without additional effects introduced by microporosity and/or small fibres.

Corrections to the actual values of important dimensions (such as channel diameters, slit widths, pore diameters and, therefore, the resulting porosity) can be taken into account during the CAD model preparation process, provided that they have been determined for a specific 3D printer and material, which is possible to some extent, but not easy. This is an important issue for future research that should consider more additive manufacturing features when designing an acoustic material.

Chapter 5

Surface roughness investigation

5.1 Introduction

This chapter aims to provide a better understanding of the effects of the additive manufacturing process on the acoustic performance of fabricated materials. Previous research has not included surface roughness arising from the layer-by-layer fabrication technique during computational modelling. The presence of the staircase effect was commonly used to explain the lack of good agreement between theoretical and experimental results, as described in detail in Section 3.3. In these cases, a direct link from the surface roughness effect to the deviation between numerical and experimental results was not established, leaving the possibility of other contributing factors open.

Approaches targeting the issue of surface roughness include applying additional post-treatment to smooth the materials' surfaces and thereby bring the actual surface topology closer to the numerically assumed surface. Zhang *et al.* (2021) investigated the effects of applying a Polydimethylsiloxane (PDMS) coating post-treatment to a 3D printed projection micro-stereolithography (PµSL) metamaterial structure to reduce the surface roughness [134]. Before this treatment, the surface roughness diminished the transmission performance and caused a mismatch between numerical and experimental results. With the improvements in surface morphology, which resulted from smoothing the rough surface finish, the transmission coefficient curve shifted closer to the numerical one.

To the author's knowledge, there has been little attempt to include the effects of manufacturing at the material design stage. Although some authors advise, for example, to take into account the expected change in the crucial dimensions of 3D printed designs [135], which, of course, requires previously acquired experience-based knowledge of the typical corrections required. However, there are no standardised procedures that take surface roughness into account. This would require their inclusion in the numerical model to match the numerical prediction to the experimental value using direct modelling. Such work has been done in 2D [130]. Other works focused on achieving a match between numerical and experimental curves by utilising the equivalent fluid model approach [136].

This chapter is based on a published article: A. Ciochon, J. Kennedy, R. Leiba, L. Flanagan, and M. Culleton, “The impact of surface roughness on an additively manufactured acoustic material: An experimental and numerical investigation”, Journal of Sound and Vibration, vol. 546, p. 117434, Mar. 2023, doi: 10.1016/j.jsv.2022.117434.

Surface roughness, as well as many other imperfections of 3D printing, usually increase the performance (e.g. sound absorption) of the acoustic material. Therefore, a reasonable approach should be to take these effects into account during the modelling and design process rather than using post-processing to remove roughness or other favourable imperfections.

This study investigates and quantifies the influence of surface roughness on the acoustic performance of a benchmark porous material produced via an extrusion-based additive manufacturing process. This represents the first step towards designing acoustic materials at the unit cell level in a manner which exploits the additive manufacturing process for improved performance.

The DENORMS benchmark design was fabricated using an extrusion-based Prusa Mini FDM 3D printer using four standard layer heights: 0.10, 0.15, 0.20 and 0.25 mm. Corresponding samples of the structures' cross-sections were manufactured for confocal microscope measurements to obtain the actual surface profiles of parts fabricated with four different layer heights. A combination of numerical and experimental approaches was used in the data analysis. The results of numerical models with geometries equivalent to four layer heights were compared to the results of an ideal structure with a perfectly smooth surface finish and to the experimental results of samples manufactured with four corresponding layer heights.

5.2 Additive manufacturing

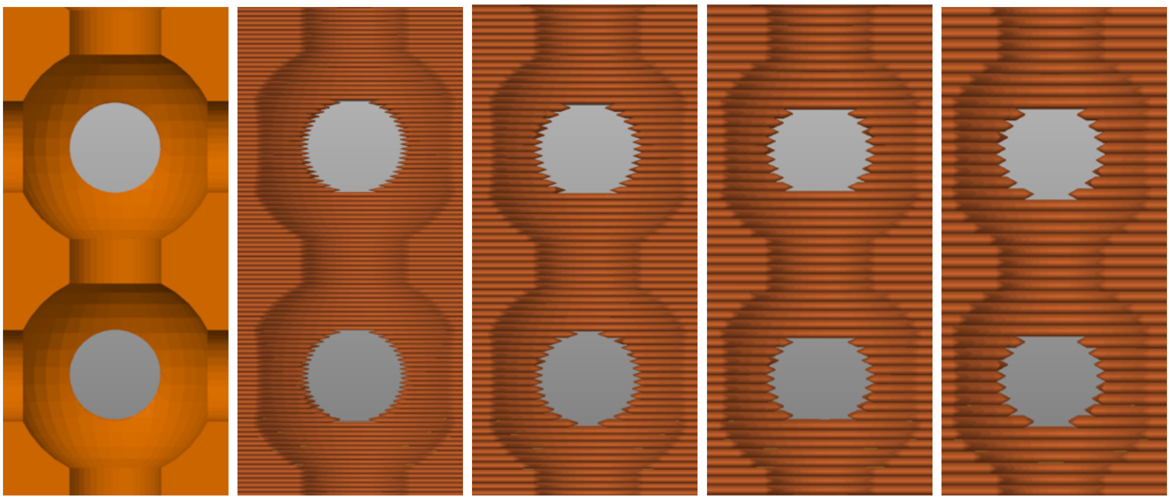

(a) Smooth (b) 0.10 mm (c) 0.15 mm (d) 0.20 mm (e) 0.25 mm

Figure 5.1: (a) Smooth CAD model of the DENORMS benchmark design and (b,c,d,e) its sliced versions produced by PrusaSlicer software using different layer heights

Four different layer heights, namely 0.10, 0.15, 0.20 and 0.25 mm, were set during the slicing of the part for additive manufacturing. The comparison between the theoretical representation of the smooth and rough DENORMS cells is illustrated in Figure 5.1.

The analysed material samples consisted of six layers of the unit cells and were manufactured as cylinders (diameter 40 mm and height 6 x 5 mm = 30 mm) suitable for the impedance tube measurements, with extrusion-based FDM 3D printer Prusa Mini (0.4 mm nozzle diameter) using PLA. The default print settings were adjusted to minimise the issue of filament stringing, described in the previous chapter, in Section 4.3.1, because the surface roughness arising from the staircase effect was the primary subject of this investigation. More details regarding the quality improvement of FDM parts and the information on the modified process parameters can be found in Appendix D.

The printing parameters were as follows: the extruder temperature was 195 °C, the perimeters printing speed was 40 mm/s, and the infill printing speed was 80 mm/s. In addition, in the slicing software PrusaSlicer, the retraction length was set to 2 mm, retraction lift z to 0 mm, retraction speed to 50 mm/s and detraction speed to 30 mm/s. Moreover, the 'Avoid crossing perimeters' feature was enabled. The filament was also put into the dry box to minimise the possible negative impact of the room temperature and humidity. Each sample was fabricated three times (A, B, C) to ensure the manufacturing process's repeatability.

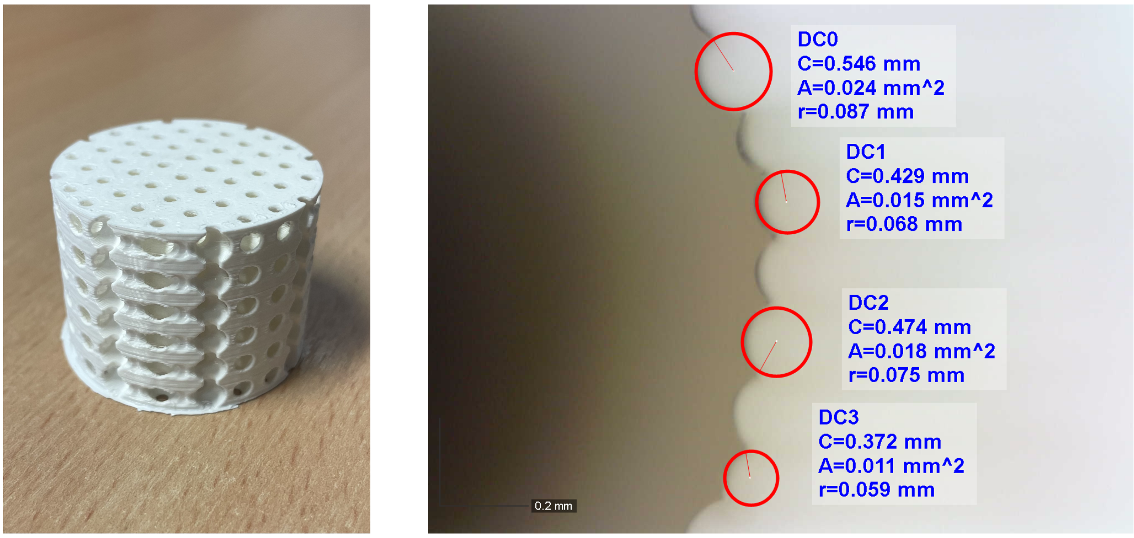

(a) Sample (b) Microscopic image

Figure 5.2: 0.15 mm layer height FDM sample (optimised print parameters)

5.2.1 Visual inspection

A sample manufactured with an exemplary layer height of 0.15 mm is shown in Figure 5.2a. From the magnified image of the detail of this sample shown in Figure 5.2b, it can be seen that for the layer height set to 0.15 mm in the slicer, the actual layer height achieved by the printer varies between 0.118 and 0.174 mm.

Moreover, the degree of variation depends on the position of the individual road along the arch of the sphere. This can be explained by the fact that the samples were printed in the vertical orientation and without any supports, which highly influences the accurate mapping of the spherical geometry. Due to this, there is a significant difference between the quality of the tops and bottoms of DENORMS spheres.

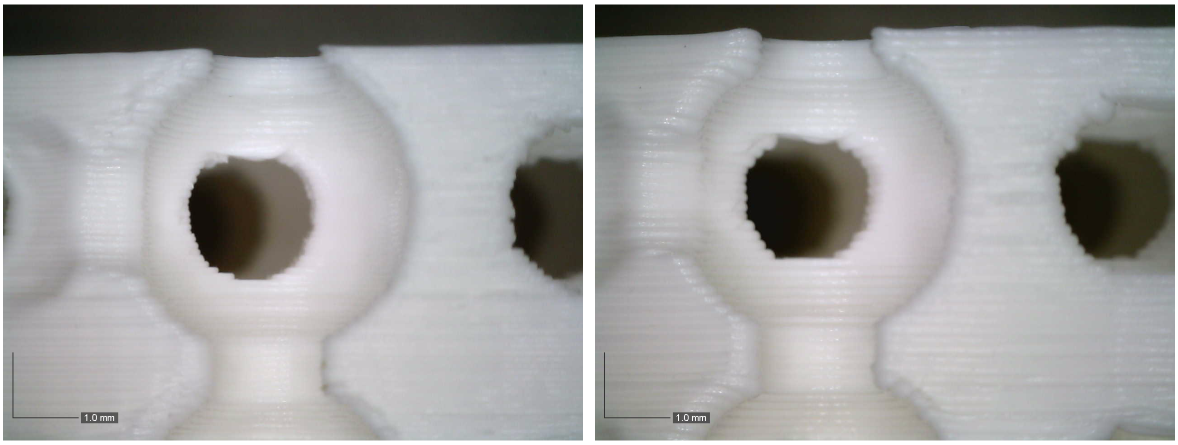

(a) 0.10 mm (b) 0.15 mm

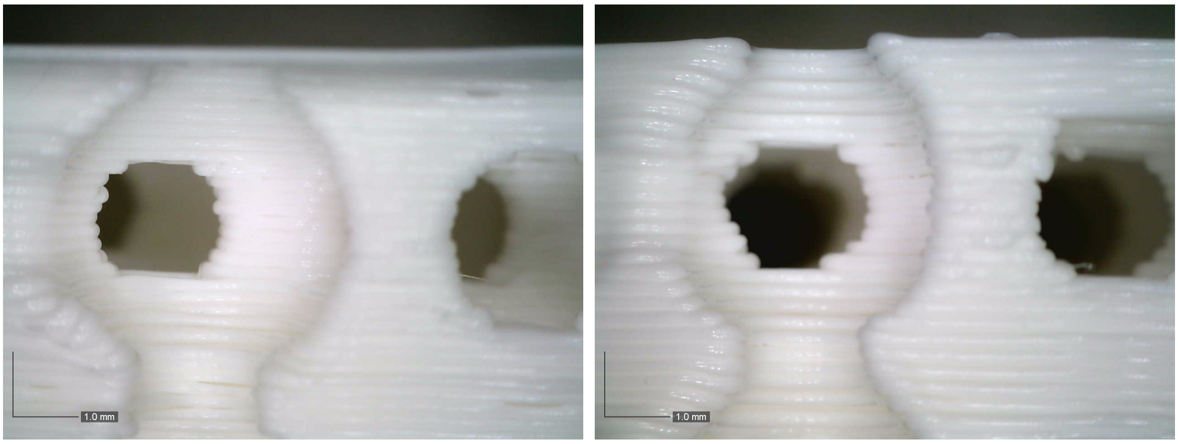

(c) 0.20 mm (d) 0.25 mm

Figure 5.3: Microscopic images of DENORMS structure manufactured with different layer heights (optimised print parameters)

The cross-sections of the DENORMS cell manufactured with different layer heights are illustrated in Figure 5.3. As seen from the microscopic images, the level of distortion of the original geometry grows with the increase of the layer height. As expected, samples manufactured with smaller layer heights are more geometrically accurate than bigger ones. Nevertheless, they are not defect-free. In the case of 0.10 mm and 0.15 mm layer heights, a curved swelling of the top, unsupported arch of the DENORMS cavity occurs. Furthermore, the issue of filament fibres was eliminated by correctly adjusting the print settings.

5.3 Acoustic evaluation

There are two strategies targeting the incorporation of surface roughness during computational modelling. The less computationally expensive one is based on the equivalent fluid approach that mimics the presence of 3D printing defects by adjusting specific air parameters, such as viscosity. It is known that surface roughness strengthens solid-liquid interactions, affecting the boundary viscosity, and becomes increasingly significant with the rise in roughness depth [137]. Therefore, altering dynamic viscosity in the model should capture additional losses within the model controlling sound absorption, such as those occurring due to surface roughness [15].

However, although fitting the numerical curve to the experimental one by systematically adjusting the air parameters in a model is relatively simple, obtaining the actual equivalent material properties of materials with complex microstructures to capture the physics correctly is challenging [138]. Therefore, the non-direct modelling approach is not the primary numerical tool in this thesis. Nevertheless, an attempt to include the presence of surface roughness by altering the air parameters was made and is described thoroughly in Section 5.3.2.

Direct modelling based on the linearised Navier-Stokes equations (Equations (4.1) to (4.3)) for viscothermal acoustics is the primary modelling strategy employed in this study. A combination of numerical and experimental techniques was applied in this study to perform the acoustic analysis.

5.3.1 Direct modelling strategy

The primary numerical modelling strategy employed in this study aimed to highlight the impact of surface roughness on the produced acoustic absorptive performance of the 3D printed material through direct modelling. Models of six layers of the unit cell were created with different roughness levels, corresponding to the four layer heights (LH) presented in Figure 5.3.

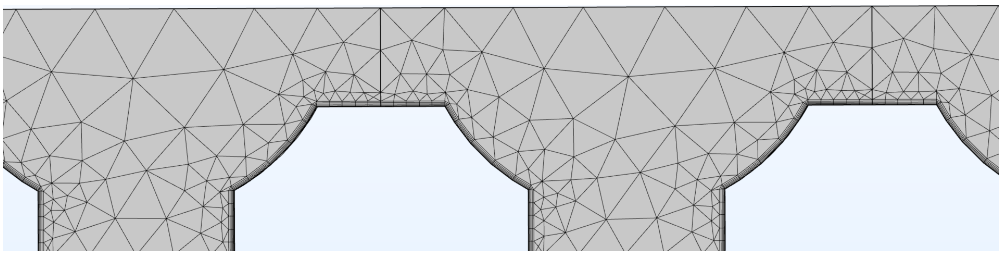

(a) COMSOL mesh of the air-saturated domain with smooth surfaces

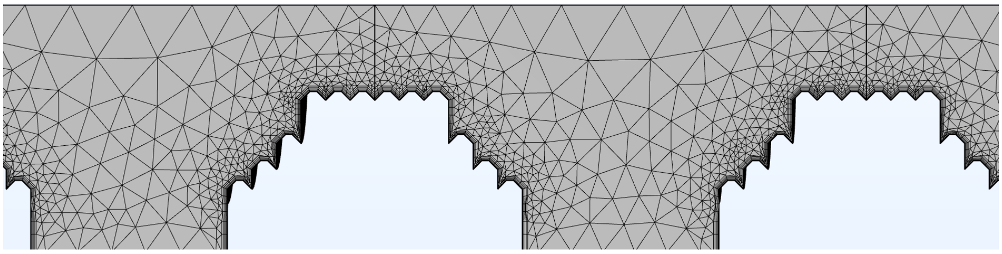

(b) COMSOL mesh of the air-saturated domain with rough surfaces obtained for 0.25 mm LH

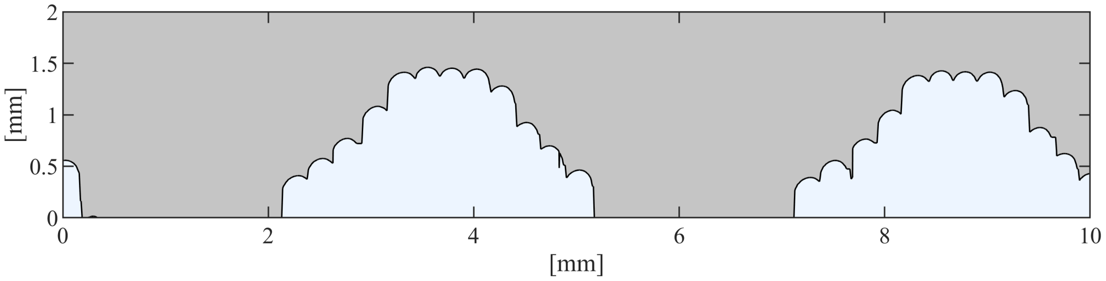

(c) 0.25 mm LH surface profile measured using confocal microscopy

Figure 5.4: Geometry creation for numerical modelling

A comparison between the computational (smooth and rough) and the actually printed geometry is displayed in Figure 5.4. The surface profile shown in Figure 5.4c was copied from Figure 4.6d and coloured to better illustrate the modelled air domain (in grey) and not-modelled solid domain (in light blue), which was provided for by imposing adequate boundary conditions.

Figure 5.5 provides a comparison between rough geometries created with four layer heights analysed in this study and the original smooth geometry.

The number of degrees of freedom per study is outlined in Table 5.1. Mesh independence was separately evaluated for each layer height value. This information is outlined in Appendix B.

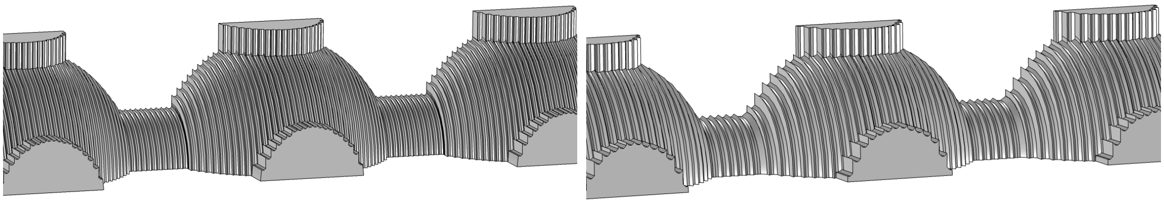

(a) 0.10 mm LH (b) 0.15 mm LH

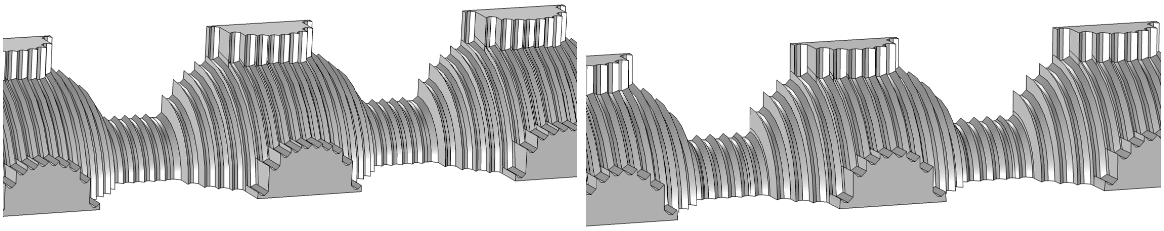

(c) 0.20 mm LH (d) 0.25 mm LH

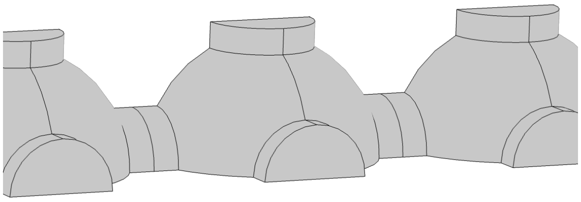

(e) Smooth

Figure 5.5: FEM model geometry comparison with smooth and rough surface finish

LH	DoF
Smooth	759585
0.10 mm	8687633
0.15 mm	8177212
0.20 mm	6671377
0.25 mm	5977069

Table 5.1: Mesh details in all models: number or degrees of freedom (DoF) for the different layer heights (LH)

5.3.2 Indirect modelling strategy

Although meshing and modelling the DENORMS benchmark design with explicitly rough surfaces is possible, it requires high computational resources. In this section, a different approach was implemented to reduce the computational cost of the numerical modelling. This approach is essentially based on the original, i.e. smooth DENORMS geometry; however, the unit cell was divided into two parts: the inner air region and an outer fluid shell (FS, marked in orange in Figure 5.6c) with altered air properties. In the fluid shell, all air properties were kept unchanged except the dynamic viscosity μ, which was altered in a parametric sweep procedure.

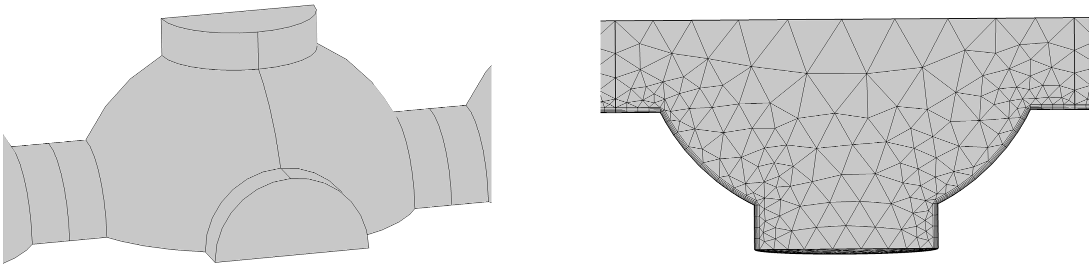

(a) Smooth geometry

(b) Smooth mesh

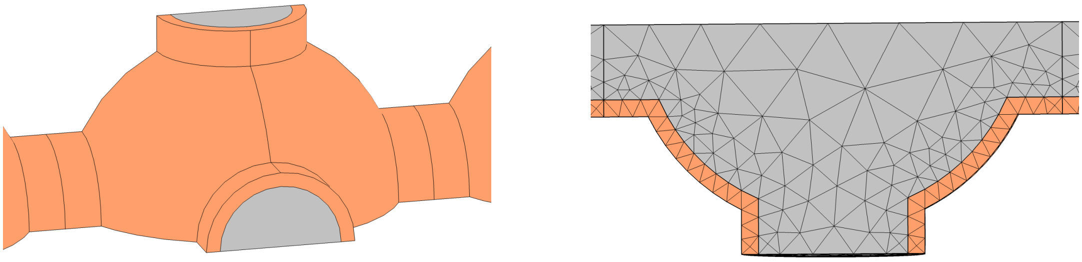

(c) Fluid shell geometry (in orange)

(d) Fluid shell mesh (in orange

Figure 5.6: Unit cell in direct and non-direct (fluid shell) modelling approaches

It was assumed that the rough surface would increase boundary layer thickness and losses compared to the smooth geometry, as described in detail in Section 5.3. The fluid shell layer was intended to modify the growth of the boundary layer through the altered dynamic viscosity. The fluid shell's extent was chosen as five times the FE boundary layer thickness of the smooth model.

Generated geometries of an individual unit cell are illustrated in Figure 5.6. Figure 5.6a shows the original geometry with a smooth wall finish. The corresponding mesh is illustrated in Figure 5.6b. The unit cell of the fluid shell geometry is depicted in Figure 5.6c. The air is grey, and the outer fluid shell with increased dynamic viscosity is shown in orange. The corresponding mesh is shown in Figure 5.6d. Numerical models generated with smooth and fluid shell geometries corresponded to a structure with six layers of the unit cell.

5.3.3 Run time comparison

All simulations were performed using Precision 5820 Desktop Workstation: Intel(R) Xeon(R) W-2265 CPU @ 3.50GHz processor, 256 GB RAM. The comparison of run times between direct and indirect modelling approaches is summarised in Table 5.2. The indirect modelling approach is much more time efficient, and the time required to solve this model is comparable to a smooth direct model.

The computational time for the indirect modelling includes the whole parametric sweep procedure. In this chapter, the parametric sweep to find the dynamic viscosity in the FS region requires the experimental data to fit, e.g. absorption curves. In the next chapter, however, the parametric sweep will be done to fit the results to the direct modelling curves.

LH	Run time
DIRECT MODELLING	
smooth	2 hours, 31 minutes, 25 seconds
0.10 mm	1 day, 8 hours, 42 minutes, 21 seconds
0.15 mm	1 day, 17 hours, 35 minutes, 55 seconds
0.20 mm	1 day, 8 hours, 4 minutes, 34 seconds
0.25 mm	1 day, 2 hours, 31 minutes, 6 seconds
INDIRECT MODELLING	
	3 hours, 46 minutes, 27 seconds

Table 5.2: Comparison of run times between direct and indirect modelling approaches

The direct and indirect approaches to modelling surface roughness use a geometry composed of unit cells (of the designed pore network) across the entire thickness (depth) of the material layer. Both methods use fully coupled, linearised Navier-Stokes equations for thermoviscous acoustics to model oscillatory flow in air saturating the pore network.

Efficient numerical modelling strategy

Surface roughness increases the effects of viscous dissipation due to increased friction between the solid walls and the air saturating the pore network. In fact, the indirect modelling approach is based on this very assumption. One may expect that viscous and thermal effects related to the propagation of acoustic waves can be separated at the unit cell level since oscillatory flow can be treated as locally incompressible [139], or that at least they are weakly coupled.

Instead of employing fully coupled thermoviscous acoustics equations solved across a series of unit cells forming the entire material thickness, one could use the uncoupled approach and solve viscous and thermal problems separately on a single periodic unit cell: the one with staircase-type surface roughness or the smooth unit cell containing a thin fluid shell of modified viscosity. The key focus lies in the oscillatory, incompressible viscous flow problem through the periodic cell, which is modelled using complex-valued Stokes flow equations featuring an added harmonic inertial component. The so-called dynamic viscous permeability function can be obtained by solving this problem and averaging the solution (i.e., the flow velocity field) over the unit cell and scaling the result.

This function considers roughness effects modelled directly or using the fluid shell approach. The dynamic viscous permeability allows one to determine (using a simple analytical formula) the effective density of the equivalent fluid that can replace the acoustic material. Effective compressibility of the equivalent fluid can be determined after solving the appropriate dynamic thermal diffusion problem. The two effective properties, i.e. the effective density and compressibility, can then be used to model sound propagation and absorption by solving the Helmholtz equation in a layer of equivalent fluid replacing the acoustic material.

In this thesis, however, the decision was made to model the entire material layer thickness (6 cells). The initial plan was to use CT scanning to obtain STL files of the individual channel of the DENORMS pore network directly from the experimental samples (without the need to create roughness patterns computationally) and use them during numerical modelling. An effort was made to extract a channel from the FDM sample using CT scanning; however, the scan's quality proved inadequate to proceed with this methodology.

5.4 Results and discussion

5.4.1 Direct modelling strategy

Experimental results of the sound absorption coefficient of DENORMS structures manufactured with different layer heights are compared in Figure 5.7a. These data are presented as the average and standard deviation of 9 tests per layer height. This data shows that with the increase of the layer height(LH), a rise in sound absorption occurs. Moreover, the peak value shifts towards lower frequencies. The results achieved by the two smallest layer heights, namely 0.10 and 0.15 mm, are very close to each other, whereas the difference between the results obtained for the two greater layer heights,i.e. 0.20 and 0.25 mm, are more distinct.

Numerical results of the sound absorption coefficient of DENORMS structures generated with the smooth and the rough surface finish are summarised in Figure 5.7b. These results show a similar trend to the experimental ones in terms of the increase of the absorption and a shift of peak value towards lower frequencies with the growth of the layer height.

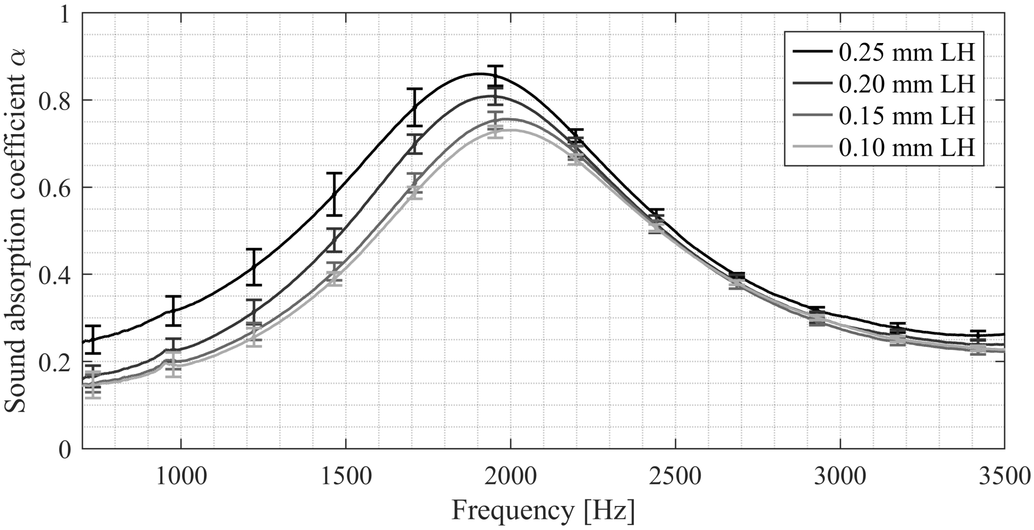

(a) Experimental results

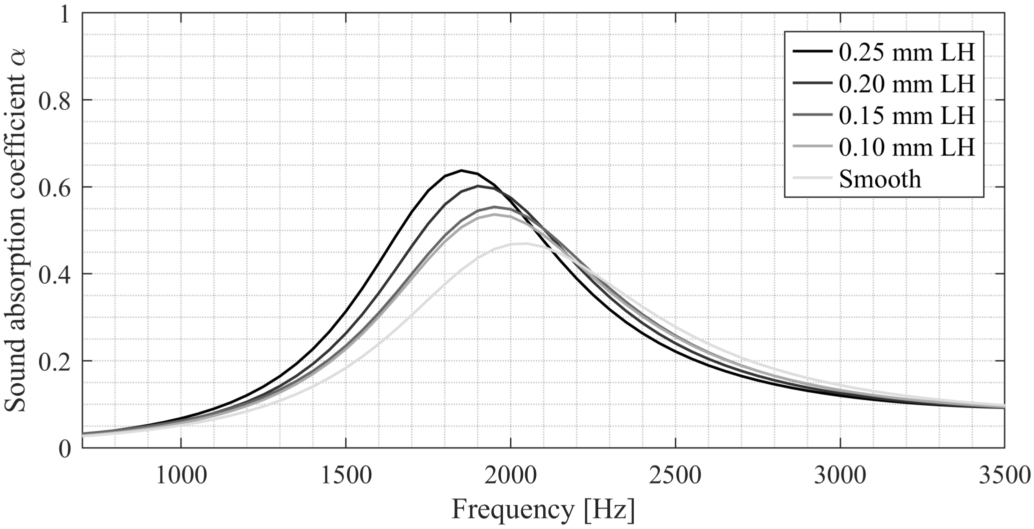

(b) Numerical results

Figure 5.7: Sound absorption coefficient: DENORMS layer 6 cell deep

However, there is no excessive sound absorption in the frequency region located further away from the peak value, which can be observed in the experimental curves. The curves for smaller layer heights, namely 0.10 and 0.15 mm, are very similar to the curve of the smooth structure, showing a relatively small effect of the modified geometry on the dissipation.

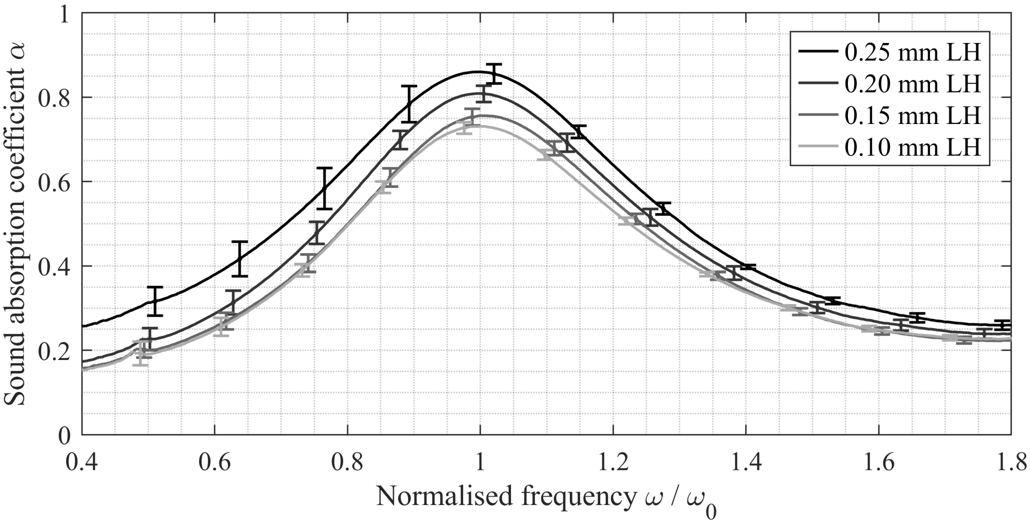

(a) Experimental results

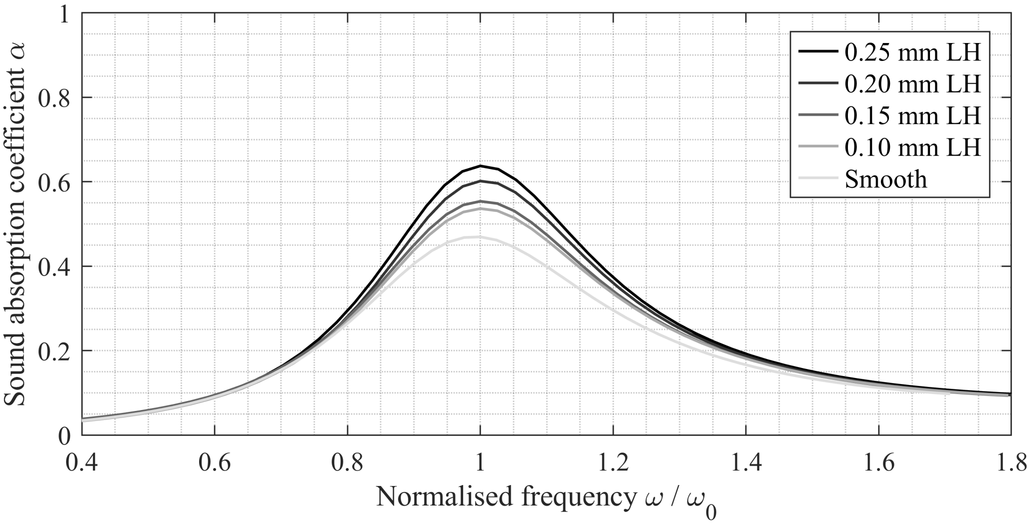

(b) Numerical results

Figure 5.8: Sound absorption coefficient: DENORMS layer 6 cell deep

To better understand the achieved results, all curves were redrawn with respect to the normalised frequency, as shown in Figure 5.8. The frequency ω_0 used for normalisation is the frequency of the respective absorption peak. A similar trend between the distances of individual curves corresponding to various layer heights can be observed in the peak region of experimental and numerical curves. However, compared to numerical curves, which nearly overlap in the frequency regions located further away from the peak, a broadband excess sound absorption is observed experimentally over the whole frequency spectrum.

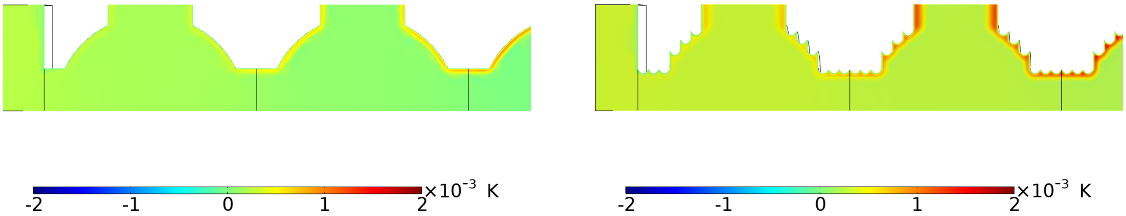

(a) Smooth (2050 Hz)

(b) 0.25 mm LH (1850 Hz)

Figure 5.9: Temperature variation [K] in the unit cell at resonant frequency (real part)

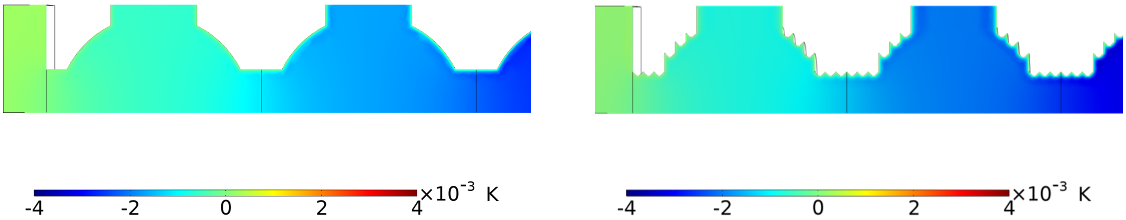

(a) Smooth (2050 Hz)

(b) 0.25 mm LH (1850 Hz)

Figure 5.10: Temperature variation [K] in the unit cell at resonant frequency (imaginary part)

To gain a better physical understanding of the mechanisms underlying the acoustic losses, temperature and velocity graphs were generated from the numerical results. Smooth and rough models were compared at their resonant frequencies. In Figure 5.9 and Figure 5.10, an increase in the thermal boundary layer thickness is observed between the models. As shown in Figure 5.9b, the temperature variation and the depth of its penetration inside the rough pore are larger owing to the presence of the grooves when compared to the smooth model displayed in Figure 5.9a.

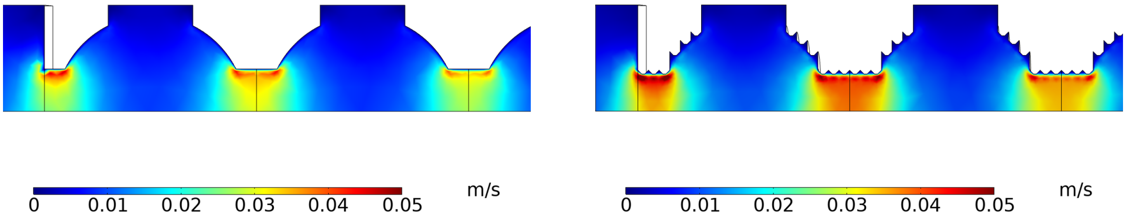

(a) Smooth (2050 Hz)

(b) 0.25 mm LH (1850 Hz)

Figure 5.11: Axial component of velocity [m/s] in the unit cell at resonant frequency (real part)

A similar effect is present in velocity graphs shown in Figure 5.11. Although most of the losses occur within the necks of the cells in both cases, there is a significant difference between the smooth and rough models. Acoustic particles achieve much higher velocity due to the presence of rough grooves, as illustrated in Figure 5.11b. Looking at both temperature and velocity graphs, it can be inferred that surface roughness increases the boundary viscosity within the system, which results in enhanced dissipation. Moreover, the presence of roughness enlarges the contact area between the air and the solid skeleton of the structure.

Overall, the experimental and numerical results show that sound absorption increases with the rise in the 3D printing layer height and the corresponding increase in surface roughness. The current study has found that the numerical and experimental curves corresponding to the various layer heights show similar trends.

However, in the case of the experimental curves, there is an excess broadband absorption that is not present in the numerical results. Additional manufacturing defects beyond the surface roughness are likely responsible for this deviation. Additional features present in the physical experiment, such as 3D printing geometrical inaccuracy, including not only the shape but also crucial dimensions, such as the diameter of cylindrical channels (necks), random print flaws (filament stringing) and microporosity of the print material [140, 141] can certainly lead to an increased broadband absorption.

Prior studies have implied that the difference between numerical and experimental results occurs due to the surface roughness of additively manufactured components. However, the findings of this work showed that this could only partially explain the gap between the results. Therefore, further investigations of this topic should be conducted. This work has demonstrated the feasibility of directly including surface roughness effects in the design stage of new materials through numerical modelling of unit cell structures.

5.4.2 Indirect modelling strategy

The results of this study are illustrated in Figure 5.12. The experimental results of the 0.10 mm layer height FDM samples are provided as a reference. The fluid shell modelling approach proved effective in predicting the magnitude of the experimental curve. In addition, the frequency of the first absorption peak is also captured in this modelling approach. This suggests that the fluid shell modelling approach could be helpful as a relatively low-cost addition to the modelling approach that can capture some of the manufacturing features.

It should be noted, however, that there is clear evidence of a higher broadband absorption in the experimental values due to the different curve shapes. It is unlikely that the modelling strategies utilised here will capture this effect even when optimised for the correct peak location and amplitude prediction. These additional broadband losses will require explanation through investigation of the fundamental physics, which may question some of the assumptions in the viscothermal modelling. Some of these discrepancies and losses may be explained by the shape and size inaccuracy as well as other effects such as heterogenous microporosity of the skeleton and/or fibres produced by filament stringing.

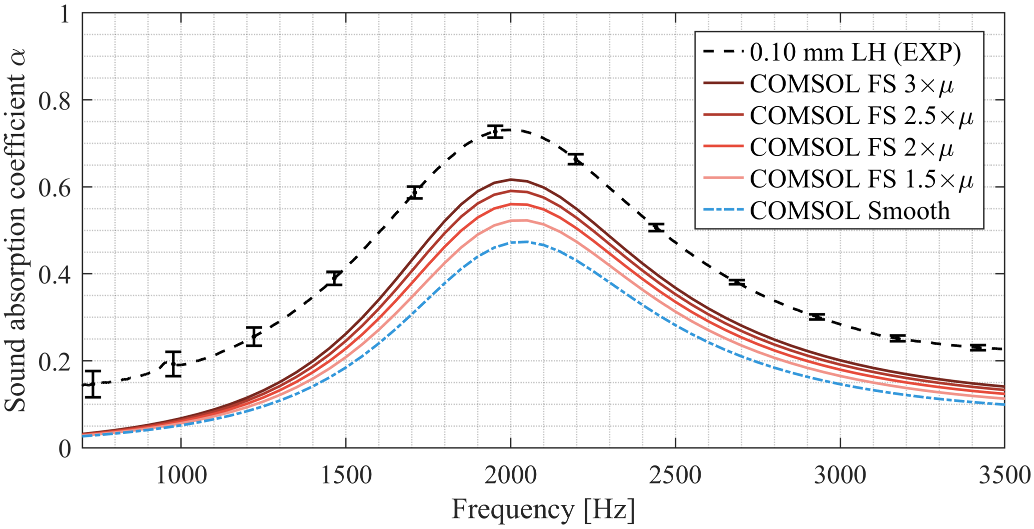

Figure 5.12: Experimental and numerical results

The modelling strategies here attempt to directly resolve the physical processes that drive the losses within the structure. Alternative approaches include equivalent fluid modelling of the whole system, but the calibration of the model constants is a complex problem in these approaches. Nevertheless, it is hoped that the work presented here will lead to clear guidelines on the impact of surface roughness on the acoustic behaviour of additively manufactured materials. This knowledge could then be fed into various modelling strategies to account for these effects.

5.5 Conclusions

This study has provided an in-depth understanding of the influence of surface roughness on the acoustic behaviour of a benchmark material produced with additive manufacturing using the FDM technology.

The process parameters of additive manufacturing were exploited to introduce a systematic variation in the surface roughness profiles by using a range of commonly used layer heights. The surface topologies were precisely measured using a confocal microscope. This data was then used to create numerical models of rough geometries. Finally, these models were used in a viscothermal numerical analysis of the lattice, exploiting efficiencies due to the repeating structure.

The magnitude of the increase in absorption due to the addition of surface roughness was nearly identical between experimental and numerical datasets. This demonstrates that surface roughness resulting from an increase in the layer height contributes to excessive sound absorption above what would be expected from a smooth numerical model.

The increase in absorption due to surface roughness introduced by various layer heights used by FDM is confirmed by numerical calculations. However, there are still discrepancies between the numerical and experimental results, which can be explained by geometric inaccuracy (in particular, the actual size of the neck is perhaps different than in the numerical model, as well as the porosity of the main pore network) and other phenomena (such as microporosity in some parts of the skeleton).

At low layer height values, there is a minimal increase in the dissipation within the material. Still, the geometry's slicing leads to volume changes within the material, which change the operating frequency. As the layer height increased, additional dissipation was observed, leading to an increase in the absorption peak value between the lowest and highest values of the layer height in both experimental and numerical datasets.

However, the gap between numerical and experimental results is only partially caused by the rough surface finish. A broadband increase in absorption is observed in the experimental data, which is not replicated in the numerical data. The increase in layer height is also linked to other manufacturing defects and alterations in geometric accuracy.

The impact of these on the experimental results must also be assessed before an exact match between numerical and experimental results can be achieved. Future work will be required to expand this research to alternative print processes and develop additional ways to incorporate additive manufacturing features into numerical modelling.

Finally, the introduced indirect modelling approach is a valuable contribution to the thesis, yielding promising outcomes while maintaining low computational costs. Nevertheless, it is essential to note that the obtained results also do not fully encompass broadband absorption as in the case of direct modelling. This approach would be very valuable if the value of, e.g. $3 \times \mu_{air}$ can always be used for a specific LH, and the thickness of the FS region would also be well-established.

To further enhance the indirect modelling strategy, future development should focus on formalizing the extent of the fluid shell region and refining the dynamic viscosity by considering a target boundary layer development. These refinements will likely contribute to a more comprehensive and accurate representation of the desired acoustic absorption properties.

Chapter 6

Surface roughness design

6.1 Introduction

In this chapter, lessons learnt from additive manufacturing of the benchmark porous material produced using FDM were applied to the design of novel acoustic absorbers. The design process was based on the knowledge and experience gained through the research described in the previous chapters.

Chapter 4 explained the possible reasons for the disagreement between numerical and experimental results of the sound absorption of a 3D printed material. The primary cause was the geometrical deviation between the final manufactured part and the original CAD design resulting from 3D printing imperfections, among which the most significant ones included surface roughness, reduced dimensional accuracy and microporosity of build material. Chapter 5 focused on understanding how the surface roughness arising from the layer height parameter contributes to the absorptive characteristics of a 3D printed material.

So far, there has been little discussion about using occurring 3D printing defects to one's advantage. Generally, they are assumed to be an unavoidable consequence of utilising this specific production method. Their extent can be controlled and minimised by proper adjustment of process parameters. Nevertheless, it is not possible to completely eliminate their presence.

Until recently, there has been no attempt to actively implement the knowledge about 3D printing imperfections into the design of novel acoustic materials. Zielinski *et al.* (2022) proposed a sound-absorbing material, the performance of which resulted not only from the designed pore network but also from the microporosity of the build material used during additive manufacturing [27]. In such a way, a double-porosity material was successfully designed, modelled and fabricated. This work is an example of making use of build material imperfections to achieve acoustic gains.

The other approach would be to utilise faults resulting from layer-by-layer manufacturing by including controlled surface roughness in the geometrical design of novel material for acoustic improvements. In this study, the novel enhancement was based on the benchmark unit cell but altered so that the geometric changes improved its behaviour.

6.2 Lessons learnt from FDM

The following section will discuss lessons learnt from additive manufacturing of DENORMS cells using FDM in more detail.

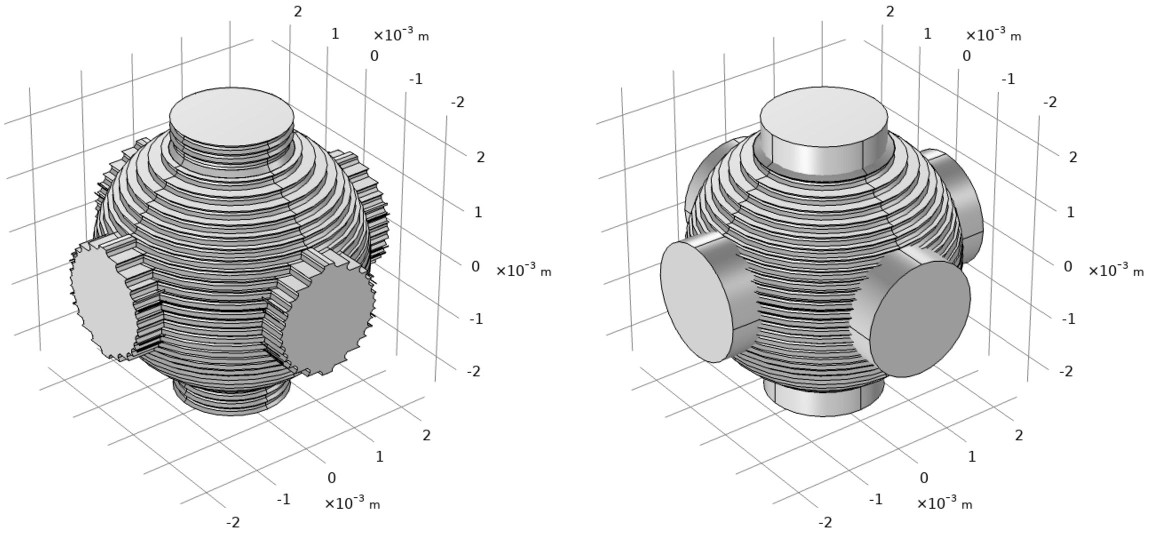

(a) All surfaces

(b) Spherical pore surface

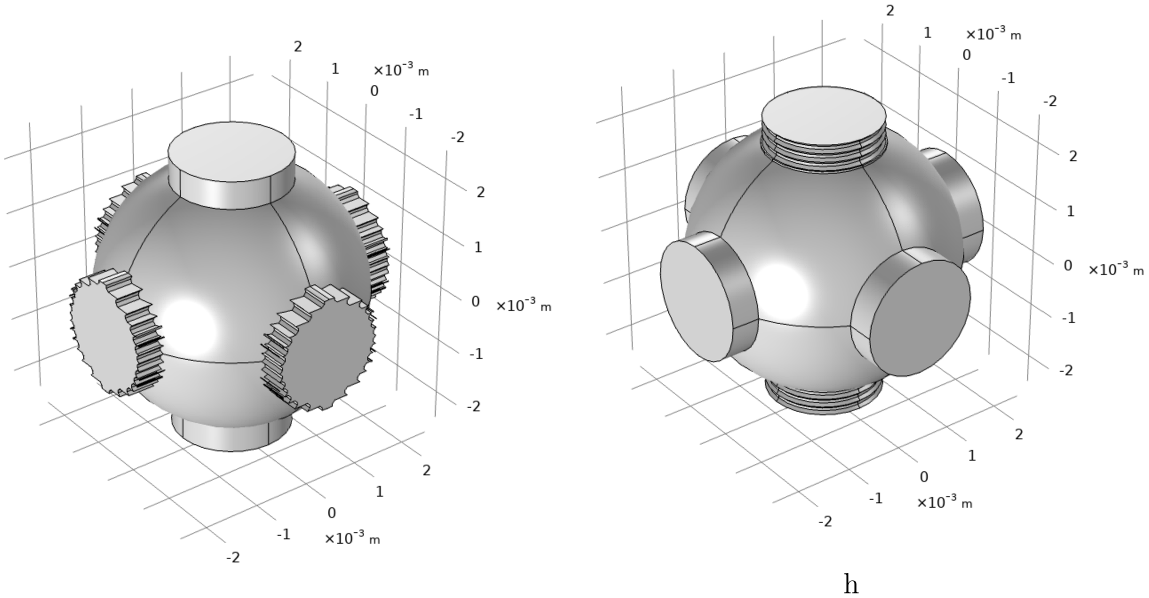

h

(c) Surfaces of side channels (perpendicular to the wave propagation direction)

(d) Surfaces of in-line channels (parallel to the wave propagation direction)

Figure 6.1: 'Extrusion-like' roughness pattern (0.15 mm layer height) applied to the various surfaces of the DENORMS unit cell in CAD

The CT scans of DENORMS samples manufactured using different 3D printing technologies, described in Section 4.3.3, provided valuable insights into parts' surface morphology and internal composition. The FDM samples were characterised by high delamination and the presence of discontinuities along geometrical contours. The observed network of inner voids in the 3D printed skeleton, unintentionally connected to the designed geometrical cavities forming the main pore network, likely influenced the acoustic behaviour of the system and provided extra absorption. This effect could be used to one's advantage but can be difficult to model due to the irregularity and heterogeneity of the micropore network of 'inner voids' and because their connections to the main pore network are usually very irregular and random, see Figure 4.11a. Therefore, a different additive manufacturing technology should be used to obtain a good match between experimental results and numerical or analytical predictions.

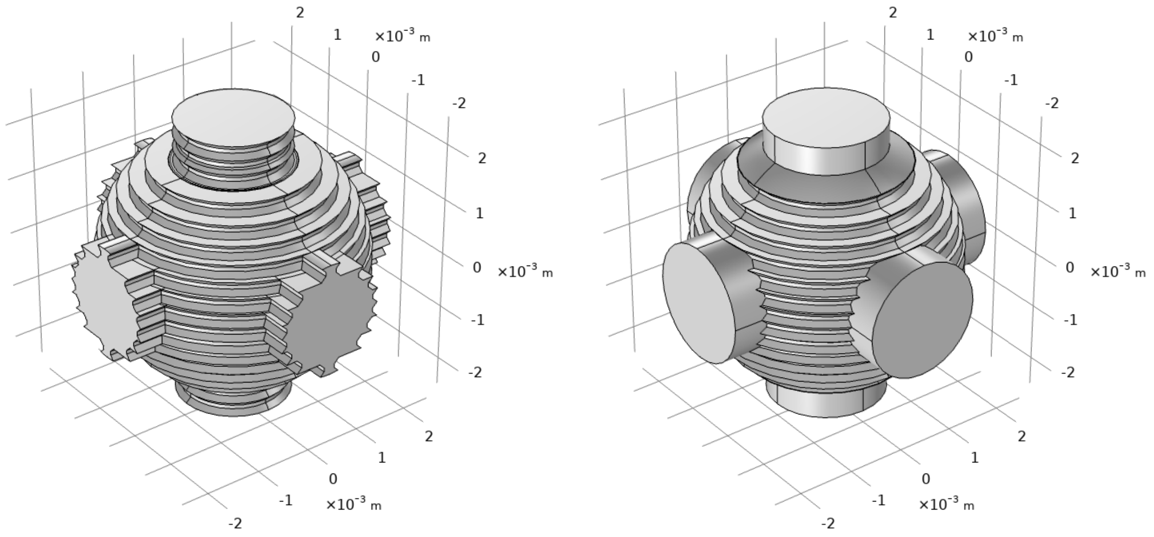

(a) All surfaces

(b) Spherical pore surface

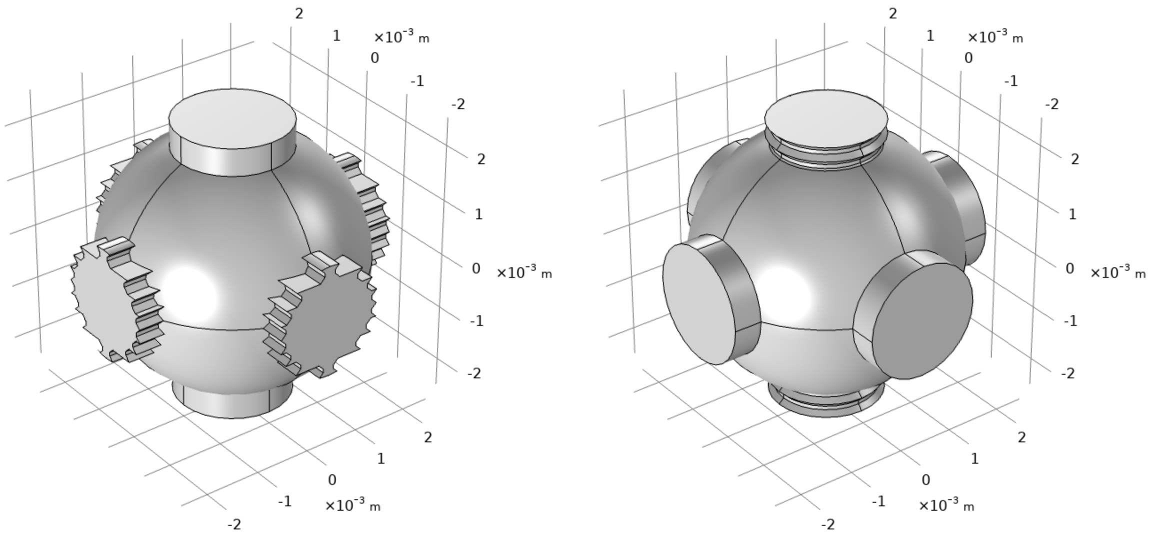

(c) Surfaces of side channels (perpendicular to the wave propagation direction)

(d) Surfaces of in-line channels (parallel to the wave propagation direction)

Figure 6.2: 'Extrusion-like' roughness pattern (0.25 mm layer height) applied to the various surfaces of the DENORMS unit cell in CAD

Another major issue in FDM samples was high surface roughness, which can only be minimised by adequately adjusting print parameters. Among them, the layer height is the most vital, and the surface quality improves by reducing it. On the other hand, it is known that surface roughness enhances the sound absorption of designed materials and can be used to one's advantage, especially since 3D printing using larger layer heights is also faster. However, it is essential to understand which parts of the benchmark geometry the roughness should be applied for the most efficient and beneficial results.

6.3 Applying lessons learnt

Given all that has been mentioned so far, one may assume that additive manufacturing flaws can be utilised for acoustic benefits. With this purpose in mind, an alteration of the benchmark design was proposed. The new unit cell takes advantage of the accurate FDM roughness pattern, which was created based on the surface profiles obtained with the help of confocal microscopy and described in detail in Section 4.3.2.

This 'extrusion-like' roughness pattern was applied to the CAD benchmark geometry in various locations i.e. surfaces: on all surfaces, only on the spherical pore surface, only on the surfaces of side channels, or finally, only on the surface of in-line channels, to investigate the influence of the roughness placement on the acoustic behaviour of the material. Note the fundamental difference between the side channels and in-line channels: the side channels are perpendicular to the wave propagation direction, while the in-line channels are parallel to this direction. Moreover, thanks to this and the symmetry of the unit cell, the airflow in the side channels is not locally 'axial'.

6.3.1 Surface roughness design

'Extrusion-like' roughness patterns corresponding to two different layer heights, namely 0.15 and 0.25 mm, were analysed in this study. The geometrical drawings of the altered cell with 0.15 mm layer height 'extrusion-like' roughness pattern applied in various locations of the DENORMS cell are illustrated in Figure 6.1. The 0.25 mm layer height 'extrusion-like' roughness pattern geometries were created in the same manner and are shown in Figure 6.2.

6.3.2 Additive manufacturing

In this investigation, MSLA was chosen as a suitable additive manufacturing method. This production technique utilises a lower layer height of 0.05 mm and, therefore, can faithfully reproduce new geometries and produce a nominally smooth original design. Moreover, CT scans, described in Section 4.3.3, revealed that MSLA samples were unaffected by the issue of discontinuities on the surface and inside the 3D printed skeleton of the considered geometry. Therefore, it can be concluded that changing the additive manufacturing method from FDM to MSLA helped eliminate the issue of the microporosity of the build material. The smoothest geometry (created from the smooth DENORMS CAD geometry) was used as a control sample and a reference material for the experimental testing.

Cylindrical samples consisting of six layers of the unit cells suitable for impedance tube measurements (40 mm diameter) were produced using Elegoo Mars 3 MSLA printer. The structures were prepared for manufacture with a 0.05 mm layer height and the standard print settings recommended by the manufacturer.

In total, nine different designs were fabricated: a smooth control sample, four 0.15 mm layer height 'extrusion-like' roughness pattern samples (roughness applied everywhere, only to spherical pores, only to side channels and only to in-line channels) and four 0.25 mm layer height 'extrusion-like' roughness pattern samples (roughness applied everywhere, only to spherical pores, only to side channels and only to in-line channels). Every design was fabricated three times (A, B, C) to ensure the repeatability of the manufacturing process. In total, 27 separate samples were produced.

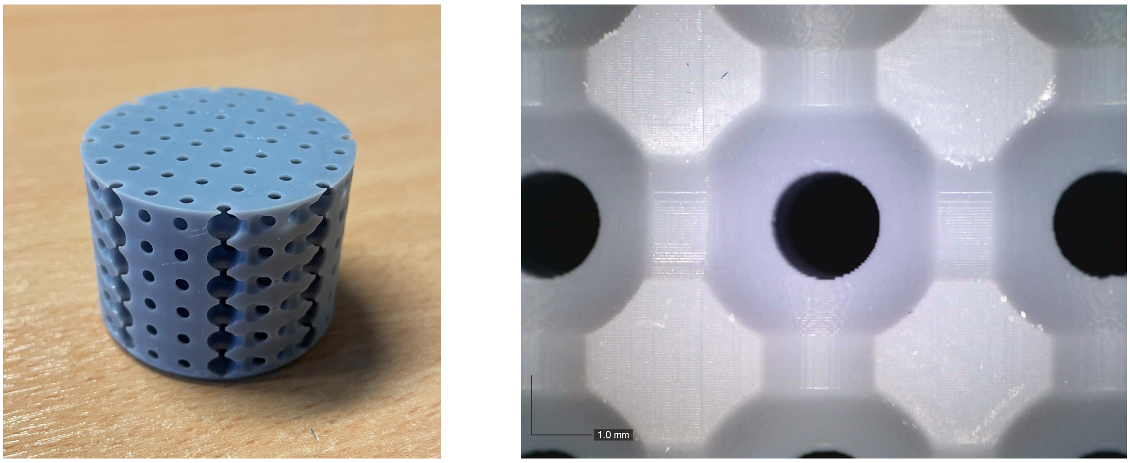

(a) Cylindrical sample (b) Cross-section

Figure 6.3: Nominally smooth, control MSLA sample

The smooth design was manufactured without any additional roughness pattern and used as a control sample. The fabricated cylindrical sample is shown in Figure 6.3a. A close-up microscopic picture illustrated in Figure 6.3b depicts the cross-section of the smooth sample.

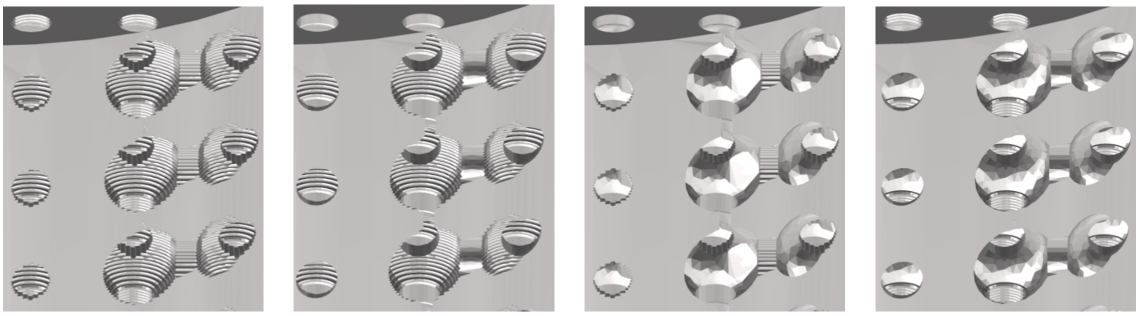

(a) Everywhere (b) Spherical pores (c) Side channels (d) In-line channels

Figure 6.4: Close-up at CAD models of cylindrical samples (in STL format) with the 0.15 mm layer height 'extrusion-like' roughness pattern applied to various DENORMS surfaces

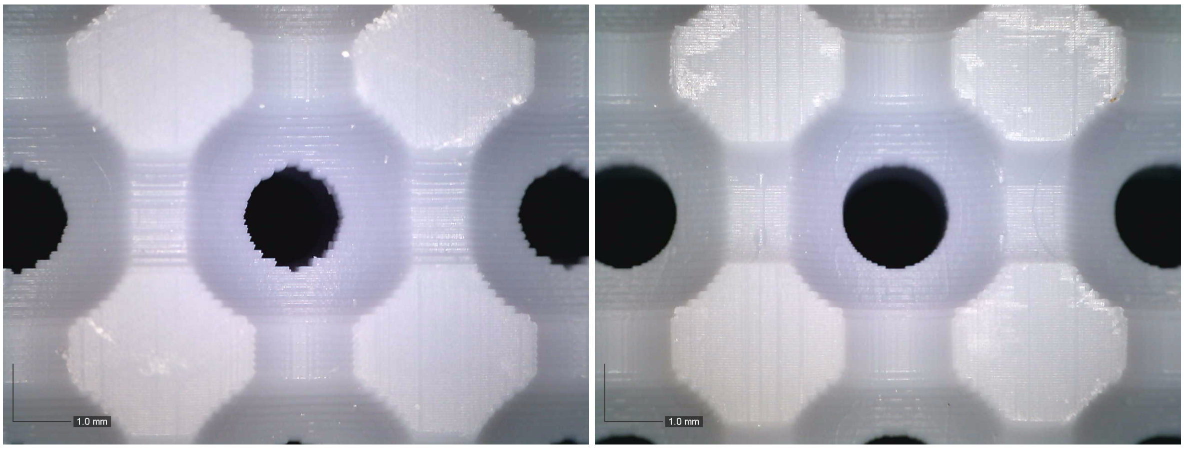

(a) Everywhere (b) Spherical pores

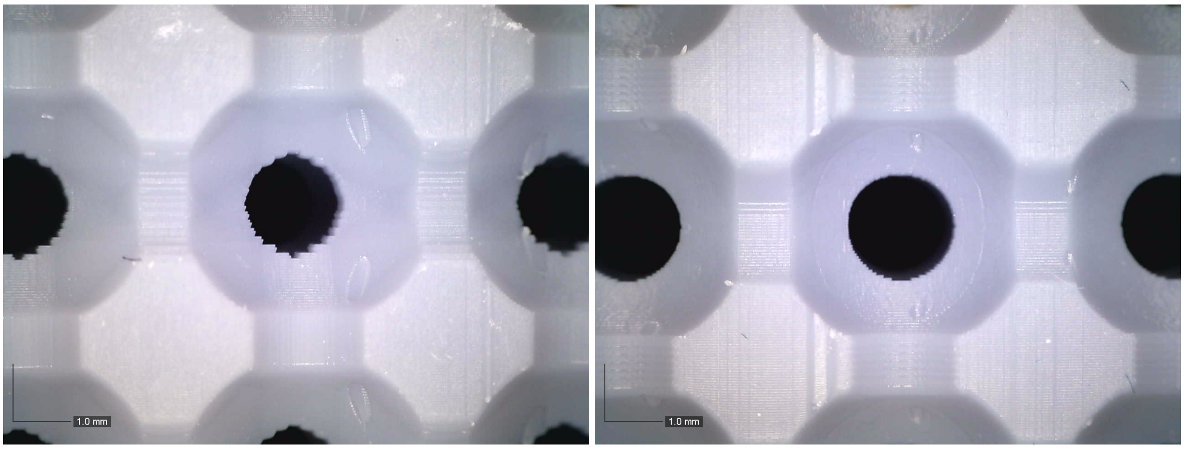

(c) Side channels (d) In-line channels

Figure 6.5: Microscopic images of MSLA samples with 0.15 mm layer height 'extrusion-like' roughness pattern applied to various parts of the DENORMS geometry

Cylindrical samples with the roughness pattern applied to various parts of the DENORMS geometry were fabricated in the same manner. The difference between the geometries coded in

STL files used for manufacturing the 0.15 mm layer height designs is displayed in Figure 6.4. The corresponding cross-sections of the fabricated samples are illustrated in Figure 6.5. The added-in-design ‘staircase’ roughness is clearly visible on individual surfaces, while the other surfaces are relatively smooth.

6.4 Acoustic evaluation

The aim of the modelling strategy implemented in this study was to investigate the influence of the surface roughness location on the produced acoustic absorptive performance of the 3D printed material through a comparison of direct and indirect modelling.

6.4.1 Equivalent dynamic viscosity establishment

First, the equivalent dynamic viscosity needed to be established based on the results of the direct and indirect modelling strategies described in Chapter 5. The direct modelling sound absorption coefficient peak data for the smooth model and both roughnesses (0.15 mm LH and 0.25 mm LH), as per Figure 5.7b, is summarised in Table 6.1.

Roughness	α
Smooth	0.47
0.15 mm LH	0.55
0.25 mm LH	0.64

Table 6.1: Direct modelling: sound absorption coefficient peak values (based on Figure 5.7b)

The indirect modelling peak data: the dynamic viscosity (μ) value and associated with it maximum sound absorption coefficient (α) value is summarised in Table 6.2, as per Figure 5.12.

μ	1	1.5	2	2.5	3
α	0.47	0.52	0.56	0.59	0.62

Table 6.2: Indirect modelling: peak data (based on Figure 5.12)

The data points summarised in Table 6.2 were used to construct an exponential curve through curve fitting, as shown in Figure 6.6.

Data plotted in Figure 6.6 was then used to find interpolated values of dynamic viscosity corresponding to the sound absorption coefficient values obtained through direct modelling for 0.15 mm and 0.25 mm LH roughnesses, as per Table 6.1. It was established that for $\alpha = 0.55$ (0.15 mm LH direct model), the corresponding viscosity factor equals $1.93 \times \mu$. For

$\alpha = 0.64$ (0.25 mm LH direct model), the corresponding viscosity factor equals $3.41 \times \mu$. The roughness and equivalent dynamic viscosity data are summarised in Table 6.3.

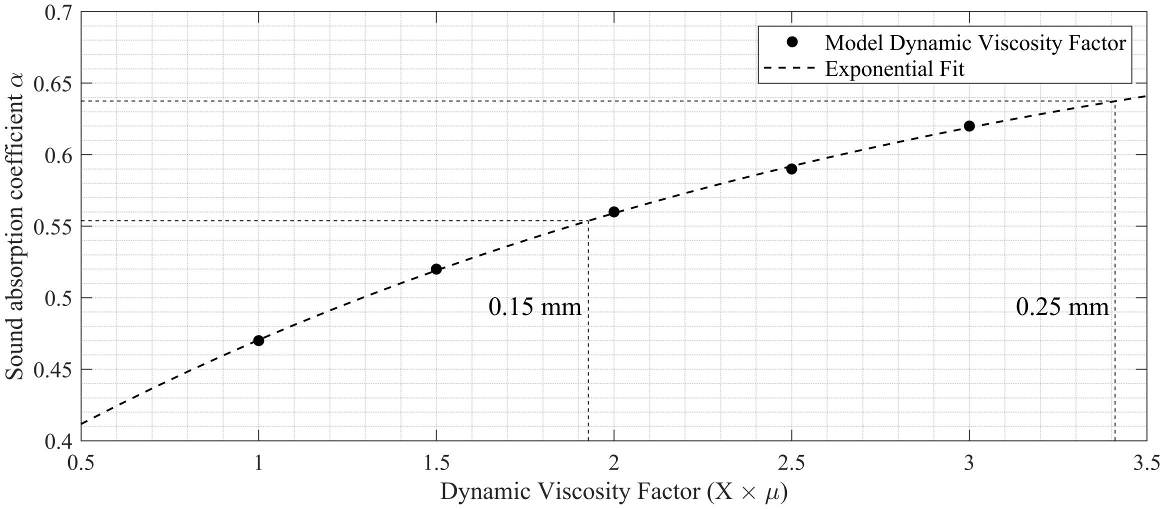

Figure 6.6: Indirect modelling: dynamic viscosity factor estimation

Fluid shell models were computed again with corrected viscosity factors: $1.93 \times \mu$ (equivalent to 0.15 mm LH direct roughness) and $3.41 \times \mu$ (equivalent to 0.25 mm LH direct roughness). The obtained results will be presented in the next section and compared to the results of the direct models.

Roughness	Equivalent dynamic viscosity
0.15 mm LH	$1.93 \times \mu$
0.25 mm LH	$3.41 \times \mu$

Table 6.3: Indirect modelling: equivalent dynamic viscosity values for direct modelling roughnesses (fluid shell thickness set as five times the boundary layer of the smooth model)

6.4.2 Modelling strategies comparison

In Chapter 5, the roughness patterns were applied to every surface of the benchmark geometry. In this subsection, additional comparison criteria for the evaluation of modelling strategies were introduced. This represents the potential for areas of additional roughness to be introduced into a design at target locations to enhance performance.

The roughness patterns were applied to the selected surfaces of the benchmark geometry: spherical pores, side channels and in-line channels. The comparison between the unit cells generated for the direct modelling simulations and the 0.15 mm LH roughness pattern is illustrated in Figure 6.7.

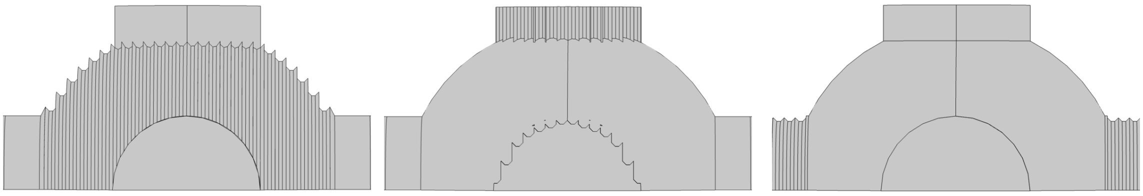

(a) Spherical pore (b) Side channels (c) In-line channels

Figure 6.7: Direct modelling: 0.15 mm LH roughness pattern applied to different surfaces of the benchmark geometry

The equivalent indirect modelling geometries are illustrated in Figure 6.8. The fluid shell region, shown in orange, was applied to selected surfaces of the benchmark geometries: spherical pores, side channels and in-line channels.

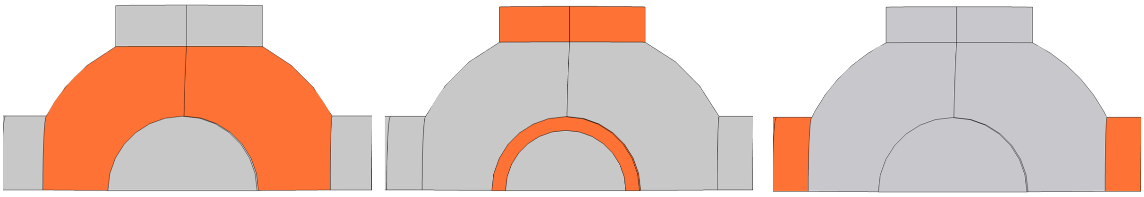

(a) Spherical pore (b) Side channels (c) In-line channels

Figure 6.8: Indirect modelling: fluid shell region applied to different surfaces of the benchmark geometry

6.5 Results

0.15 mm LH

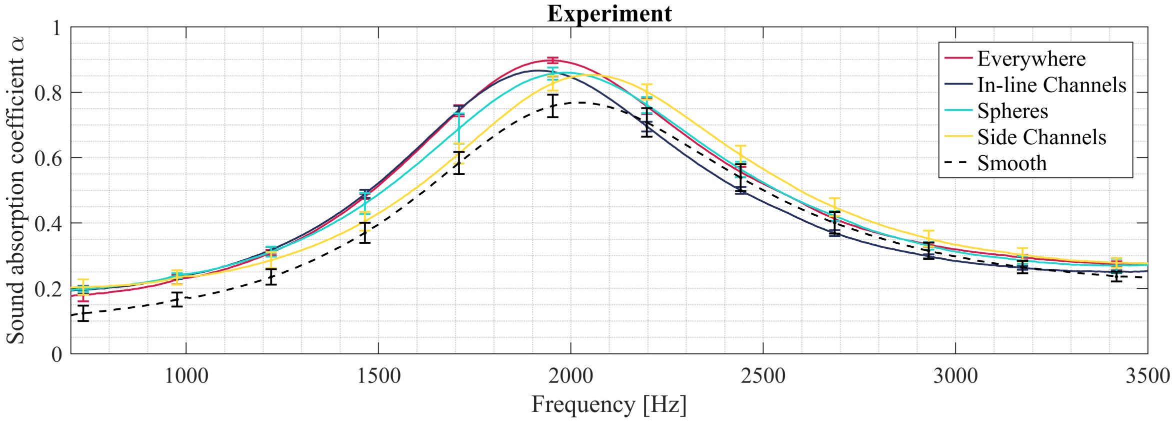

Figure 6.9: Experimental results measured for MSLA samples: 0.15 mm LH ‘extrusion-like’ roughness pattern

Figure 6.9 presents experimental results of the sound absorption coefficient of the materials with the 0.15 mm LH ‘extrusion-like’ roughness pattern applied to various surfaces of the base geometry. The measurements were performed in an impedance tube for MSLA samples; see Figure 6.5. The results are compared against the smooth design, which experimentally is the nominally smooth sample manufactured using MSLA technology without any additional roughness pattern (see Figure 6.3). As expected, the presence of roughness increases the sound absorption and shifts the position of the peak towards lower frequencies.

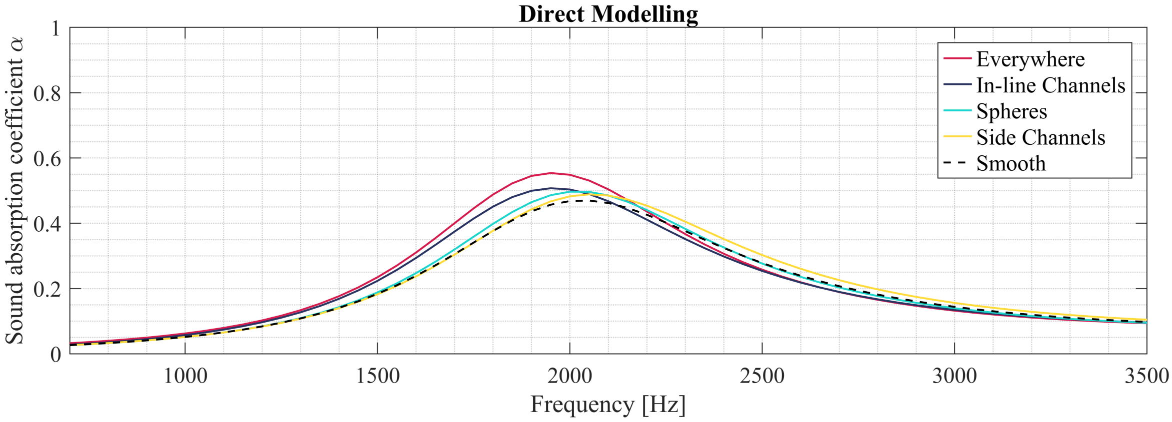

(a) Direct modelling strategy: 0.15 mm LH roughness pattern

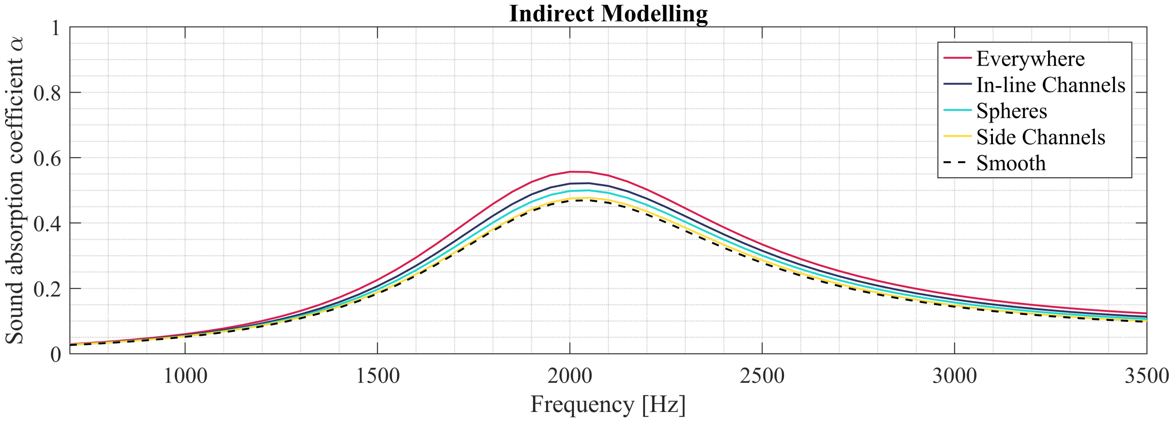

(b) Indirect modelling strategy: $1.91 \times \mu$

Figure 6.10: Numerical results

Figure 6.10 compares the direct and indirect modelling strategies employed to capture roughness effects. In the case of direct modelling, the 0.15 mm LH roughness pattern was applied to different parts of the benchmark geometry. In the case of indirect modelling, the fluid shell region with the altered air properties ($1.91 \times \mu$) was implemented in corresponding locations to capture the roughness effects and reduce computational costs. The results are compared against the smooth design, which numerically is the smooth geometry.

The results of both modelling strategies agree regarding the peak value for all roughness locations. The shift of the peak frequencies is observed for the direct modelling strategy. The indirect modelling does not capture that effect. However, it does not consider volume change that is accounted for by the direct modelling.

The increase in absorption due to surface roughness introduced by various layer heights used by FDM is confirmed by numerical calculations as well as MSLA samples with designed staircase roughness. However, there are still discrepancies between the numerical and experimental results, which can be explained by geometric inaccuracy (in particular, the actual size of the in-line channel is perhaps different than in the numerical model, as well as the porosity of the main pore network).

0.25 mm LH

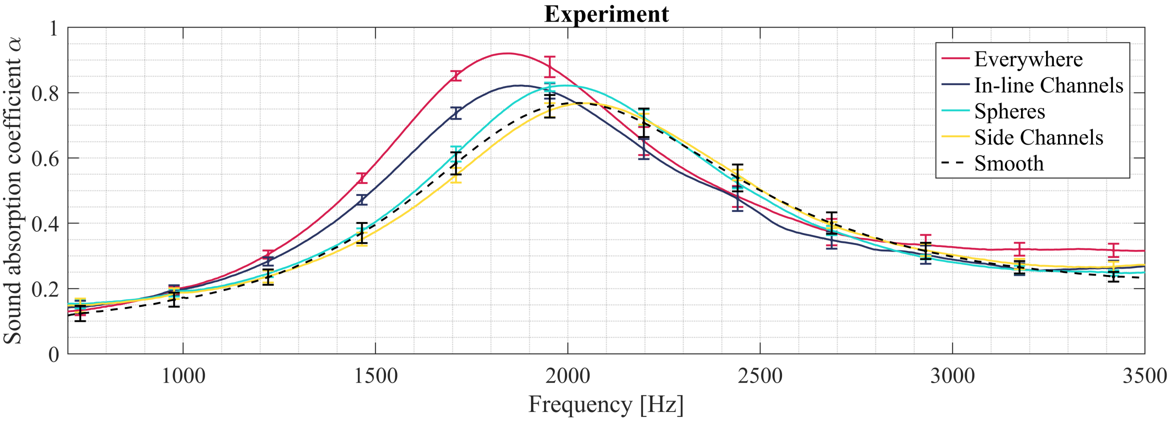

Figure 6.11: Experimental results measured for MSLA samples:
0.25 mm LH ‘extrusion-like’ roughness pattern

The experimental results obtained for the 0.25 mm layer height roughness pattern are set out in Figure 6.11. The observed acoustic contributions of specific roughness locations are larger in magnitude than in the case of the 0.15 mm layer height pattern discussed in the previous subsection, cf. Figure 6.9 and Figure 6.11.

Figure 6.12 provides a comparison between the direct and indirect modelling strategies applied in this study to capture surface roughness effects. In the case of direct modelling, the 0.25 mm LH ‘extrusion-like’ roughness pattern was implemented in different parts of the benchmark geometry. In the case of indirect modelling, the fluid shell region with the altered air properties ($3.41 \times \mu$) was applied to the corresponding locations to capture the roughness effects and decrease the computational cost. The results are compared against the smooth design, which numerically is the smooth geometry.

The results of both considered strategies are in good agreement regarding the peak value for almost all roughness locations. The only observed difference occurs in the case of the roughness on in-line channels. In direct modelling and experiments, the roughness on in-line channels and spherical pores provides the same extent of acoustic losses. However, indirect modelling results suggest that the roughness on spherical pores contributes less to the sound absorption coefficient than the in-line channels. Moreover, in the case of the indirect modelling strategy, we do not observe the frequency shift of the peak as these models do not take volume change arising from the presence of roughness into account.

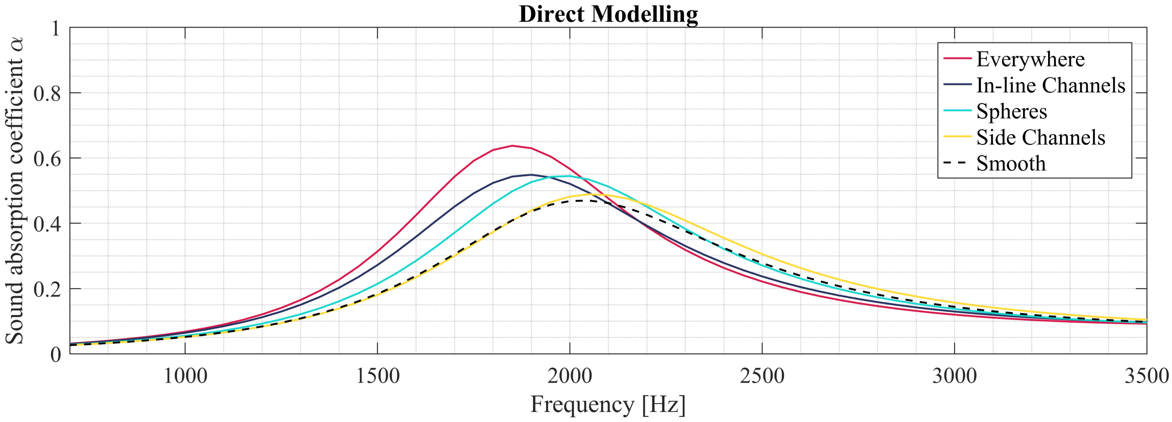

(a) Direct modelling strategy: 0.25 mm LH roughness pattern

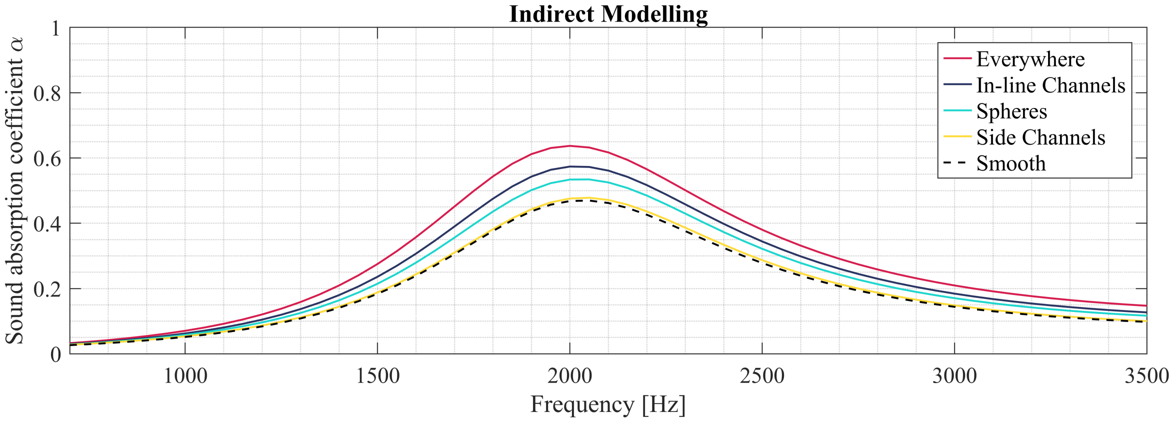

(b) Indirect modelling strategy: $3.41 \times \mu$

Figure 6.12: Numerical results

For sound absorption, the most important seems to be the airflow through in-line channels parallel to the direction of wave propagation. The surface roughness effect of these channels is responsible for a significant increase in the viscous acoustic wave energy dissipation. The size and roughness of these channels significantly affect (decrease) the viscous permeability and therefore (increase) airflow resistivity. They also influence the viscous characteristic length. The roughness in these channels should increase the phase of the dynamic (i.e. complex) viscous permeability function. As a result, the first absorption peak is shifted to a lower frequency.

Roughness on other surfaces is less important, although, in the case of 0.25 mm LH, it can also affect porosity, etc. In particular, the roughness in the side channels (which are perpendicular to the main flow and wave propagation direction) is almost negligible or at least less important. This also happens due to symmetry, meaning the flow in the side channels is not 'through'.

6.5.1 Dimensional data analysis

To better understand the changes from the smooth model, the dimensional data of the unit cells was inspected and compared. The volume (of the pore network) and surface area (of solid walls) of the smooth unit cell (determined from its CAD model) are summarised in Table 6.4. All indirect models, with fluid shell regions applied in different configurations, are based on the geometry of the smooth unit cell.

Pore volume [m^3]	Surface area [m^2]
5.442 E-8	8.072 E-5

Table 6.4: Geometrical parameters of the smooth/fluid shell unit cell

In this study, all geometries considered in direct numerical and experimental results were created based on the same CAD designs generated directly from COMSOL. For comparison purposes, the data of the 0.15 mm LH and 0.25 LH 'extrusion-like' roughness pattern models are summarised in Table 6.5 and Table 6.6, respectively. Both tables contain the percentage change (Δ%) calculated between the rough designs' volume and surface area values and corresponding dimensions of the original smooth design (taken from Table 6.4).

Location	Pore volume [m^3]	Δ%	Surface area [m^2]	Δ%
Everywhere	5.010 E-8	-7.9%	1.091 E-4	+35.2%
In-line channels	5.411 E-8	-0.6%	8.188 E-5	+1.4%
Spherical pores	5.160 E-8	-5.2%	1.025 E-4	+27.0%
Side Channels	5.352 E-8	-1.7%	8.505 E-5	+5.4%

Table 6.5: Geometrical parameters of the 0.15 mm LH roughness pattern unit cell

Location	Pore volume $[m^3]$	$\Delta\%$	Surface area $[m^2]$	$\Delta\%$
Everywhere	4.717 E-8	-13.3%	1.084 E-4	+34.3%
In-line channels	5.389 E-8	-1.0%	8.188 E-5	+1.4%
Spherical pores	4.973 E-8	-8.6%	1.016 E-4	+25.9%
Side Channels	5.304 E-8	-2.5%	8.412 E-5	+4.2%

Table 6.6: Geometrical parameters of the 0.25 mm LH roughness pattern unit cell

As seen from the tables above, the presence of a roughness pattern decreased the pore network's volume (and porosity) and increased the surface area of solid walls. That resulted in the enlargement of the contact area between the air and the solid skeleton of the structure. The roughness applied to the most extensive parts of the considered geometries, either everywhere or only to the spherical pores, had the most profound effect on the geometrical parameters compared to the smooth unit cell. The presence of both in-line and side channels similarly influenced the considered dimensions.

Taken together, these results suggest that surface roughness influences two significant aspects of the considered system. First, the absorption peak's position is determined by the geometrical location of the applied roughness. Roughness applied only to in-line channels showed the closest match with the roughness applied everywhere, in terms of both numerical and experimental results. This is the location where most of the acoustic losses in the DENORMS geometry occur, as previously described in Section 5.4.

Therefore, in future designs, roughness should be applied in the most acoustically essential locations to avoid the frequency shift. Furthermore, although roughness applied only in those parts of the geometry did not influence much the unit cell volume and surface area in comparison to the smooth cell, significant improvement of the sound absorption was achieved for both 0.15 mm LH and 0.25 mm LH 'extrusion-like' roughness patterns.

Second, the presence of roughness significantly influenced the volume and surface area of the most extensive component of the designs, the spherical pores, and, consequently, the porosity. By altering those geometrical dimensions, the acoustic behaviour of the system was enhanced notably, to an extent comparable to the roughness applied only to the in-line channels in terms of the increase of absorption. On the other hand, a frequency shift was observed in the case of both 0.15 mm LH and 0.25 mm LH 'extrusion-like' roughness patterns.

6.5.2 Run time comparison

The numerical simulations were carried out using a commercial finite element analysis software package, COMSOL Multiphysics 6.1. All simulations were performed using Precision 5820 Desktop Workstation: Intel(R) Xeon(R) W-2265 CPU @ 3.50GHz processor, 256 GB RAM.

The comparison of run times between direct and indirect modelling approaches is summarised in Table 6.7 and Table 6.8. The indirect modelling approach is much more time efficient, and the results obtained closely match the direct modelling results regarding the sound absorption coefficient value.

Roughness	Parameter	Direct (0.15 mm LH)	Indirect ($1.93 \times \mu$)
Everywhere	Degrees of freedom Computational time [s]	**8168615** **154551**	**829441** **8342**
	α	0.55	0.56
In-line channels	Degrees of freedom Computational time [s]	**1346641** **12862**	**374606** **1674**
	α	0.51	0.52
Spherical pores	Degrees of freedom Computational time [s]	**5764411** **95661**	**575487** **3373**
	α	0.51	0.50
Side Channels	Degrees of freedom Computational time [s]	**2216838** **15250**	**312439** **1109**
	α	0.49	0.48

Table 6.7: Modelling strategies comparison

Roughness	Parameter	Direct (0.25 mm LH)	Indirect ($3.41 \times \mu$)
Everywhere	Degrees of freedom Computational time [s]	**5968078** **96611**	**829441** **8342**
	α	0.65	0.64
In-line channels	Degrees of freedom Computational time [s]	**1097077** **9425**	**374606** **1674**
	α	0.55	0.58
Spherical pores	Degrees of freedom Computational time [s]	**3794424** **40525**	**575487** **3373**
	α	0.54	0.53
Side Channels	Degrees of freedom Computational time [s]	**1585353** **9877**	**312439** **1109**
	α	0.49	0.48

Table 6.8: Modelling strategies comparison

6.6 Conclusions

The first aim of this investigation was to implement insights gained from the additive manufacturing of an acoustic material into the design of novel porous absorbers. With that in mind, the benchmark design produced using FDM was assessed using a combination of non-destructive testing methods. As a result, it was discovered that three main issues affecting the faithfulness of reproduction of CAD geometry include microporosity of built material, limited geometrical accuracy and surface roughness.

As these nominally flawed occurrences increase the absorptive characteristics of the considered system, the next objective was to take advantage of their presence in a new, altered geometrical design. For that reason, a roughness pattern was created based on the confocal microscope measurements of the FDM samples and used as a new design for additive manufacturing using MSLA. Various design alterations of the benchmark design were proposed to assess the influence of the roughness location on the acoustic performance. Roughness was applied everywhere, only to the surface of spherical pores, only to side channels, or only to in-line channels.

The second aim of this investigation was to explore different numerical strategies which capture the influence of surface roughness effects on acoustic behaviour. The intention was to propose a low-cost modelling strategy that can be utilised for the inclusion of surface roughness effects in the design and optimisation of acoustic material. The results of the two computational methods were compared to each other and with experimental results.

The first method, direct modelling, utilises a geometrical representation of roughness to capture the corresponding acoustic losses accurately. This method captures the change in absorption magnitude and associated frequency shirts due to changes in geometry. Its main drawback is the high computational cost related to the creation of the geometry, meshing and solving.

The second method, indirect modelling, mimics the presence of roughness by adjusting air parameters in the selected regions of the smooth geometry to reduce the numerical burden. This method captures accurately the changes in absorption magnitude but does not capture the frequency shift. The advantage of this method is that it can be tuned to different manufacturing layer heights or surface features and that it is generally in excess of one order of magnitude faster than the direct method.

The following conclusions can be drawn from the present study. Foremost, the presence of a roughness pattern was most crucial in the location where most viscous losses occur. In the case of the DENORMS cell, that was the in-line channels (parallel to the direction of wave propagation and the main direction of the flow induced by it). Although the roughness applied there did not influence the pore volume (and porosity) or surface area much, in terms of peak location, it had the same influence as roughness applied everywhere (therefore, including the in-line channels). Moreover, a significant absorption increase was also achieved.

This research has also shown that the porosity and surface area of solid walls are two vital parameters interconnected with each other. The presence of roughness changes their values in comparison to the smooth design and, as a result, alters the acoustic behaviour.

The results of the direct and indirect numerical strategies agree regarding the peak value of the sound absorption. The implementation of the fluid shell contributed to the notable reduction of the computational cost by lowering the number of degrees of freedom in meshing and, as a result, decreasing the computational time.

Further work needs to be done to investigate the geometrical shape of roughness on the acoustic performance of novel porous materials. An optimal surface morphology that exploits the benefits of increased roughness while controlling for changes in volume and surface area may exist. Such a pattern should be applied to the most acoustically significant parts of the base design.

Moreover, to further enhance the indirect modelling strategy, future development should focus on formalizing the extent of the fluid shell region and refining the dynamic viscosity by considering a target boundary layer development. These refinements will likely contribute to a more comprehensive and accurate representation of the desired acoustic absorption properties which makes the method suitable for use in a design process. In general, both the surface roughness effects and the changes to the volume and surface area of the whole system should be taken into account, or else there may be a shift to the intended operating frequency of the design.

Chapter 7

Practical application of 3D printed acoustic materials

7.1 Introduction

The primary objective of the study presented in this chapter was to develop tools useful for enhancing the low-frequency behaviour of a commercial acoustic silencer (Zehnder CSI 350 DN 125), shown in Figure 7.1, by applying a low-cost and low-effort approach. An acoustic material containing lattices of subwavelength unit cells and resonating structures was designed for a target frequency and 3D printed for that purpose. The silencer was first tested without any alterations. In the next step, it was disassembled and modified by partly applying the 3D printed material to its interior. The altered silencer was then reassembled and retested. The improvement in transmission loss was experimentally demonstrated by comparing the results of the original and altered silencers.

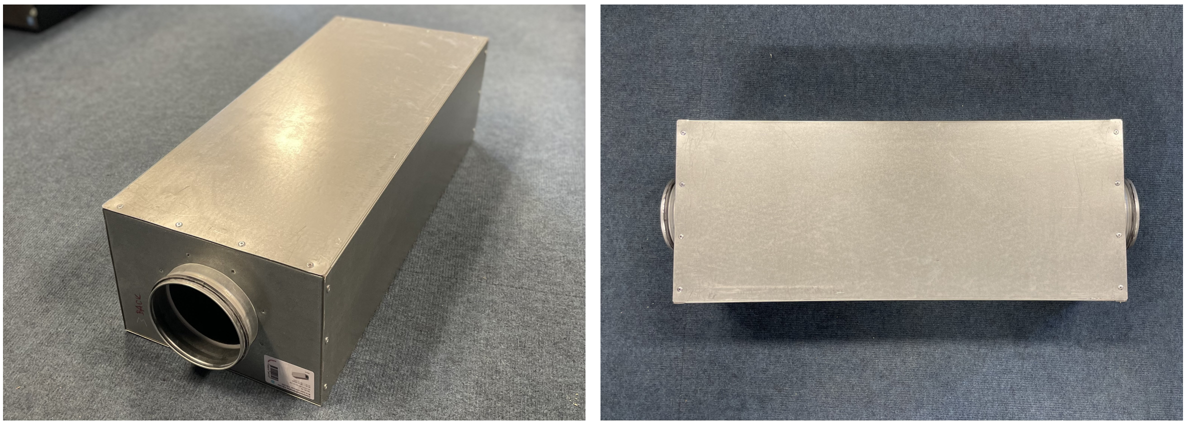

Figure 7.1: Comercial acoustic silencer

This research indicates that 3D printed materials can be designed for a target frequency and improve the tonal behaviour of the system based on conventional porous materials while being cost-effective. The findings show that superior low-frequency sound attenuation can be achieved using low-cost novel acoustic materials. These results offer insights into the potential for the industrial application of 3D printed materials for the building acoustics sector.

This chapter is based on a conference paper: A. Ciochon, J. Kennedy, “3D printed acoustic materials for the performance enhancement of a building acoustics silencer”, in 52nd International Congress and Exposition on Noise Control Engineering (INTER-NOISE 2023), Chiba, Greater Tokyo, Japan, Aug. 2023

7.2 Design process

7.2.1 Unit cell optimisation

Direct modelling strategy

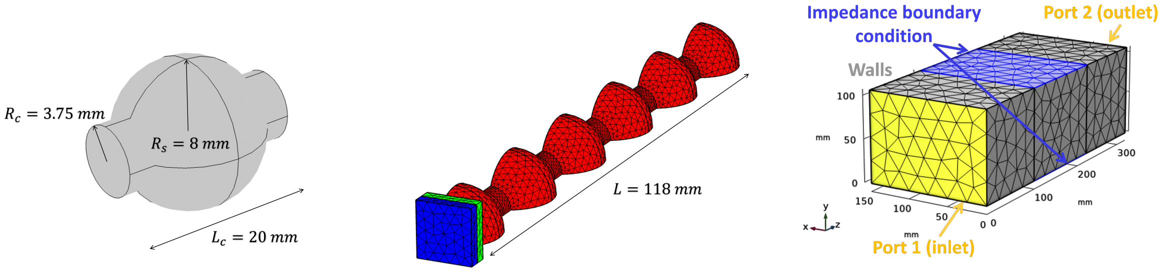

(a) Unit cell (b) Impedance model (c) Transmission loss model

Figure 7.2: COMSOL modelling

The proposed structure designed for the low-frequency acoustic improvements is a lattice of interconnected unit cells, which form an open-pore network and act as a chain of resonators. The unit cell, illustrated in Figure 7.2a, is defined by three geometrical parameters: radius of the sphere (R_s), radius of the cylinder (R_c) and length of the cylinder (L_c).

A model shown in Figure 7.2b was used to obtain real and imaginary impedance values of the designed system. The modelling strategy employed in this study utilises a detailed model of the unit cell lattice to provide data for an impedance boundary condition in a full-pressure acoustic model of a rectangular duct. The rectangular duct model, Figure 7.2c, enables the optimisation of the sound transmission loss through modifications to the unit cell geometry in the thermoviscous sub-model, Figure 7.2b.

Harmonic viscothermal analyses are solved in the considered frequency range for the model shown in Figure 7.2b. Surface acoustic impedance is then calculated on the frontal (blue) rectangular boundary shown in Figure 7.2b. The found surface acoustic impedance (i.e. complex, frequency-dependent function) is applied on the light-blue rectangular side boundary indicated in the duct shown in Figure 7.2c to perform transmission analyses.

The key geometrical parameters of the design were investigated and optimised in a parametric sweep to hit the target frequency of 550 Hz. The constraints analysed in this study were as follows: 6 mm $< R_s <$ 9.5 mm, 0.75 mm $< R_c <$ 4 mm, 18 mm $< L_c <$ 20 mm. The optimised parameters are the following: R_s = 8 mm, R_c = 3.75 mm and L_c = 20 mm. The length of the individual chain was kept constant at six unit cells.

The pressure acoustic model of a rectangular duct, illustrated in Figure 7.2c, was used to calculate the transmission loss of the system. The cross-section of the duct (150 mm x 107 mm) corresponds to the physical dimensions of the silencer's channel (shown in Figure 7.11a). 107 mm is the average height of the channel. The impedance values of the optimised geometrical design obtained from the previous model (Figure 7.2b) were implemented as a boundary condition to mimic the actual system and reduce computational cost.

The impedance boundary condition applied to the two active sections is shown in blue (see Figure 7.2c). Their surface area corresponds to the total surface area of unit cells of the designed 3D printed blocks, shown in Figure 7.7 and Figure 7.8 (in Section 7.2.2), i.e., 91 (perforations) x 20 mm x 20 mm = 36400 mm^2. In the model shown in Figure 7.2c, the two active areas (these areas are placed next to each other to form the blue rectangle shown in Figure 7.2c) have dimensions 150 mm x 121.5 mm each and together have the active area of 36450 mm^2, to which the impedance boundary condition is applied. The length of the perforated wall (121.5 mm) was chosen so that the model of that surface matches the actual total perforated wall surface of the physical 3D printed samples.

The hard wall boundary condition is marked in grey. A plane wave was imposed at the inlet, shown in yellow. Port boundary conditions were used at the inlet and outlet of the tube.

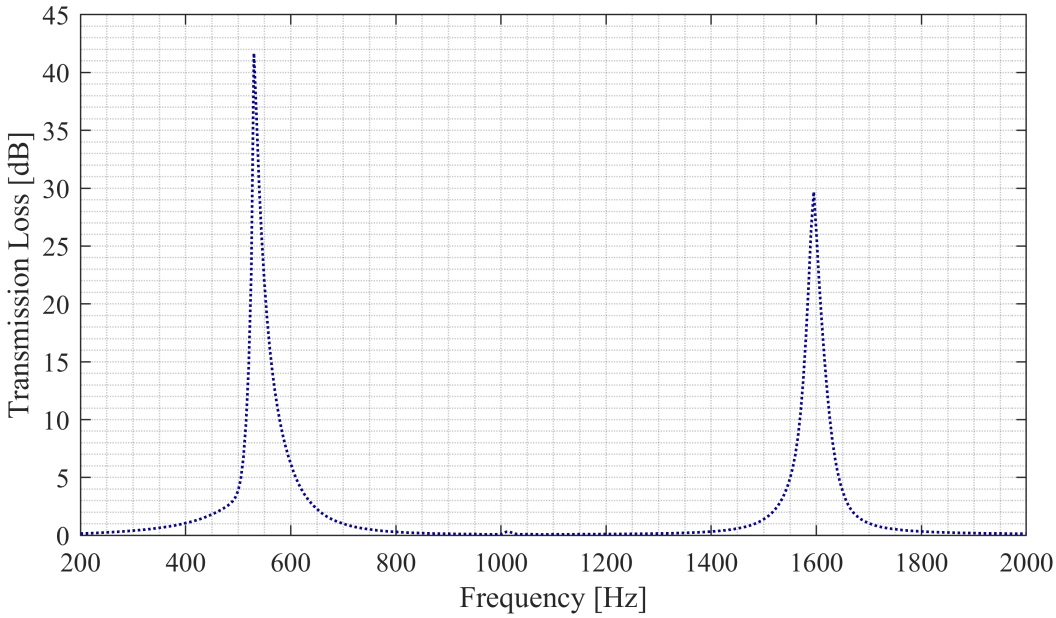

Figure 7.3: Numerical transmission loss (direct modelling)

The numerical transmission loss results of the optimised geometrical design are illustrated in Figure 7.3. The designed system exhibits tonal behaviour at two frequencies, 550 Hz and 1650 Hz, where superior noise reductions are achieved.

Indirect modelling strategy

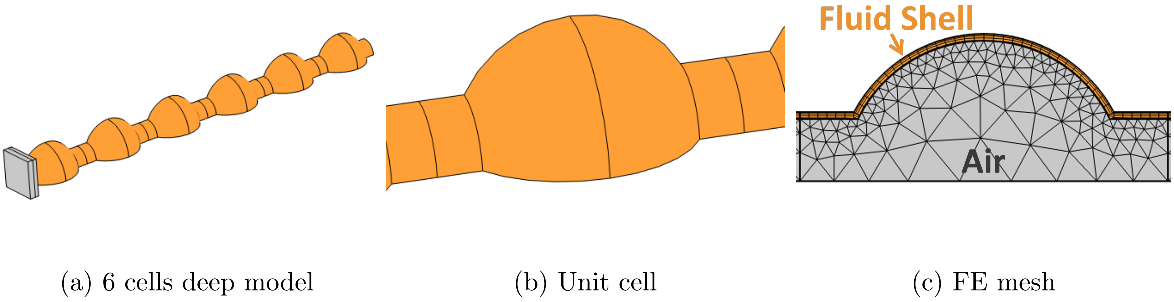

(a) 6 cells deep model (b) Unit cell (c) FE mesh

Figure 7.4: Fluid shell impedance model

A fluid shell modelling strategy, discussed in Section 5.3.2, was also implemented in this study to investigate the influence of roughness on the performance of the designed structure. The unit cell was divided into two distinct parts: an inner air region and an outer fluid shell (FS) characterized by a modified dynamic viscosity.

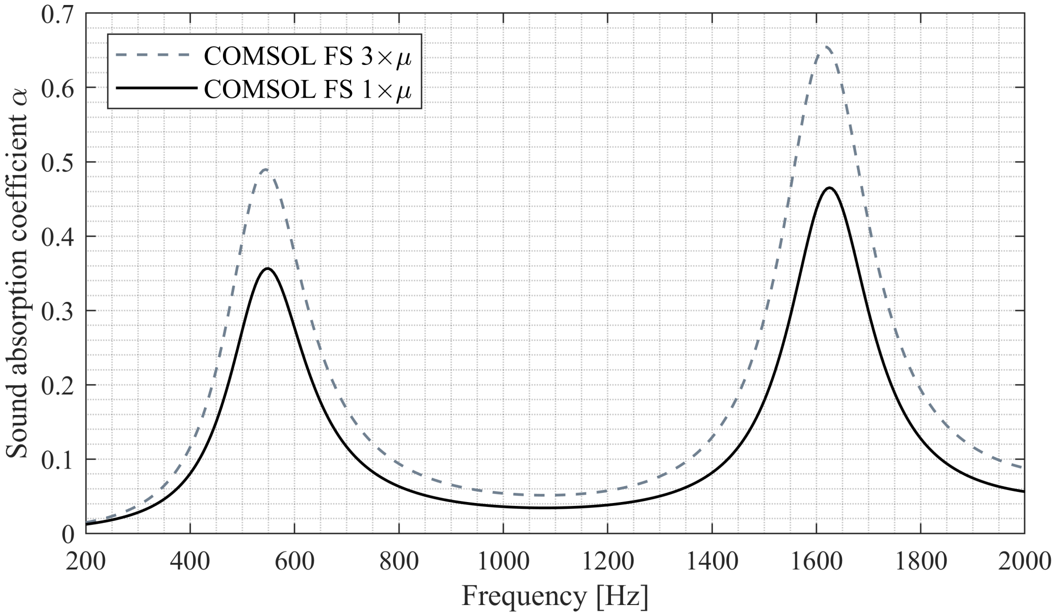

Figure 7.5: Numerical sound absorption calculations with the fluid shell

All air properties remained unchanged within the fluid shell, except for the dynamic viscosity μ. In the first case, μ was not modified (condition comparable with the direct modelling strategy and assumption of smooth walls). In the second case, μ was multiplied by three (assumption of rough walls).

The fluid shell layer was designed to modify the growth of the viscous boundary layer through the altered dynamic viscosity. Specifically, the extent of the fluid shell was selected to be three times the depth of the 3D printing pattern, that is, 0.375 mm. Generated geometries of the impedance model are illustrated in Figure 7.4. The fluid shell region is indicated in orange.

The calculated predictions of the sound absorption coefficient are presented in Figure 7.5. As expected, the increase in dynamic viscosity (corresponding to the presence of roughness) led to a rise in absorptivity compared to the smooth model, where the dynamic viscosity remained unaltered.

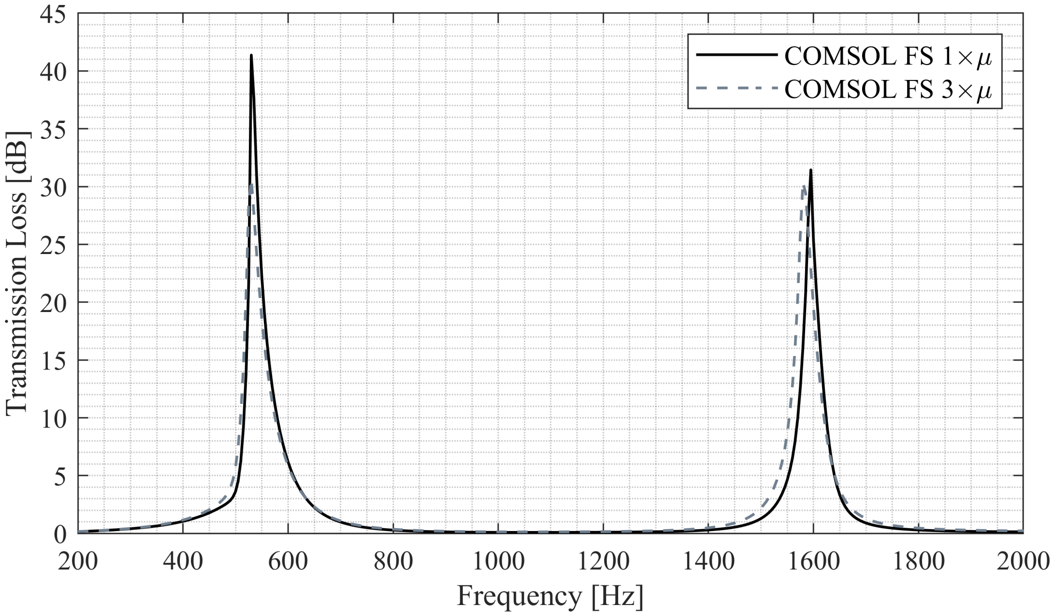

Figure 7.6: Numerical transmission loss calculations with the fluid shell

The corresponding transmission loss results are illustrated in Figure 7.6. Surprisingly, an opposite trend can be observed in this case. The curve with unaltered dynamic viscosity (representing a smooth model) achieved much higher transmission loss values. The obtained results match the results of the direct modelling strategy, shown in Figure 7.3. Increased dynamic viscosity (representing the model with rough surfaces) decreased the transmission loss performance of the structure, especially in the case of the first peak in the lower-frequency region.

Two factors influence the transmission loss in the silencer. The first is resistive dissipation, which is associated with normal incidence absorption. The second is the reactive part caused by resonant reflection from the designed resonator chains, which has the predominant effect on the behaviour of the designed system. The increased viscosity reduces the quality factor of the resonator, which leads to a decrease in the reactive contribution to the transmission loss.

The considered geometrical dimensions are optimised neither for normal incidence absorption nor transmission loss. That's why in the case of the absorption shown in Figure 7.5, we approach the optimal value of the impedance by increasing μ (associated with the presence of roughness). On the other hand, in the case of the transmission loss illustrated in Figure 7.6, increasing μ results in a shift away from the (unknown) optimum.

Analytical models which can be used to establish geometrical dimensions for optimal transmission loss are presented in Appendix E.2.

7.2.2 Acoustic-material solution design

Chains of six cells of the optimised unit-cell design were arranged in the form of two blocks: a smaller structure (shown in Figure 7.7) and a larger structure (illustrated in Figure 7.8). The cross-section shapes of the blocks (as shown in Figure 7.7b and Figure 7.8b) corresponded to the shape of the foam lining of the factory-made, unaltered silencer (shown in Figure 7.11a) and roughly followed its curvature (c.f. Figure 7.11a and Figure 7.11b). The thickness of the designed blocks was kept the same as the thickness of the foam: 150 mm.

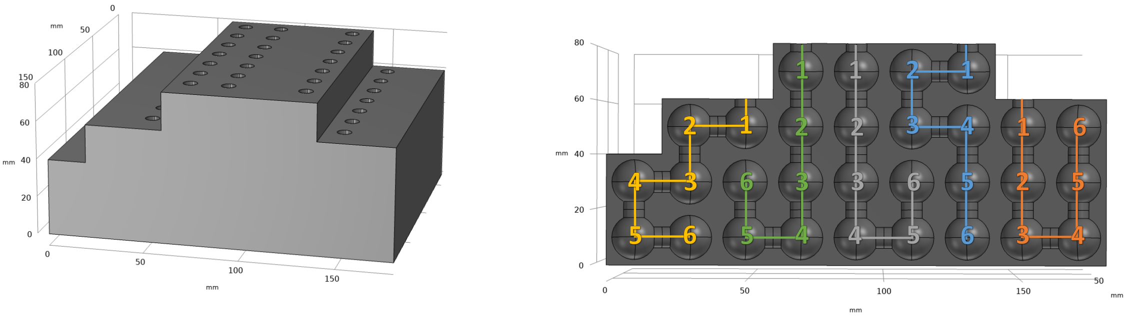

(a) Geometry

(b) Cross section

Figure 7.7: Smaller structure

The interior layout of the lattice of unit cells employs a space coiling approach to fit the maximum number of unit cell chains into the blocks of material. The chains of 6 unit cells are wrapped around the interior of the blocks, see Figures 7.7b and 7.8b, with the inlets visible in Figures 7.7a and 7.8a.

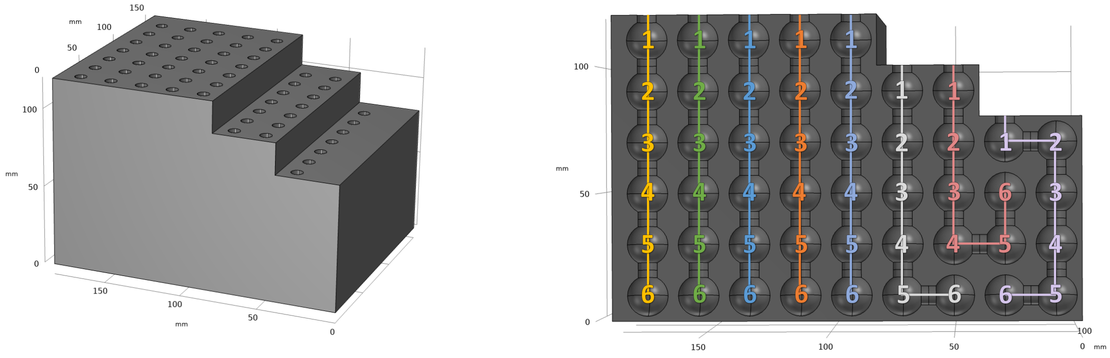

(a) Geometry

(b) Cross section

Figure 7.8: Larger structure

The designed structures were manufactured using FDM-based Prusa i3 MK3S+, 15% infill and the roughest 0.30 mm layer height. These settings were chosen to minimise the print time and build material usage. Both blocks were designed to have an estimated print material volume below 1 kg to allow fabrication using a single filament spool. The printer's build volume (250 mm x 210 mm x 210 mm) was also considered during the design process.

The slicing software estimated the volume of the smaller structure at 625 g and the larger structure at 925 g, which led to the estimated cost of the build material required for manufacturing at 27 Euros and 42 Euros, respectively. The estimated print time was calculated at 34 hours for the smaller structure and 51 hours for the larger structure. The 3D printed blocks are shown in Figure 7.9.

The difference between altered and unaltered silencer's interior is presented in the schematic shown in Figure 7.10, where the light-grey areas show the position and shape of the foam lining. In Figure 7.10b, some parts of the lining are replaced with 3D printed structures, marked in black.

The difference between altered and unaltered silencer's interior lining is displayed in Figure 7.11. Figure 7.11a shows the interior of the unaltered silencer, which was disassembled right after initial experimental testing. Then, the foam lining was cut out to leave space for the 3D printed structures. The lining of the altered silencer is shown in Figure 7.11b. Finally, the modified silencer was reassembled in a way that provided a good seal and static placement of the blocks.

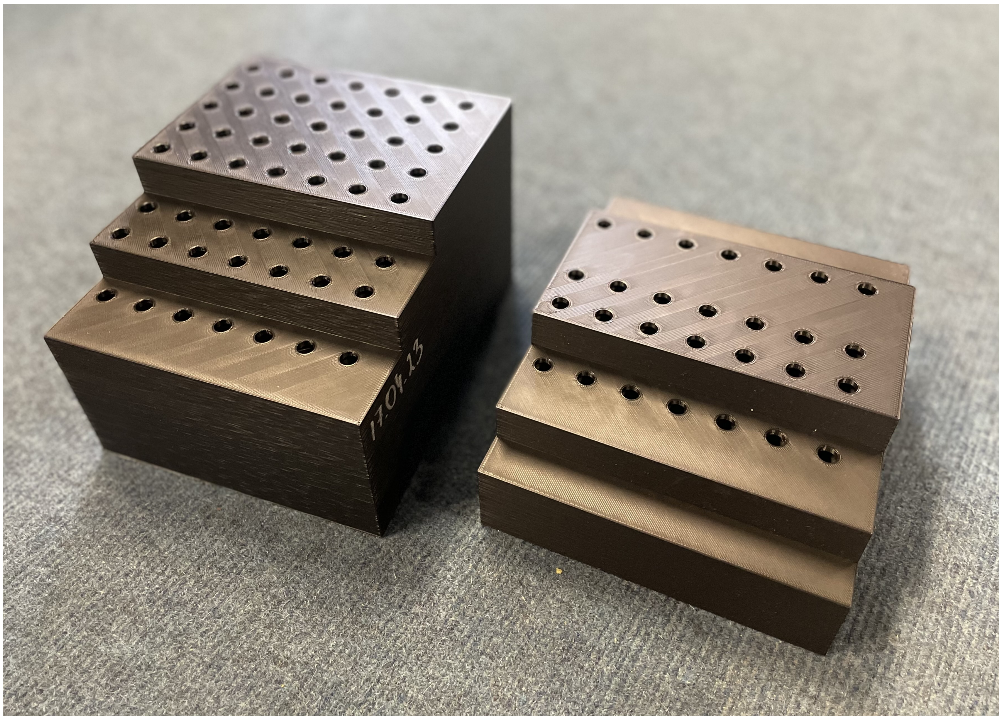

Figure 7.9: 3D printed structures

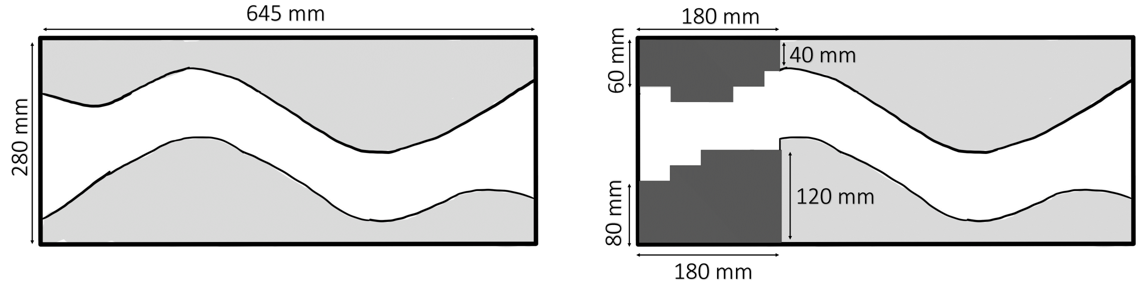

(a) Unaltered silencer

(b) Altered silencer

Figure 7.10: Interior schematic

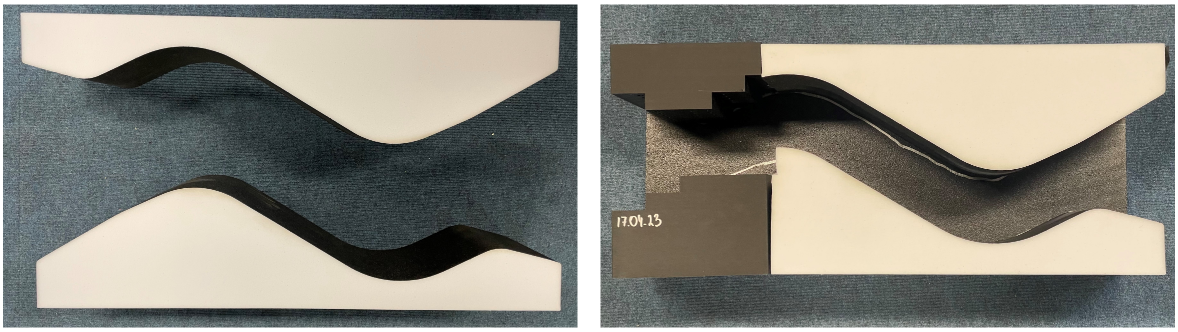

(a) Unaltered silencer

(b) Altered silencer

Figure 7.11: Interior lining

7.3 Experimental investigation

The transmission loss of unaltered (i.e. reference configuration) and altered silencers was measured using an impedance tube in a normal incidence setup according to ASTM E2611. The information regarding the testing procedure can be found in Section 1.3.3. The custom rig used for the experimental testing is shown in Figure 1.5.

7.4 Results and discussion

Figure 7.12 compares the continuous transmission loss measured for two silencers, i.e. the original (unaltered) and altered configuration. It is apparent from this graph that the 3D printed acoustic material improved the performance of the modified silencer: additional significant (peak) transmission losses are observed in the regions around two frequencies, 650 Hz and 1650 Hz. These two frequency regions of the excessive transmission losses were previously identified using numerical analyses (cf. Figure 7.12 and Figure 7.6), which confirms that they are caused by the presence of the 3D printed structures. The observed frequency range and performance increase agree qualitatively with the numerical predictions shown previously in Figure 7.6.

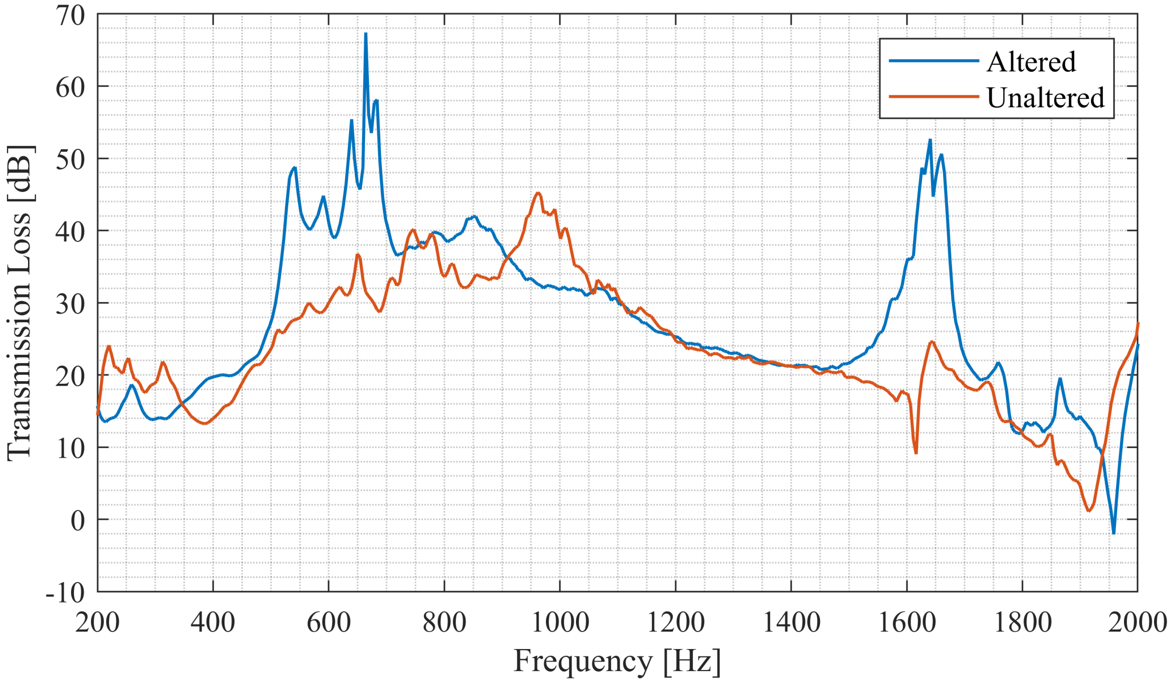

Figure 7.12: Transmission loss (measurement results)

Furthermore, despite removing the part of the foam lining, the broadband performance is maintained over the almost full frequency range. The designed material added superior quasi-tonal losses around the predicted frequencies on top of the broadband performance of the foam liner.

The experimental results with respect to octave bands can be compared in Figure 7.13. From this data, it can be seen that the altered silencer shows superior performance in the low-frequency 500 Hz octave band. At the same time, this effect was not achieved at the cost of decreased performance in other frequency bands, where two silencers exhibit similar behaviour.

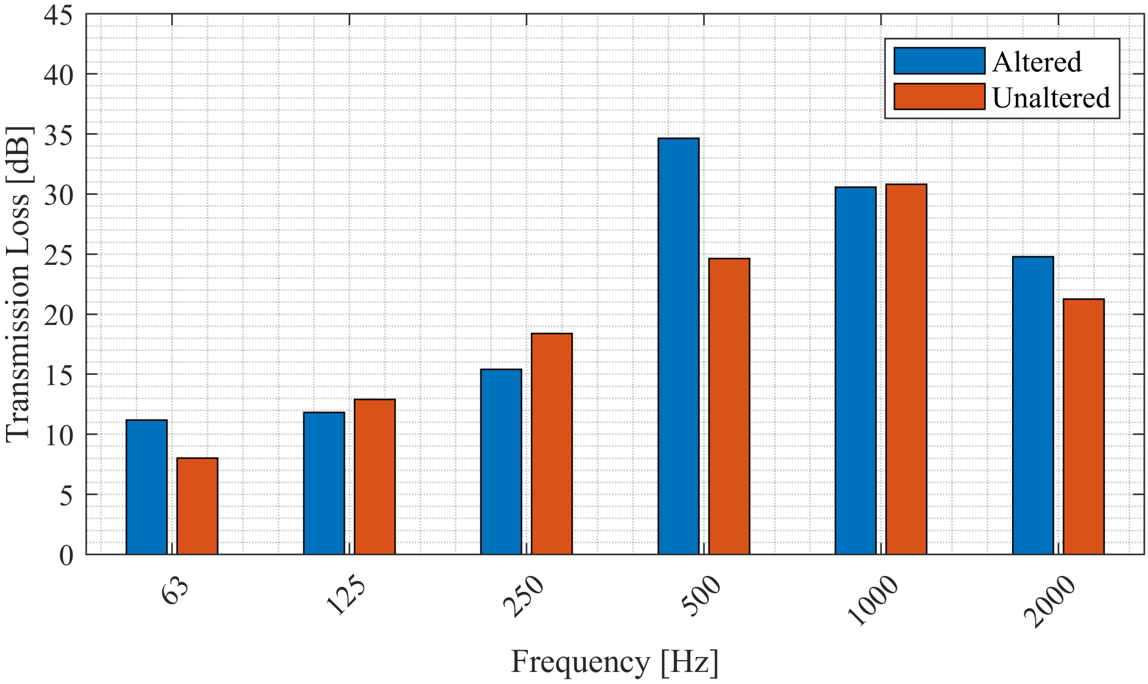

Figure 7.13: Transmission loss (octave bands)

The differences between the results of two silencers with respect to octave bands are given in Table 7.1 for comparison.

Center Frequency [Hz]	63	125	250	500	1000	2000
Δ TL [dB]	3.2	-1	-3	10	-0.3	3.5

Table 7.1: Transmission loss difference (octave bands)

7.5 Conclusions

The study presented in this chapter was conducted to design and 3D print an acoustic-material solution for the low-frequency enhancement of a commercial acoustic silencer and evaluate its performance. The results of this investigation show that low-cost 3D printing methods can be used to manufacture fully customised acoustic materials for superior transmission loss at target frequencies. For that reason, 3D printed acoustic materials can be used together with classical foam liners to improve their broadband behaviour and tune the overall performance of the silencer to the noise at specific frequencies of interest.

This approach opens the possibility of bespoke enhancements to off-the-shelf components that can be rapidly designed and deployed in an industrial setting. In this case, enhancements of over 30 dB were achieved at the target frequency with minimal material cost and no negative impact on the existing broadband silencer performance.

Finally, the fluid shell modelling approach provided valuable insights into the impact of surface roughness on the acoustic performance of the designed structure. The evidence from this study suggests that although roughness is beneficial in normal incidence absorption, it can negatively affect transmission loss. More work must be done to improve the design process so the geometrical dimensions of the considered structures are optimised for maximum losses (absorption or transmission loss). It is known that roughness increases airflow resistivity by reducing the permeability of the material. Perhaps the ‘bad’ roughness increases the static airflow resistivity (i.e. reduces the static viscous permeability) too much, which leads to a more ‘reflective’ material with lower transmission losses. Therefore, the ‘good’ roughness should increase the phase or imaginary (lossy) part of the material’s dynamic viscous permeability.

Chapter 8

Conclusions

8.1 General conclusions

The primary aim of this thesis was to design a novel cellular acoustic material suitable for additive manufacturing that has been optimised through an iterative loop of numerical modelling and experimental validation and to demonstrate a practical application of such 3D printed materials. This aim was achieved.

In the pursuit of this goal, the following intermediate objectives were set and accomplished:

- To investigate and determine the acoustic impact of additive manufacturing on the performance of the benchmark material and compare it among three distinctive 3D printing technologies (Chapter 4).
- To update the numerical models to capture the actual manufactured material's performance and improve their suitability as a material design tool (Chapter 5).
- To develop material enhancements based on the benchmark unit cell's geometry but altered in such a way as to improve its acoustic performance, additively manufacture it and perform an acoustic evaluation to assess its effectiveness (Chapter 6).
- To demonstrate a practical implementation of additively manufactured acoustic materials for performance enhancement of a commercial off-the-shelf building acoustics silencer (Chapter 7).

8.2 Summary of conclusions

Chapter 4 set out to determine the influence of the additive manufacturing process on the acoustic performance of the benchmark material. In this study, three distinctive 3D printing technologies were considered: extrusion-based FDM, photopolymerisation-based MSLA and PBF-based SLM. Various NDT techniques were implemented to perform the quality inspection of samples manufactured using different 3D printing processes. Finally, a combination of numerical and experimental methods was used for the acoustic evaluation. The main conclusions drawn from this study are as follows:

- The additive manufacturing process heavily influences the acoustic properties of produced parts. The mismatch between numerical or analytical prediction and experimental results, in terms of the magnitude of absorption and peak location, is caused by the distortion of the idealised, smooth CAD geometry. Occurring shape deformation results from layer-by-layer fabrication and other characteristics specific to different 3D printing methods. Two major issues present in all considered print processes are surface roughness and reduced dimensional accuracy. In addition, extrusion- and PBF-based techniques are also subject to the microporosity of the build material. Furthermore, some defects are specific to different technologies and include: filament stringing (FDM), material shrinkage and expansion, and varying build quality along the z-axis (MSLA), and satellite particles (SLM).

- The presence of additive manufacturing defects enhanced the performance of benchmark design in comparison to numerical predictions. Nevertheless, despite this improvement in the magnitude of the acoustic absorption, none of the manufactured samples operated at the target frequency. Perhaps dedicated corrections for 'reduced dimensional accuracy' (especially the actual values of channel diameter) could improve this.

The study presented in Chapter 5 was undertaken to investigate the effects of surface roughness on the acoustic performance of the benchmark material. Analysed samples were produced using FDM and standard layer heights specific to this technology. The surface profiles obtained with a confocal microscope were used to design realistic, rough computational geometries of numerical models, which corresponded to physical samples produced with different layer heights. Experimental and numerical investigation was carried out to evaluate the acoustic impact of surface roughness. The following conclusions can be drawn from this study:

- Surface roughness resulting from increasing the layer height plays a part in excessive sound absorption above what is expected from the smooth numerical model. At lower layer height values, a minimal increase in the dissipation within the material occurs. Nevertheless, the slicing procedure affects the volume of the geometry and leads to a change in the operating frequency. Additional dissipation is observed at higher layer height values, increasing the absorption peak value in both experimental and numerical datasets.

- Surface roughness is only partially responsible for the mismatch between numerical predictions and experimental results. A broadband increase in absorption is present in the experimental data, which is not replicated in the numerical data. It should be noted that the increase in layer height is also related to other 3D printing defects influencing dimensional accuracy.

- Surface roughness increases the boundary layer thickness within the system, leading to enhanced dissipation. Moreover, roughness enlarges the contact area between the air and the solid skeleton of the structure.

In Chapter 6, the aim was to actively use the knowledge gained from two previously discussed chapters to design material enhancements. Taking advantage of the acoustic potential of surface roughness was the main idea behind this study. That being the case, new designs were created by applying roughness patterns to the walls of the smooth, benchmark geometry. Those patterns were based on confocal microscope data of FDM samples for two layer heights: 0.15 and 0.25 mm. Various design alterations of the benchmark design were proposed to assess the influence of the roughness location on the acoustic performance. Roughness was applied to different parts of the geometry: on all surfaces, only on the spherical pore surface, only on the surfaces of side channels, or finally only on the surface of in-line channels. MSLA was chosen as a suitable manufacturing method as it utilises low layer height and can produce a smooth, nominal benchmark design. The smooth geometry was used as a control sample to assess the effectiveness of applied artificial roughness. Moreover, MSLA is not affected by the microporosity of printing material. Therefore, the frequency shift between numerical predictions and experimental results can be avoided or minimised. The acoustic evaluation combined numerical and experimental methods. The main conclusions drawn from this study are as follows:

- The geometrical location of the applied roughness determines the position of the absorption peak. Roughness should be applied to most acoustically significant locations to avoid the frequency shift. Moreover, although the roughness applied only there did not change the volume or surface area much compared to the smooth design, a significant increase in the magnitude of absorption was achieved.

- Volume and surface area are two essential and correlated parameters of the considered pore network system. The presence of roughness decreases the system's volume and increases the surface area compared to the smooth design. This change alters the acoustic behaviour and leads to an increase in the magnitude of absorption. However, when the roughness pattern was applied elsewhere than the most acoustically important location of the benchmark geometry, a frequency shift was observed.

The purpose of the study presented in Chapter 7 was to demonstrate a practical application of 3D printed acoustic materials. A novel acoustic-material solution, in the form of a lattice of subwavelength unit cells, was designed for the target frequencies of interest, manufactured and applied to the interior of a commercial building acoustic silencer. The performance enhancement with regard to transmission loss achieved by the acoustic-material solution was experimentally demonstrated through a comparison of the original and altered silencers. The following conclusions can be drawn from this study:

- Affordable 3D printing techniques can be utilised to produce fully customised acoustic materials that offer exceptional transmission loss at specific frequencies of interest. This enables the creation of highly effective custom-made solutions for superior acoustic performance.
- By combining 3D printed acoustic materials with traditional foam liners, it is possible to enhance the broadband characteristics of an acoustic system and target specific frequencies of interest. Furthermore, this approach allows for a more comprehensive optimisation of the silencer's functionality to achieve desired acoustic outcomes.
- This approach presents an opportunity for tailored improvements to off-the-shelf components, which can be rapidly designed and implemented in an industrial environment. In addition, it opens the possibility for effective optimisation of existing commercial components.
- The findings from this study indicate that while roughness proves advantageous in terms of normal incidence absorption, it can have a negative impact on transmission loss.

8.3 Research contribution

This thesis has provided a deeper insight into the impact of additive manufacturing on the acoustic properties of 3D printed materials. This first study has, for the first time, used multiple NDT techniques, including confocal microscopy and CT scanning, to examine the surface finish and the internal composition of an additively manufactured acoustic material. In addition, this work broadens the knowledge of the acoustic implications of 3D printing defects used to explain the observed mismatch between experimental curves of sound absorption of the same geometry produced using different additive manufacturing technologies.

The findings reported here shed new light on the potential of 3D printing defects, particularly surface roughness, to improve the performance of additively manufactured acoustic materials. This is the first study to update the 3D geometry of the numerical model of the idealised, smooth benchmark geometry with an authentic roughness pattern based on the confocal microscope measurements and numerically assess the impact of surface roughness using a direct, fully-coupled thermoviscous modelling approach.

This study has also been one of the first attempts to take advantage of 3D printing defects to design material enhancements. Previous research utilised the acoustic potential of microporosity of build material. In this study, artificially applied surface roughness was used to enhance the acoustic performance of the benchmark design.

This research has demonstrated practical applications of 3D printed materials for the acoustic performance enhancement of off-the-shell commercial components. In addition, these findings should also help other researchers design novel acoustic materials for noise and vibration control.

8.4 Suggestions for future work

Although manufacturing defects are unavoidable in 3D printing, the results presented in this thesis indicate that they can be utilised for acoustic improvements. Therefore, in the future, it will be crucial to use this knowledge when proposing new material designs.

This research has brought up many questions. For example, despite the fact that the knowledge of the acoustic influence of 3D printing defects has been widened, further work is required to develop more computationally efficient ways to incorporate those additive manufacturing features into numerical modelling. Further studies need to be carried out to improve the indirect modelling strategy utilising the fluid shell approach. More work also needs to be done on improving the design process so that the geometrical dimensions of the unit cell are optimised for maximum absorption or transmission loss.

A natural progression of this work is also to investigate the acoustic influence of the geometrical shape of artificial roughness used while designing novel porous materials. More research is needed to develop an optimal surface morphology that exploits the benefits of increased roughness while controlling for volume and surface area changes. Moreover, this roughened geometry could also be implemented in the off-the-shelf components, such as acoustic silencers, to enhance their performance further.

Bibliography

[1] European Parliament and the Council. Directive 2002/49/EC of the European Parliament and of the Council of 25 June 2002 relating to the assessment and management of environmental noise. *Official Journal*, L 189:12, 2002.

[2] European Environment Agency. Environmental noise in Europe, 2020. EEA Report 22/2019, Publications Office of the European Union, Luxembourg, 2020.

[3] G. Palma, H. Mao, L. Burghignoli, P. Göransson, and U. Iemma. Acoustic metamaterials in aeronautics. *Applied Sciences*, 8(6):971, 2018. ISSN 2076-3417. doi: 10.3390/app8060971.

[4] L. Y. L. Ang, Y. K. Koh, and H. P. Lee. Acoustic metamaterials: A potential for cabin noise control in automobiles and armored vehicles. *International Journal of Applied Mechanics*, 08(5):1650072, 2016. ISSN 1758-8251. doi: 10.1142/S1758825116500721.

[5] C. Bujoreanu and M. Benchea. Experimental study on HVAC sound parameters. *IOP Conference Series: Materials Science and Engineering*, 147:012051, 2016. ISSN 1757-8981, 1757-899X. doi: 10.1088/1757-899X/147/1/012051.

[6] L. Cherney, K. Neath. Understanding & Reducing Air System Noise. Technical report, AMCA International, Arlington Heights, IL, 2021.

[7] The Engineering Equipment and Materials Users Association. Silencers and acoustic enclosures. A guide to the selection and assessment. Edition 2. Technical Report 161, London, 2014.

[8] A. Srivastava. Elastic metamaterials and dynamic homogenization: a review. *International Journal of Smart and Nano Materials*, 6(1):41–60, 2015. ISSN 1947-5411. doi: 10.1080/19475411.2015.1017779.

[9] E. Barchiesi, M. Spagnuolo, and L. Placidi. Mechanical metamaterials: a state of the art. *Mathematics and Mechanics of Solids*, 24(1):212–234, 2019. ISSN 1081-2865. doi: 10.1177/1081286517735695.

[10] Q. Y. Lu and C. H. Wong. Additive manufacturing process monitoring and control by non-destructive testing techniques: challenges and in-process monitoring. *Virtual and Physical Prototyping*, 13(2):39–48, 2018. ISSN 1745-2759, 1745-2767. doi: 10.1080/17452759.2017.1351201.

[11] Energetics Incorporated. Measurement Science Roadmap for Metal-Based Additive Manufacturing. Workshop Summary Report, National Institute of Standards and Technology, Columbia, Maryland, 2013.

[12] S. A. Cummer, J. Christensen, and A. Alù. Controlling sound with acoustic metamaterials. *Nature Reviews Materials*, 1(3):16001, 2016. ISSN 2058-8437. doi: 10.1038/natrevmats.2016.1.

[13] J. Kennedy, L. Flanagan, L. Dowling, G. J. Bennett, H. Rice, and D. Trimble. The Influence of Additive Manufacturing Processes on the Performance of a Periodic Acoustic Metamaterial. *International Journal of Polymer Science*, 2019:e7029143, 2019. ISSN 1687-9422. doi: 10.1155/2019/7029143.

[14] T. G. Zieliński, K. C. Opiela, P. Pawłowski, N. Dauchez, T. Boutin, J. Kennedy, D. Trimble, H. Rice, B. Van Damme, G. Hannema, R. Wróbel, S. Kim, S. Ghaffari Mosanenzadeh, N. X. Fang, J. Yang, B. Briere de La Hosseraye, M. C.J. Hornikx, E. Salze, M.-A. Galland, R. Boonen, A. Carvalho de Sousa, E. Deckers, M. Gaborit, and J.-P. Groby. Reproducibility of sound-absorbing periodic porous materials using additive manufacturing technologies: Round robin study. *Additive Manufacturing*, 36:101564, 2020. doi: 10.1016/j.addma.2020.101564.

[15] L. C. Flanagan. *Modelling techniques to inform the design of sub-wavelength periodic acoustic structures*. PhD Thesis, Trinity College Dublin, 2022.

[16] D. Deery, L. Flanagan, G. O'Brien, H. J. Rice, and J. Kennedy. Efficient modelling of acoustic metamaterials for the performance enhancement of an automotive silencer. *Acoustics*, 4(2):329–344, 2022. doi: 10.3390/acoustics4020020.

[17] P.M. Morse and K.U. Ingard. *Theoretical Acoustics.* Princeton University Press, Princeton, New Jersey, 1 edition, 1986. ISBN 0-691-08425-4.

[18] A.D. Pierce. *Acoustics. An Introduction to Its Physical Principles and Applications.* Springer Cham, New York, 3 edition, 2019. ISBN 978-3-030-11213-4.

[19] ISO 10534-2:1998. Acoustics — Determination of sound absorption coefficient and impedance in impedance tubes — Part 2: Transfer-function method. European Standard, European Committee for Standardization, Brussels, Belgium, 1998.

[20] D. Deery, L. Flanagan, G. O'Brien, H. J. Rice, and J. Kennedy. Efficient modelling of acoustic metamaterials for the performance enhancement of an automotive silencer. *Acoustics*, 4(2):329–344, 2022. ISSN 2624-599X. doi: 10.3390/acoustics4020020.

[21] L. Flanagan, D. Heaphy, J. Kennedy, R. Leiba, and H. Rice. Development of acoustic "meta-liners" providing sub-wavelength absorption. *International Journal of Aeroacoustics*, 19(6):310–323, 2020. ISSN 1475-472X. doi: 10.1177/1475472X20954894.

[22] ASTM E2611-09. Standard Test Method for Measurement of Normal Incidence Sound Transmission of Acoustical Materials Based on the Transfer Matrix Method. Standard, ASTM International, West Conshohocken, PA, 2009.

[23] Aniwaa SAS. Prox dmp 200, (accessed June 6, 2023). URL `https://www.aniwaa.com/product/3d-printers/3d-systems-prox-dmp-200/`.

[24] H. Hoppen, H. Suresh, F. Langfeldt, W. Gleine, and O. v. Estorff. Impact of surface roughness on acoustic resonators made of closed-cell lightweight foams. In *27th International Congress on Sound and Vibration, ICSV 2021*, 2021. ISBN 978-83-7880-799-5.

[25] J.F. Ning and G.P. Zhao. A fractal study of sound propagation characteristics in roughened porous materials. *Wave Motion*, 68:190–201, 2017. ISSN 01652125. doi: 10.1016/j.wavemoti.2016.09.013.

[26] K. Sakagami, M. Kusaka, T. Okuzono, and S. Nakanishi. The effect of deviation due to the manufacturing accuracy in the parameters of an MPP on its acoustic properties: Trial production of MPPs of different hole shapes using 3d printing. *Acoustics*, 2(3): 605–616, 2020. doi: 10.3390/acoustics2030032.

[27] T. G. Zieliński, N. Dauchez, T. Boutin, M. Leturia, A. Wilkinson, F. Chevillotte, F.-X. Bécot, and R. Venegas. Taking advantage of a 3D printing imperfection in the development of sound-absorbing materials. *Applied Acoustics*, 197:108941, 2022. doi: 10.1016/j.apacoust.2022.108941.

[28] T. G. Zielinski, N. Dauchez, T. Boutin, M. Leturia, A. Wilkinson, F. Chevillotte, F.-X. Bécot, and R. Venegas. 3d printed sound-absorbing materials with double porosity. *INTER-NOISE and NOISE-CON Congress and Conference Proceedings*, 265(3):4100–4109, 2023. doi: 10.3397/IN_2022_0586.

[29] M. Vasina, K. Monkova, P. P. Monka, D. Kozak, and J. Tkac. Study of the sound absorption properties of 3d-printed open-porous ABS material structures. *Polymers*, 12 (5):1062, 2020. ISSN 2073-4360. doi: 10.3390/polym12051062.

[30] C. Zwikker and C.W. Kosten. *Sound absorbing materials.* Elsevier Publishing Company, New York, 1949. ISBN 978-0444406613.

[31] L. Cremer and H.A. Mueller. *Principle and Applications of Room Acoustics*, volume 2. Peninsula Publishing, Newport Beach, CA, 2016. ISBN 978-0932146304.

[32] J. F. Allard and N. Atalla. *Propagation of Sound in Porous Media: Modelling Sound Absorbing Materials.* John Wiley & Sons, Chichester, United Kingdom, 2 edition, 2009. ISBN 978-0-470-74661-5.

[33] M. Kleiner. *Acoustics and Audio Technology.* J. Ross Publishing, Inc., Fort Lauderdale, FL, 3 edition, 2012. ISBN 978-1-60427-052-5.

[34] L. Cao, Q. Fu, Y. Si, B. Ding, and J. Yu. Porous materials for sound absorption. *Composites Communications*, 10:25–35, 2018. ISSN 24522139. doi: 10.1016/j.coco.2018.05.001.

[35] H. Hassanpour Guilvaiee, F. Toth, and M. Kaltenbacher. A non-conforming finite element formulation for modeling compressible viscous fluid and flexible solid interaction. *International Journal for Numerical Methods in Engineering*, 123(24):6127–6147, 2022. ISSN 1097-0207. doi: 10.1002/nme.7106.

[36] H. Kuttruff. *Acoustics. An Introduction.* Taylor & Francis, Oxford, 2006. ISBN 0-203-97089-6.

[37] H. Kuttruff. *Room Acoustics*. Spon Press, London, 4 edition, 2000. ISBN 0-419-24580-4.

[38] F. van der Eerden. *Noise reduction with coupled prismatic tubes*. PhD Thesis, University of Twente, 2000.

[39] M. Hannink. *Acoustic resonators for the reduction of sound radiation and transmission*. PhD Thesis, University of Twente, 2007.

[40] X. Cai, Q. Guo, G. Hu, and J. Yang. Ultrathin low frequency sound absorbing panels based on coplanar spiral tubes or coplanar helmholtz resonators. *Applied Physics Letters*, 105(121901), 2014. doi: 10.10163/1.4895617.

[41] A. Chen, X. Zhao, Z. Yang, S. Anderson, and X. Zhang. Broadband labyrinthine acoustic insulator. *Physical Review Applied*, 18(064057), 2022. doi: 10.1103/PhysRevApplied.18.064057.

[42] B. Kim, S. Kim, Y. Park, M. Mieremet, H. Yang, J. Baek, and S. Choi. Development of a slit-type soundproof panel for a reduction in wind load and low-frequency noise with helmholtz resonators. *Applied Sciences*, 11(18), 2021. doi: 10.3390/app11188678.

[43] M.A. Temiz, I. Lopez Arteaga, G. Efraimsson, M. Abom, and A. Hirschberg. The influence of edge geometry on end-correction coefficients in micro-perforated plates. *Journal of the Acoustical Society of America*, 138:3668–3677, 2015. doi: 10.1121/1.4937748.

[44] A. Aulitto, A. Hirschberg, and I. Lopez Arteaga. Influence of geometry on acoustic end-corrections of slits in microslit absorbers. *Journal of the Acoustical Society of America*, 149:3073–3085, 2021. doi: 10.1121/10.0004826.

[45] R. Tayong, Th. Dupont, and Ph. Leclaire. Experimental investigation of holes interaction effect on the sound absorption coefficient of micro-perforated panels under high and medium sound levels. *Applied Acoustics*, 72:777–784, 2011. doi: 10.1016/j.apacoust.2011.04.011.

[46] J.-P. Groby, R. Pommier, and Y. Aurégan. Use of slow sound to design perfect and broadband passive sound absorbing materials. *Journal of the Acoustical Society of America*, 139:1660–1671, 2016. doi: 10.1121/1.4945101.

[47] A. J. Dell. *Low Frequency Attenuation of Sound with Acoustic Metamaterials.* PhD Thesis, The University of Sheffield, 2022.

[48] A. Aulitto. *Sound absorption mechanisms in perforated plates.* PhD Thesis, Eindhoven University of Technology, 2023.

[49] D. Y. Maa. Potential of microperforated panel absorber. *Journal of the Acoustical Society of America*, 104:2861–2866, 1998.

[50] J. Liu, H. Guo, and T. Wang. A review of acoustic metamaterials and phononic crystals. *Crystals*, 10(4), 2020. doi: https://doi.org/10.3390/cryst10040305.

[51] A. C. Hladky-Hennion and V. Romero-Garcia, editors. *Fundamentals and Applications of Acoustic Metamaterials: From Seismic to Radio Frequency*, volume 1. John Wiley & Sons, Hoboken, NJ, 2019. ISBN 978-1-119-64916-8.

[52] M. R. Haberman and M. D. Guild. Acoustic metamaterials. *Physics Today*, 69(6):42–48, 2016. ISSN 0031-9228. doi: 10.1063/PT.3.3198.

[53] S. Kumar and H. Pueh Lee. Recent advances in active acoustic metamaterials. *International Journal of Applied Mechanics*, 11(8):1950081, 2019. ISSN 1758-8251. doi: 10.1142/S1758825119500819.

[54] A. Gebhardt, J. Kessler, and L. Thurn. *3D Printing: Understanding Additive Manufacturing.* Carl Hanser Verlag GmbH & Co. KG, Munich, 2 edition, 2018. ISBN 978-1-56990-702-3 978-1-56990-703-0. doi: 10.3139/9781569907030.

[55] S.-H. Ahn, M. Montero, D. Odell, S. Roundy, and P. K. Wright. Anisotropic material properties of fused deposition modeling ABS. *Rapid Prototyping Journal*, 8(4):248–257, 2002. ISSN 1355-2546. doi: 10.1108/13552540210441166.

[56] Q. Ge, Z. Li, Z. Wang, K. Kowsari, W. Zhang, X. He, J. Zhou, and N. X. Fang. Projection micro stereolithography based 3d printing and its applications. *International Journal of Extreme Manufacturing*, 2(2):022004, 2020. ISSN 2631-7990. doi: 10.1088/2631-7990/ab8d9a.

[57] B. N. Turner, R. Strong, and S. A. Gold. A review of melt extrusion additive manufacturing processes: I. process design and modeling. *Rapid Prototyping Journal*, 20(3): 192–204, 2014. ISSN 1355-2546. doi: 10.1108/RPJ-01-2013-0012.

[58] B. N. Turner and S. A. Gold. A review of melt extrusion additive manufacturing processes: II. Materials, dimensional accuracy, and surface roughness. *Rapid Prototyping Journal*, 21(3):250–261, 2015. ISSN 1355-2546. doi: 10.1108/RPJ-02-2013-0017.

[59] 3D Natives. Everything you need to know about support structures in 3d printing, (accessed July 10, 2023). URL `https://www.3dnatives.com/en/support-structures-in-3d-printing-120420234/#!`

[60] C.A. Griffiths, J. Howarth, G. de-Almeida Rowbotham, and A. Rees. Effect of Build Parameters on Processing Efficiency and Material Performance in Fused Deposition Modelling. *Procedia CIRP*, 49:28–32, 2016. ISSN 22128271. doi: 10.1016/j.procir.2015.07.024.

[61] F. Rayegani and G. C. Onwubolu. Fused deposition modelling (FDM) process parameter prediction and optimization using group method for data handling (GMDH) and differential evolution (DE). *The International Journal of Advanced Manufacturing Technology*, 73(1), 2014. ISSN 0268-3768, 1433-3015. doi: 10.1007/s00170-014-5835-2.

[62] A. Bagsik and V. Schöppner. Mechanical Properties of Fused Deposition Modeling Parts Manufactured with ULTEM*9085. In *69th Annual Technical Conference of the Society of Plastics Engineers 2011 (ANTEC 2011)*, page 1294–1298, Boston, Massachusetts, USA, 2011.

[63] T.-M. Wang, J.-T. Xi, and Y. Jin. A model research for prototype warp deformation in the FDM process. *The International Journal of Advanced Manufacturing Technology*, 33(11):1087–1096, 2007. ISSN 0268-3768, 1433-3015. doi: 10.1007/s00170-006-0556-9.

[64] A. Peng and X. Xiao. Investigation on reasons inducing error and measures improving accuracy in fused deposition modeling. *International Journal on Advances in Information Sciences and Service Sciences*, 4(5):149–157, 2012. ISSN 1976-3700, 2233-9345. doi: 10.4156/aiss.vol4.issue5.18.

[65] D. Pollard, C. Ward, G. Herrmann, and J. Etches. Filament temperature dynamics in fused deposition modelling and outlook for control. *Procedia Manufacturing*, 11:536–544, 2017. ISSN 2351-9789. doi: 10.1016/j.promfg.2017.07.147.

[66] J. S. Chohan and R. Singh. Pre and post processing techniques to improve surface characteristics of FDM parts: a state of art review and future applications. *Rapid Prototyping Journal*, 23(3):495–513, 2017. ISSN 1355-2546. doi: 10.1108/RPJ-05-2015-0059.

[67] J. W. Stansbury and M. J. Idacavage. 3d printing with polymers: Challenges among expanding options and opportunities. *Dental Materials*, 32(1):54–64, 2016. ISSN 0109-5641. doi: 10.1016/j.dental.2015.09.018.

[68] D. M. Shah, Jo. Morris, T. A. Plaisted, A. V. Amirkhizi, and C. J. Hansen. Highly filled resins for DLP-based printing of low density, high modulus materials. *Additive Manufacturing*, 37:101736, 2021. ISSN 2214-8604. doi: 10.1016/j.addma.2020.101736.

[69] H. Kadry, S. Wadnap, C. Xu, and F. Ahsan. Digital light processing (DLP) 3d-printing technology and photoreactive polymers in fabrication of modified-release tablets. *European Journal of Pharmaceutical Sciences*, 135:60–67, 2019. ISSN 0928-0987. doi: 10.1016/j.ejps.2019.05.008.

[70] E. Moraru, D. Besnea, O. Dontu, G. I. Gheorghe, and Victor C. Applications of additive technologies in realization of customized dental prostheses. In G. I. Gheorghe, editor, *Proceedings of the International Conference of Mechatronics and Cyber-MixMechatronics – 2018*, Lecture Notes in Networks and Systems, pages 8–17, Cham, 2019. Springer International Publishing. ISBN 978-3-319-96358-7. doi: 10.1007/978-3-319-96358-7_2.

[71] W. Zhu, X. Ma, M. Gou, D. Mei, K. Zhang, and S. Chen. 3d printing of functional biomaterials for tissue engineering. *Current Opinion in Biotechnology*, 40:103–112, 2016. ISSN 0958-1669. doi: 10.1016/j.copbio.2016.03.014.

[72] A. D. Price. Photopolymerization of 3d conductive polypyrrole structures via digital light processing. In *Electroactive Polymer Actuators and Devices (EAPAD) 2016*, volume 9798, pages 216–222. SPIE, 2016. doi: 10.1117/12.2205918.

[73] M. Zarek, M. Layani, S. Eliazar, N. Mansour, I. Cooperstein, E. Shukrun, A. Szlar, D. Cohn, and S. Magdassi. 4d printing shape memory polymers for dynamic jewellery and fashionwear. *Virtual and Physical Prototyping*, 11(4):263–270, 2016. ISSN 1745-2759. doi: 10.1080/17452759.2016.1244085.

[74] C. Zhou, H. Ye, and F. Zhang. A novel low-cost stereolithography process based on vector scanning and mask projection for high-accuracy, high-speed, high-throughput, and large-area fabrication. *Journal of Computing and Information Science in Engineering*, 15(1), 2015. ISSN 1530-9827. doi: 10.1115/1.4028848.

[75] Prusa Research a.s. Types of printers and their differences, (accessed January 24, 2023). URL `https://help.prusa3d.com/article/types-of-printers-and-their-differences_112464#sla`.

[76] F. P. W. Melchels, J. Feijen, and D. W. Grijpma. A review on stereolithography and its applications in biomedical engineering. *Biomaterials*, 31(24):6121–6130, 2010. ISSN 0142-9612. doi: 10.1016/j.biomaterials.2010.04.050.

[77] Z.-c. Zhang, P.-l. Li, F.-t. Chu, and G. Shen. Influence of the three-dimensional printing technique and printing layer thickness on model accuracy. *Journal of Orofacial Orthopedics / Fortschritte der Kieferorthopädie*, 80(4):194–204, 2019. ISSN 1434-5293, 1615-6714. doi: 10.1007/s00056-019-00180-y.

[78] D. Wu, Z. Zhao, Q. Zhang, H. Qi, and D. Fang. Mechanics of shape distortion of DLP 3D printed structures during UV post – curing. *Soft Matter*, 15, 2019. doi: 10.1039/C9SM00725C.

[79] K. Mostafa, A. J. Qureshi, and C. Montemagno. Tolerance Control Using Subvoxel Gray-Scale DLP 3D Printing. In *ASME 2017 International Mechanical Engineering Congress and Exposition*, volume 2, Tampa, FL, 2017. American Society of Mechanical Engineers. ISBN 978-0-7918-5835-6. doi: 10.1115/IMECE2017-72232.

[80] P. F. Jacobs. Fundamentals of Stereolithography. In *Proceedings of the International Solid Freeform Fabrication Symposium*, pages 196–211, Valencia, CA, 1992. 3D Systems, Inc.

[81] P. J. Bártolo, editor. *Stereolithography: Materials, Processes and Applications*. Springer US, Boston, MA, 2011. ISBN 978-0-387-92903-3 978-0-387-92904-0. doi: 10.1007/978-0-387-92904-0.

[82] B. Steyrer, B. Busetti, G. Harakály, R. Liska, and J. Stampfl. Hot Lithography vs. room temperature DLP 3D-printing of a dimethacrylate. *Additive Manufacturing*, 21: 209–214, 2018. ISSN 2214-8604. doi: 10.1016/j.addma.2018.03.013.

[83] M. Monzón, Z. Ortega, A. Hernández, R. Paz, and F. Ortega. Anisotropy of Photopolymer Parts Made by Digital Light Processing. *Materials*, 10(1):64, 2017. ISSN 1996-1944. doi: 10.3390/ma10010064.

[84] Formlabs Inc. Introduction to post-curing prints, 2022 (accessed January 26, 2023). URL `https://support.formlabs.com/s/article/Introduction-to-Post-Curing-Prints?language=en_US`.

[85] A. Ferraro, M. Pirozzi, E. Annacondia, and L. D. Donato. Powder bed fusion/sintering machines: safety at workplaces. *Procedia Manufacturing*, 42:370–374, 2020. ISSN 2351-9789. doi: 10.1016/j.promfg.2020.02.061.

[86] Ltd. HANA AMT Co. SLM(PBF) -, (accessed January 27, 2023). URL `https://hanaamt.com/powder-production/slm-pbf/`.

[87] S. Sun, M. Brandt, and M. Easton. Powder bed fusion processes. In *Laser Additive Manufacturing*, pages 55–77. Elsevier, 2017. ISBN 978-0-08-100433-3. doi: 10.1016/B978-0-08-100433-3.00002-6.

[88] B. Ferrar, L. Mullen, E. Jones, R. Stamp, and C. J. Sutcliffe. Gas flow effects on selective laser melting (SLM) manufacturing performance. *Journal of Materials Processing Technology*, 212(2):355–364, 2012. ISSN 0924-0136. doi: 10.1016/j.jmatprotec.2011.09.020.

[89] N. T. Aboulkhair, N. M. Everitt, I. Ashcroft, and C. Tuck. Reducing porosity in AlSi10Mg parts processed by selective laser melting. *Additive Manufacturing*, 1-4:77–86, 2014. ISSN 2214-8604. doi: 10.1016/j.addma.2014.08.001.

[90] S. E. Brika, M. Letenneur, C. A. Dion, and V. Brailovski. Influence of particle morphology and size distribution on the powder flowability and laser powder bed fusion manufacturability of Ti-6Al-4V alloy. *Additive Manufacturing*, 31:100929, January 2020. ISSN 2214-8604. doi: 10.1016/j.addma.2019.100929.

[91] A. Boschetto, L. Bottini, L. Macera, and F. Veniali. Post-Processing of Complex SLM Parts by Barrel Finishing. *Applied Sciences*, 10(4):1382, 2020. ISSN 2076-3417. doi: 10.3390/app10041382.

[92] S. Rahmati and E. Vahabli. Evaluation of analytical modeling for improvement of surface roughness of FDM test part using measurement results. *The International Journal*

of Advanced Manufacturing Technology, 79(5-8):823–829, 2015. ISSN 0268-3768, 1433-3015. doi: 10.1007/s00170-015-6879-7.

[93] P. M. Pandey, V. R. Nallagundla, and S. G. Dhande. Slicing procedures in layered manufacturing: A review. *Rapid Prototyping Journal*, 9:274–288, 2003. doi: 10.1108/13552540310502185.

[94] S. Hällgren, L. Pejryd, and J. Ekengren. 3d data export for additive manufacturing - improving geometric accuracy. *Procedia CIRP*, 50:518–523, 2016. ISSN 2212-8271. doi: 10.1016/j.procir.2016.05.046.

[95] A. Barari, H. A. Kishawy, F. Kaji, and M. A. Elbestawi. On the surface quality of additive manufactured parts. *The International Journal of Advanced Manufacturing Technology*, 89(5):1969–1974, 2017. ISSN 1433-3015. doi: 10.1007/s00170-016-9215-y.

[96] B. Nourghassemi. *Surface roughness estimation for FDM systems.* Master's thesis, Toronto Metropolitan University, 2011.

[97] J. Khodaii and A. Rahimi. Improving the surface roughness in stereolithography by controlling surface angle, hatch spaces, and postcuring time. *Engineering Reports*, 2(6): e12193, 2020. ISSN 2577-8196. doi: 10.1002/eng2.12193.

[98] M. A. Melia, J. G. Duran, J. R. Koepke, D. J. Saiz, B. H. Jared, and E. J. Schindelholz. How build angle and post-processing impact roughness and corrosion of additively manufactured 316L stainless steel. *npj Materials Degradation*, 4(1):1–11, 2020. ISSN 2397-2106. doi: 10.1038/s41529-020-00126-5.

[99] M. K. Kim, I. H. Lee, and H.-C. Kim. Effect of fabrication parameters on surface roughness of FDM parts. *International Journal of Precision Engineering and Manufacturing*, 19(1):137–142, 2018. ISSN 2234-7593, 2005-4602. doi: 10.1007/s12541-018-0016-0.

[100] D. Ahn, J.-H. Kweon, S. Kwon, J. Song, and S. Lee. Representation of surface roughness in fused deposition modeling. *Journal of Materials Processing Technology*, 209(15):5593–5600, 2009. ISSN 0924-0136. doi: 10.1016/j.jmatprotec.2009.05.016.

[101] P. M. Pandey, N. V. Reddy, and S. G. Dhande. Improvement of surface finish by staircase machining in fused deposition modeling. *Journal of Materials Processing Technology*,

132(1):323–331, 2003. ISSN 0924-0136. doi: https://doi.org/10.1016/S0924-0136(02)00953-6.

[102] D. Greitemeier, C. Dalle Donne, F. Syassen, J. Eufinger, and T. Melz. Effect of surface roughness on fatigue performance of additive manufactured ti–6al–4v. *Materials Science and Technology*, 32(7):629–634, 2016. ISSN 0267-0836, 1743-2847. doi: 10.1179/1743284715Y.0000000053.

[103] K. Mumtaz and N. Hopkinson. Top surface and side roughness of inconel 625 parts processed using selective laser melting. *Rapid Prototyping Journal*, 15(2):96–103, 2009. doi: 10.1108/13552540910943397.

[104] A. Dolenc and I. Mäkelä. Slicing procedures for layered manufacturing techniques. *Computer-Aided Design*, 26(2):119–126, 1994. ISSN 00104485. doi: 10.1016/0010-4485(94)90032-9.

[105] E. Sabourin, S. A. Houser, and Jan Helge B. Adaptive slicing using stepwise uniform refinement. *Rapid Prototyping Journal*, 2(4):20–26, 1996. ISSN 1355-2546. doi: 10.1108/13552549610153370.

[106] J. Tyberg and J. Helge Bøhn. Local adaptive slicing. *Rapid Prototyping Journal*, 4(3):118–127, 1998. ISSN 1355-2546. doi: 10.1108/13552549810222993.

[107] A. Pino, J. Pladellorens, and J. Colom. Method of measure of roughness of paper based in the analysis of the texture of speckle pattern. *Proceedings of SPIE - The International Society for Optical Engineering*, 7387, 2010. doi: 10.1117/12.869655.

[108] C. Sahay and S. Ghosh. Understanding Surface Quality: Beyond Average Roughness (Ra). In *2018 ASEE Annual Conference & Exposition Proceedings*, page 31176. ASEE Conferences, 2018. doi: 10.18260/1-2--31176.

[109] T. C. Kone, R. Panneton, and T. Dupont. Thermo-visco-acoustic metamaterials to damp acoustic modes in a complex geometry. In *26th International Congress on Sound and Vibration 2019 (ICSV26)*, Montreal, Canada, 2019. Canadian Acoustical Association.

[110] A. Cortis and J. G. Berryman. Frequency-dependent viscous flow in channels with fractal rough surfaces. *Physics of Fluids*, 22(5):053603, 2010. ISSN 1070-6631, 1089-7666. doi: 10.1063/1.3407659.

[111] O. Umnova, K. Attenborough, H.-C. Shin, and A. Cummings. Deduction of tortuosity and porosity from acoustic reflection and transmission measurements on thick samples of rigid-porous materials. *Applied Acoustics*, 66(6):607–624, 2005. ISSN 0003682X. doi: 10.1016/j.apacoust.2004.02.005.

[112] M. R. Stinson and Y. Champoux. Propagation of sound and the assignment of shape factors in model porous materials having simple pore geometries. *The Journal of the Acoustical Society of America*, 91(2):685–695, February 1992. ISSN 0001-4966. Publisher: Acoustical Society of America.

[113] S. Y. Song, X. H. Yang, F. X. Xin, S. W. Ren, and T. J. Lu. Modeling of roughness effects on acoustic properties of micro-slits. *Journal of Physics D: Applied Physics*, 50 (23):235303, May 2017. ISSN 0022-3727. Publisher: IOP Publishing.

[114] K. Attenborough. Macro- and micro-structure designs for porous sound absorbers. *Applied Acoustics*, 145:349–357, February 2019. ISSN 0003-682X.

[115] K. Attenborough. Microstructures for lowering the quarter wavelength resonance frequency of a hard-backed rigid-porous layer. *Applied Acoustics*, 130:188–194, January 2018. ISSN 0003-682X.

[116] S. Song, X. Yang, F. Xin, and T. J. Lu. Modeling of surface roughness effects on Stokes flow in circular pipes. *Physics of Fluids*, 30(2):023604, 2018. ISSN 1070-6631, 1089-7666. doi: 10.1063/1.5017876.

[117] Z. Xu, X. Peng, X. Liu, F. Xin, and T. J. Lu. Modified theory of a microperforated panel with roughened perforations. *EPL (Europhysics Letters)*, 125(3):34004, 2019. ISSN 1286-4854. doi: 10.1209/0295-5075/125/34004.

[118] M. Duan, C. Yu, Z. Xu, F. Xin, and T. J. Lu. Acoustic impedance regulation of helmholtz resonators for perfect sound absorption via roughened embedded necks. *Applied Physics Letters*, 117(15):151904, 2020. doi: 10.1063/5.0024804.

[119] B. Msallem, N. Sharma, S. Cao, F. S. Halbeisen, H.-F. Zeilhofer, and F. M. Thieringer. Evaluation of the dimensional accuracy of 3d-printed anatomical mandibular models using FFF, SLA, SLS, MJ, and BJ printing technology. *Journal of Clinical Medicine*, 9 (3):817, 2020. ISSN 2077-0383. doi: 10.3390/jcm9030817.

[120] M. Chung, N. Radacsi, C. Robert, E. D. McCarthy, A. Callanan, N. Conlisk, P. R. Hoskins, and V. Koutsos. On the optimization of low-cost FDM 3d printers for accurate replication of patient-specific abdominal aortic aneurysm geometry. *3D Printing in Medicine*, 4(1):2, 2018. ISSN 2365-6271. doi: 10.1186/s41205-017-0023-2.

[121] A. Bellini, S. Guceri, and M. Bertoldi. Liquefier dynamics in fused deposition. *Journal of Manufacturing Science and Engineering*, 126(2):237–246, 2004. ISSN 1087-1357. doi: 10.1115/1.1688377.

[122] U. M. Dilberoglu, S. Simsek, and U. Yaman. Shrinkage compensation approach proposed for ABS material in FDM process. *Materials and Manufacturing Processes*, 34(9):993–998, 2019. ISSN 1042-6914, 1532-2475. doi: 10.1080/10426914.2019.1594252.

[123] D. Karalekas and A. Aggelopoulos. Study of shrinkage strains in a stereolithography cured acrylic photopolymer resin. *Journal of Materials Processing Technology*, 136(1): 146–150, 2003. ISSN 0924-0136. doi: 10.1016/S0924-0136(03)00028-1.

[124] A. du Plessis, S. M. J. Razavi, and F. Berto. The effects of microporosity in struts of gyroid lattice structures produced by laser powder bed fusion. *Materials & Design*, 194: 108899, 2020. ISSN 0264-1275.

[125] K. Chin Ang, K. Fai Leong, C. Kai Chua, and M. Chandrasekaran. Investigation of the mechanical properties and porosity relationships in fused deposition modelling-fabricated porous structures. *Rapid Prototyping Journal*, 12(2):100–105, 2006. ISSN 1355-2546. doi: 10.1108/13552540610652447.

[126] X. Wang, L. Zhao, J. Y. H. Fuh, and H. P. Lee. Effect of porosity on mechanical properties of 3d printed polymers: Experiments and micromechanical modeling based on x-ray computed tomography analysis. *Polymers*, 11(7):1154, 2019. ISSN 2073-4360. doi: 10.3390/polym11071154.

[127] F. Zhang, Y. Ma, J. Liao, V. Breedveld, and R. P. Lively. Solution-based 3d printing of polymers of intrinsic microporosity. *Macromolecular Rapid Communications*, 39(13): 1800274, 2018. ISSN 1521-3927. doi: 10.1002/marc.201800274.

[128] J. P. Oliveira, A. D. LaLonde, and J. Ma. Processing parameters in laser powder bed fusion metal additive manufacturing. *Materials & Design*, 193:108762, 2020. ISSN 0264-1275. doi: 10.1016/j.matdes.2020.108762.

[129] R. Sailesh, L. Yuvaraj, J. Pitchaimani, M. Doddamani, and L. B. Mailan Chinnapandi. Acoustic behaviour of 3d printed bio-degradable micro-perforated panels with varying perforation cross-sections. *Applied Acoustics*, 174:107769, 2021. doi: 10.1016/j.apacoust.2020.107769.

[130] J. Boulvert, J. Costa-Baptista, T. Cavalieri, M. Perna, E. R. Fotsing, V. Romero-García, G. Gabard, A. Ross, J. Mardjono, and J.-P. Groby. Acoustic modeling of micro-lattices obtained by additive manufacturing. *Applied Acoustics*, 164:107244, 2020. doi: 10.1016/j.apacoust.2020.107244.

[131] S. Kumar, T. B. Xiang, and H. P. Lee. Ventilated acoustic metamaterial window panels for simultaneous noise shielding and air circulation. *Applied Acoustics*, 159:107088, 2020-02. doi: 10.1016/j.apacoust.2019.107088.

[132] J. Carbajo, J.M. Molina-Jordá, L.P. Maiorano, and N.X. Fang. Sound absorption of macro-perforated additively manufactured media. *Applied Acoustics*, 182:108204, 2021. doi: 10.1016/j.apacoust.2021.108204.

[133] G. do N. Almeida, E. F. Vergara, L. R. Barbosa, and R. Brum. Low-frequency sound absorption of a metamaterial with symmetrical-coiled-up spaces. *Applied Acoustics*, 172: 107593, 2021. doi: 10.1016/j.apacoust.2020.107593.

[134] K. P. Zhang, Y. F. Liao, B. Qiu, Y. K. Zheng, L. K. Yu, G. H. He, Q. N. Chen, and D. H. Sun. 3D Printed Embedded Metamaterials. *Small*, 17(50):2103262, 2021. ISSN 1613-6810, 1613-6829. doi: 10.1002/smll.202103262.

[135] T. G. Zieliński, F. Chevillotte, and E. Deckers. Sound absorption of plates with micro-slits backed with air cavities: Analytical estimations, numerical calculations and experimental validations. *Applied Acoustics*, 146:261–279, 2019. ISSN 0003682X. doi: 10.1016/j.apacoust.2018.11.026.

[136] J. Boulvert, T. Cavalieri, V. Romero-García, G. Gabard, and J.-P. Groby. Optimization of 3D printed porous materials accounting for manufacturing defects. *INTER-NOISE and NOISE-CON Congress and Conference Proceedings*, 263(3):3143–3148, 2021. doi: 10.3397/IN-2021-2314.

[137] M. Papanikolaou, M. Frank, and D. Drikakis. Effects of surface roughness on shear viscosity. *Physical Review E*, 95(3):033108, 2017. ISSN 2470-0045, 2470-0053. doi: 10.1103/PhysRevE.95.033108.

[138] L. Lei, N. Dauchez, and J. D. Chazot. Prediction of the six parameters of an equivalent fluid model for thermocompressed glass wools and melamine foam. *Applied Acoustics*, 139:44–56, 2018. ISSN 0003-682X. doi: 10.1016/j.apacoust.2018.04.010.

[139] T. G. Zieliński, R. Venegas, C. Perrot, M. Červenka, F. Chevillotte, and K. Attenborough. Benchmarks for microstructure-based modelling of sound absorbing rigid-frame porous media. *Journal of Sound and Vibration*, 483:115441, 2020. ISSN 0022-460X. doi: 10.1016/j.jsv.2020.115441.

[140] T. G. Zielinski, N. Dauchez, T. Boutin, F. Chevillotte, F.-X. Bécot, and R. Venegas. 3d printed axisymmetric sound absorber with double porosity. In *30th ISMA conference on Noise and Vibration Engineering*, page 15, 2022.

[141] K. C. Opiela, T. G. Zieliński, and K. Attenborough. Predicting sound absorption in additively manufactured microporous labyrinthine structures. In *30th ISMA conference on Noise and Vibration Engineering*, page 10, 2022.

[142] K.R. Rajagopal. A new development and interpretation of the navier–stokes fluid which reveals why the “stokes assumption” is inapt. *International Journal of Non-Linear Mechanics*, 50:141–151, 2013. ISSN 00207462. doi: 10.1016/j.ijnonlinmec.2012.10.007.

[143] G. Buresti. A note on stokes’ hypothesis. *Acta Mechanica*, 226(10):3555–3559, 2015. ISSN 0001-5970, 1619-6937. doi: 10.1007/s00707-015-1380-9.

[144] COMSOL. Acoustics module user’s guide. version: Comsol 5.4, 2018 (accessed November 28, 2023). `https://doc.comsol.com/5.4/doc/com.comsol.help.aco/AcousticsModuleUsersGuide.pdf`.

[145] Y. Wu, Qingxuan L., J. He, J. Feng, and T. Chen. Deep-subwavelength broadband sound absorbing metasurface based on the update finger coiling-up method. *Applied Acoustics*, 195:108846, 2022. ISSN 0003682X. doi: 10.1016/j.apacoust.2022.108846.

[146] L. D. Landau and E. Lifshitz. *Fluid Mechanics*, volume 6 of *Course of Theoretical Physics*. Pergamon Press, Oxford, UK, 2 edition, 1987. ISBN 9781483161044.

[147] M. J. Lighthill. *Waves in Fluids*. Cambridge University Press, Cambridge, UK, 1978. ISBN 0521216893.

[148] R. Billard, G. Tissot, G. Gabard, and M. Versaevel. Numerical simulations of perforated plate liners: Analysis of the visco-thermal dissipation mechanisms. *The Journal of the Acoustical Society of America*, 149(1):16–27, 2021. ISSN 0001-4966. doi: 10.1121/10.0002973.

Appendix A

Air properties

A.1 Air properties

The air parameters used in all numerical and analytical models in this thesis are listed in Table A.1.

Variable	Name	Value	Unit
T_0	Ambient temperature	293.15	K
p_0	Atmospheric pressure	101325	Pa
c_0	Speed of sound	343	m/s
ρ_0	Density	1.20	kg/m^3
μ_0	Dynamic viscosity	$1.825e$-5	Pa·s
μ_b	Bulk viscosity	0	Pa·s
C_p	Heat capacity at constant pressure	1007	$\mathrm{J/(kg \cdot K)}$
k	Thermal conductivity	0.02514	$\mathrm{W/(m \cdot K)}$
γ	Ratio of specific heats	1.4	1
Pr	Prandtl number	0.72	1

Table A.1: Properties of air in all models

Appendix B

Mesh independence study

B.1 Smooth and rough geometries (neglected roughness on side channels)

Figure B.1 illustrates original rough geometries used for the mesh convergence study. Originally, the roughness of the side channels was neglected, and these side cylinders were created with a smooth surface finish. This decision was made because of the main interest in the effect of the surface roughness on the air propagation in the z-direction, i.e. along the material thickness, and the limitations of the computational power to generate and solve such models.

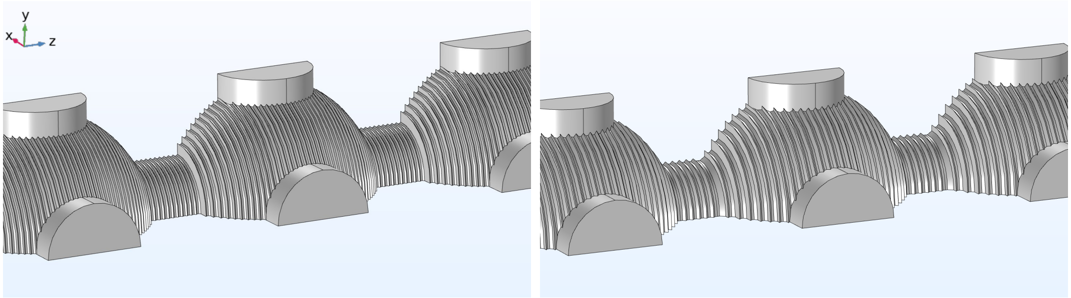

(a) 0.10 mm LH (b) 0.15 mm LH

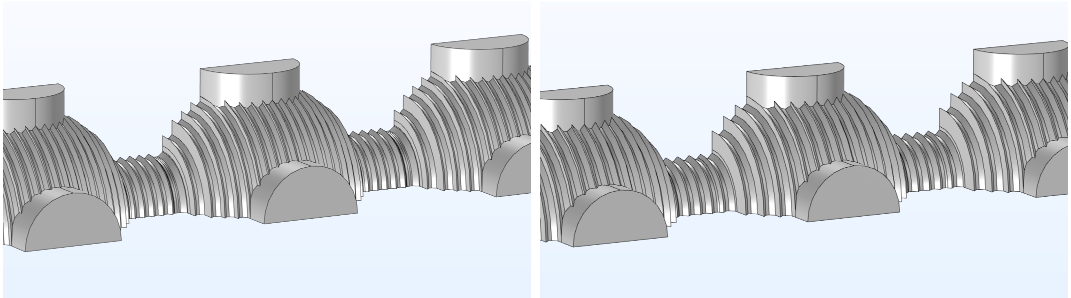

(c) 0.20 mm LH (d) 0.25 mm LH

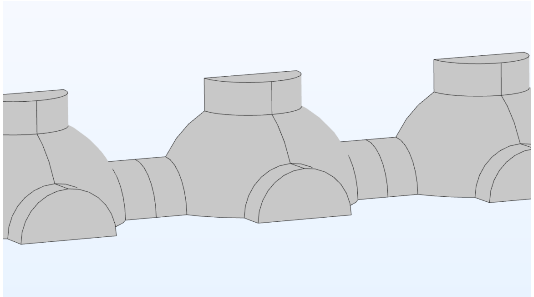

(e) Smooth

Figure B.1: FEM model geometry comparison with smooth and rough surface finish (the surface roughness of the side channels is ignored here; cf. Figure 5.5, where the side channels are rough)

B.2 Mesh independence study

The mesh data of the DENORMS geometry with smooth and rough surfaces shown in Figure B.1 are summarised in Table B.1. Only the three densest meshes are presented. Meshes No. 2 shows sufficient convergence; therefore, this type of meshes (i.e. with a density of this order) was selected for further calculations.

Layer height (LH)	Parameter	Mesh 1	**Mesh 2**	Mesh 3
Smooth	Degrees of freedom	623087	**759585**	1445023
	Frequency [Hz]	2050	**2050**	2050
	α	0.47706	**0.47355**	0.46952
0.10 mm	Degrees of freedom	1806812	**6424023**	16260040
	Frequency [Hz]	1950	**1950**	1950
	α	0.5418	**0.5299**	0.52963
0.15 mm	Degrees of freedom	2080749	**6604091**	16260040
	Frequency [Hz]	1950	**1950**	1950
	α	0.5411	**0.53731**	0.5370
0.20 mm	Degrees of freedom	2839260	**5285220**	11708458
	Frequency [Hz]	1900	**1900**	1900
	α	0.5926	**0.5913**	0.5895
0.25 mm	Degrees of freedom	1720705	**5130150**	9619616
	Frequency [Hz]	1850	**1850**	1850
	α	0.6304	**0.6244**	0.6235

Table B.1: Mesh independence study of DENORMS smooth and rough cell models (neglected roughness on side channels)

The parameters of the converged meshes for every layer height are summarised in Table B.2. α is the sound absorption coefficient found at the peak frequency.

B.3 Roughness of side channels

The parameters of the converged meshes were then used to create meshes for rough geometries with included roughness of side channels, shown in Figure 5.5. The final mesh data is outlined in Table 5.1. The viscous boundary layer thickness was used as a meshing parameter in the simulations considered in this study. The meshes comprised tetrahedral elements for the bulk and sweep elements for the boundary layer.

Layer height (LH)	Parameter	Value
Smooth (i.e. LH = 0 mm)	Maximum element size	0.00122 m
	Minimum element size	5.7E-3 m
	Maximum element growth rate	1.5
	Curvature factor	0.2
	Resolution of narrow regions	1
	Degrees of freedom	759585
	Frequency [Hz]	2050
	α	0.47355
0.10 mm	Maximum element size	0.000895 m
	Minimum element size	6.5E-5 m
	Maximum element growth rate	1.3
	Curvature factor	0.3
	Resolution of narrow regions	0.7
	Degrees of freedom	8687633
	Frequency [Hz]	1950
	α	0.53651
0.15 mm	Maximum element size	0.00179 m
	Minimum element size	1.3E-4 m
	Maximum element growth rate	1.4
	Curvature factor	0.4
	Resolution of narrow regions	0.7
	Degrees of freedom	8177212
	Frequency [Hz]	1950
	α	0.55384
0.20 mm	Maximum element size	0.00114 m
	Minimum element size	4.88E-5 m
	Maximum element growth rate	1.35
	Curvature factor	0.3
	Resolution of narrow regions	0.85
	Degrees of freedom	6671377
	Frequency [Hz]	1900
	α	0.6017
0.25 mm	Maximum element size	0.00114 m
	Minimum element size	4.88E-5
	Maximum element growth rate	1.35
	Curvature factor	0.3
	Resolution of narrow regions	0.85
	Degrees of freedom	5977069
	Frequency [Hz]	1850
	α	0.63755

Table B.2: Converged mesh (Mesh 2) data of DENORMS designs with smooth and rough surfaces (in the latter case for different layer heights)

Appendix C

Bulk viscosity influence

C.1 Introduction

The analysis of fluid flows commonly involves solving the Navier–Stokes equation, with one of its fundamental assumptions being Stokes' hypothesis. In the context of a Newtonian fluid, Stokes' hypothesis assumes the bulk viscosity μ_b to be zero, suggesting that all losses are primarily associated with shearing.

There are varying opinions on the appropriate value of the bulk viscosity μ_b. In this thesis and other works [32], the bulk viscosity is neglected and set to zero. However, according to other authors, in some situations, bulk viscosity effects are not negligible [142, 143]. The Thermoviscous Acoustics module within COMSOL assumes, by default, the bulk viscosity to be $\mu_b = 0.6 \times \mu$ for air [144]. Bulk viscosity is a measure of a fluid's resistance to volume change. Therefore, incorporating it into the model should represent supplementary losses that govern sound attenuation within the system [15].

Hence, both approaches are considered valid for modelling purposes, and the influence of the chosen bulk viscosity value on the sound absorption coefficient will be investigated in this Appendix.

C.2 Numerical model setup

In this investigation, two different models of six layers of the DENORMS unit cell were taken into account. First, it was the initial smooth model of benchmark geometry, as per Figure 4.17. Second, it was the rough model with the 0.25 mm LH pattern applied to its surfaces, as per Figure 5.5d.

Two configurations of the numerical models were considered. In the first arrangement, all air properties were set according to Table A.1 with the bulk viscosity μ_b set to zero and, therefore, neglected. In the second configuration, all these values were kept unchanged, except for the bulk viscosity set to $\mu_b = 0.6 \times \mu$.

C.3 Results and discussion

The effects of the chosen bulk viscosity value are summarised in Figure C.1. The numerical incorporation of bulk viscosity does not appear to change the shape of the sound absorption curve or increase its magnitude significantly. For the smooth unit cell, a small rise in the peak value can be observed for the $\mu_b = 0.6 \times \mu$ model in comparison to the $\mu_b = 0$ model, which can be explained by the inclusion of additional losses. In the case of the rough unit cell, the results of both models are almost identical. The difference between these two curves ($\mu_b = 0.6 \times \mu$ and $\mu_b = 0$) is of 10^{-6} to 10^{-4} order of magnitude.

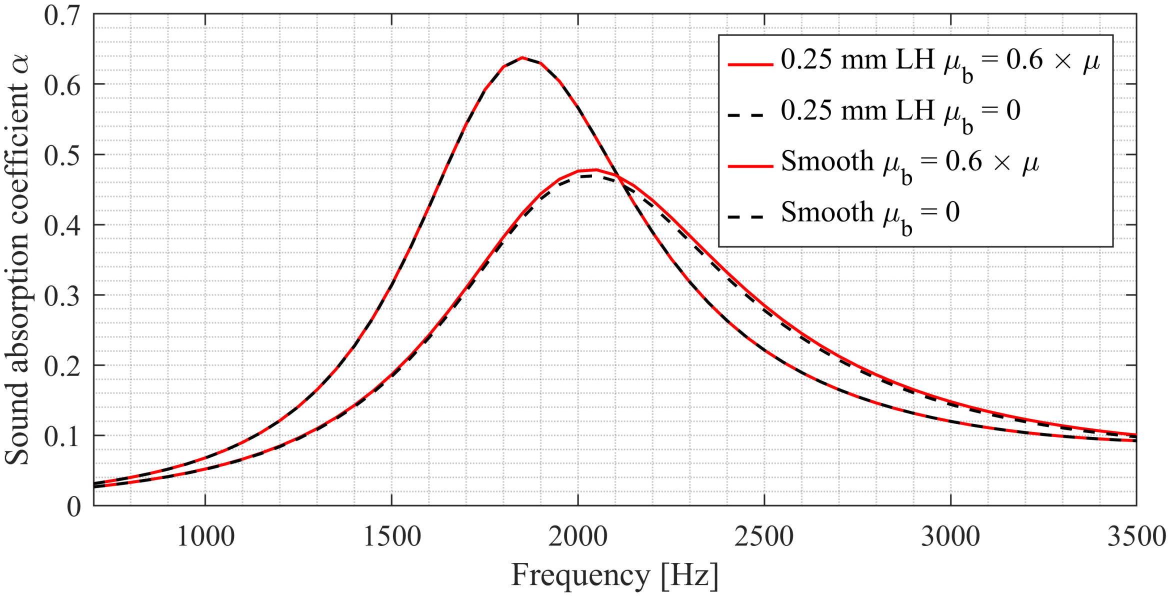

Figure C.1: Influence of bulk viscosity on sound absorption coefficient for six layers of smooth and rough DENORMS unit cells

These findings validate the justification for excluding bulk viscosity in the numerical modelling approach employed in this thesis.

Appendix D

Quality improvement of FDM parts

D.1 Introduction

Extrusion-based additive manufacturing remains the most popular 3D printing technology researchers use for novel acoustic material development. Among all the studies discussed in Section 3.3, the benchmark design DENORMS was the only structure to be manufactured not only using FDM but also via more complex and costly photopolymerisation- and PBF-based techniques. Several factors that contributed to the success and popularity of FDM include: low operating costs, a wide range of print materials and easy handling of non-toxic waste.

For that reason, extrusion-based 3D printing is a suitable choice for the initial prototyping stage of acoustic material development. After optimising the geometrical design, the parts should be manufactured using printing materials suitable for real-world applications in the automotive or aerospace industry to produce fully functional parts. Those materials should be high temperature resistant and be characterised by high impact strength. Photopolymer resins fulfilling those criteria are available on the market. Metal powders are also clearly a suitable material choice.

In extrusion-based additive manufacturing, produced parts suffer from low geometric accuracy and surface roughness as the nozzle size and the precision of the extruder movements determine the print resolution. The quality of 3D printed parts can; however, be improved. The following sections will discuss two major approaches, process parameter optimisation and post-processing. All samples considered in this study were manufactured using Prusa Mini FDM 3D printer.

D.2 Parameter optimization

The quality of additively manufactured parts can be improved by adjusting the default printing parameters before production. The general settings recommended by the 3D printer's manufacturer are calibrated for generic, large-scale objects and may not be suitable for the production of complex microstructures, such as metamaterials.

This appendix is based on a conference paper: A. Ciochon, J. Kennedy, "Practical guidance on the additive manufacturing of acoustic materials", in 52nd International Congress and Exposition on Noise Control Engineering (INTER-NOISE 2023), Chiba, Greater Tokyo, Japan, Aug. 2023

The original cylindrical samples, described in detail in Section 4.2, were manufactured using default printing parameters. Several NDT techniques were used for quality control, as per Section 4.3. Except for surface roughness occurring due to the staircase effect, thoroughly investigated in Chapter 5 and Chapter 6, produced parts were heavily affected by the issue of filament fibres trapped in the cavities.

All samples considered in this study, printed with default and altered process settings, were manufactured using the same Verbatim PLA filament.

D.2.1 Pre-processing

Parameter	Default value	New value
FILAMENT SETTINGS		
Extruder temperature	215°C	195°C
PRINT SETTINGS		
Perimeters printing speed	50 mm/s	40 mm/s
PRINTER SETTINGS		
Retraction length	3.2 mm	2 mm
Retraction lift z	0.2 mm	0 mm
Retraction speed	70 mm/s	50 mm/s
Deretraction speed	40 mm/s	30 mm/s

Table D.1: Default and altered 3D printing parameters

To improve the quality of FDM parts and eliminate the issue of filament stringing, several default printing parameters were adjusted in the slicing software PrusaSlicer. Multiple 3D printing attempts were performed to establish their optimal values. The comparison between the default and altered values of the adjusted parameters is summarised in Table D.1. Moreover, the ‘Avoid crossing perimeters’ feature was enabled. The filament was also put inside a dry box to minimise the possible negative impact of the room temperature and humidity.

D.2.2 Additive manufacturing

Standard layer heights were used during the fabrication of parts: 0.10, 0.15, 0.20 and 0.25 mm. For each of the chosen layer heights, three cylindrical samples were manufactured to account for the repeatability of the additive manufacturing process. Each of these samples corresponded to a six-cell deep array.

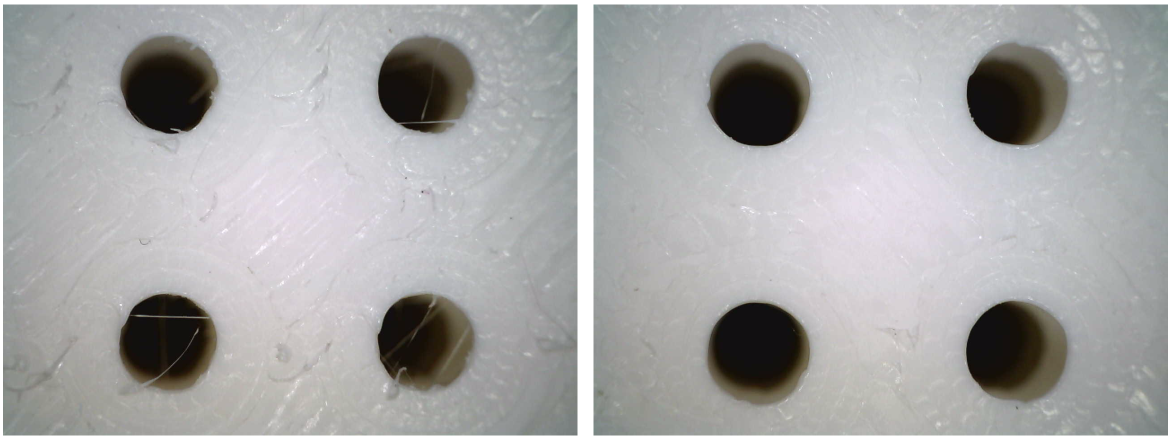

(a) Default printing parameters (b) Altered printing parameters

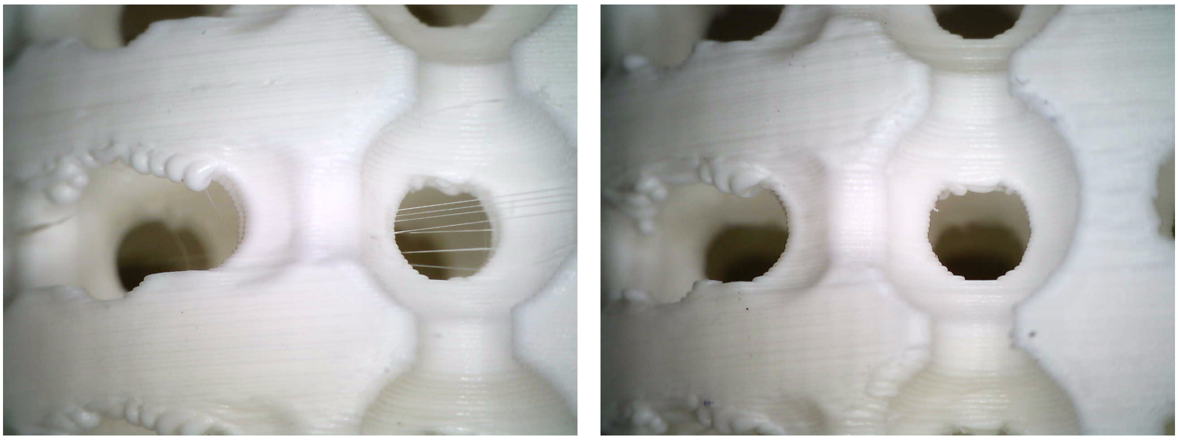

(c) Default printing parameters (d) Altered printing parameters

Figure D.1: Samples manufactured with different 3D printing parameters

Visual inspection

Samples produced with altered 3D printing parameters were inspected using a digital microscope and compared against samples manufactured with default settings. Figure D.1 illustrates the difference between the quality of DENORMS cylinders manufactured with two types of considered settings. As seen from the figures, altering the parameters improved the quality of samples and eliminated the stringing issue.

D.2.3 Acoustic evaluation

A combination of numerical and experimental techniques was applied in this study to perform the acoustic analysis. The assessment was carried out by comparing the numerical results of a smooth idealised DENORMS geometry with the experimental results of DENORMS samples manufactured using FDM with default and altered 3D printing parameters.

D.2.4 Results and discussion

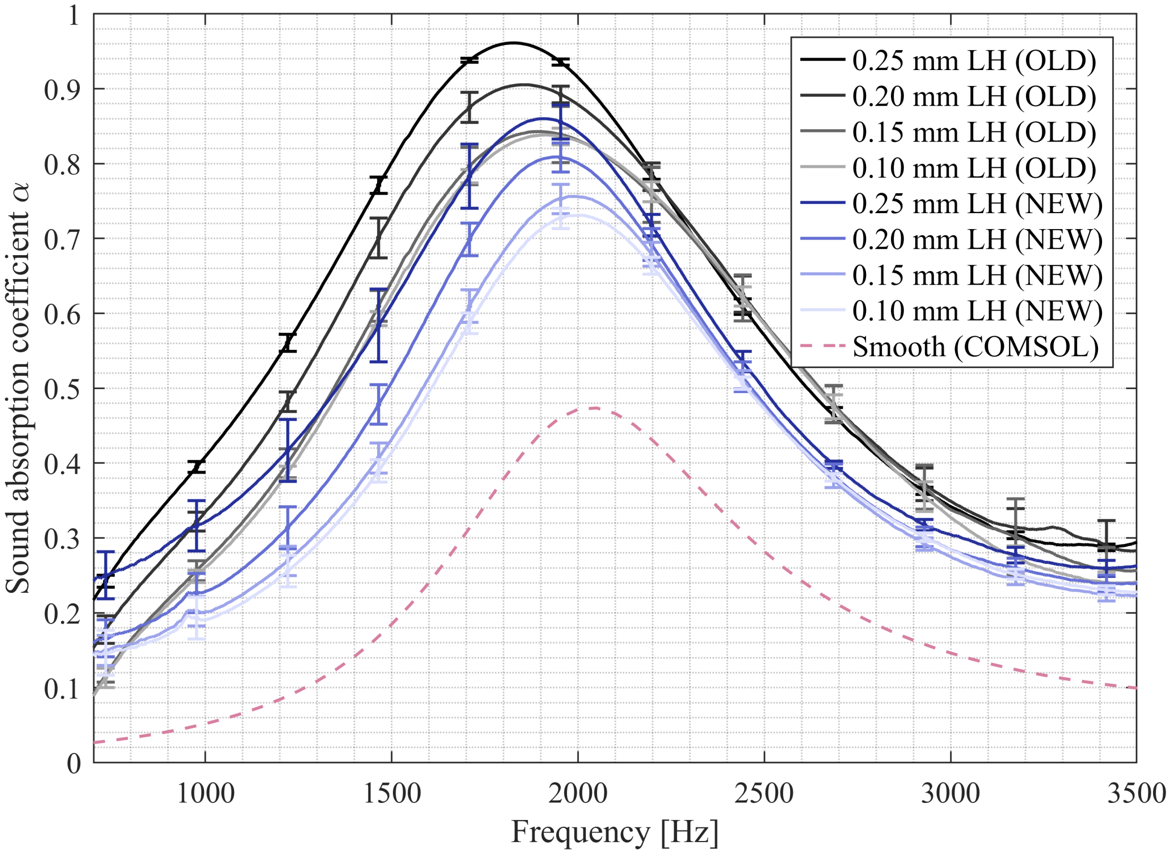

Figure D.2: Experimental and numerical results of the sound absorption coefficient

Figure D.2 presents the experimental results of FDM samples produced with different layer heights using default and altered printing parameters and compares against the numerical results of the smooth, idealised DENORMS geometry. It is apparent from this figure that improving the quality of samples by eliminating the filament stringing issue decreased excessive sound absorption. The altered samples shifted closer to the numerical prediction. Moreover, the shape of the experimental curves changed and began to resemble the shape of the numerical curve more, especially in the lower frequency region. However, even with this quality improvement, there is still a significant difference in the magnitude of absorption between experimental and numerical results. Nevertheless, simple adjustment of printing parameters (lowering printing speeds, decreasing extruder temperature) notably improved the coherence between numerical and experimental results.

D.3 Post-processing

Post-processing of produced samples is another approach to improving the quality in additive manufacturing. The rough surface finish of FDM parts can be diminished by various smoothing procedures. However, in the case of complex microstructures, applying vapours is the most suitable method.

Extrusion-based additive manufacturing technologies are commonly used at home, often for hobby purposes. However, very few commercial vapour smoothing machines exist on the market, and they can be expensive. For that reason, hobbyists and 3D printing enthusiasts developed alternative do-it-yourself solutions. Self-made vapour smoothing systems utilise acetone to melt the outer surfaces of ABS parts. In this method, the 3D printed part is placed on a raised platform in an enclosed container made of material that will not dissolve upon contact with acetone, such as glass or polypropylene. In the next step, tissue papers, which have been soaked in acetone, are placed inside the box. The container is then closed, but not fully sealed, to prevent potential hazards resulting from the pressure buildup. The smoothing occurs inside the chamber, and the part is taken out when it reaches the desired smoothness level.

Heat and air circulation should be introduced for this post-processing method to efficiently reach and smooth the inner parts of complex microstructures. This can be achieved by adding a fan inside the container. Unfortunately, this solution presents another fire hazard. For that reason, in this investigation, a mid-range commercial desktop post-processing machine, Polysher, was used to improve the surface quality of additively manufactured samples. Polysher creates a fine mist of isopropyl alcohol to smoothen out parts produced using compatible filaments developed by Polymaker, PolySmooth.

D.3.1 Additive manufacturing

DENORMS benchmark design was manufactured using the 0.15 mm layer height, PolySmooth teal filament, and altered, optimised printing parameters, as per Appendix D.2. Three cylindrical samples were produced. Two were chosen for post-processing, and one was supposed to be the control sample to assess the efficiency of vapour smoothing. Each of these cylinders corresponded to a six-cell deep array. Additionally, two halves of the DENORMS sample were manufactured separately to investigate the depth of the vapour penetration.

Visual inspection

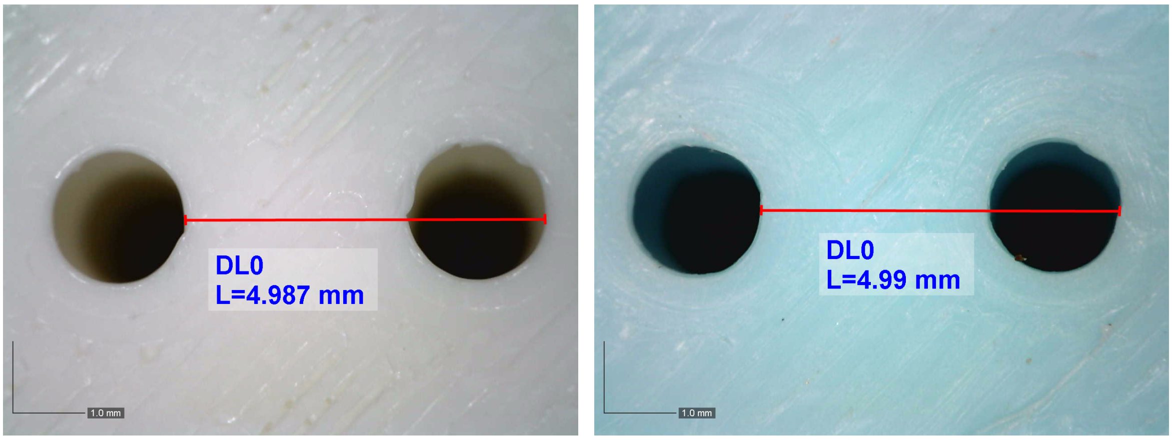

(a) PLA (b) PolySmooth

Figure D.3: Raw 0.15 mm layer height samples produced with same optimised settings using the same Prusa Mini FDM printer

The raw PolySmooth sample was visually compared with the PLA sample to establish whether filament change affected dimensional accuracy. Digital microscope pictures of the tops of both cylindrical samples showed Figure D.3 illustrate that no significant change occurred.

D.3.2 Post-processing method

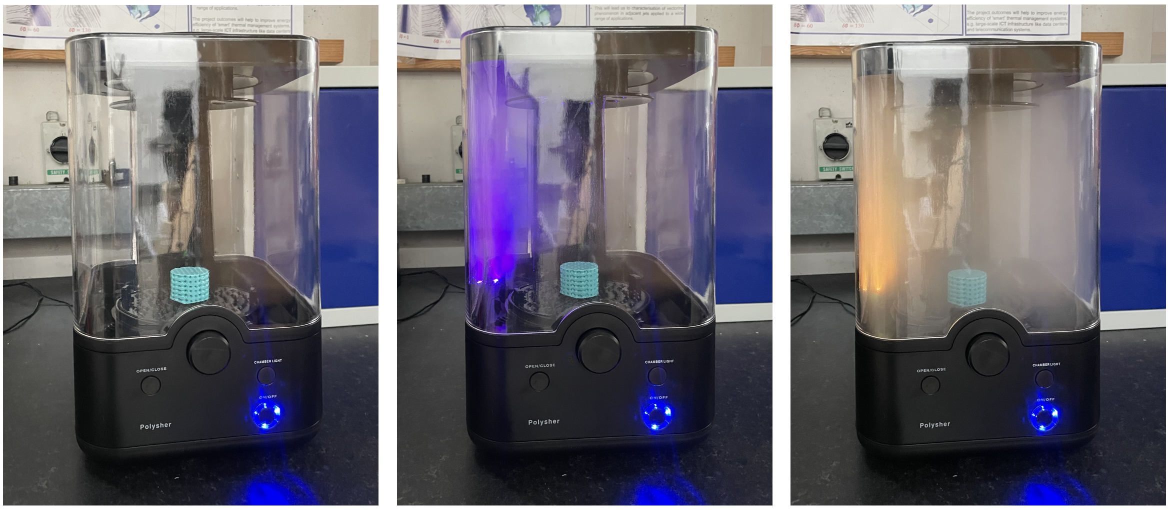

(a) (b) (c)

Figure D.4: Post-processing of FDM parts via vapour smoothing

The vapour smoothing procedure is shown in Figure D.4. The DENORMS cylinder was first placed inside Polysher (Figure D.4a). Next, the nebuliser created an alcohol mist and distributed it inside the chamber (Figure D.4b). The part placed on a rotating platform was exposed to the effect of the vapour for a duration of 40 minutes, as recommended by the machine's manufacturer (Figure D.4c). After the cycle was completed, the polished sample was left to dry and solidify.

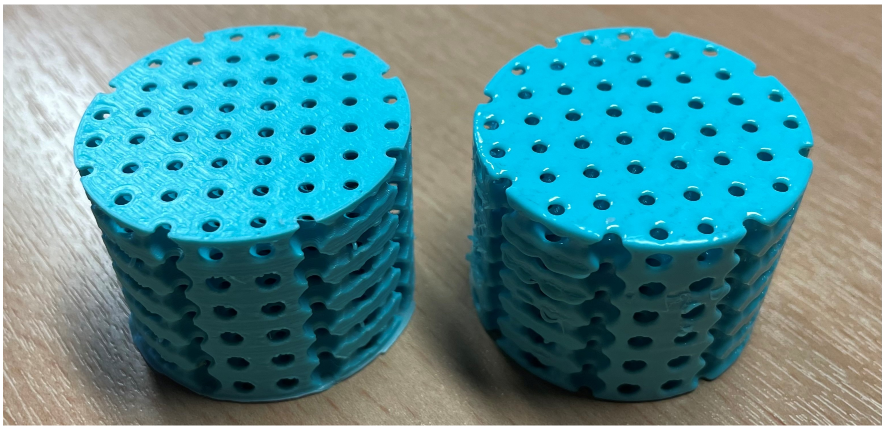

Figure D.5: Comparison between raw (on the left side) and post-processed (on the right side) FDM part

Visual comparison between the raw and post-processed samples is illustrated in Figure D.5. Figure D.6 compares the inner surface finish of both parts more thoroughly.

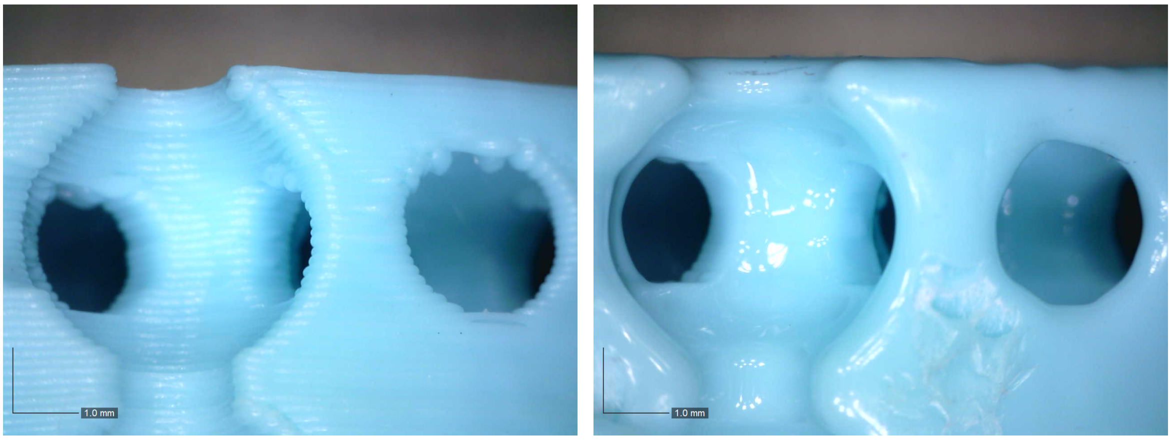

(a) Raw part (b) Post-processed part

Figure D.6: Surface finish of inner cavity of FDM PolySmooth parts

In the final step, a cylinder assembled out of two separately manufactured sample halves (Figure D.7a) was tied with a string and post-processed, in the same manner, using Polysher. The vapour smoothed out the outer surface of the sample, shown in Figure D.7b. On the other hand, the inner surface illustrated in Figure D.7c remained rough, and the individual layer lines are clearly visible. As seen from the figures, the alcohol mist did not penetrate the structure and was effective only on outer surfaces.

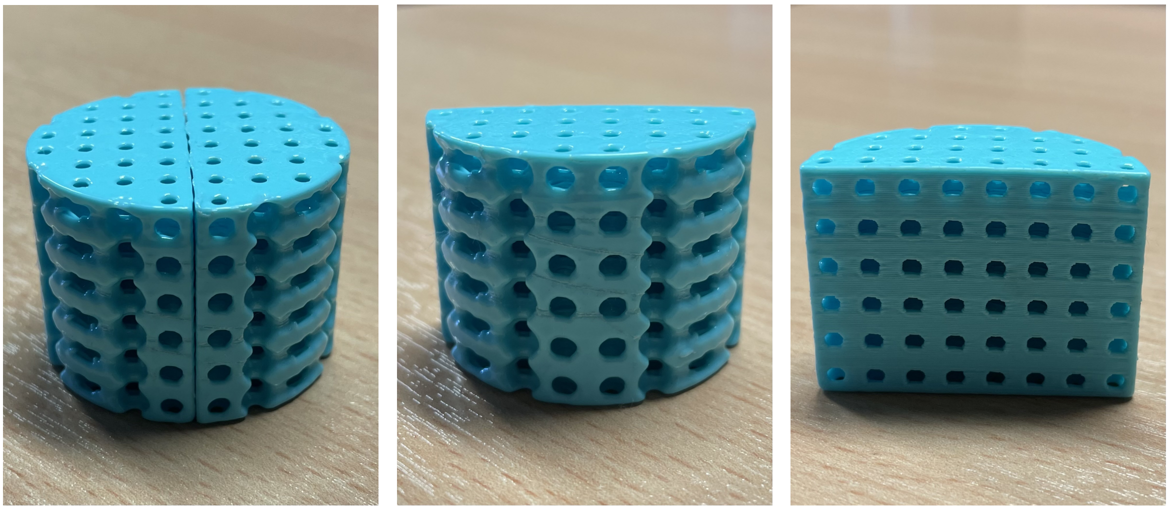

(a) Assembled cylinder (b) Outer surface (c) Inner surface

Figure D.7: Investigation of the vapour penetration depth

D.3.3 Acoustic evaluation

This evaluation compared the experimental results of 0.15 mm layer height rough (raw) and smooth (post-processed) PolySmooth samples, investigated in this section, with 0.15 mm layer height PLA sample produced with optimised printing parameters, as described in Appendix D.2.

D.3.4 Results and discussion

Figure D.8 compares the sound absorption of different FDM samples manufactured using the same layer height and the same printing settings. The post-processing of the PolySmooth part did not affect the material's behaviour, which was expected, as the alcohol vapour smoothened only the exterior surface. However, what is interesting in this data is the significant difference between the results of two not post-processed parts, PolySmooth raw and PLA. These findings suggest the acoustic characteristics of the chosen printing material have a significant influence on the performance of designed micro lattices and pore networks. Therefore, they should be considered during the acoustic material design process.

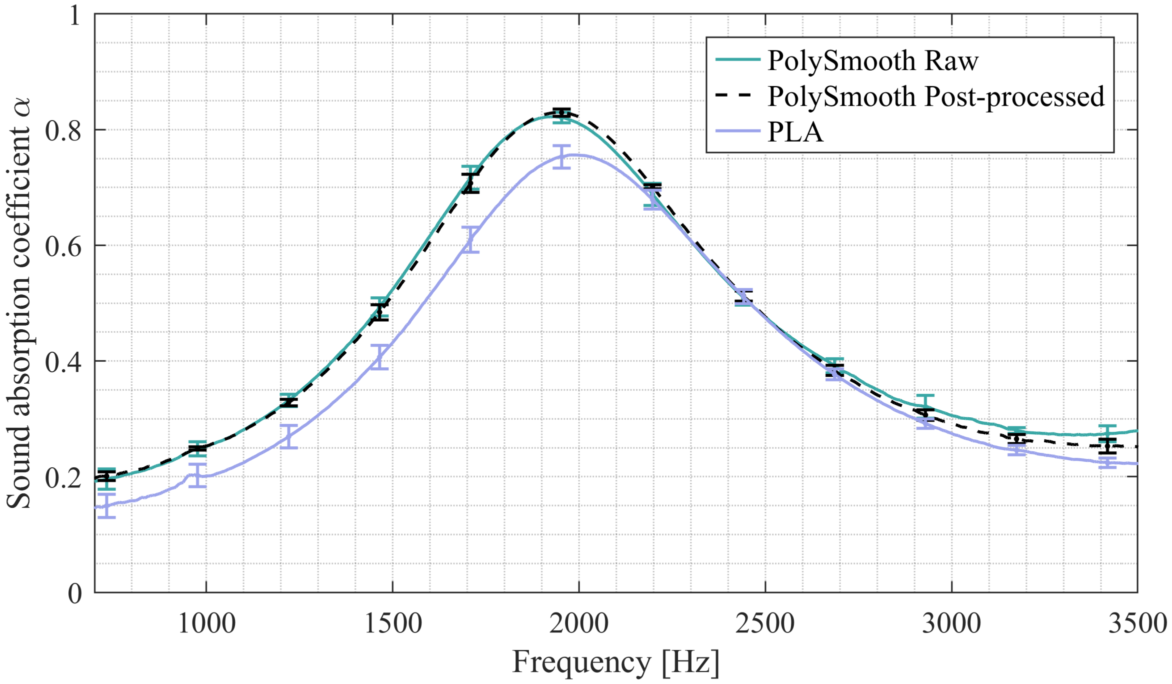

Figure D.8: Experimental results of the sound absorption coefficient: 0.15 mm layer height FDM samples

D.4 Conclusions

The present study focused on improving the quality of FDM parts and determining its effect on the acoustic performance of manufactured samples. Two major approaches for enhancing the quality in additive manufacturing include pre-processing by optimising printing parameters before production and post-processing by applying additional finishing treatments to the fabricated part. The benchmark design DENORMS was the subject of this investigation. All manufacturing procedures were carried out using Prusa Mini FDM printer.

The first part of this study was undertaken to eliminate the issue of filament stringing in voids and investigate its influence on the extensive sound absorption of the whole system. For that reason, process parameters were adjusted before manufacturing. By decreasing printing speeds and lowering extruder temperature, the quality of samples was enhanced, and DENORMS voids were no longer subject to the presence of filament fibres. This improvement enabled the experimental curves of sound absorption to shift closer to the numerical predictions. Furthermore, the shape of experimental curves changed, especially in lower frequency region, and began to resemble the numerical curve more. Nevertheless, the FDM samples are still subject to other 3D printing defects, such as surface roughness, microporosity of build material and reduced dimensional accuracy, which increase the magnitude of the experimental peak and shift its position compared with the numerical prediction.

The second part of this study set out to determine the effectiveness of post-processing in improving the quality of FDM parts. That being the case, the benchmark design was manufactured using the optimised printing parameters and 0.15 mm layer height. In addition, the printing material was changed from the default PLA to the special PolySmooth filament, explicitly designed for the Polysher post-processing unit to create 3D models with smooth surfaces. Produced parts underwent vapour smoothing procedures in Polysher. The visual inspection showed that alcohol mist smoothed only outer surfaces and did not penetrate deeper inside the lattice. Therefore, no considerable differences were observed between the control, raw PolySmooth sample and post-processed PolySmooth samples. However, a comparison between both types of PolySmooth samples and previously investigated PLA samples showed a significant influence of the chosen filament on the acoustic behaviour of the benchmark design. These findings suggest that the printing material's properties should always be considered.

These findings provide valuable insights for future research. Applied pre-processing by optimising process parameters and choice of printing material proved to have a substantial effect on the acoustic properties of the 3D printed benchmark design. However, considerably more work will need to be done to improve the effectiveness of post-processing vapour techniques in smoothing interior or micro lattice structures.

It is better to keep microfibers, microporosity and similar imperfections as they increase sound absorption. However, these effects should be taken into account during numerical modelling, which is not an easy task.

Appendix E

Acoustic models

E.1 Sound absorption model for normal incidence

Consider a flat wall at $x = 0$ with perforations of diameter d in a square array with distance H between perforations. The perforations have a depth $L >> d$ and are closed at $x = L$. This sample is placed in a wide impedance tube. For a theoretical model, we isolate one single perforation. The acoustic field in the impedance tube in the region I ($x < 0$) is the superposition of an incoming plane wave of amplitude p_I^+ and a reflected plane wave with amplitude p_I^- (at $x = 0$).

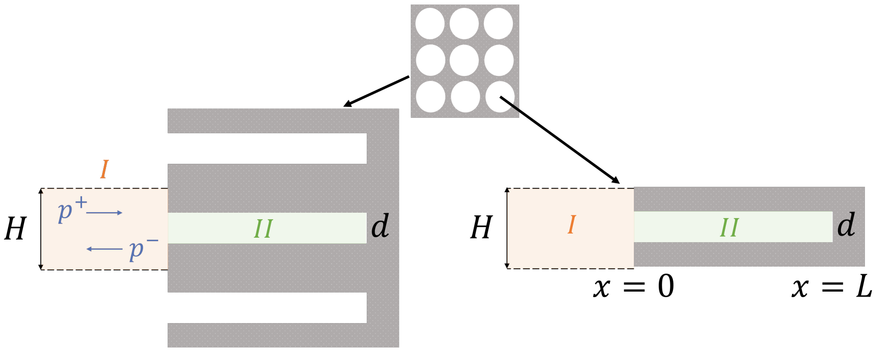

Figure E.1: Absorption model - schematic

Consider, as an approximation, a semi-infinite duct of square cross-section area H^2 ($x < 0$) terminated at $x = 0$ by a rigid flat wall with at its centre a perforation of diameter $d < H$. For region II (within the perforation $x > 0$), there is a uniform pipe of cross-section diameter d and length L terminated by a closed wall, as illustrated in Figure E.1. The square-duct walls are actually 'virtual' boundaries. Hence, there are no visco-thermal losses on these boundaries due to symmetry. The losses due to interaction with the flat wall at $x = 0$ will be neglected. The losses are assumed to be due to visco-thermal effects in the perforation. The effect of the non-uniformity of the acoustic field at the perforation inlet will be neglected. This effect can be taken into account by adding an end correction to the perforation depth [17, 18, 43–45]. It appears to be a small correction ($O(d)$) that will be neglected.

A plane wave propagation and a high Stokes number ($St = \frac{d}{\delta_v} >> 1$) are assumed. The viscous boundary layer thickness δ_v is given by Equation (E.1).

$$\delta_v = \sqrt{\frac{2\mu}{\rho\omega}} \tag{E.1}$$

where μ is the dynamic viscosity, ρ is the density of air saturating the perforation and duct, and $\omega = 2\pi f$ is the angular frequency (f is the standard frequency).

The acoustic field in the region I (the wide impedance tube) is given by Equation (E.2).

$$p(x,t) = (p_I^+ e^{-ik_I x} + p_I^- e^{ik_I x})e^{i\omega t} \tag{E.2}$$

where the wavenumber $k_I = k_0 = \frac{\omega}{c_0}$ (here, k_0 and c_0 are the wavenumber and speed of sound in air, respectively). The acoustic field in region II (the narrow perforations) is given by Equation (E.3).

$$p(x,t) = (p_{II}^+ e^{-ik_{II} x} + p_{II}^- e^{ik_{II} x})e^{i\omega t} \tag{E.3}$$

The wave number k_{II} is given by Equation (E.4).

$$k_{II} = k_0(1 + (1-i)\frac{\delta_v}{d}(1 + \frac{\gamma - 1}{\sqrt{Pr}})) \tag{E.4}$$

where γ is the Poisson ratio of specific heats and Pr is the Prandtl number for air.

The p_I^+ is given. By neglecting the heat transfer at the closed pipe termination $x = L$, the boundary condition in the first-order approximation is given by Equation (E.5).

$$p_{II}^+ e^{-ik_{II}L} - p_{II}^- e^{ik_{II}L} = 0 \tag{E.5}$$

The application of the equation of momentum (linearised Bernoulli's equation) to the transition between region I and region II yields, in first-order approximation, a continuity of pressure given by Equation (E.6) [17, 18].

$$p_I^+ + p_I^- = p_{II}^+ + p_{II}^- \tag{E.6}$$

The mass conservation equation implies first-order approximation given by Equation (E.7).

$$H^2 k_0 (p_I^+ - p_I^-) = \frac{\pi(d - (1-i)\delta_v)^2}{4} k_{II}(p_{II}^+ - p_{II}^-) \tag{E.7}$$

The above equations are used to find normalised impedance $z = \frac{Z}{Z_0}$, where Z_0 is the characteristic impedance of air and Z is the surface impedance at $x = 0$ ('seen' form $x < 0$), which is determined by Equation (E.8) (valid only for $\frac{d}{\delta_v} >> 1$).

$$z = \frac{1+R}{1-R} = \frac{k_{II}}{k_0}\left(\frac{1 + e^{-2ik_{II}L}}{1 - e^{-2ik_{II}L}}\right)\frac{4}{\pi}\left(\frac{H}{(d - (1-i)\delta_v)}\right)^2 \tag{E.8}$$

where $R = \frac{z-1}{z+1}$ is the reflection coefficient which can be used to calculate the absorption coefficient $\alpha = 1 - |R|^2$.

In the first approximation, the maximum absorption is expected to be close to the quarter wavelength resonance $e^{2ik_0L} = 1$. This allows an estimation of the absorption coefficient.

E.1.1 Prediction of an optimum absorption

Considering the geometry described above (Figure E.1) with $H = 5$ mm and $L = 30$ mm, the absorption coefficient α has been calculated as a function of the frequency f for various diameters. The value of the pitch $H = 5$ mm of the perforation array and of the pore depth $L = 30$ mm correspond to the DENORMS model. The pore diameter d has been varied around the value used for the DENORMS geometry $d = 2.00$ mm, allowing comparison between the DENORMS porous plate and the simple straight channel perforations. Results are displayed in Figure E.2. One observes that a maximum in absorption occurs close to the quarter-wavelength resonance frequency of the pores $f_{resonance} \simeq \frac{c_0}{4L} = 2.86$ kHz. This maximum is because the power dissipated scales quadratically with the amplitude of the pressure fluctuations in the resonator $|p(L)|$. At resonance, this pore-pressure-fluctuation amplitude $|p(L)|$ is much larger than the incident wave amplitude $|p_I^+|$.

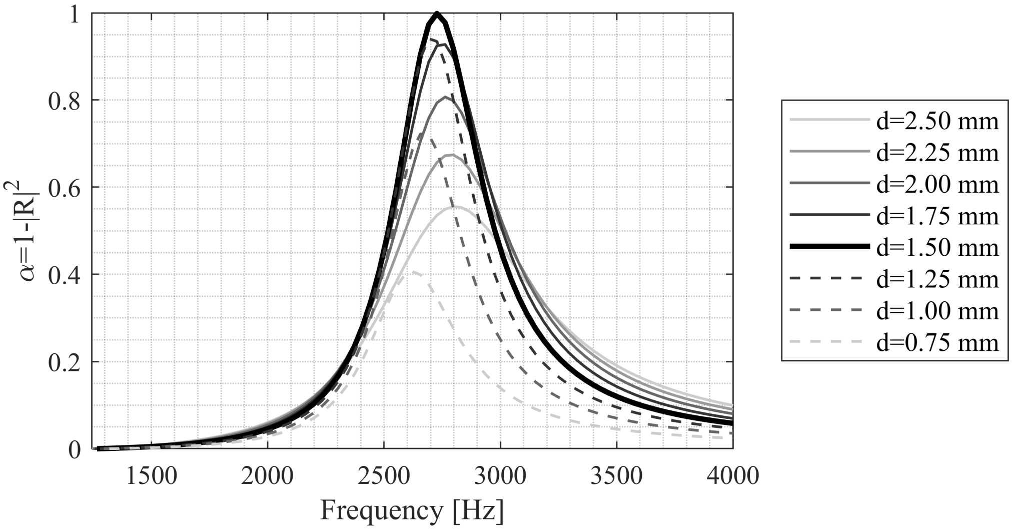

Figure E.2: Absorption model - results

Figure E.2 summarises the obtained analytical results for perforation with a varying diameter d. Data from this graph suggests that the global behaviour of the DENORMS geometry matches the performance of this simplified, perforated plate model. However, the major difference between these two geometries is the working frequency. By introducing spherical cavities to the tube resonator in the DENORMS cell, the shift of the peak frequency towards lower frequencies was achieved (about 30% lowering).

At first sight, the surprising result is the existence of an optimum value of the pore diameter d to maximize the sound absorption factor α_{max}. In the present case, the optimal diameter is $d = 1.5\ mm$. The acoustic power dissipated in the pores also scales with the square of the amplitude of the pressure fluctuations $|p(L)|$.

The ratio $Q = |p(L)/p(0)|$ of the pressure fluctuations at the closed end of the pore $|p(L)|$ to the inlet pressure fluctuation $|p(0)|$ is called the quality factor of the resonator. For given incident-wave amplitude p_I^+, the pore pressure amplitude $|p(L)|$ at the resonance frequency depends on the quality factor of the resonator, which apparently does strongly depend on d. The inlet pressure fluctuation amplitude $|p(0)|$ varies between $|p_I^+|$ for full absorption ($p_I^- = 0$) and $2|P_I^+|$ for full reflection ($|p_I^-| = |p_I^+|$). Hence, the inlet pressure $p(0)$ varies at most a factor 2 while the quality factor Q can vary by a few orders of magnitudes. For narrow tubes ($d/\delta_v = O(1)$ and $d << H$), the quality factor is limited by friction losses in the pore and is very low. The quality factor increases with increasing pore diameter d because $\mathrm{Im}[k_{II}]$ is inversely proportional to the diameter d. When the pore diameter d approaches H, the radiation from the pore to the main pipe is such that there is no resonance. The quality factor is low ($Q = 1$ because there is no resonance $|p(0)| = |p(L)|$). Therefore, one expects that there is a critical diameter for which there is a maximum of Q. This implies maximum absorption upon normal incidence α_{max}. One finds that there is (for the specified values of $H = 5.0$ mm and $L = 30$ mm) an optimum α_{max} close to unity for $d = 1.5$ mm. This indicates that the choice of parameters ($d = 2.0$ mm) of the DENORMS geometry is reasonable but might not be optimal.

A drawback of the quarter-wavelength resonance is that it imposes a minimum plate thickness if we want to achieve a specific resonance frequency. This plate thickness can be reduced by coiling up the pore [15, 40, 41, 46, 145].

E.1.2 Comparison with the numerical and experimental results

Figure E.3 provides a comparison of experimental and numerical results presented in Chapter 4 with the analytical predictions obtained from the model discussed in this Appendix. The experimental curve represents the results of the highest-quality SLM samples, and the numerical curve represents the results of the smooth COMSOL model. Two analytical curves were drawn on this graph, one closely corresponding to the DENORMS geometry (perforation length $L = 30$ mm and diameter $d = 2$ mm) and a second one with parameters altered in such a way to match the numerical curve closely (perforation length $L = 41$ mm and diameter $d = 2.7$ mm).

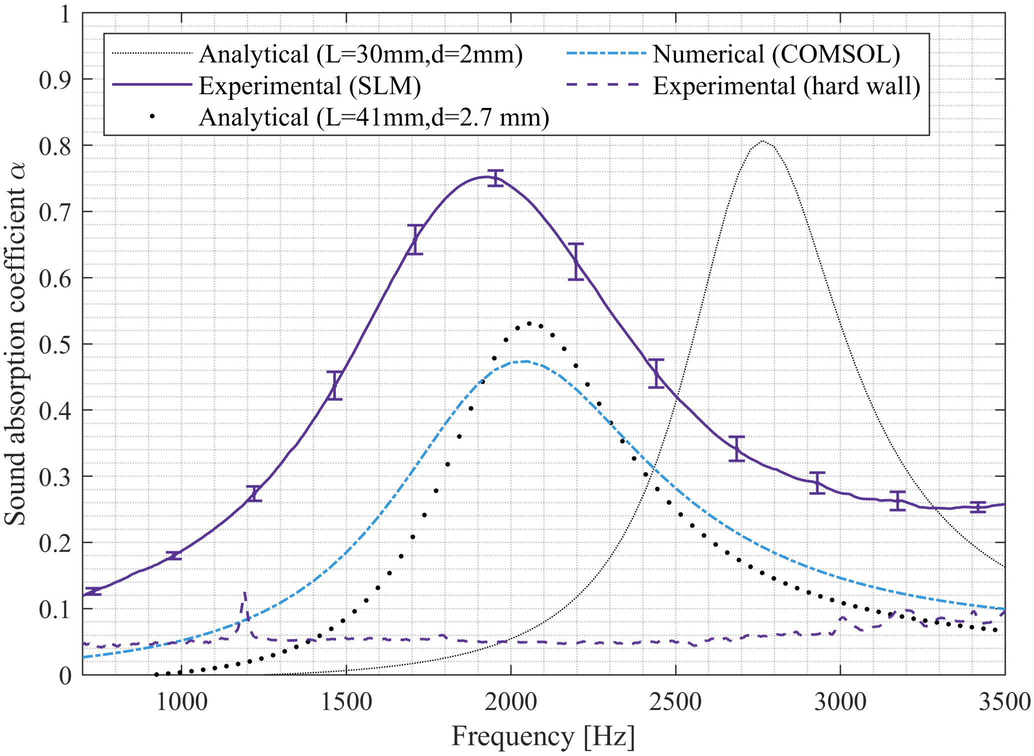

Figure E.3: Sound absorption results comparison

Based on this data, it is evident that the analytical model can effectively capture the performance of the DENORMS geometry. Furthermore, the model offers a reasonable prediction of the order of magnitude without the need for parameter tuning. The observed absorption peak can be attributed to a quarter-wavelength resonance, with a quality factor significantly affected by radiation losses.

The uncertainty of about 3 % in the perforation radius between different physical samples was demonstrated through digital microscopy and discussed in detail in Section 4.3.1. This reduced dimensional accuracy caused by additive manufacturing contributes to the variations in the experimental results. It can be used to explain differences demonstrated through the error bars. However, it is not the most important cause for the mismatch between experimental results and analytical or numerical predictions.

Finally, Figure E.3 has been supplemented with an experimental curve of a hard wall termination. Theoretically, such a metal plate should be almost perfectly reflective, and, therefore, its absorption coefficient should be close to zero. The absorption due to heat transfer at a flat wall follows Landau and Lifchitz [146] $\alpha = 4\frac{\gamma-1}{c}\sqrt{\frac{\pi f \nu}{Pr}} = O(10^{-3})$ in the kHz range. The non-zero absorption in an empty impedance tube is also due to losses on the tube walls. Therefore, the presented experimental results of the hard wall termination indicate the extent of the measurement error (10%). This suggests that, especially in the higher-frequency region, the behaviour of the impedance tube can at least partially explain the difference between theory and experiment.

E.2 Transmission loss model for a muffler

E.2.1 Single lumped side branch model

Consider a main duct segment with a surface area S and N thin cylindrical perforations with diameter d in the side walls, see Figure E.4(a). The perforations have a depth $L >> d$ and are closed at $y = +L$. For a very crude theoretical model, all the perforations are lumped together into a single side branch of a surface area S_p. Plane waves are assumed in this side branch with a wave number k_{II} corresponding to the wave number calculated using the thin Stokes boundary layer approximation (Eq. E.4). Assuming low frequencies, the acoustic field in the main pipe is also described in terms of plane waves. The acoustic field in the duct in the region I ($x < 0$), see Figure E.4(b), is the superposition of an incoming plane wave of amplitude p_I^+ and a reflected plane wave with amplitude p_I^- (at $x = 0$). In the main pipe, it is assumed that visco-thermal dissipation is negligible. Hence $k_I = \frac{\omega}{c_0}$.

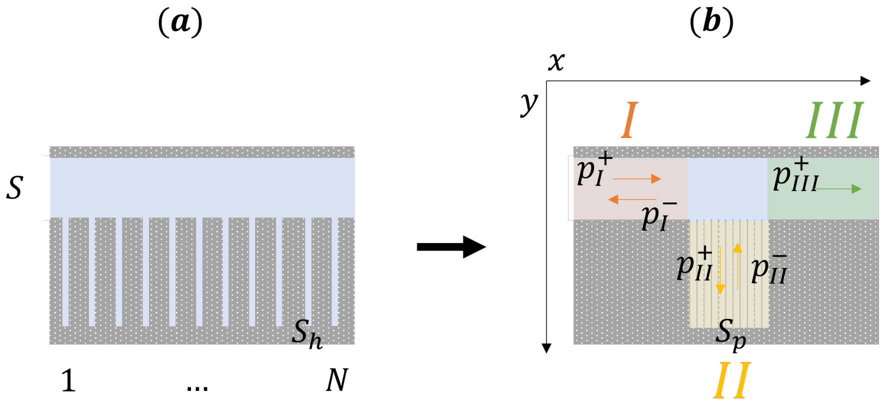

Figure E.4: Lumped side branch transmission loss model - schematic: (a) duct with N perforations, (b) duct with a single lumped side branch

For region II (within the perforation $x \approx 0$), there is a uniform pipe of length L terminated by a closed wall, as illustrated in Figure E.4(b). The surface area of a lumped perforation is given by Equation (E.9).

$$S_p = nS_h = n\frac{\pi}{4}(d - 2d_v)^2 \tag{E.9}$$

where N is the total number of perforations, S_h is the surface area of a single perforation, R_p is the radius of a single perforation and $d_v = \frac{1}{2}(1-i)\delta_v$ is the displacement thickness [147], which takes the effect of the viscosity on the volume flux into account.

The losses due to interaction with the flat wall at $y = L$ will be neglected. The losses are assumed to be due to visco-thermal effects in the perforation. The effect of the non-uniformity of the acoustic field at the perforation inlet will be neglected. This could be taken into account by introducing end-corrections to the branches of the junction [148]. The acoustic field in the region II is the superposition of an incoming plane wave of amplitude p_{II}^+ and a reflected plane wave with amplitude p_{II}^-.

The acoustic field in the duct in the region III ($x > 0$) is described only by an incoming plane wave of amplitude p_{III}^+. In other words, the reflected plane wave of amplitude p_{III}^- is assumed to be negligible ($p_{III}^- = 0$).

The application of the equation of momentum (Linearized Bernoulli [17, 18, 147]) to the transition between region I and region III yields:

$$|p_I - p_{III}| = \left|\rho\frac{d}{dt}\int_I^{III} \vec{u}.d\vec{x}\right| = O\left(\frac{\omega|p_{III}|D}{c_0}\right) \tag{E.10}$$

Hence, in first-order approximation for low frequencies ($kD << 1$ with D the characteristic length scale of the junction), there is a continuity of pressure given by Equation (E.11).

$$p_I^+ + p_I^- = p_{III}^+ \tag{E.11}$$

The application of the equation of momentum (Linearized Bernoulli Equation (E.10)) to the transition between region I and region II yields, in first-order approximation, a continuity of pressure given by Equation (E.12).

$$p_I^+ + p_I^- = p_{II}^+ + p_{II}^- \tag{E.12}$$

The amplitude of the velocity fluctuation outside the viscous boundary layers u_i in region $i = I, II$ or III is given in terms of the wave amplitude by:

$$u_i = \frac{k_i}{\rho\omega}(p_i^+ - p_i^-) \tag{E.13}$$

The corresponding volume flux is this velocity multiplied by the cross-sectional area corrected for the displacement thickness times the perimeter. Neglecting the mass change in the junction of the main pipe and the side branch, one should have a continuity of volume fluxes at the junction [18]. This is a consequence of the linearized integral mass conservation law at low frequencies $kD << 1$. The continuity of volume flux at the junction is given by Equation (E.14)

$$p_I^+ - p_I^- - p_{III}^+ = \left(\frac{k_{II}}{k_I}\right)\left(\frac{S_p}{S}\right)(p_{II}^+ - p_{II}^-) \tag{E.14}$$

The condition of zero velocity at $y = +L$, the closed end-wall of the perforations, is described by Equation (E.15).

$$p_{II}^+ e^{-ik_{II}L} - p_{II}^- e^{ik_{II}L} = 0 \tag{E.15}$$

By combining the above equations, one finds Equation (E.16):

$$\frac{-2p_I^-}{p_I^+ + p_I^-} = (\frac{k_{II}}{k_I})\frac{S_p i \tan(k_{II}L)}{S} \tag{E.16}$$

The reflection coefficient R is then calculated as per Equation (E.17).

$$R = \frac{p_I^-}{p_I^+} = \frac{-(\frac{k_{II}}{k_I})(\frac{iS_p\tan(k_{II}L)}{2S})}{1 + (\frac{k_{II}}{k_I})(\frac{iS_p\tan(k_{II}L)}{2S})} \tag{E.17}$$

where $k_I \approx \frac{\omega}{c_0}$.

The transmission coefficient T is given by Equation (E.18).

$$T = \left|\frac{p_{III}^+}{p_I^+}\right| = \left|1 + \frac{p_I^-}{p_I^+}\right| \tag{E.18}$$

Finally, the transmission loss TL of the considered system is obtained through Equation (E.19).

$$TL = -20\log_{10}(T) \tag{E.19}$$

Prediction of transmission loss

Considering the geometry described above (Figure E.4) with $L = 118$ mm and $N = 91$, the transmission loss TL has been calculated as a function of the frequency f for various perforation diameters d. The chosen values of perforation depth $L = 118$ mm and the number of perforations $N = 91$ correspond to the DENORMS-based silencer geometry discussed in Chapter 7. By varying the perforation radius R_p around the value employed in the DENORMS-based silencer geometry ($R_p = \frac{d}{2} = 3.75$ mm), a comparison can be made between the DENORMS-based porous sample and the simple straight channel perforations. The results are presented in Figure E.5. It is evident from the graph that the transmission loss increases with an increase in the perforation radius.

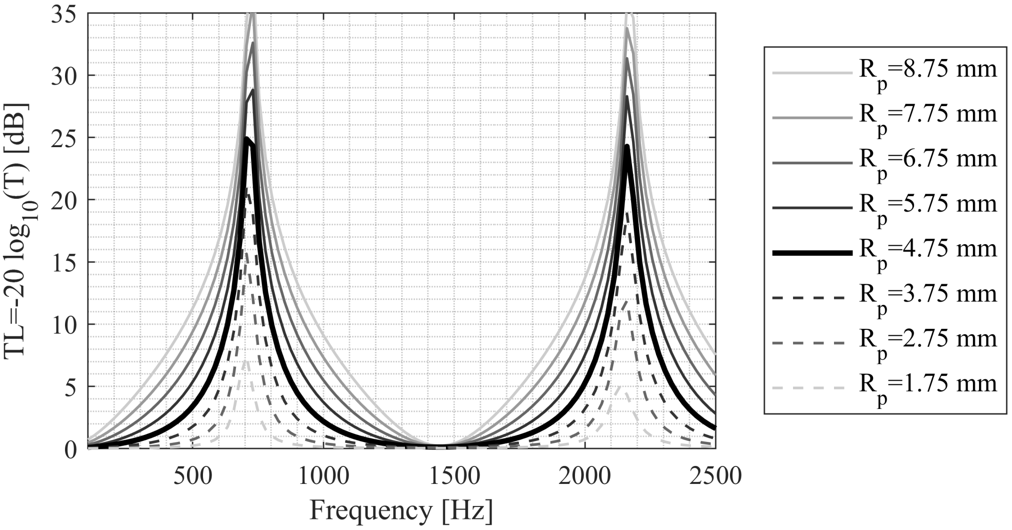

Figure E.5: Lumped side branch transmission loss - results

Figure E.5 provides a comprehensive overview of the analytical results obtained for perforations with varying radii R_p. These data can be cross-referenced with the information presented previously in Chapter 7. Such a comparison reveals that the analytical model effectively predicts the order of magnitude of damping. However, the primary distinction between these two geometries lies in their operational frequencies. By incorporating spherical cavities into the tube resonator within the DENORMS-based geometry, a noticeable shift of the peak frequency towards lower frequencies was achieved, resulting in a significant reduction of approximately 20% in the peak frequency. A steady increase in transmission losses with the increase in perforation radius R_p can be observed. This indicates that the contribution of the perforations is, to a large part, a reactive contribution. In the frictionless limit, a quarter-wavelength side branch imposes a zero transmission $T = 0$ (singularity in TL). Finite transmission losses at the quarter-wavelength resonance frequency are due to friction losses in the side branch.

E.2.2 Multiple side branches model

Consider a main duct with a cross-sectional surface area S. In the side walls of the duct (x, z) plane, there are N rows of M perforations; see Figure E.6(a). The rows are in the z direction. The distance in the x direction between successive rows is H. Each perforation is circular with a radius $R_p = d/2$. The perforations have a depth $L >> R_p$ and are closed at $y = +L$. For a theoretical model, we lump all M perforations of each row (in the z direction) together into one side branch of a cross-sectional surface area S_h. There are N of such lumped side branches in the x direction; see Figure E.6(b). While considering a single such side branch shown in Figure E.6(c), three different positions along the main duct can be distinguished: $j-1$ just after the $n-1 = \left[\frac{1}{2}(j+1)-1\right]$-th side branch, j just before the $n = \frac{1}{2}(j+1)$-th side branch and $j+1$ just after the $n = \frac{1}{2}(j+1)$-th side branch.

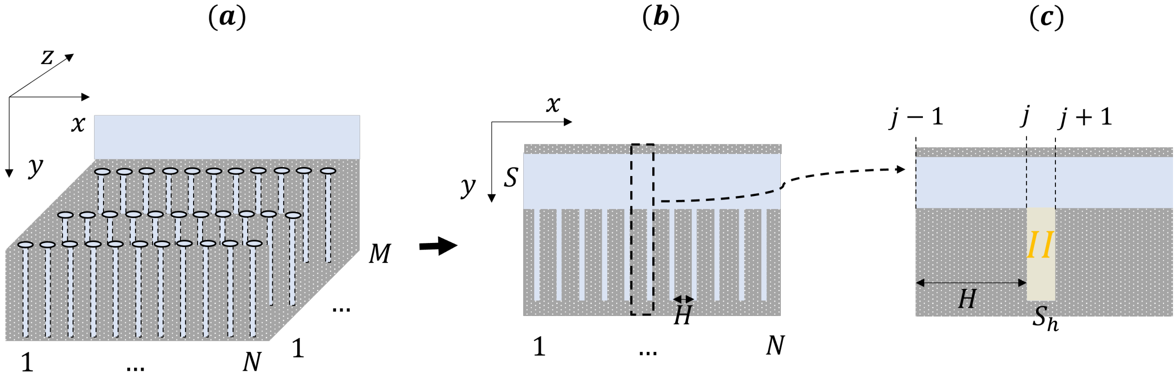

Figure E.6: Multiple side branches transmission loss model - schematic: (a) the perforations are organized in N rows of M perforations, the row is along the z-direction, (b) each row of M perforations is lumped into a side branch, the distance in the x-direction (along the main channel axis) between two successive rows is H, (c) a close-up of the side branch $n = \frac{1}{2}(j+1)$

The acoustic field in position j is described by the superposition of the plane waves p_j^+ and p_j^-, which are related to the plane waves p_{j-1}^+ and p_{j-1}^- at position $j-1$ by Equation (E.20) and Equation (E.21), respectively.

$$p_j^+ = e^{-i\frac{\omega}{c_0}H} p_{j-1}^+ \tag{E.20}$$

$$p_j^- = e^{+i\frac{\omega}{c_0}H} p_{j-1}^- \tag{E.21}$$

where H is the distance between two rows of M perforations lumped into a side branch.

The application of the equation of momentum (Linearized Bernoulli Eq.E.10) to the transition between positions $j-1$ and j along the main duct yields in first-order approximation a continuity of pressure given by Equation (E.22).

$$p_j^+ + p_j^- = p_{j+1}^+ + p_{j+1}^- \tag{E.22}$$

The application of the equation of momentum (Linearized Bernoulli) to the transition between position j and the region II inside separated perforation yields, in first-order approximation, a continuity of pressure given by Equation (E.23).

$$p_j^+ + p_j^- = p_{II}^+ + p_{II}^- = p_{II}^+(1 + e^{-2ik_{II}L}) \tag{E.23}$$

The continuity of volume flux is given by Equation (E.24).

$$p_j^+ - p_j^- - p_{j+1}^+ + p_{j+1}^- = (\frac{S_h}{S})(p_{II}^+ - p_{II}^-) = (\frac{S_h k_{II}}{S k_0}) p_{II}^+ (1 - e^{-2ik_{II}L}) = (\frac{S_h k_{II}}{S k_0})(p_j^+ + p_j^-) i \tan(k_{II}L) \tag{E.24}$$

where $S_h = M\frac{\pi}{4}(d - 2d_v)^2$ is the area of the side branch (lumped row of M perforations), $d = 2R_p$ is the diameter of the perforation and $d_v = \frac{1}{2}(1-i)\delta_v$ is the displacement thickness.

The condition of zero velocity at $y = +L$, the closed end-wall of the perforation, is described by Equation (E.25).

$$p_{II}^+ e^{-ik_{II}L} - p_{II}^- e^{ik_{II}L} = 0 \tag{E.25}$$

The reflection coefficient R is given as:

$$R = \frac{p_{inlet}^-}{p_{inlet}^+} = \frac{p_{j=1}^-}{p_{j=1}^+} \tag{E.26}$$

The transmission coefficient T is given as:

$$T = \frac{p_{outlet}^+}{p_{inlet}^+} = \frac{p_{j=2N}^+}{p_{j=1}^+} \tag{E.27}$$

By combining the above equations, one finds Equations (E.28) to (E.31).

$$\begin{bmatrix} 1 & 1 \\ (1-\frac{c_0 k_{II}}{\omega}\frac{S_h}{S} i\tan(k_{II}L)) & (-1-\frac{c_0 k_{II}}{\omega}\frac{S_h}{S} i\tan(k_{II}L)) \end{bmatrix} \begin{bmatrix} p_j^+ \\ p_j^- \end{bmatrix} = \begin{bmatrix} 1 & 1 \\ 1 & -1 \end{bmatrix} \begin{bmatrix} p_{j+1}^+ \\ p_{j+1}^- \end{bmatrix} \tag{E.28}$$

$$\begin{bmatrix} p_{j+1}^+ \\ p_{j+1}^- \end{bmatrix} = \begin{bmatrix} \frac{1}{2} & \frac{1}{2} \\ \frac{1}{2} & -\frac{1}{2} \end{bmatrix} \begin{bmatrix} 1 & 1 \\ (1-\frac{c_0 k_{II}}{\omega}\frac{S_h}{S} i\tan(k_{II}L)) & (-1-\frac{c_0 k_{II}}{\omega}\frac{S_h}{S} i\tan(k_{II}L)) \end{bmatrix} \begin{bmatrix} p_j^+ \\ p_j^- \end{bmatrix} = A \begin{bmatrix} p_j^+ \\ p_j^- \end{bmatrix} \tag{E.29}$$

$$\begin{bmatrix} p_j^+ \\ p_j^- \end{bmatrix} = \begin{bmatrix} e^{-i\frac{\omega}{c_0}H} & 0 \\ 0 & e^{i\frac{\omega}{c_0}L} \end{bmatrix} = B \begin{bmatrix} p_{j-1}^+ \\ p_{j-1}^- \end{bmatrix} \tag{E.30}$$

$$\begin{bmatrix} p_{j+1}^+ \\ p_{j+1}^- \end{bmatrix} = AB \begin{bmatrix} p_{j-1}^+ \\ p_{j-1}^- \end{bmatrix} \tag{E.31}$$

Finally, a model with N side branches (lumped rows of M perforations) and anechoic pipe termination ($p_{j=2N}^- = 0$) can be described by Equation (E.32).

$$(AB)^N \begin{bmatrix} 1 \\ R \end{bmatrix} = \begin{bmatrix} T \\ 0 \end{bmatrix} \Rightarrow TL = -20\log_{10}(T) = -10\log_{10}(T^2) \tag{E.32}$$

Prediction of transmission loss

Considering the geometry described above (Figure E.6) with $L = 118$ mm perforation length, distance $H = 10$ mm between rows of perforations, $N = 13$ rows ($N = N_l + N_s = 8 + 5$, as per Figure E.7) of $M = 7$ perforations, the transmission loss TL has been calculated as a function of the frequency f for various diameters. The selected values of perforation depth $L = 118$ mm and the number of perforations $N\ x\ M = 91$ correspond to the DENORMS-based silencer geometry discussed in Chapter 7.

Although in the physical samples, the distance between almost all perforations was $H = 20$ mm, in the simplified analytical model, we stack all the perforations from the larger (subjacent) and smaller (superjacent) structures next to each other into one structure. As the total length of the duct should be similar to the experimental one, we need to divide the original distance by two to fit all the perforations into one similar-sized block, and as a result,

$H = 10$ mm. The main channel cross-sectional area $S = 0.04 \times 0.15\text{m}^2$ corresponds to the narrowest cross-section of the muffler channel.

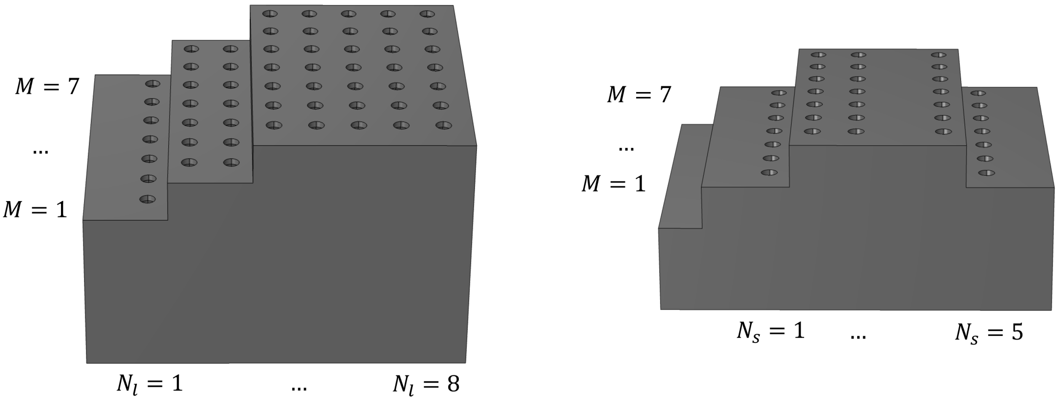

(a) Larger structure (b) Smaller structure

Figure E.7: N rows of M perforations in transmission loss samples used on the sides of the inlet section of the muffler channel (the shape of the channel is shown in Fig. 7.10)

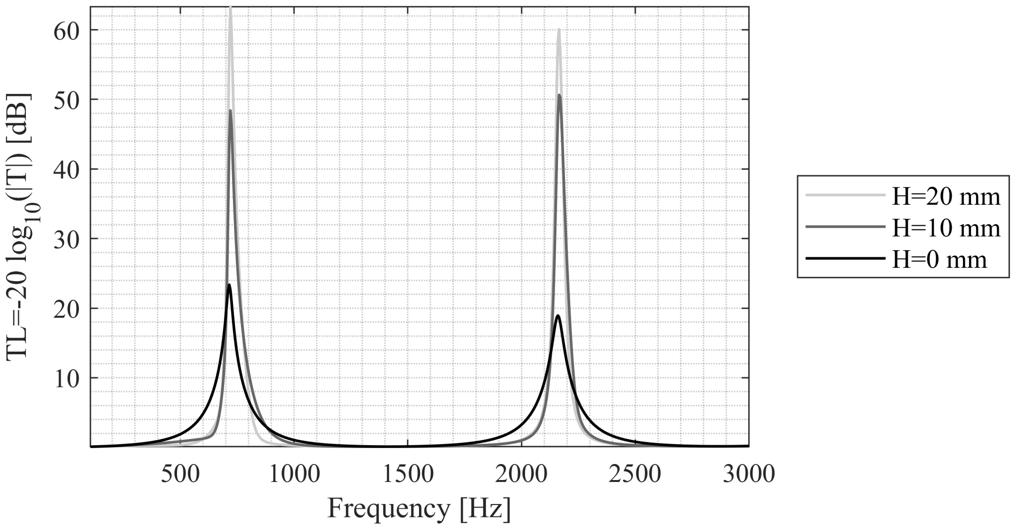

Figure E.8: Multiple side branches transmission loss - results. Influence of the distance between perforations H for a model with perforation radius $R_p = 3.75$ mm and perforation depth $L = 118$ mm

Figure E.8 highlights the influence of the distance between perforations H on the transmission loss. By lowering it from $H = 20$ mm to $H = 10$ mm, more reasonable results are generated. It should be noted that by setting $H = 0$ mm, the model lumps all perforations together, similarly to the previously discussed single-lumped side branch model. Therefore, the $H = 0$ mm curve resembles the curve drawn for $R_p = 3.75$ mm from Figure E.5.

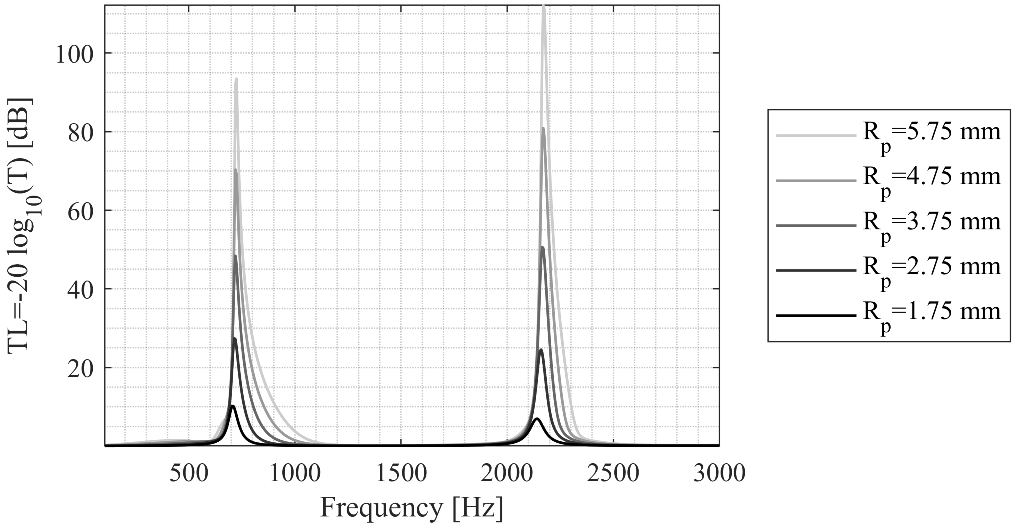

Figure E.9: Multiple side branches transmission loss - results. Influence of perforation radius for a model with $N = 13$ rows of $M = 7$ perforations ($L = 118$ mm) lumped into $N = 13$ side branches distant by $H = 10$ mm from each other

The results presented in Figure E.9 illustrate that the transmission loss increases with an increase in the perforation radius. By adjusting the perforation radius R_p around the value used in the DENORMS-based silencer geometry ($R_p = \frac{d}{2} = 3.75$ mm), a comparison can be made between the DENORMS-based porous sample and the simple straight channel perforations. The results of the multiple-side branches model, illustrated in Figure E.5, are similar to those of the single lumped side branch model, discussed in the previous section. In this case, we also observe that incorporating spherical cavities into the tube resonator within the DENORMS-based geometry resulted in a significant shift of the peak frequency towards lower frequencies. Again, for the multiple side branch model, the steady increase of transmission losses TL with increasing R_p indicates a strong contribution of reactive losses.

E.2.3 Comparison with the measured transmission losses of a muffler

Figure E.10 presents a comprehensive comparison between the experimental results of transmission loss discussed in Chapter 7 and the analytical predictions derived from the models presented in this Appendix. The experimental curve is the difference between the results of the original (unaltered) silencer and an altered silencer with a modified interior. Two analytical curves were drawn on this graph, and the parameters used for the calculations correspond to the dimensions of the samples applied to the interior of the silencer, in particular $R_p = 3.75$ mm. The number of perforations was chosen as $N = 91$ for the single lumped side branch model, and $N = 13$ rows of $M = 7$ perforations for the multiple side-branches model with $H = 10$ mm. In the multiple side-branch model, $N \times M = 91$ corresponds to the total number of perforations. The sample thickness was increased to $L = 160$ mm to shift the position of analytical peaks towards lower frequencies to an extent comparable to the experimental results. Note that the deeper perforation $L = 160$ m also reduces the transmission losses by about 8 dB compared to results for $L = 118$ mm displayed in Figure E.9.

Figure E.10 show that despite the numerous simplifications made in both analytical models, they are indeed capable of globally capturing the performance of the modified silencer. The prediction accuracy is higher for the multiple-side branch model by 22 dB compared to the single-lipped side branch model. This is because the multiple-side branches model considers the sample geometry in more detail, leading to more accurate predictions. The model provides a tool to obtain, with a minimum of computational effort, some insight into the influence of parameters such as the channel cross-sectional areas S, the perforation radius R_p, the distance between rows of perforations H, and the number of perforations $N \times M$.

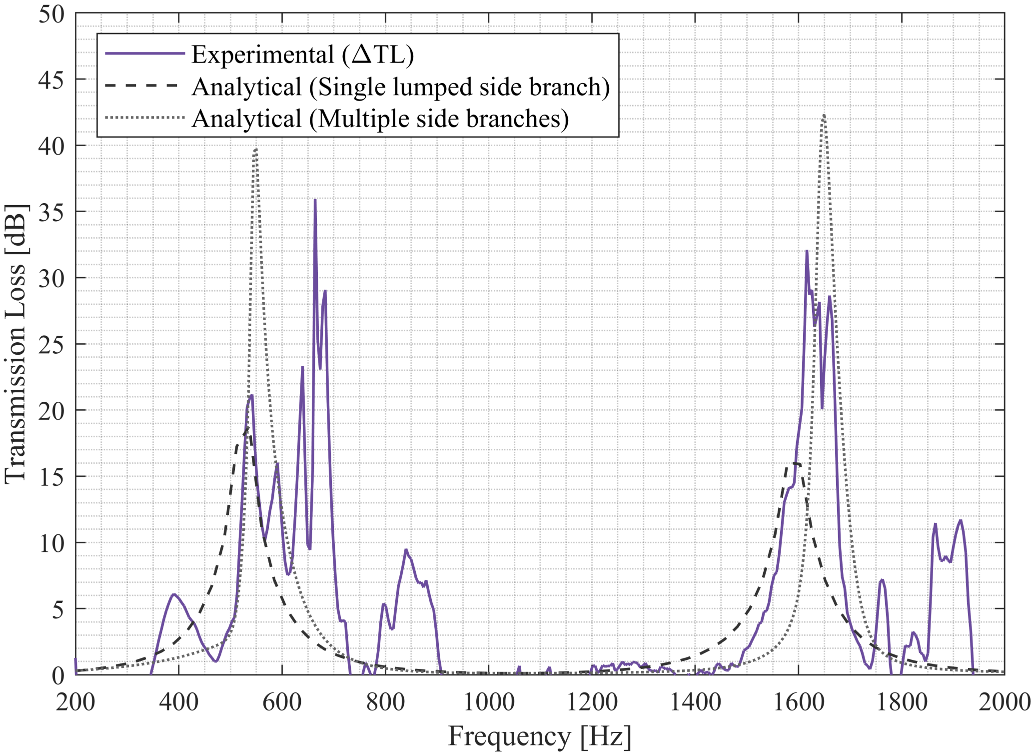

Figure E.10: Transmission loss - results comparison

The ‘multiple-peak structure’ observed in the absorption losses around the resonance frequencies could result from variations in the resonance frequency of the pores due to manufacturing defects. This is similar to the behaviour observed by Flanagan [15] in normal incidence absorption for samples with non-uniform pore depth. In the present case, it would be due to manufacturing inaccuracies, resulting in a non-uniform pore depth. The model could be extended to account for such a non-uniformity of the perforation geometry. The variation in the cross-sectional area of the main channel could also be implemented in a low-frequency, quasi-one-dimensional approximation.

E.3 Conclusions

Simplified analytical models were introduced to describe the phenomena of acoustic absorption and transmission loss. These models were developed to capture the observed performance of designed and 3D printed materials. Additionally, a comparison between DENORMS-based structures and simple straight channel perforations enabled a better understanding of the variations in performance between these two types of geometries. The main conclusions drawn from this study are as follows:

- The primary advantage of the DENORMS geometry, compared to tube resonators, lies in its operating frequency range. The introduction of spherical cavities to the tube resonator in the DENORMS cell leads to the shift of the peak frequency towards lower frequencies.

- There is an optimal cylindrical pore diameter to maximise sound absorption upon normal incidence. Therefore, while the chosen geometrical parameters of the DENORMS cell in this study are reasonable, they may not be optimal for achieving maximum sound absorption.

- The simplified low-frequency quasi-one dimensional models are useful to obtain insight into the effect of various parameters (pore geometry, number of pores, pore density, duct cross-sectional area...). They can be used for a rough scan of design parameters before carrying out time-consuming calculations with more complex models (detailed 3-D numerical simulations).